ISSN No. 2231-3273

INTERNATIONAL JOURNAL OF ENGINEERING SCIENCES AND MANAGEMENT

A Bi-annual Research Journal of

DRONACHARYA GROUP OF INSTITUTIONS

GREATER NOIDA, U.P., INDIA

Vol. IV | Issue II | Jul-Dec 2014

ISSN No. 2231-3273

INTERNATIONAL JOURNAL OF ENGINEERING SCIENCES AND MANAGEMENT

Vol. IV | Issue II | Jul-Dec 2014

ISSN No. 2231-3273

INTERNATIONAL JOURNAL OF ENGINEERING SCIENCES AND MANAGEMENT

A Bi-annual Research Journal of
DRONACHARYA
GROUP OF INSTITUTIONS
GREATER NOIDA, U.P., INDIA

Volume IV | Issue II | Jul-Dec 2014

INTERNATIONAL JOURNAL OF ENGINEERING, SCIENCES AND MANAGEMENT

Editorial Information:
For details please write to the Executive Editor, International Journal of Engineering, Sciences and Management, Dronacharya Group of Institutions, # 27, Knowledge Park-III, Greater Noida – 201308 (U.P.), India.

Telephones:
Landline: +91-120-2323854, 2323855, 2323856, 2323857
Mobile: +91-8826006878

Telefax:
+91-120-2323853

E-mail:
advisor.r&d@gnindia.dronacharya.info
director@gnindia.dronacharya.info
info@dronacharya.info

Website:
www.dronacharya.info
www.ijesm.in

ADVISORY BOARD

MEMBERS

FROM THE DESK OF
EXECUTIVE EDITOR...

Dear Readers,

It gives me immense pleasure to inform that Vol. IV / Issue II (Jul-Dec 2014) of our International Journal of Engineering Sciences & Management has been published as planned. The notable feature is that with each issue, the Journal is gaining momentum with increased visibility. This has brought great joy and happiness to the entire fraternity of the journal and honorable members of the Editorial and Advisory Board. The board members rich experience and varied expertize is providing immense succour in propelling the journal to attain an envious position in areas of research and development. The distinctive feature is indexing of the journal by Jour Informatics, Index Copernicus and DOAJ. It is a matter of great pride and honor that the journal has been viewed by researchers from seventy six countries across the globe. The aim of journal is to percolate knowledge in various research fields and elevate high end research. This objective is being pursued vigorously by providing the necessary eco-system for research and development.

Large number of research papers were received from all over the globe which underwent peer review for final acceptance. We thank all the authors for soliciting the journal. We also extend our appreciation for the efforts put in by the reviewers who so carefully perused the papers and carried out justified evaluation. Based on their evaluation, we could accept sixteen research papers for this issue across the disciplines. We are certain that these papers will provide qualitative information and thoughtful ideas to our accomplished readers. We convey our thanks to the Editorial Board, Advisory Board and all office bearers who have made possible the publication of this journal in the planned time frame.

We invite all the authors and their professional colleagues to submit their research papers for publication in our forthcoming issue i.e. Vol. V / Issue I / Jan-Jun 2015 as per the "Scope and Guidelines to Authors" given at the end of this issue. Any comments and observations for the improvement of the journal are most welcome.

We wish all readers meaningful and quality time while going through the journal.

Wg Cdr (Prof) TPN Singh [Veteran]
Executive Editor
International Journal of Engineering, Sciences and Management (IJESM)
A bi-annual Research Journal of Dronacharya Group of Institutions, Greater Noida, UP, India.

Jul 2014

CONTENTS

QUATERNION ATTITUDE ESTIMATION

Jacob S. Bailey
Graduate Student
Department of Mechanical Engineering
California State University Fullerton, Fullerton, CA 92831, USA

Sang June Oh*
Assistant Professor
Department of Mechanical Engineering
California State University Fullerton, Fullerton, CA 92831, USA
Email: sjoh@fullerton.edu
Tel: +1 657-278-2458
*Corresponding author

ABSTRACT

This paper presents a systematic approach to a low cost, readily available solution for orientation estimation using commonly available computing and sensing resources. A Quaternion state is employed to facilitate the use of the linear Kalman Filter algorithm for state estimation. Low cost, commercially available accelerometers, gyroscopes, and compass sensors are employed for measurement. The filter model is developed and simulated by use of the popular commercial software, MATLAB/Simulink. The objective of the paper is to develop a mathematical model of the system under estimation, and provide reasonable estimates of its performance, obtained through numerical simulation.

Keywords: *Quaternion, attitude, estimation, Kalman filter*

1. INTRODUCTION

The state of orientation measurement technology commercially available today is primarily focused on individual sensors. Many sensors are currently available for reasonable prices, with good performance in their intended area of application. Examples include the accelerometers used to sense tilting in computers and smartphones, and position transducers used for accurate measurement in electro-mechanical systems. However, given the performance and accuracy required by most modern robotics applications, many of these sensors fall short of expectations. Accelerometers, gyroscopes, and magnetometers are all commonly used orientation measurement devices, yet each has its own drawbacks when used in high accuracy applications. The approach taken here is to essentially combine these devices into one measurement unit, to achieve accuracy in measurement greater than the sum of individual parts.

Open source and low cost designs of similar hardware have existed in the past, with limited commercial availability, but have had issues either with still high costs (most run in excess of $100 USD), the design lacking in documentation, or the system lacking in performance. Commercial products which achieve good performance and reliability can cost in excess of $1,000 USD per unit. The system model is developed using modern computer simulation-based techniques, through the MATLAB/Simulink mathematical modeling environment. The objective of this research paper is to develop a mathematical model of the system under estimation, and provide reasonable estimates of its performance, obtained through numerical simulation. A secondary objective is to facilitate future use of Hardware-in-the-Loop (HIL) simulation/implementation via Simulink's Arduino Support Package. This technique combines computer simulation with code running on the target hardware, allowing a seamless transition between computer model and real world hardware. This work will focus on dealing with the mathematical modeling and simulation of the state dynamic model and Kalman Filter. MATLAB code will be used to verify that the performance of the proposed filter is indeed an adequate construction and coding platform in the simulation domain.

2. MATHEMATICAL MODELING

In an ideal case, a single orientation sensor, such as an accelerometer, would provide all the information necessary to accurately determine the orientation of a rigid body to which it was attached. Real world considerations, including system noise and sensor offset errors, preclude this case in all but the least critical applications. In applications which require highly accurate measurements, as in most modern robots and control systems, it is necessary to incorporate additional information about the system under measurement in order to improve estimates of its state. It is well known that Kalman Filter provides such an approach. The algorithm, pioneered by its namesake in 1960, combines system measurements with a model of the dynamics of the system [1]. The algorithm also makes a few basic assumptions on the system measurement process. The key assumption is that errors in the measurement and prediction phase can be represented by random variables with zero mean and Gaussian probability distribution. Eqs. (1) and (2) represent the generic model used in Kalman Filter.

$$x_{k+1} = Ax_k + Bu_k + w_k \quad (1)$$
$$z_k = Hx_k + v_k \quad (2)$$

The vector *x* represents the state of the system, and *z* represents the measurements made by the sensors. The vectors w and v each represent the Gaussian noise added to the system by errors in measurement and state update. The following six equations represent a brief summary of the mathematical algorithm originally proposed by Kalman [2], [3].

$$\hat{x}_0, P_0 \quad (3)$$
$$\hat{x}_k^- = A\hat{x}_{k-1} \quad (4)$$
$$P_k^- = AP_{k-1}A^T + Q \quad (5)$$
$$K_k = P_k^- H^T \left(HP_k^- H^T + R\right)^{-1} \quad (6)$$
$$\hat{x}_k = \hat{x}_k^- + K_k(z_k - H\hat{x}_k^-) \quad (7)$$
$$P_k = P_k^- - K_k H P_k^- \quad (8)$$

In this notation, the superscript ¯ implies the *a priori* information, or the prediction and covariance of that prediction, based on the state dynamics model. Given the initial conditions for the state estimate and covariance in Eq. (3), Eqs. (4) through (8) are iterated continuously to give constant estimates of the state, which are represented by vectors not having the - superscript. Q and R represent the covariance matrices of the state and measurement models, respectively.

In order to implement the Kalman Filter algorithm, the minimum model elements to be supplied by the designer are:

- State vector, $\hat{\mathbf{x}}$
- System model matrices A, H, Q, and R
- Initial values of the state estimate and covariance $(\hat{\mathbf{x}}_0, \mathbf{P}_0)$

2.1 System State Dynamics For this work, we have chosen to estimate the orientation of a rigid body which is free to move about in space. The classic method of describing the orientation of a rigid body, as observed from a fixed coordinate system, is by use of the three Euler Angles: yaw, pitch and roll. Euler Angles represent the minimum state in this case, as there are only three degrees of freedom in the body's orientation. There are an additional three degrees of freedom in the body's translational motion, but we concern ourselves here with the rotational orientation only. For the purposes of this work, we will assume a North-East-Down (NED), right-handed coordinate system for the body axes, and an Earth-Centered-Earth Fixed coordinate system for the earth axes. The coordinate system is illustrated in Figure 1.

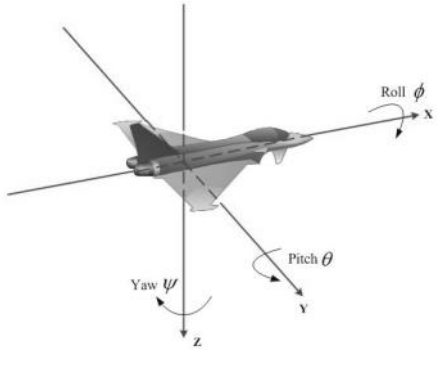

Fig. 1. North-East-Down Right-Handed Coordinate System

Euler angles, despite their ubiquity in system description, present multiple challenges to the designers of attitude estimation and control systems: nonlinear relationships in differentiation, and a phenomenon known as gimbal lock [4]. Gimbal lock occurs when one Euler angles reaches a value of +/- 90 degrees, and thus places one axis of rotation (referenced to the body) orthogonal to one of the axes of measurement (referenced to the earth). In this situation, one of the Euler angles becomes indeterminate with measurement.

The nonlinear relationship in differentiation can be seen by examining the rotation of coordinates necessary to relate the body rates, as measured by a gyroscope attached to the rigid body, to the Euler rates, as measured in the fixed reference system. In order to relate the body rates to the Euler rates, we can use the relation shown in Eq. (9). Here, p, q, and r represent the rotational rates about the body axes.

$$\begin{bmatrix} \dot{\varphi} \\ \dot{\theta} \\ \dot{\psi} \end{bmatrix} = \begin{bmatrix} 1 & \sin\varphi \tan\theta & \cos\varphi \tan\theta \\ 0 & \cos\varphi & -\sin\varphi \\ 0 & \sin\varphi \sec\theta & \cos\varphi \sec\theta \end{bmatrix} \begin{bmatrix} p \\ s \\ r \end{bmatrix} \tag{9}$$

Due to the angular nature of the computation, there is no method to rearrange Eq. (9) such that a linear relationship between Euler angles and Euler rates can be shown [3]. Thus, there is no linear representation of the system state, if the state is chosen as the Euler angles. The solution to this particular problem is a different choice in state variables. As opposed to the non-linear three rotation model shown previously, it is possible to represent the rotation of a rigid body with only one rotation, about an arbitrary axis. This approach was developed simultaneously by Rodrigues and Hamilton, and can be most easily represented through the use of the Quaternion [4]. There has been extensive study of Quaternion applied to variants of the Kalman filtering algorithm [5] – [8]. In this paper, the Quaternion is used with the most basic form of Kalman filtering as described in Section 1. Also, most of the mathematical development in Sections 2.1-2.3 are based previous work, found in references [8] – [12].

Employing the Quaternion as the rotational state allows a significant improvement in the linearity of the system dynamics. Eqs. (10) through (12) shows the new state dynamics model. It is this linearization that allows the use of the traditional Kalman Filter algorithm for estimation in this application.

$$\hat{x} = \hat{q} = \begin{bmatrix} q_1 \\ q_2 \\ q_3 \\ q_4 \end{bmatrix} \tag{10}$$

$$\dot{\hat{x}} = \frac{1}{2} \begin{bmatrix} 0 & -r & -s & -p \\ r & 0 & -p & s \\ s & p & 0 & -r \\ p & -s & r & 0 \end{bmatrix} \hat{x} \tag{11}$$

$$\dot{\hat{x}} = A\hat{x} \tag{12}$$

To conclude the discussion of state and dynamics, it is necessary to provide a model for the covariance of the state prediction noise. For the purposes of this model, we assume the noise covariance to be equal amongst all four components of the quaternion state. Expressed succinctly,

2.2. System Measurement With a linear model for system dynamics and noise in hand, we turn our attention to the system measurements. It is necessary to define the model which will be used to translate measurements taken from the sensors into updates to the state of the system, which we have modeled with the quaternion, as discussed above. We will discuss the measurement model for each individual sensor first, and combine them in the end to form one cohesive measurement model for the system.

2.2.1. Gyroscope Measurements The measurement model for the gyroscope has been discussed previously in section 2.1. Gyroscopes measure angular rates, rather than orientation. As such, the measurements from the gyroscope would need to be integrated over time, and an initial orientation assumed, in order to provide for updates to the state from the gyroscope. Since this necessarily involves some form of numerical inaccuracy when dealing with real-world implementation, and we have already included the gyroscope measurements in the state dynamics model, we will not incorporate them in the measurement model. Although the gyroscope does not provide for direct measurement of the state of the system, it does provide measurement of the rates of change for the state variables, which allows for a greater degree of accuracy in the numerical prediction portion of the filtering algorithm.

2.2.2. Accelerometer Measurements An accelerometer is a simple device which measures the magnitude of accelerations along a specific axis. The accelerometer used here is assumed to be capable of measurement in three orthogonal axes. Despite having measurement capability in three axes, however, for this purpose, the accelerometer will have at least one redundant measurement at any given time. This is due to the alignment of the gravity vector with one of the axes (the z-axis) of the coordinate system assumed for the problem. Thus, we cannot measure any rotation about this particular axis using the gravity vector alone. We can, however, measure rotation about the other two axes, using Eqs. (14) through (16). These transforms are based on those found in [3].

$$\varphi = sin^{-1}\frac{a_y}{\|\vec{g}\|} \tag{14}$$

$$\theta = sin^{-1}\frac{a_x}{(\|\vec{g}\| * cos\,\varphi)} \tag{15}$$

$$\vec{g} = a_x\hat{\imath} + a_y\hat{\jmath} + a_z\hat{k} \tag{16}$$

Here, a_x, a_y, and a_z are the measured magnitude components of the gravity vector. It is important to note that this measurement model assumes that the system under measurement experiences no significant accelerations due to its motion within the world frame (i.e. the coordinate frame within which we take the measurements is assumed to be inertial). In the event of a non-inertial body frame, adjustments would need to be made to the measurement model to accommodate these accelerations.

2.2.3. Magnetometer Measurements In order to solve the redundant measurement problem of the accelerometer mentioned earlier, we introduce one final sensor into the system: the magnetometer. A magnetometer is used to measure the strength of earth's magnetic field relative to the axis on which it operates. In this case, we will again assume a three axis measurement device. To determine the yaw angle from the magnetometer readings, we must first 'tilt-compensate' the readings. This is due to the fact that, as with the accelerometer, the readings will vary with the orientation of the sensor. Appropriately incorporating the current orientation of the system, the yaw angle can be determined from Eqs. (17) and (18), as developed by Freescale Semiconductor [13]. Since this model is to be used only for simulation purposes, no magnetic declination ('soft iron') or board level interference ('hard iron') effects are taken into consideration. A hardware implementation of this system would obviously need to account for both of these sources of error in the measurement.

$$\psi = tan^{-1}\left(\frac{B_z sin\,\varphi - B_y cos\,\varphi}{B_x cos\,\theta + B_y sin\,\theta\, sin\,\varphi + B_z sin\,\theta\, cos\,\varphi}\right) \tag{17}$$

$$\vec{B} = B_x\hat{\imath} + B_y\hat{\jmath} + B_z\hat{k} \tag{18}$$

2.2.4. Comprehensive Measurement Model At present, we have incorporated measurements from three independent sensors into the model. However, the accelerometer and magnetometer measurements are currently in a form that is unsuitable for use in our application. As discussed in Section 2.1, the orientation quaternion is chosen as the state for this model. Thus, the Euler angle measurements must be translated to quaternion form. To accomplish this, we simply apply the transformation from Euler angles to Quaternion, as shown in Eq. (19) [3].

$$\hat{q} = \begin{bmatrix} q_1 \\ q_2 \\ q_3 \\ q_4 \end{bmatrix} = \begin{bmatrix} cos\frac{\varphi}{2}cos\frac{\theta}{2}cos\frac{\psi}{2} + sin\frac{\varphi}{2}sin\frac{\theta}{2}sin\frac{\psi}{2} \\ sin\frac{\varphi}{2}cos\frac{\theta}{2}cos\frac{\psi}{2} - cos\frac{\varphi}{2}sin\frac{\theta}{2}sin\frac{\psi}{2} \\ cos\frac{\varphi}{2}sin\frac{\theta}{2}cos\frac{\psi}{2} + sin\frac{\varphi}{2}cos\frac{\theta}{2}sin\frac{\psi}{2} \\ cos\frac{\varphi}{2}cos\frac{\theta}{2}sin\frac{\psi}{2} - sin\frac{\varphi}{2}sin\frac{\theta}{2}cos\frac{\psi}{2} \end{bmatrix} \tag{19}$$

Since we have measured all the state variables, the measurement matrix can be taken as the identity matrix.

$$H = \begin{bmatrix} 1 & 0 & 0 & 0 \\ 0 & 1 & 0 & 0 \\ 0 & 0 & 1 & 0 \\ 0 & 0 & 0 & 1 \end{bmatrix} = I_4 \tag{20}$$

Finally, with the measurement model in hand, we have left only the task of providing a model of the noise inherent in the measurements. It is important to note that the measurement matrix, *H*, describes only the transfer of the measured orientation quaternion to the system model. In general, the linear Kalman Filter algorithm is only applicable to linear systems (systems which have linear state dynamics, as well as linear relationships between measurements and state). However, in this case, we are presented with a system model which involves a number of nonlinear mathematics in order to transform the measured quantities (accelerations and magnetic fields) to the state of the system.

With this in mind, it is imperative to somehow *linearize* this system in order to make it suitable for use with the Kalman Filter algorithm. By transforming the measured quantities first to Euler angles, and then to the orientation quaternion, we have done just that. The final output of the measurement functions is a Quaternion, which can be incorporated with the system in linear fashion. However, the noise model for this measurement presents a slight wrinkle. In order to keep the system linear, we can assume that the measurement noise is additive in the Quaternion space, i.e. Eq. (2) applies once we have obtained the Quaternion measurement at each time step. This is the key assumption in this implementation of Kalman Filtering.

As done previously, we will assume that the noise associated with each of the four elements of the measured Quaternion have the same statistical properties, and the covariance of the measured Quaternion can be represented as shown in Eq. (21).

$$R = \begin{bmatrix} \sigma_r^2 & 0 & 0 & 0 \\ 0 & \sigma_r^2 & 0 & 0 \\ 0 & 0 & \sigma_r^2 & 0 \\ 0 & 0 & 0 & \sigma_r^2 \end{bmatrix} = \sigma_r^2 I_4 \tag{21}$$

2.3. Discrete System Model To this point, we have successfully developed a model for the state dynamics of the system, as well as the measurements obtained through the three sensors employed. We have achieved the parameters set out in Eqs. (1) and (2). However, the model developed in the previous section assumed a continuous time system. The Kalman Filter algorithm was in fact developed for use in discrete time systems. Since the ultimate target platform is pseudo-real time digital computation on the Arduino, it is necessary to discretize the model, by making a few basic assumptions. These are summarized below.

- The entire filter will operate at a set, constant sampling frequency, f_s. This will lead to a constant period of time T between intervals.
- Measurements from each of the sensors are taken at each and every sampling instant.
- Measurement sampling takes a negligible portion of time at each sampling instant.

By these assumptions, we note that the three matrices *Q*, *R*, and *H* do not need to be changed to incorporate sampling. The state matrix, *A*, however, will need to be changed. Since *A* represents differentiation in continuous time, we can use the forward integration rule (also known as Euler integration) to convert the system to discrete time, as shown below in Eqs (22) through (24).

$$\hat{q}_{k+1} = \hat{q}_k + T\dot{\hat{q}}_k \tag{22}$$

$$\dot{\hat{q}}_k = A\hat{q}_k \tag{23}$$

$$\hat{q}_{k+1} = \hat{q}_k + T\left(A\hat{q}_k\right) = (I_4 + TA)\hat{q}_k \tag{24}$$

$$A_d = \frac{1}{2}\begin{bmatrix} 2 & -r & -s & -p \\ r & 2 & -p & s \\ s & p & 2 & -r \\ p & -s & r & 2 \end{bmatrix} \tag{25}$$

Also, as mentioned in the Introduction to Section 2, we require initial estimates of the state of the system, as well as its covariance. Given that the system will have an unknown state before the filter begins working, we will assume zero initial conditions for simplicity. This is stated mathematically in Eqs. (26) and (27).

$$\hat{x}_0 = \begin{bmatrix} 1 \\ 0 \\ 0 \\ 0 \end{bmatrix} \tag{26}$$

$$P_0 = \vec{0} \tag{27}$$

3. SIMULATION RESULTS

3.1. Step Input (simultaneous step input at X, Y, and Z axis)

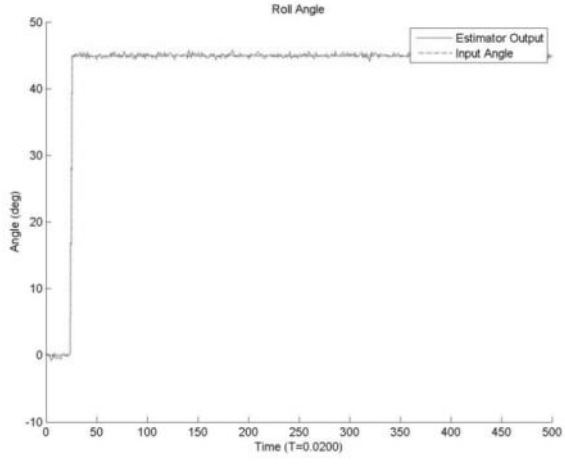

Fig. 2. Roll Angle: Estimator Output vs. Input (45 degrees, 3 axes simultaneous step input)

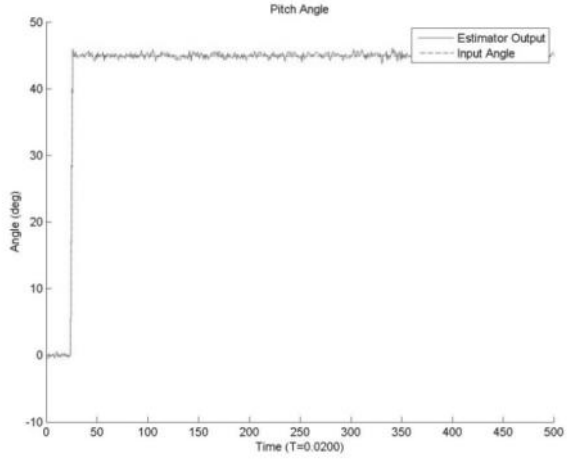

Fig. 3. Pitch Angle: Estimator Output vs. Input (45 degrees, 3 axes simultaneous step input)

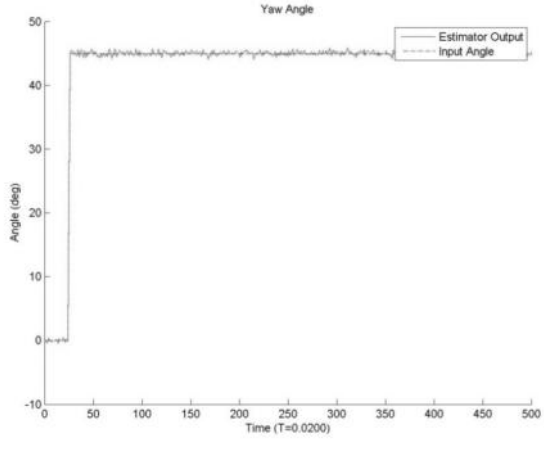

Fig. 4. Yaw Angle: Estimator Output vs. Input (45 degrees, 3 axes simultaneous step input)

3.2. Single Frequency Sinusoidal Input (simultaneous step input at X, Y, and Z axis)

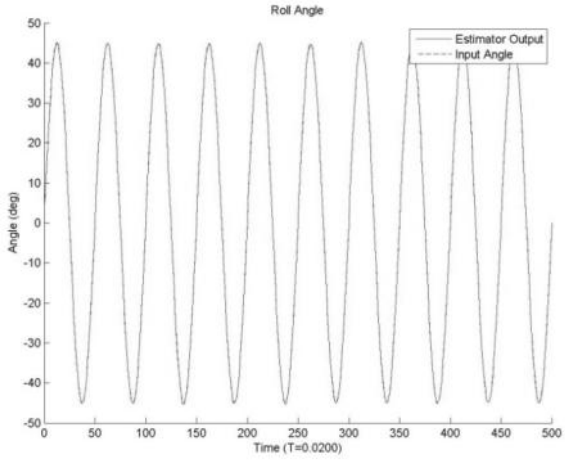

Fig. 5. Roll Angle: Estimator Output vs. Input (45 degrees sine, 3 axes simultaneous sinusoidal input)

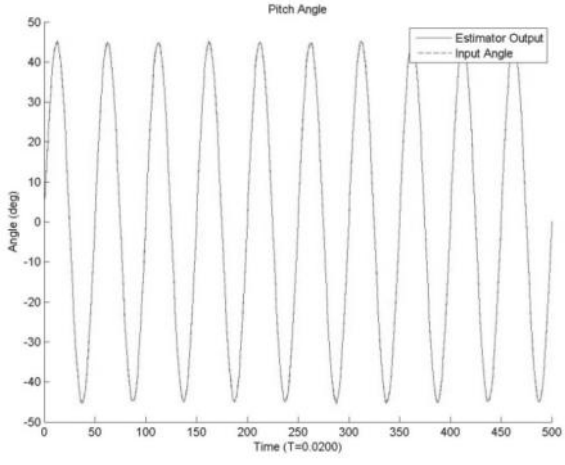

Fig. 6. Pitch Angle: Estimator Output vs. Input (45 degree sine, 3 axes simultaneous sinusoidal input)

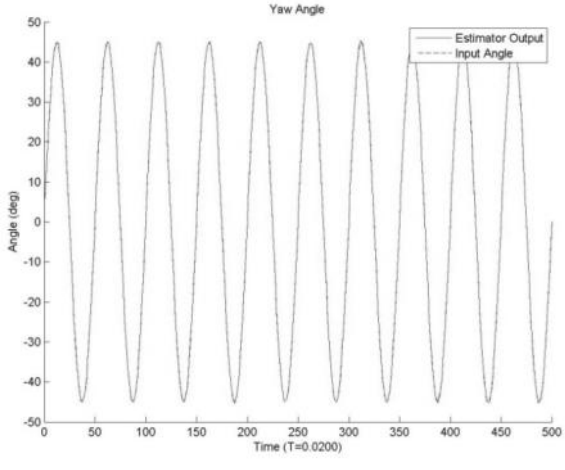

Fig. 7. Yaw Angle: Estimator Output vs. Input (45 degrees sine, 3 axes simultaneous sinusoidal input)

3.3. Multiple Frequency Sinusoidal Input (simultaneous step input at X, Y, and Z axis)

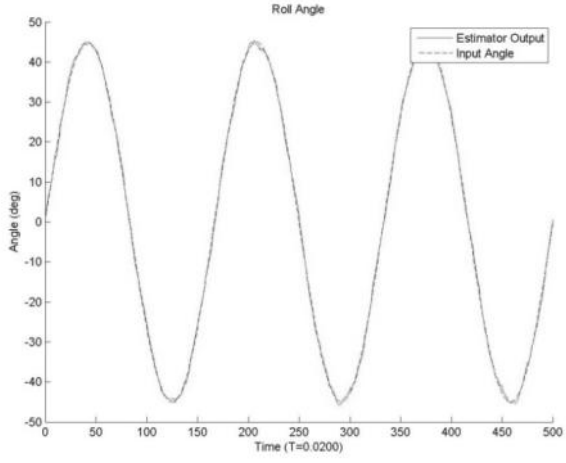

Fig. 8. Roll Angle: Estimator Output vs. Input (45 degrees sine, 3 axes multiple frequencies (0.3, 0.9, 2 Hz))

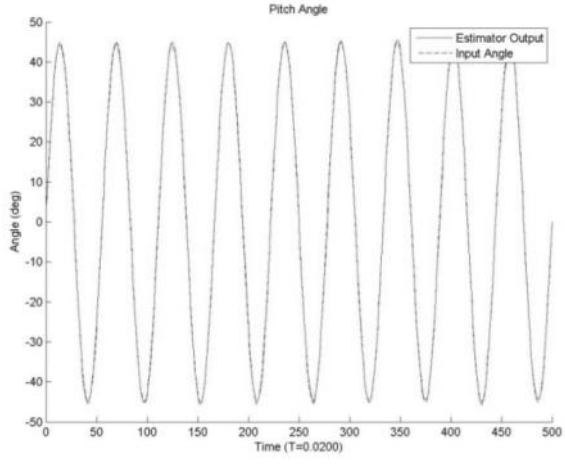

Fig. 9. Pitch Angle: Estimator Output vs. Input (45 degrees sine, 3 axes multiple frequencies (0.3, 0.9, 2 Hz))

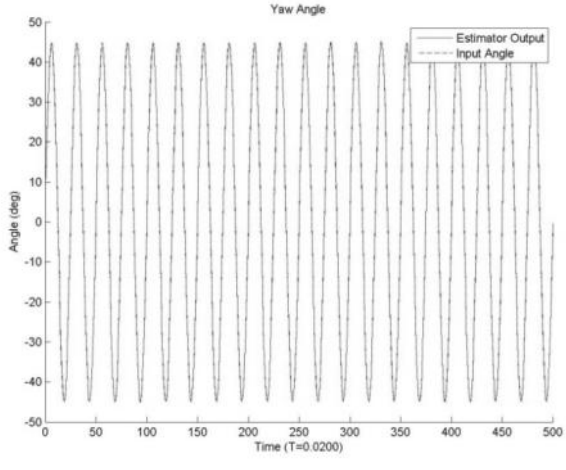

Fig. 10. Yaw Angle: Estimator Output vs. Input (45 degrees sine, 3 axes multiple frequencies (0.3, 0.9, 2 Hz))

4. CONCLUSION

Upon review of the figures presented in Section 3, it is apparent that the proposed filter has achieved satisfactory performance in estimation throughout simulation. In each test case, the estimator output in all three axes very closely matches the simulated input to the system. As expected, the combination of the three measurement devices has yielded positive results in the ability of the system to accurately measure its orientation in all three axes. It is important to note that the simulated sensor inputs included simulated device noise. The noise was assumed to be zero mean, Gaussian, and uncorrelated, since the sensors will each be independent electronic devices. The parameters used to characterize the simulated noise are shown below in Table 1.

Table 1: Summary of simulated noise parameters

Device	σ	**Units**
Accelerometer	0.005	*G*
Gyroscope	0.005	*Rad/s*
Magnetometer/Compass	0.005	*Gauss*

Indeed these are modest values to assume for the noise generated by actual measurement devices. However, they are not unreasonably small, and serve to provide a good illustration of the system and filter under expected conditions. After simulation, it is apparent that the system is primed for real world testing. For immediate future study, the system will be constructed and tested using the Arduino MEGA 2560 platform, and the results of these tests will be published.

REFERENCES

1. Kalman, R.E., *A New Approach to Linear Filtering and Prediction Problems*, ASME Journal of Basic Engineering, 82(D), 1960, pages 35-45.
2. Welch, G. & Bishop, G., *An Introduction to the Kalman Filter*, UNC-Chapel Hill, 2006, TR 95-041
3. Kim, P., *Kalman Filter for Beginners with MATLAB Examples*, Republic of Korea: A-JIN Publishing Company, 2010
4. Vince, J., *Quaternions for Computer Graphics*, London, Springer, 2011
5. Hall, J. K., Knoebel, N.B., & McLain, T. W., *Quaternion Attitude Estimation for Miniature Air Vehicles Using a Multiplicative Extended Kalman Filter*, IEEE/ION Position, Location and Navigation Symposium, 2008, pages 1230-1237
6. Lefferts, E.J., Markley, F.L., Shuster, M.D., *Kalman Filtering for Space Attitude Estimation*, Journal of Guidance, Control, and Dynamics, Vol.5, No. 5, 1982, pages 417-429
7. Baerveldt, A.J., Klang, R., *Low-cost and Low-weight Attitude Estimation System for an Autonomous Helicopter*, IEEE International Conference on Intelligent Engineering Systems (INES), 1997, pages 391-395.
8. Kim, S.-G., Crassidis, J.L., Cheng, Y, Fosbury, A.M., Junkins, J.L., *Kalman Filtering for Relative Spacecraft Attitude and Position Estimation*, Journal of Guidance, Control and Dynamics, Vol. 30, No. 1, 2007, pages 133-143
9. Choukroun, D., Bar-Itzhack, I., & Oshman, Y., *A Novel Quaternion Kalman Filter*, IEEE Transactions on Aerospace and Electronic Systems, Vol. 42, Issue 1, 2006, pages 174-190.
10. Kraft, E., *A Quaternion-based Unscented Kalman filter for Orientation Tracking*, Proceedings of the Sixth International Conference of Information Fusion, Vol. 1. 2003, pages 47-54.
11. Mayhew, C.G., Sanfelice, R.G. & Teel, A.R., *On Quaternion-Based Attitude Control and the Unwinding Phenomenon*, American Control Conference, June-July 2011, pages 299-344.
12. Yadlin, R., *Attitude Determination and Bias Estimation Using Kalman Filtering*, US Air Force Academy Report, 2009
13. Freescale Semiconductor, *Implementing a Tilt-Compensated eCompass using Accelerometer and Magnetometer Sensors*, Freescale Xtrinsic, 2012

IDENTIFICATION OF SIZE AND LOCATION OF A SINGLE BENDING CRACK IN A MARINE PROPELLER SHAFT USING STATIC PARAMETERS OF STRAIN AND DISPLACEMENT

Ridwan Hossain
Graduate Student
Faculty of Engineering & Applied Science
Memorial University of Newfoundland
230 Elizabeth Ave, St John's, NL, Canada A1B 3X9
E-mail: rbh546@mun.ca
Tel: +1 709 765 3220

Arisi S.J. Swamidas*
B.E (Civil), M.Eng (Structures), Ph.D (Eng. Mechanics) (I.I.T Madras)
Honorary Research Professor of Civil Engineering
Faculty of Engineering and Applied Science
Memorial University
St. John's, NF, Canada A1B 3X5
E-mail: aswamidas@mun.ca
Tel: (709) 737-7983
*Corresponding author

ABSTRACT

The study proposes a simpler but effective method for crack detection in a marine propeller shaft based on static displacement and strain. A small scale real life propeller shaft system used in an earlier analysis, at the Faculty of Engineering and Applied Science, Memorial University, St. John's, NL, has been used in this study; and only the weight of the system along with the added mass of the water has been considered for crack detection. A finite element analysis carried out by ABAQUS showed that cracking is possible under such loading conditions; hence a crack detection method has been proposed. The strains and displacements are measured at four different (previously identified critical) locations for un-cracked conditions and the same measurement is repeated for several pre-defined crack locations and crack depth ratios. Based on the changes in the above parameters, it is shown that crack sizes and locations can be properly identified in structures under such loading conditions, using this method.

Keywords: *Rotor Shaft, Crack Detection, Finite Element Analysis, Static Measurement, Overhanging Propeller*

1. INTRODUCTION

Shafts are the most common components used in all kinds of rotating machinery and mechanical equipment and in most high performance rotating devices. They are amongst components that are subjected to the most strenuous working conditions. Besides, the current trends among the machine users to utilize the machinery beyond the expected life period and the practice of run up and run down of machines twice or more per day are causing unexpected stress conditions on shaft's performance. Hence the number of shaft crack incidents has increased dramatically over the last few years.

According to the technical bulletin of Bently-Nevada[1] one manufacturer has logged more than 28 incidents in North America over the past 10 years in the power generation industry alone. And the manufacturer indicates that this is a partial list only. Among the four basic failure mechanisms i.e. corrosion, wear, overload and fatigue, corrosion and wear almost never causes shaft failure (unless they act along with fatigue) and of the rest two, fatigue is more prominent than overload. The rapidly fluctuating nature of bending/shear stresses could be held responsible for this phenomenon of cracking along with rotating unbalance and accidental mass eccentricity.

Propeller and rotor shaft components are the key components of any marine propulsion system and the rotor shaft is placed within the stern tube bearing. The sheer purpose of the marine propeller shaft is to transfer the torque from the engine to propeller and the axial forces from the propeller to the thrust bearing. A schematic view of a marine propulsion system is presented in Fig.1. The combined bending and torsion with various degrees of stress concentration mainly causes cracks in such shafts. Other than that, the tribological wear at places where it co-acts with the seals and sleeves (along with the fluctuating fatigue loads) also leads to shaft failure [2].

Fig.1. Schematic view of marine propulsion system

Arisoy et al3carried out a failure analysis of a 17-4 PH stainless steel sailboat propeller shaft, which failed earlier than its normal usage life, using both macroscopic visual inspection and microscopic inspection with a light optical stereoscopic microscope (Fig 2); they stated that the failure was primarily due to torsional moments acting on the propeller. The striation marks shown in the above figure also indicate that bending was associated with the torsional fatigue in that case. Since failure in this case occurred at the location where the propeller was mounted to the shaft, it also indicates the presence of heavy bending and torsional moments (perpendicular and transverse to its rotating direction) on the rotating propeller blades. Fig. 3 provides a better illustration about the crack initiation and propagation in a rotating shaft due to bending. The bending crack often moves along the plane, perpendicular to its longitudinal axis, and causes failure.

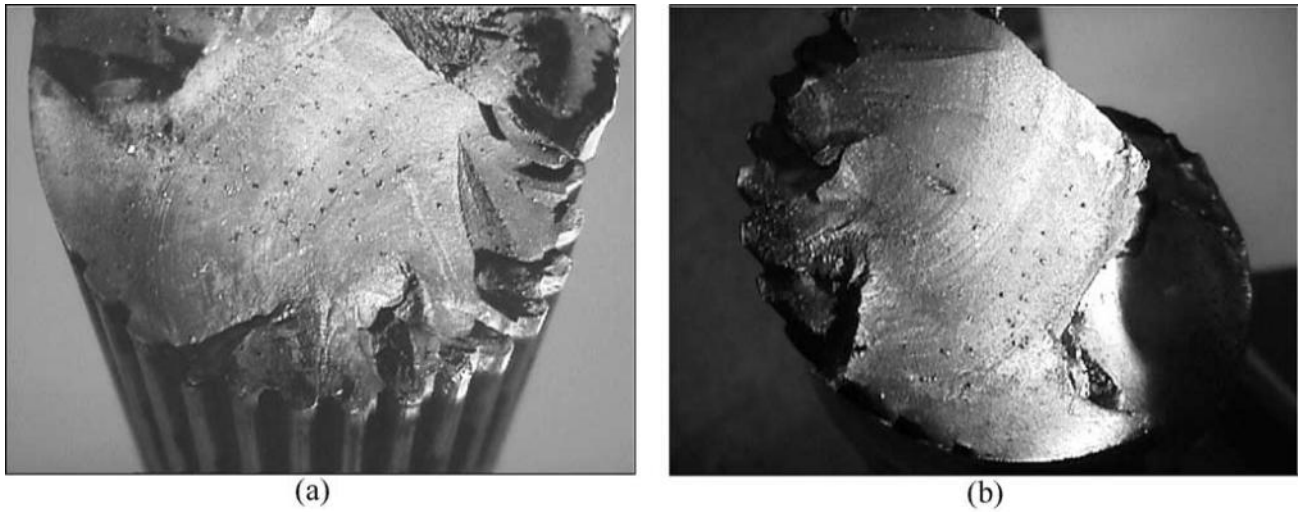

Fig. 2. (a) and (b) show the fractured surface of the failed propeller shaft macroscopically [Arisoy et al (2003)].

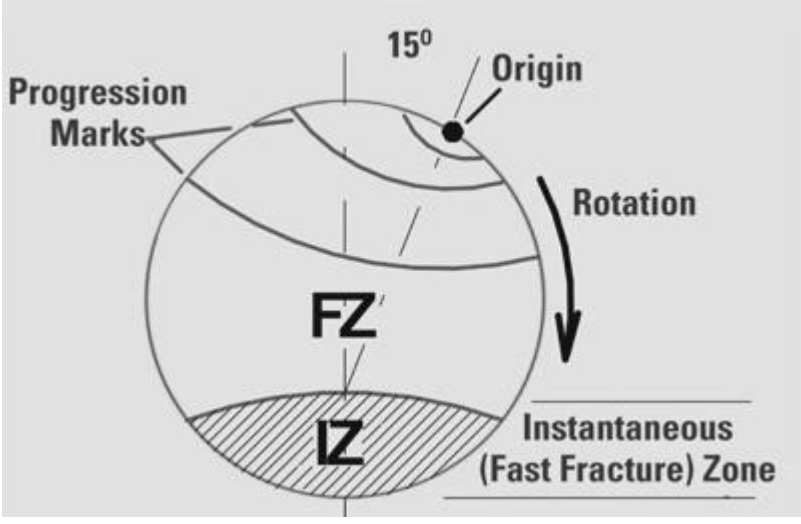

Fig. 3. Crack initiation and propagation due to rotating bending (*Source: http://www.mt-online.com*)

In the present investigation, a single crack caused by bending of shaft due to the weight of rotor and propeller system is analyzed using finite element procedure for a marine propeller shaft. The possibility of crack initiation and propagation was validated by measuring the maximum strains (and the consequent stresses) caused by the weight of the rotor shaft and propeller system and added mass of the water. Based on the static response, a crack detection method (both location and extent) has been proposed following an earlier study carried out by Hossain et al[4].

2. CRACK DETECTION METHODOLOGY

Most of the crack detection method in marine propeller shafts are based on visual inspection, as most of the propeller shafts are made of stainless steel and the surfaces of inspection are not uniform and smooth enough; hence ultrasound or eddy current measurements cannot be relied upon. The frequency response and the modal analysis provide large amount of information and sometimes it is not feasible to measure responses at critical locations. On the other hand, static analysis procedure is easily executable and provides easily measurable information for many types of structures. Furthermore, static analysis requires less theoretical underpinnings and hence provides easily comprehensible results and conclusions pertaining to damage detection. Compared to dynamic analysis, little attention has been paid to the use of static analysis in damage detection so far.

The static analysis is mostly done either by model based approach or finite element analysis. One of the difficulties of model based approach is finding an effective parameter estimation algorithm as the presence of noise and sparsity of data makes it difficult to identify damage. To overcome this problem, Hjelmstad and Shin [5] proposed an adaptive parametric grouping and a data perturbation scheme. Their proposed algorithm was based on the property change of the structure and, to identify the properties and assess the change in the properties, they used a parameterized finite element model along with the measurement obtained from a static test. Di Paola and Bilello[6] proposed a damage identification procedure for Euler-Bernouli beams by reducing the governing equation for damaged structure to a Fredholm integral of second kind in terms of bending moment. According to their literature, the solution of the integral depends explicitly on the variation of stiffness parameter caused by the presence of damage and hence it can be used in damage identification procedure by comparing the theoretical and measured response from the damaged and undamaged beams. Buda and Caddemi [7] modeled the flexural stiffness of an Euler-Bernouli beam as an internal hinge restrained by a rotational spring whose “equivalent” stiffness was dependent on damage extent at the crack location. By avoiding closure or propagation of cracks, i.e., assuming the behavior of the beam to be linear, they proposed of an 'ineffective zone' due to the presence of a concentrated damage and mentioned that due to the low stress level of such 'ineffective zone', it reduces the flexural stiffness adjacent to the crack. With this approach they were able to generate a fourth order differential equation in terms of deflection by combining equilibrium, compatibility and constitutive equations.

Another proposed method of using static response as a damage identification parameter is Finite Element Analysis. Prabhakar et al[8] propose mechanical impedance as a potential parameter for crack detection by analyzing the influence of an

open and breathing crack on the mechanical impedance of a rotor bearing system using FEM. They observed substantial change in the normalized mechanical impedance due to the presence of the crack and identified a definite trend depending upon the location and size of the crack. Kisa and Gurel[9] used a combination of finite element analysis and synthesis method (substructure technique) for non-propagating cracks in beams with circular cross section. Umesha et al[10] proposed a new method for locating and quantifying damage by using the static deflection profile as an input signal for wavelet (Symlet) analysis. This method emphasized on measuring the deflection at a particular point since in real life it is often very difficult to measure deflection at several points due to the requirement of large amount of instrumentation. They used a fixed beam with single damage to demonstrate the method. The damage was modeled as a reduced stiffness element in finite element analysis. Based on the work of Poudel et al[11] , the stiffness of the damaged beam was modeled and an equation of deflection for concentrated load on that beam was obtained. The measured or calculated deflections were then treated as spatial distributed signals in wavelet analysis. For that signal, the continuous wavelet transform was obtained and wavelet coefficients were computed. When the wavelet coefficients were plotted against the length of the beam, it showed a sudden change or peak at the locations of the damage, sensor location and supports. By eliminating the location of the sensor and support, the location of the damage was determined. A generalized curve was then plotted with all maximum wavelet coefficients of the deflection response at the damaged point. The severity of the damage was then obtained by mapping the calculated wavelet co-efficient in the generalized curve.

Tlaisi et al [12] carried out experimental measurements (for impedance measurement) and numerical studies, using finite element procedure, to examine the crack development in rotating shafts. The experimental study was carried out using a modal analysis software, LMS test lab, and the numerical study was carried out using ANSYS software. Impedance and velocity frequency functions were used for crack detection and they were measured in the vertical direction for resonant and anti-resonant frequencies. These parameters showed significant variation for crack depths greater than 0.2 and 0.25 hence it was proposed as a tool for crack detection in such shafts. Also it should be observed that most of the crack detection methodologies developed earlier use only the changes observed in the identified parameters (frequencies, FRF amplitudes, displacements, slopes, strains or others), this study also utilizes the maximum changes observed in the identified parameters to predict the crack location and size.

The earlier work by Hossain et al[4] carried out a finite element analysis of an overhanging propeller shaft with a concentrated load at the end and concluded that percentage changes in deflection and strain provided much larger changes than frequencies obtained from the work of Tlaisi et al[12]. By measuring strain and displacement changes that occur at a number of locations, they were able to detect the optimum locations for measuring strain and displacement where these two parameters show maximum variations, irrespective to the location and size of crack. Based on the outcome of the above study, they proposed a much simpler crack detection method for this type of structures, using only two measurement sensors. In this study, a similar approach has been taken, by considering a more realistic scenario where the load considered will be only the weight of the shaft and the propeller, and the effect of the associated added mass of water has been reckoned for determining the possibility of cracking of propeller shaft.

3. PRE-PROCESSING OF THE SYSTEM COMPONENT

The finite element model of the rotor shaft has four major components, viz., the shaft, fixed end support, intermediate support and the propeller. The CAD model for all the four components were generated in the computer software SOLIDWORKS. The rotor shaft is 1300 mm in length and 15.75 mm in diameter and is made of mild steel; the center of the intermediate support is located at 1,000 mm from the fixed end.

The propeller considered in this analysis is a 4-bladed propeller (Fig. 4) used earlier by Tlaisi et al [12]for crack detection using mechanical impedance procedure. The propeller weighs 15.39N and is made of commercial bronze having a density of 8800kg/m^3. Since the weight of the system will be considered as the only load in analysis, it is very important to model the propeller exactly. Due to the 3D nature of the propeller blade profiles, the exact CAD model generation was a difficult task and to solve the problem, a 3D laser scanner was used. The scanner used in this analysis was a high-speed Terrestrial Laser Scanner (TLS) which produced dense point clouds based on the actual shape. The propeller was scanned on both sides and for each side, a point cloud was obtained. Both the point clouds were then merged and a single point cloud was generated, as in Figure 5. The combined point cloud was then exported into SOLIDWORKS and by following

the location of the points the CAD model of the propeller was generated. From SOLIDWORKS the weight was evaluated and was found to be in agreement with the actual measured weight.

Fig. 4. Propeller used in the analysis

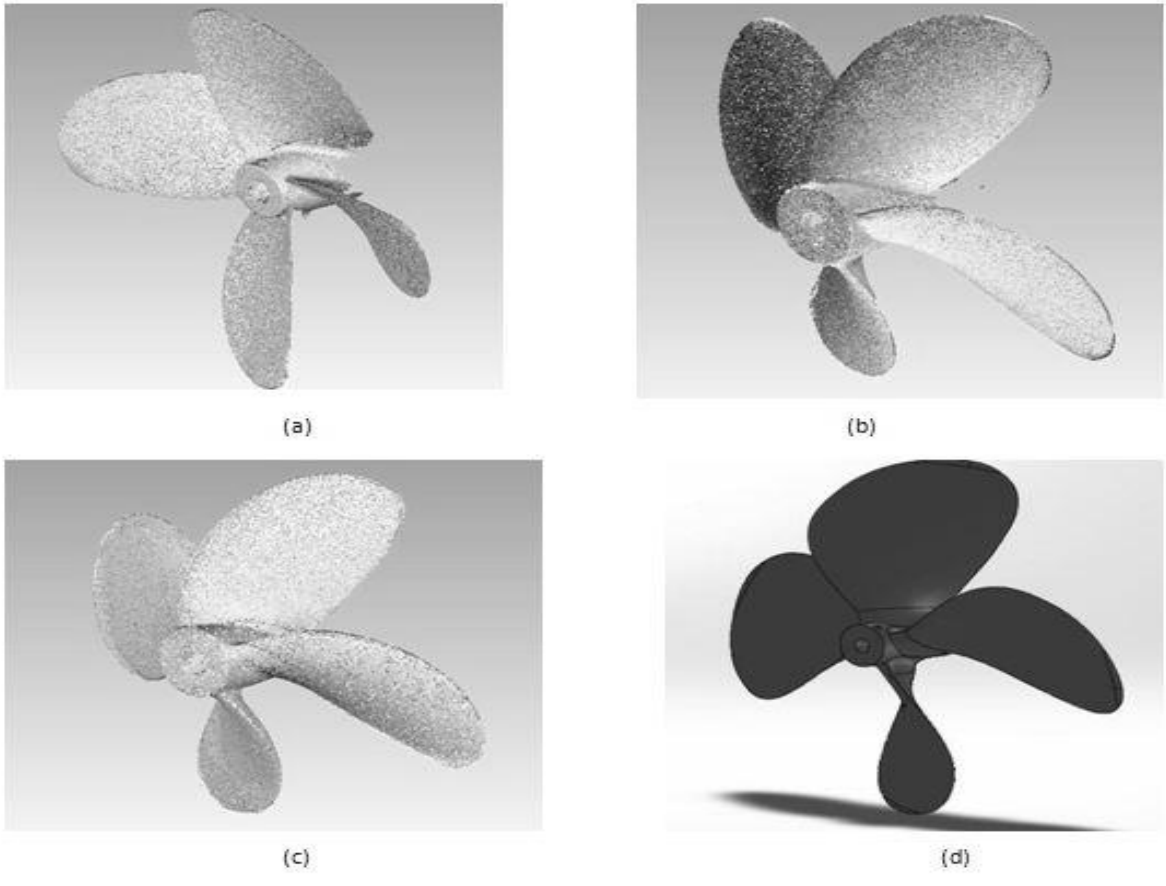

Fig. 5. Propeller; (a) Scanned point cloud of side 1; (b) Scanned point cloud of side 2; (c) Combined point cloud; (d) CAD model

The finite element analysis was carried out using the well-known finite element package ABAQUS. All the parts were first assembled in SOLIDWORKS and the assembly was converted into a parasolid. The parasolid was then imported into ABAQUS graphic user interface (GUI); in the GUI the number of data points to be used for the analysis was reduced from 200,000 to 40000. The section used in the whole model was solid homogeneous section. The earlier analysis [13] showed

that the surface strain change was only significant near the point of contra-flexure and in this study it was found to be located at 418mm from the fixed end. In addition, displacement changes were also found to be prominent at the overhanging end and at locations in between 700-800 mm from the fixed end. Consequently, the strain sensor locations were considered at 410mm and 530 mm from the fixed end and the displacement sensor locations were considered at 710 mm from the fixed end and at the overhanging end.

A seam crack was used to represent the cracking section of the rotor shaft. The seam of the crack defines an edge or a face in the model that is originally closed but can open during analysis. To create the seam crack the shaft was cell-partitioned at the desired location. That cell partition was then defined as a seam crack, shown in Figures 6. Quadratic Tetrahedral elements (C3D10) have been used for the mesh generation. The element type belongs to the 3D stress family and the shape functions are quadratic in nature; the elements around the crack are clustered together to properly represent the singularity effect present at the crack tip.

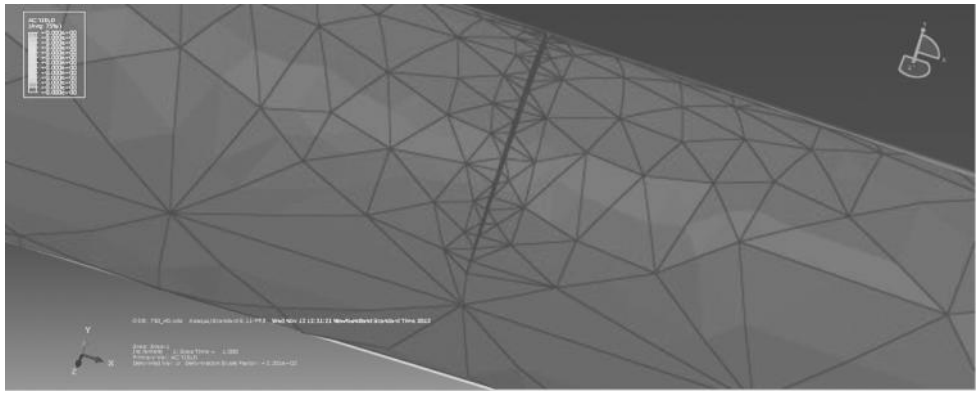

Fig. 6. Seam crack; Crack location: at 750mm, Crack depth ratio: 0.4

4. RESULTS & DISCUSSION

4.1 Possibility of Cracking The possibility of cracking was validated by computing the maximum strain (and the consequent stress) the shaft would experience during bending. Considering the added mass of water and the weight of the system, the maximum surface strain (over the intermediate support) obtained was 77 micro-strains. Since the shaft was executing a rotational motion, the strain range at the maximum strain location would be twice the static strain, viz., 154 με (equivalent stress would be 30.8 MPa). If we consider the expression used by Chattopadhyay[14] for crack threshold stress intensity factor:

$$a_{th} = \frac{1}{\pi}\left(\frac{\Delta K_{th}}{\Delta S}\right)^2$$

where, the threshold stress intensity factor ΔK_{th} was taken as 10MPa $\sqrt{m}$ and threshold notch radius (for crack initiation) a_{th} = 5mm; then the nominal surface stress range ΔS obtained was 79.79 MPa. This would require a stress amplification factor of 2.591 (since the computed nominal stress range was 30.8 MPa) to initiate cracking in steel at the hotspot location. Considering that a run up and down operation would occur, during the start-up and slowing down of the rotating shaft and propeller, the excitation of natural frequencies during this operation would generate large dynamic strain amplifications; also the fretting wear caused by the tribological contact of rotating shaft with the hardened sleeve (of the bearing) would be locations for stress amplification in the rotor shaft[2]. Moreover the blade bending caused during thrust generation in propeller will also cause additional bending stresses in the rotor shaft. As a consequence the required stress amplification of factor of 2.57 will be easily available to initiate cracking in the shaft. So the initiation and the propagation of crack under current loading scenario seem to be possible for the rotating propeller shaft.

4.2 Displacement Results The displacements have been plotted as the percentage difference (between the cracked and un-cracked shaft) against crack depth ratio. For each sensor location individual plot represents the variation of displacement against crack depth ratio for different specified locations. For each location, the obtained result shows that the percentage change in displacements increases almost in an exponential manner as the crack grows larger (Figures 7 & 8). Comparing this result with the earlier work by Tlaisi et al[12] , it was found that the displacement changes provides much higher values than the frequency changes. It was found that the percentage difference for displacement was up to 21.5% (for the crack

located at 750 mm) for the sensor located at 710mm (see Figure 7) and 22.6% (for crack located at 1030 mm) for the sensor located at 1300mm, whereas the frequency change was only 6% for 0.6 crack depth ratio. It should also be observed that the exponential percentage changes in displacements are noticeable only beyond a crack depth ratio of 0.3 to 0.4; hence the use of displacement changes as a crack predication parameter would not be sensitive enough if they are used below a crack depth ratio of 0.3. It should be observed that the displacements are quite small and they need to be measured with proper devices to obtain correct results. This should not be held as a limitation of the method since in prototype situations, the displacements will be amplified by the scale ratio used in modelling the structure for small scale testing.

4.3 Strain Results Similar to displacements, the percentage differences in strains have been plotted against the crack depth ratios in Figures 9 & 10. As observed earlier, the percentage differences were found to increase in an exponential manner with crack depth ratio and it showed larger changes than displacements, especially if the crack was within the intermediate support. The maximum percentage difference obtained at 410 mm was 33.3% when the crack was located at 400 mm; when the strain sensor was at 530 mm the change was 14.9%, when the crack was located at 750 mm (for a crack depth ratio of 0.6). Both of these values are much higher than frequency change (6%) and one of them was even higher than the displacement change as well. The limitation observed here is that for crack located beyond the intermediate support, strain changes did not provide significant variations. The same limitations given above for displacement changes, concerning detecting crack initiation, were also observed for strain changes. Hence displacement and strain changes do not seem to be sensitive enough for detecting crack initiation in rotating shafts. It can also be seen from Figure 9, that if the crack was located at 400 mm, then the crack initiation can be detected even from a crack depth ratio of 0.15 (by the sensor located 410 mm).

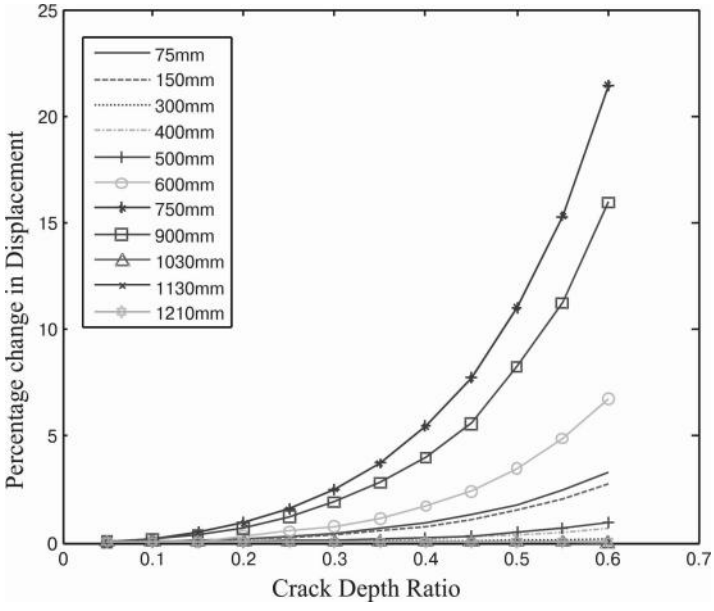

Fig. 7: Percentage change in displacement against crack depth ratio for displacement sensor located at 710mm from the fixed end (different curves show the location of the crack from fixed end).

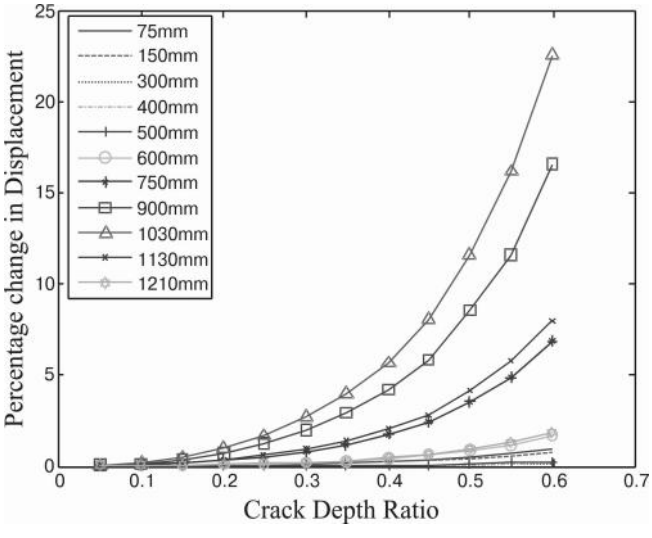

Fig 8. Percentage change in displacement against crack depth ratio for displacement sensor located at 1300mm from the fixed end (different curves show the location of the crack from fixed end)

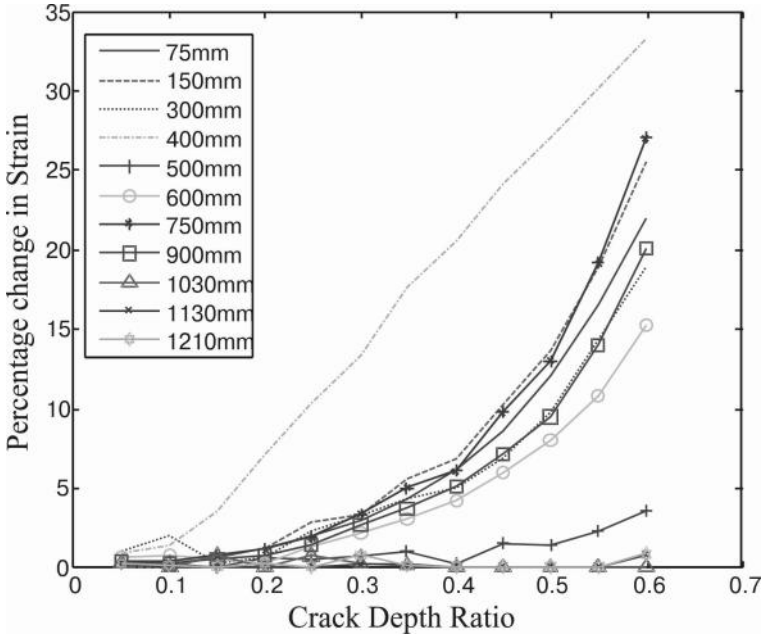

Fig. 9. Percentage change in strain against crack depth ratio for strain sensor located at 410mm from the fixed end (different curves show the location of the crack from fixed end)

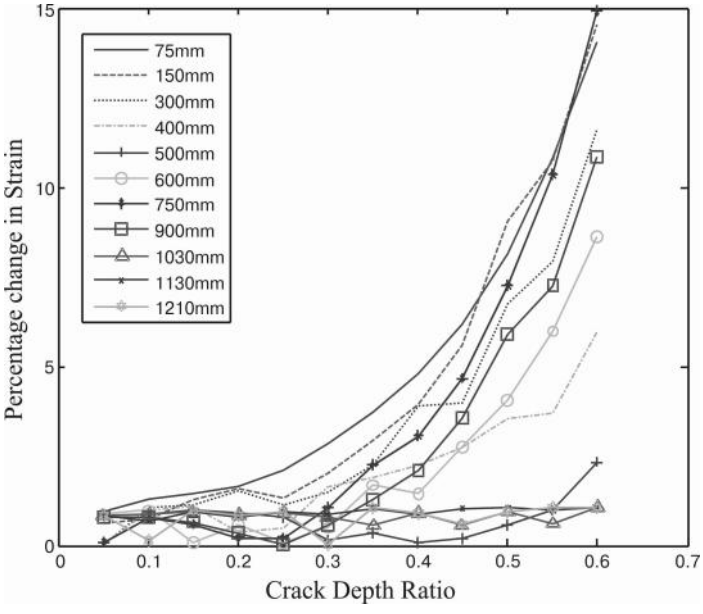

Fig. 10. Percentage change in strain against crack depth ratio for strain sensor located at 530mm from the fixed end (different curves show the location of the crack from fixed end)

4.4 Slopes of Percentage Differences in Displacements and Strains Although the percentage changes, for both displacements and strains, are much higher than the frequency change (due to the exponential nature of the curves) they are not very sensitive for early crack detection. Hence, to overcome this deficiency in the crack detection proposed above, the slopes of each displacement/strain percentage difference curve were plotted against crack depth ratios in Figures 11, 12, 13, and 14. Most of the slope curves showed exponential increases against crack depth ratios. However, the first point in the crack depth growth (for a crack depth ratio of 0.05, in the numerical computation) was not considered as it gave an unexpected high value. Since the strains were picked out manually using visual estimation, the raw plot of these slopes did not give a smooth curve; hence a five-point averaging procedure was carried out to reduce the variableness of the data. The maximum slope for strain (or percentage rate of change of strain as a function of crack depth increase) was found to be up to 176.6% and 112.1% at 410 mm and 530 mm respectively for the 0.6 crack depth ratio. For the same crack depth ratios, the maximum slope for displacement was found to increase to 124.2% and 127.9% at 710 mm and 1300 mm respectively. These plots could be used as effective tools for early crack detection as for most cases, even for the 0.1 crack depth ratio these plots provide significant amounts of change in the slope. So when over a period of measurement, significant changes in slopes occur (say from 5 to 8 or 10%) one can be sure that a crack has initiated in the rotor shaft, and the methodology given below can be used to detect the probable location and size of the crack.

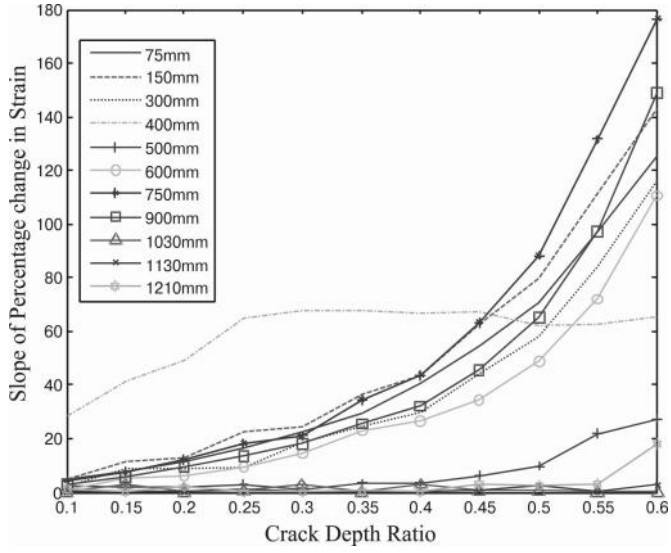

Fig. 11. Slope of percentage change in strain against crack depth ratio for strain sensor located at 410mm from the fixed end (different curves show the location of the crack from fixed end)

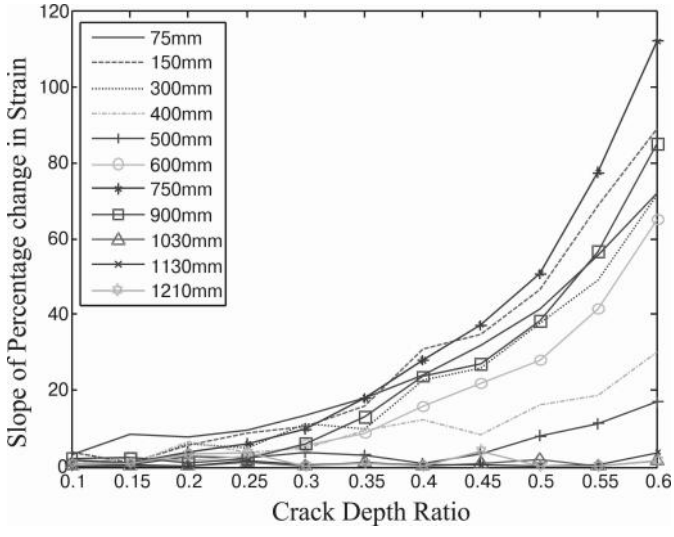

Fig. 12. Slope of percentage change in strain against crack depth ratio for strain sensor located at 530mm from the fixed end (different curves show the location of the crack from fixed end)

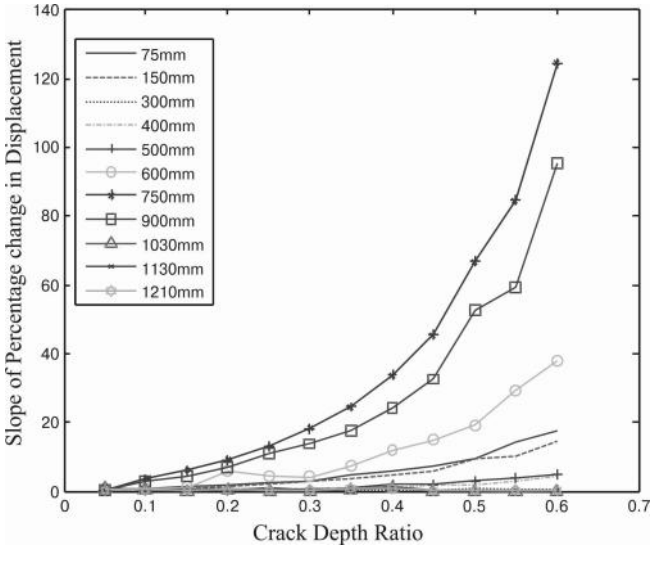

Fig. 13. Slope of percentage change in displacement against crack depth ratio for displacement sensor located at 710mm from the fixed end (different curves show the location of the crack from fixed end)

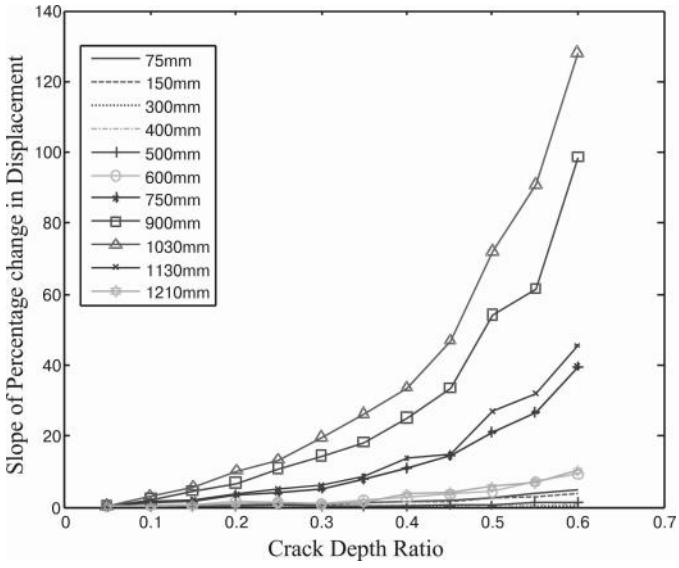

Fig. 14. Slope of percentage change in displacement against crack depth ratio for displacement sensor located at 1300mm from the fixed end (different curves show the location of the crack from fixed end)

4.5 Procedure for Crack Detection The earlier study by Hossain et al[13] considered the percentage differences that occurred in displacements and strains of the rotor shaft, as crack detection tool. But as discussed in the previous section, the slope of percentage difference provides an early indication of the crack initiation and presence than percentage difference; hence in this study the slope of percentage difference is used as the crack detection tool. Any two sensor values can be used to detect the initiation/presence of small cracks; it should be noted that the strains (as well as the differences and slopes) do not show much variation beyond intermediate support. Therefore it would be more practical to use either a combination of displacement and displacement or strain and displacement changes and slopes in crack detection.

The crack detection has been carried out with a Microsoft Excel macro enabled workbook. The responses stated above was first imported into the workbook and a macro has been developed using the built-in Visual Basic. When the macro is being run, it asks for the two responses. Based on the input it receives, it calculates the crack depth ratio for each of the above mentioned locations. The intermediate points are calculated using linear interpolation between the points. By plotting the calculated crack depth ratio against the crack location, the location and the size of the crack is detected.

4.5.1 Displacement-Displacement Sensors Let's say we have obtained a value of 5 as slope of percentage difference in both the displacement sensors. After putting these values in input dialogue box, the macro calculates the crack depth ratio for each locations and puts them in some other part of the worksheet. Then the crack depth ratio is plotted against crack location using MATLAB. The two curves intersect at a location of 850mm and at a crack depth ratio of 0.2 (Figure 15) . This gives the location and size of the crack. These values have been verified to be proper by referring to the earlier computed values.

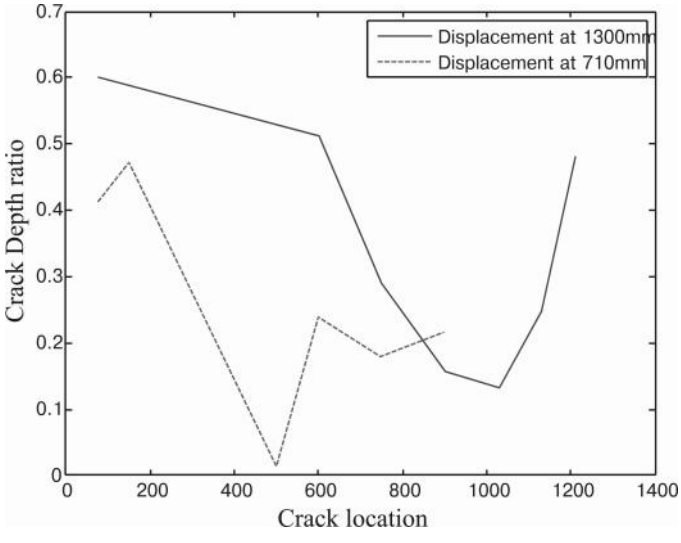

Fig. 15: Computed Crack Depth ratio against crack location; the point of intersection gives the size and location of the crack

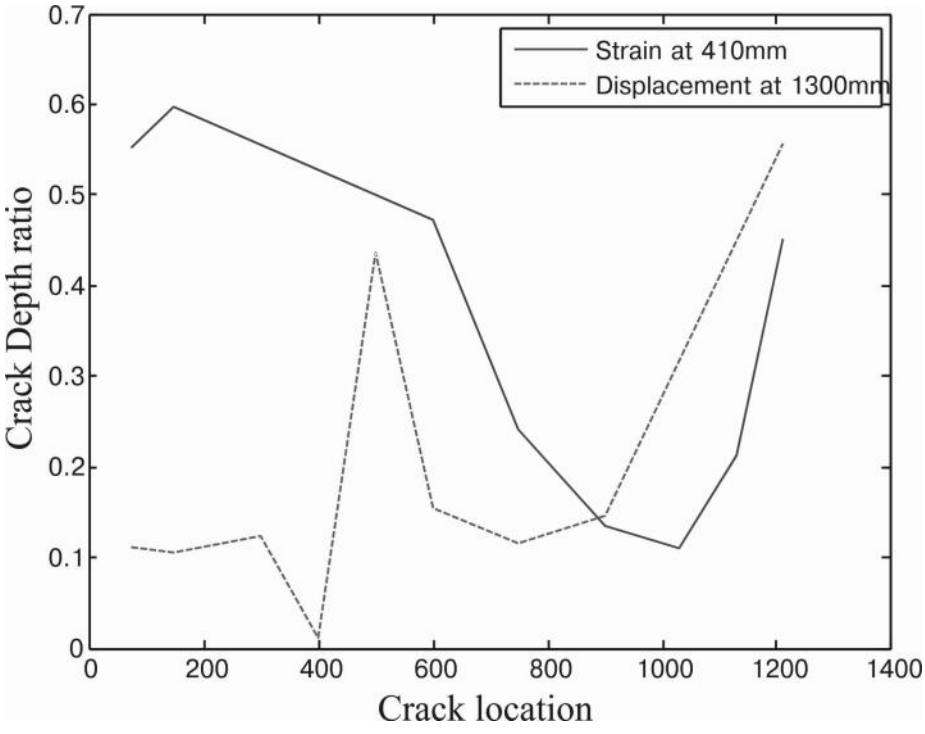

Fig. 16. Computed Crack Depth ratio against crack location; the point of intersection gives the size and location of the crack

4.5.2 Strain-Displacement Sensor Similarly if we obtain a value of 5.5 as slope of percentage difference from the strain sensor at 410mm and a value of 4 as the slope of percentage change from the displacement sensor at 1300mm, the two curves intersect at a location of 885mm at a crack depth ratio of 0.14 (Figure 16). These values have also been determined to be the correct values by referring to the earlier computed values.

5. CONCLUSION

The study outlines a simple but effective method to identify the probable location and size of the crack in a marine propeller shaft. The following conclusions can be made based on the outcome:

a) The load due to the weight of the marine propeller system causes sufficient stress to initiate and propagate cracks in the shaft.

b) Both the displacement and strain values show better percentage changes than frequency change and they can be used as effective tools for identifying crack propagation.

c) The slopes of percentage changes of displacements and strains show even higher changes and can be very useful for early crack detection. However, precision is required in measurement.

d) Since only large strain variations occur near the point of contra-flexure, they cannot detect crack presence beyond the intermediate support. Hence, a combination of results from strain-displacement sensors is required to use this method.

e) Cracks can be detected without disassembling the whole system which is more convenient than the current methods.

f) Only two sensors are required to identify crack location and size.

ACKNOWLEDGEMENTS

The authors would like to express their appreciation and thanks to Dr. R Seshadri, for his encouragement and financial support of this research. The authors would also like to thank the Faculty of Engineering and Applied Science for the facilities provided for experimental measurements and numerical analyses.

REFERENCES

1. Bently Nevada. *Early shaft crack detection on rotating machinery using vibration monitoring and diagnostics.* ; 270.
2. Bielawski P. *Diagnostics of marine propeller shafts.* Journal of Polish CIMAC Selected full texts. 2011;6(2):31-40.
3. Arisoy CF, Basman G, Sesen MK. *Failure of a 17-4 PH stainless steel sailboat propeller shaft.* Eng Failure Anal. 2003;10(6):711-717. http://dx.doi.org/10.1016/S1350-6307(03)00041-4. doi: 10.1016/S1350-6307(03)00041-4.
4. Hossain RB, Seshadri R, Swamidas AS. *Identification of the size and location of A crack, using statical deformations of A marine rotor shaft with A propeller at the overhanging end.* International Workshop on Smart Materials, Structures & SHM in conjunction with NDT in Canada 2013 Conference & NDT for the Energy Industry. 2013Calgary, Alberta, CANADA.
5. Hjelmstad KD, Shin S. *Damage detection and assessment of structures from static response.* J Eng Mech. 1997;123(6):568-576. http://dx.doi.org/10.1061/(ASCE)0733-9399(1997)123:6(568). doi: 10.1061/(ASCE)0733-9399(1997)123:6(568).
6. Di Paola M, Bilello C. *An integral equation for damage identification of euler-bernoulli beams under static loads.* J Eng Mech. 2004;130(2):225-234. http://dx.doi.org/10.1061/(ASCE)0733-9399(2004)130:2(225). doi: 10.1061/(ASCE)0733-9399(2004)130:2(225).
7. Buda G, Caddemi S. *Identification of concentrated damages in euler-bernoulli beams under static loads.* J Eng Mech. 2007;133(8):942-956. http://dx.doi.org/10.1061/(ASCE)0733-9399(2007)133:8(942). doi: 10.1061/(ASCE)0733-9399(2007)133:8(942).
8. Prabhakar S, Sekhar AS, Mohanty AR. *Detection and monitoring of cracks using mechanical impedance of rotor-bearing system.* J Acoust Soc Am. 2001;110(5):2351-2359. doi: http://dx.doi.org/10.1121/1.1412447.
9. Kisa M, Arif Gurel M. *Free vibration analysis of uniform and stepped cracked beams with circular cross sections.* Int J Eng Sci. 2007;45(2):364-380.
10. Umesha PK, Ravichandran R, Sivasubramanian K. *Crack detection and quantification in beams using wavelets.* Computer-Aided Civil and Infrastructure Engineering. 2009;24(8):593-607. http://dx.doi.org/10.1111/j.1467-8667.2009.00618.x. doi: 10.1111/j.1467-8667.2009.00618.x.
11. Poudel UP, Fu G, Ye J. *Wavelet transformation of mode shape difference function for structural damage location identification.* Earthquake Engineering and Structural Dynamics. 2007;36(8):1089-1107. http://dx.doi.org/10.1002/eqe.673. doi: 10.1002/eqe.673.
12. Tlaisi A, Swamidas A, Akinturk A, Haddara MR. *Crack detection in shafts using mechanical impedance measurements.* Mechanical Engineering Research. 2012;2(2).
13. Chattopadhyay S. *Design fatigue curves based on small crack growth and crack closure.* Journal of Applied Science & Engineering Technology. 2008;2.

POWER AND SPEED PERFORMANCE OF INVERTER CHAINS IN THE NANOSCALE DOMAIN

Pradeep Nair
Computer Engineering Program
California State University, Fullerton CA 92831, USA
Phone: +1-657-278-3375
E-mail: pnair@fullerton.edu

ABSTRACT

As transistors scale to the nanoscale domain and become diversified, their behavior can substantially vary from that of traditional MOS transistor structures. The evaluation of the speed-power tradeoffs of MOS-based circuits in the nanoscale-domain thus becomes very significant. In this work, the speed and power dissipation characteristics of various configurations of a common circuit, the non-inverting fixed-stage-ratio inverter chain, were investigated for various technology nodes, namely 32 nm, 22 nm, and 16 nm. Two different types of transistor models were employed. It was observed that technology scaling is accompanied by a reduction in dynamic energy-delay costs. Also, an increase in the number of stages in the chain caused an increase in the dynamic energy-delay costs of the chain. Leakage current is significantly increased as the technology node is scaled down from 22 nm to 16 nm.

Keywords – *Inverter-chain; energy-delay product; dynamic power; leakage power*

1. INTRODUCTION

Ever since the advent of the Integrated Circuit[1] (IC), the field of IC technology and integration has been witnessing continual progress in accordance with the now-famous *Moore's law*[2], an augural observation attributed to Intel Corporation co-founder Gordon Moore. Moore noted that the number of components (transistors) that can be integrated on to a given area of silicon real estate of an IC chip increases at a rapid rate. Moore's law later led Intel Corporation executive David House to predict that the performance capability of processor ICs doubles approximately every 18 months[3]. With Moore's law as the guiding principle, IC technology has witnessed steady progress over the years and it is now possible to integrate millions of transistors in a single IC chip using Very Large Scale Integration (VLSI) techniques. The burgeoning growth of the personal computing, consumer electronics and smartphone markets in the last few years is largely due to the successes and capabilities achieved in the areas of VLSI with respect to component speed enhancement and miniaturization. The increased capabilities, however, have brought along new challenges that must be addressed. The high amount of integration density in recent state-of-the-art ICs has resulted in higher heat densities, increased power dissipation and decreased reliability. To address these challenges and to keep up with Moore's law, the semiconductor industry has been innovating continually through process scaling and the introduction of new transistor materials and structures. According to the ITRS, the growth of the semiconductor industry has now moved on from an era of '*classical scaling*' to an era of '*equivalent scaling'*, in which strained silicon, high-k materials etc. are used to build transistors[4].

As transistors diversify and shrink into the nanoscale domain, the speed and power dissipation characteristics of a circuit can vary dramatically based on the transistor type and technology node used. In this work, the speed and power dissipation characteristics of the inverter chain, one of the common circuits used to model the general behavior of multi-stage combinational circuits is investigated for different transistor types and technologies. The objective is to identify the shifts in the speed-power tradeoff patterns as the transistor technologies are scaled down to the nanoscale domain. The knowledge obtained could be applied to identify the effects of scaling and transistor structure selection on the speed and power performance of the inverter chain.

The remainder of this paper is organized as follows: Section 2 provides background information about the inverter chain. Section 3 summarizes some of the related work related to inverter chain. Section 4 describes the methodology and

tools adopted in this work. Section 5 analyzes the results and section 6 concludes the paper.

2. BACKGROUND INFORMATION

An inverter chain is used to drive a large capacitive load using multiple inverters. The goal is to be able to drive the load without incurring large delay and power costs[5]. In a fixed-stage-ratio inverter chain, the transistors of the first inverter are sized in such a way so as to have equal rise and fall times at the inverter output. Thereafter, the size of the PMOS and NMOS transistors are increased by a fixed factor, known as the *stage ratio*, as the chain is traversed from the input to the output. The number of stages in the chain is related to the stage ratio of the chain by the following equation[5]:

$$N = (\ln (C_N/C_0))/\ln K \quad (1)$$

where, N is the number of stages in the chain, C_N is the load capacitance connected to the output of the last inverter in the chain, C_0 is the capacitance connected to the input of the first inverter in the chain, and K is the fixed stage ratio.

3. RELATED WORK

Several papers from the literature have focused on the speed, drive capability, sizing, and power dissipation of the inverter chain. Some of the related work is summarized here.

An analytical timing model for the delay of a CMOS inverter was described by Bisdounis et al[6]. Another work by the same authors, presented a formula for determining the short-circuit power dissipation of the CMOS inverter based upon the analytical expressions of the inverter output waveform[7].

A delay and power expression for a CMOS inverter driving a resistive-capacitive (RC) load was presented by Adler et al[8]. The authors derived their inverter delay and power expression based on the Alpha-Power Law transistor model by Sakurai et al[9].

Stojanovic et al.[10] studied the effects of gate-sizing and supply voltage scaling to combinational circuits including the inverter chain with the objective of minimizing energy consumption for a given delay. They applied the concept of energy sensitivities and concluded that energy savings of 40 to 70 percent are possible for a delay penalty of 20 percent.

Amelifard et al.[11] addressed the problem of fanout-tree optimization in their work. The problem was formulated as an inverter chain optimization problem and focuses on the minimization of power consumption of the inverter chain. The authors of this work demonstrated that in the case of fanout trees with multiple sinks, optimization of the area of the tree does not necessarily lead to a power-optimized fanout tree design. They also propose power-optimization methods for the fanout tree through the use of multiple threshold voltages and multiple channel lengths.

Dutta et al.[12] derived an optimum stage ratio to minimize the power-mismatch jitter product of a tapered inverter chain. They found this stage ratio value to be lower than that required for minimum delay and the stage ratio required for minimizing the power-delay product. They verified their results through simulation for the 180 nm and 90 nm technology nodes.

Corsonello et al.[13] recently proposed a mathematical model to predict the output amplitude and time of the output overshoot/undershoot for a CMOS inverter operating in the sub-threshold domain. They verified their model using an inverter-chain of five series-connected sub-threshold inverters.

As transistors scale to the nanoscale domain, they begin to deviate substantially from their ideal behavior[14]. This, combined with the fact that newer transistor structures also exhibit a behavior different from traditional MOS transistor structures, makes the evaluation of the speed-power tradeoffs of the nanoscale-domain inverter chain very important.

4. METHODOLOGY AND TOOLS

Prior to the investigation of the inverter chain, a single inverter driving another identical inverter was first considered and subjected to sizing so that the rise-time and fall-time delays were as close as possible. Extensive simulations were performed to arrive at a suitable Wp/Wn ratio using Synopsys HSPICE[15] simulator. Two types of transistor models

were obtained from the Predictive Technology Model website[16,17,18]. One of these types is composed of transistor models optimized for low-power operation while the other type is composed of transistor models optimized for high-speed operation. Models for the 32 nm, 22 nm and 16 nm technology nodes were used in the simulation. It was observed that a Wp/Wn ratio = 1.8 was good enough to obtain a near-symmetric rise and fall times in the inverter even though this ratio is less than the value obtained analytically in Kang et al[19].

The W_p value obtained using this ratio was rounded off to the next higher integer during simulation. The W_n and W_n values used for the single inverter driving another identical inverter are summarized in Table 1 for each technology node considered in this work.

Table 1. W_n and W_p values used for a single inverter driving another identical inverter for each technology node

	L = 16 nm	L = 22 nm	L = 32 nm
W_n	32 nm	44 nm	64 nm
W_p	58 nm	80 nm	116 nm

For a given technology node, the transistor sizes and capacitance values in the inverter chain were varied in accordance with the stage ratio, K. The C_0 and C_N values used for each technology node considered in this work are summarized in Table 2.

Table 2. C_0 and C_N values used for each technology node

	L = 16 nm	L = 22 nm	L = 32 nm
C_0	0.1 fF	0.1414 fF	0.2 fF
C_N	5 fF	7.07 fF	10 fF

Once the Wp/Wn ratio of 1.8 was obtained, the stage ratios of the inverter ratios were calculated for the following cases: 2 stages in the chain (N=2), N=4 and N=6. The value of the stage ratios were obtained using Eq. (1). The value chosen for CN/C0 ratio was 50. The stage ratio values obtained were K=7.07 (for N=2), K=2.66 (for N=4), and K=1.92 (for N=6). Another case with a stage ratio of K=2.71, which was derived in by the text book Yeap[5] was also chosen for comparison. These cases were designated using the following labels: N2, N4c1, N6, and N4c2 respectively. As the nodes were scaled up, the values of the capacitance and transistor sizes in the chain were multiplied by a scaling factor of 1.414.

5. RESULTS

The average propagation delays, measured in picoseconds, for various inverter chain configurations are shown in Figure 1 and Figure 2 for the low-power and high-speed cases, respectively. In both cases, it can be observed that the delay increases with the number of stages in the inverter chain and with the stage ratio. Also, the delay increases at a more rapid rate when the number of stages in the chain is increased from 4 to 6 as compared to the case when the number of stages is increased from 2 to 4. Interestingly, for the low-power case, the propagation delay increased when the nodes where scaled down from 32 nm, indicating that transistors optimized for low-power operation need not become faster with technology scaling. However, as far as the high-speed case is concerned, the propagation delays decreased with technology scaling, as expected. In both cases, the speed performance of the N4c1 configuration (4 stages; stage ratio K=2.66) and the N4c2 configuration (4 stages; stage ratio K=2.71) were found to be similar.

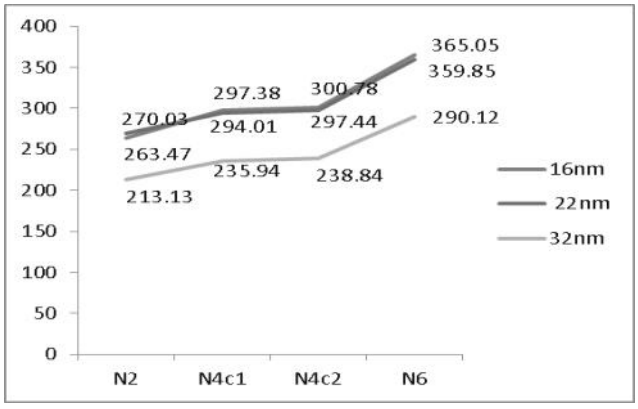

Fig. 1. Propagation delay values for various inverter chain configurations in picoseconds (low-power case)

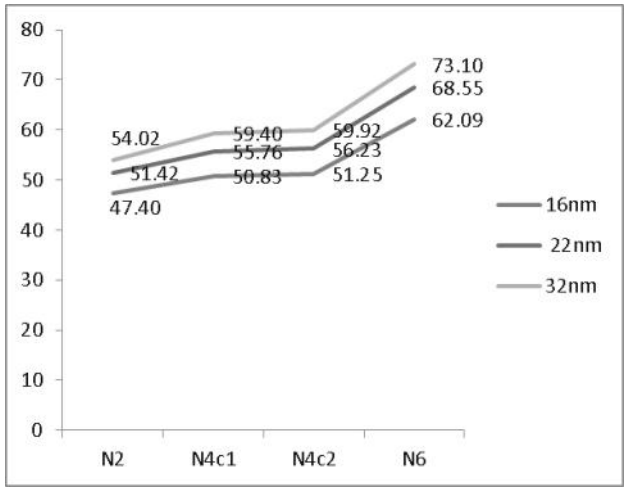

Fig. 2. Propagation delay values for various inverter chain configurations in picoseconds (high-speed case)

Figure 3 and Figure 4 show the average dynamic power dissipation, measured in microwatts, for the low-power and high-speed cases of various inverter chain configurations, respectively. In both cases, dynamic power dissipation increases with the number of stages in the chain. Also, it was observed that technology scaling resulted in reduced dynamic power dissipation. In both cases, the dynamic power dissipated by the N4c1 and N4c2 configurations was found to be similar. From Figures 1 through 4, it can be deduced that increasing the number of stages in the chain from 4 to 6 affects the propagation delay of the inverter chain more sharply than the dynamic power dissipation.

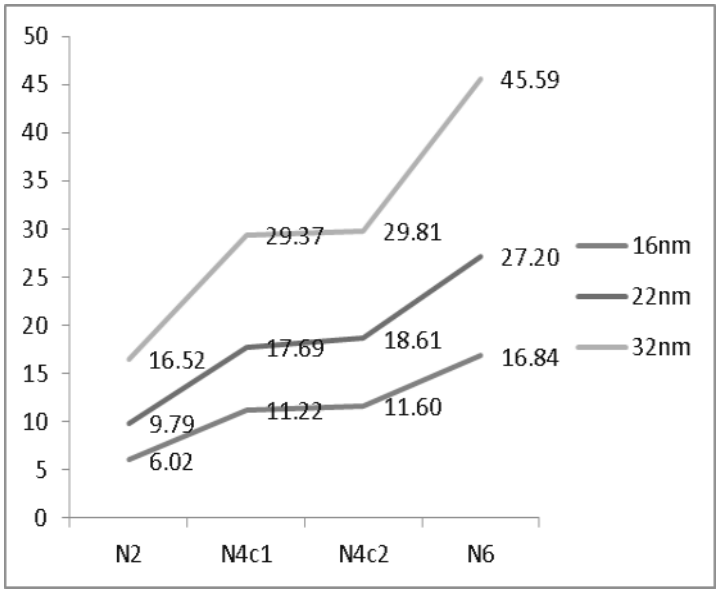

Fig. 3. Dynamic power dissipation of various inverter chain configurations in microwatts (low-power case)

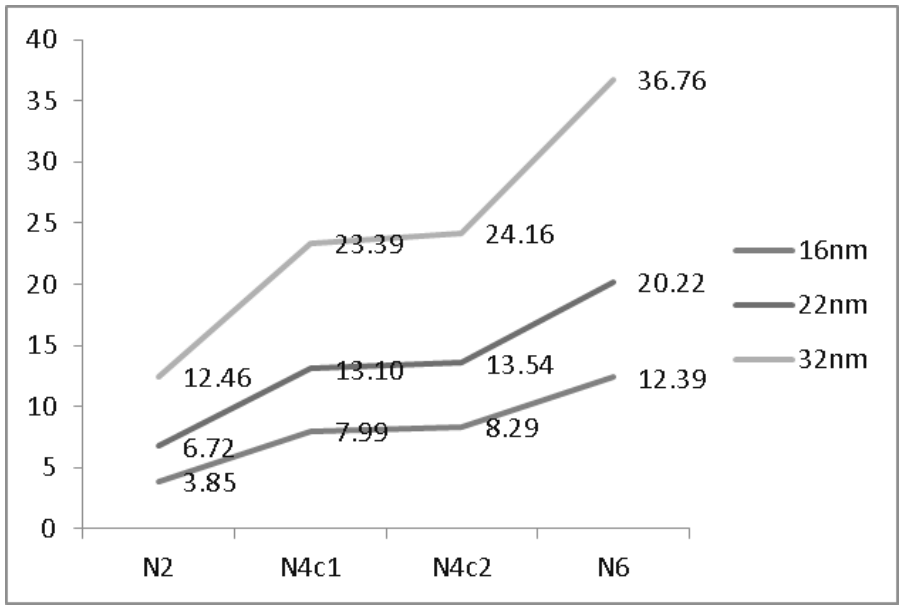

Fig. 4. Dynamic power dissipation of various inverter chain configurations in microwatts (high-speed case)

In order to ascertain the energy-delay tradeoffs, the product of dynamic power dissipation and square of the propagation delay was calculated for each of the various inverter chains employed in this work. This product is basically an energy-delay product (EDP) measure and is expressed in units of 10^{-24}Js or yoctojoule-seconds (yJs) in this work. The EDP values for the low-power and high-speed cases are shown in Figure 5 and Figure 6, respectively. In both cases, it can be seen that energy-delay costs increase with an increase in the number of inverter-chain stages. Also, energy-delay costs increase with a steeper slope as the number of stages in the inverter chain is increased from 4 to 6. Also, scaling down the technology node resulted in reduced energy-delay costs in both cases. In the low-power case, the energy-delay costs showed only a slight decrease from 32 nm to 22 nm but a marked decrease from 22 nm to 16 nm. In the high-speed case, the energy-delay product decrease followed a more uniform pattern, with the EDP decreasing by a factor of 2 in most cases.

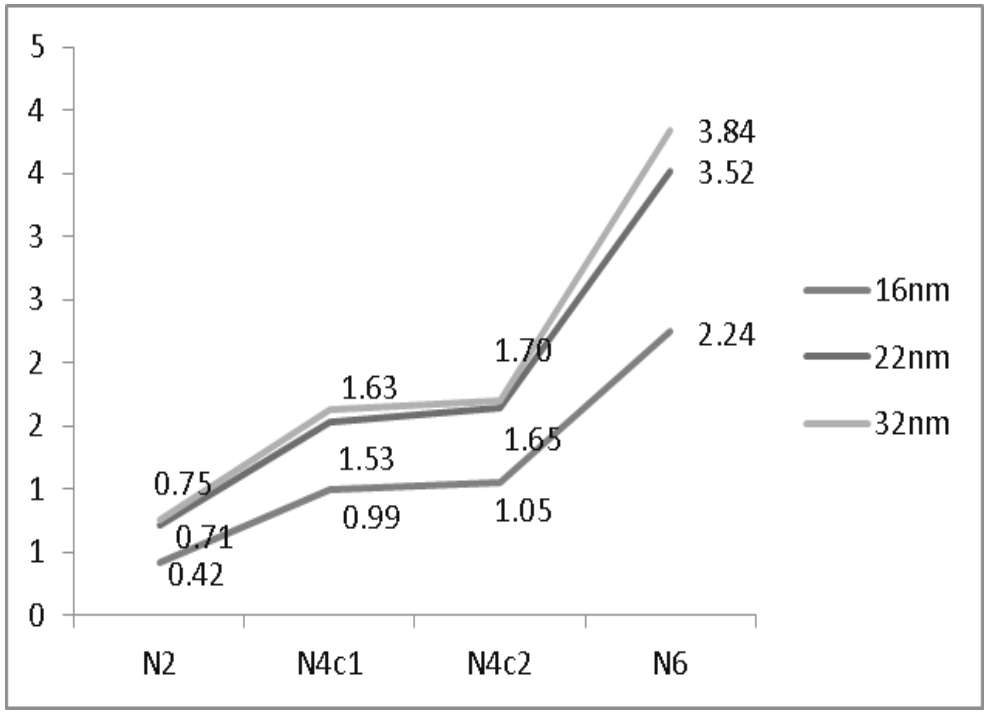

Fig. 5. Dynamic Energy-Delay Product of various inverter chain configurations in yoctojoule-seconds (low-power case)

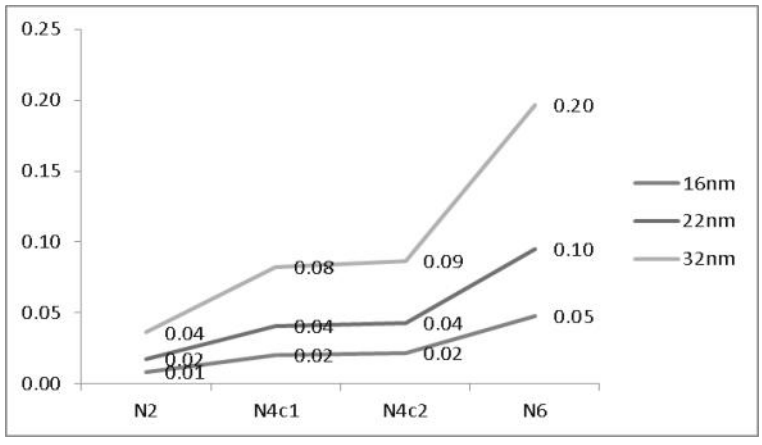

Fig. 6.Dynamic Energy-Delay Product of various inverter chain configurations in yoctojoule-seconds (high-speed case)

As leakage power dissipation is a major factor in nanoscale domain, the leakage power dissipation of the inverter chain configurations were also calculated from leakage current measurements. The leakage power dissipation variations, in nanowatts, seen among the various chain configurations are shown in Figure 7 (low-power case) and Figure 8 (high-speed case). As expected, technology scaling resulted in an increase in leakage power dissipation in both cases, with leakage power dissipation trends showing a sharper increase from 22 nm to 16 nm. The high-speed configurations suffer from significant leakage as compared to the low-power configurations. Also, it was observed that leakage power dissipation increased with an increase in the number of inverter-chain stages. At the 16 nm node, the leakage power dissipation increases with a steeper slope with an increase in the number of stages than at the 22 and 32 nm nodes.

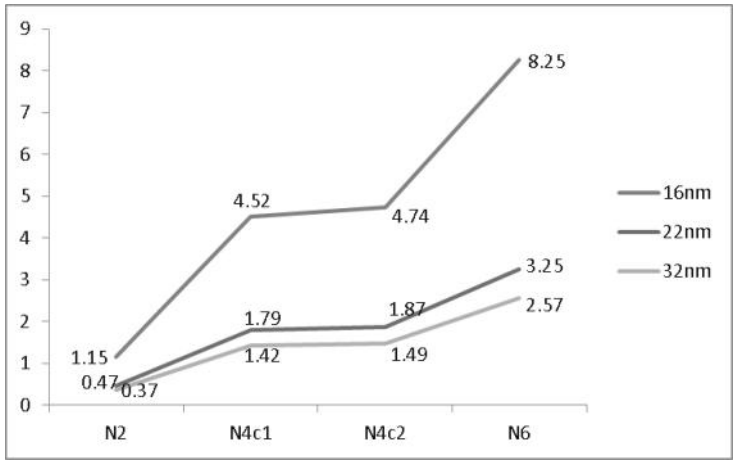

Fig. 7. Leakage power dissipation of various inverter chain configurations in nanowatts (low-power case)

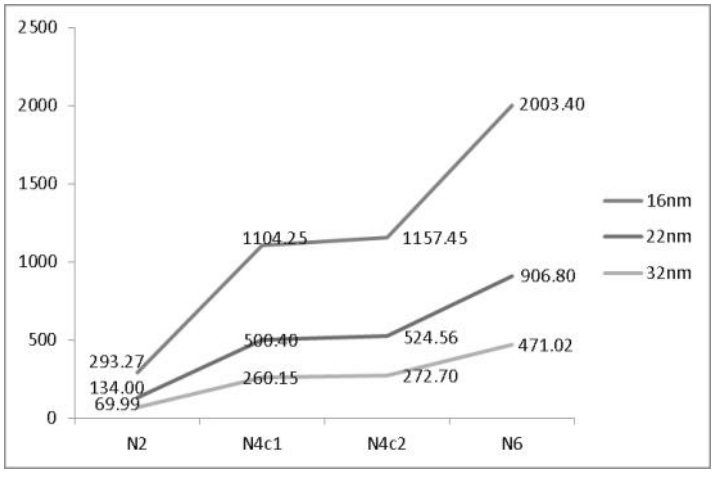

Fig. 8. Leakage power dissipation of various inverter chain configurations in nanowatts (high-speed case)

6. CONCLUSION

In this work, the power and speed performance of various non-inverting *fixed-stage-ratio* inverter-chain configurations were investigated at three different technology nodes, namely, 32 nm, 22nm and 16 nm. Both low-power and high-speed transistors models were employed in this work. The number of stages in the inverter-chain varied between 2 and 6. The stage ratio of the chain was determined based upon the number of stages in the chain. A 4-stage inverter-chain model with an analytically-derived optimal stage-ratio was also employed in this work for comparison purposes. In general, it was observed that the dynamic energy-delay costs of the inverter chain increased with an increase in the number of stages in the chain. Also, dynamic energy-delay costs increase with a steeper slope as the number of stages in the inverter chain is increased from 4 to 6. Technology scaling was accompanied by a reduction in the energy-delay costs. Leakage current is significantly increased as the technology node is scaled down from 22 nm to 16 nm.

REFERENCES

1. Kilby, J.S. *Invention of the Integrated Circuit*. IEEE Transactions on Electron Devices, **23**, 1976, p.648-654.
2. Moore, G.E. *Cramming More Components onto Integrated Circuits*. Electronics, **38**, 1965, p.114-117.
3. Edwards, C. *The Many Lives of Moore's Law*, Engineering and Technology Magazine, **3**, 2008.Available online at http://eandt.theiet.org/magazine/2008/01/moores-law.cfm
4. ITRS 2013 Executive Summary. Available online at http://public.itrs.net/ Links/2013ITRS/2013Chapters/2013ExecutiveSummary.pdf
5. Yeap, G.K. *Practical Low Power Digital VLSI Design*. Kluwer Academic Publishers, 1998. Ch.4.
6. Bisdounis, L.; Koufopavlou, O. & Nikolaidis, S. *Modelling Output Waveform and Propagation Delay of a CMOS Inverter in the Submicron Range*. IEE Proc.-Circuits Devices Syst., **145**, 1998, p. 402-408.
7. Bisdounis, L.; Nikolaidis, S. & Koufopavlou, O. *Propagation Delay and Short-Circuit Power Dissipation Modeling of the CMOS Inverter*. IEEE Transactions on Circuits and Systems-I: Fundamental Theory and Applications, **45**, 1998, p. 259-270.
8. Adler, V. & Friedman, E.G. *Delay and Power Expressions for a CMOS Inverter Driving a Resistive-Capacitive Load*. Analog Integrated Circuits and Signal Processing, **14**, 1997, p. 29-39.
9. Sakurai, T. & Newton, A.R. *Alpha-Power Law MOSFET Model and Its Applications to CMOS Inverter Delay and Other Formulas*. IEEE Journal of Solid-State Circuits, **25**, 1990, p. 584-594.
10. Stojanovic, V.; Markovic, D.; Nokolic, B.; Horowitz, M.A. & Brodersen, R.W. *Energy-Delay Tradeoffs in Combinational Logic using Gate Sizing and Supply Voltage Optimization*. Presented at the 28th European Solid-State Circuits Conference, 2002, ESSCIRC 2002, p. 211-214.
11. Amelifard, B; Fallah, F. & Pedram, M. *Low-Power Fanout Optimization Using Multi Threshold Voltages and Multi Channel Lengths*. IEEE Transactions on Computer-Aided Design of Integrated Circuits and Systems, **28**, 2009, p. 478-489.
12. Dutta, R; Bhattacharyya, T.K.; Gao, X. & Klumperink E.A.M. *Optimized Stage Ratio of Tapered CMOS Inverters for Minimum Power and Mismatch Jitter Product*. Presented at the 23rd International Conference on VLSI Design, 2010, VLSI '10, p. 152-157.
13. Corsonello, P.; Frustaci, F, Lanuzza, M. & Perri. S. *Over/Undershooting Effects in Accurate Buffer Delay Model for Sub-Threshold Domain*. IEEE Transactions on Circuits and Systems-I: Regular Papers, **61**, 2014, p. 1456-1464
14. Rabaey, J. *Low Power Design Essentials*. Springer, 2009. Ch.2.
15. Synopsys website. Available online at http://www.synopsys.com/tools/Verification/AMSVerification/ CircuitSimulation/HSPICE/Pages/default.aspx
16. Predictive Technology Model (PTM) website. Available online at http://ptm.asu.edu/
17. Zhao,W. & Cao, Y. *New generation of Predictive Technology Model for sub-45nm design exploration*. Presented at ISQED, 2006, p.585-590,.
18. Zhao,W. & Cao, Y. *New generation of Predictive Technology Model for sub-45nm early design exploration*. IEEE Transactions on Electron Devices, **53**, 2006, p. 2816-2823.
19. Kang. S-M. & Leblebici, Y. *CMOS Digital Integrated Circuits*. Tata-McGraw Hill, 3rd Edition, 2003, Ch.5.

GAIN IMPROVEMENT BY PERIODIC DISCONTINUITIES IN EXPONENTIALLY TAPERed SLOT ANTENNA

Sanjay Kumar*
Defence Avionics Research Establishment (Former Principal Advisor of DARE)
Kaggadaspura Main Road,
C V Raman Nagar, Bangalore-560093
Tel.No. 080-25047522
Email: tnksk@yahoo.co.in
*Corresponding author

Saurabh Shukla
Defence Avionics Research Establishment (DARE)
Kaggadaspura Main Road,
C V Raman Nagar, Bangalore-560093
Tel.No. 080-25047607
Email: saurabh.dare@gmail.com

ABSTRACT

A technique of gain improvement in ETSA at lower frequency is reported in this paper. The gain improvement is realized by using periodic discontinuities in the ground plane of ETSA. The periodic discontinuities are easy to design and help in realizing more gain without any change in the physical dimension of the antenna. This technique has been implemented in a 5-19 GHz ETSA and comparison in gain and VSWR has been presented. An analysis of the effect of gain improvement on the principle beamwidths has also been done and presented in this paper. The design and simulations with and without periodic discontinuities have been carried out using CST Microwave Studio 2011.

Keywords—*Periodic discontinuities, Exponentially Taper Slot Antenna (ETSA), Ground plane and Gain.*

1. INTRODUCTION

There are mainly four types of Tapered Slot Antenna (TSA). They are Exponentially Tapered Slot Antenna (ETSA), Linear Tapered Slot Antenna (LTSA), Continuous Width Tapered Slot Antenna (CWTSA) and Dual Exponentially Tapered Slot Antenna (DETSA). ETSA is also called Vivaldi Antenna which radiates equal in E and H-plane beam width. The ETSA radiates very well when final width of the slot is equal or more than $\lambda/2$. All types of TSA are widely used in Antenna arrays to achieve high ERP with wide angle scanning capabilities. The use of the ETSA is limited by its gain, especially at the lower end of its frequency band. The directivity of an ETSA depends upon its tapered length and is given as [1] [2]:

$$D = 10\log\left(\frac{10\,L}{\lambda_0}\right) \quad \ldots (1)$$

Where,

D = Directivity of ETSA (dB)

L = Taper Length (mm)

λ_o= Wavelength (mm) corresponding to operating frequency

The equation (1) suggests that ETSA gain can be increased by increasing the taper length of the antenna. But sometimes, the increase in taper length is restricted by the available space. Hence, a different approach is required to enhance the ETSA gain without affecting its physical size.

As per the theory, the gain of an antenna at a specific frequency is given as:

$$G = \frac{4\pi A_e}{\lambda^2} \qquad \ldots (2)$$

Where,

G = gain of the Antenna
A_e = effective aperture of Antenna
λ = wavelength corresponding to operating frequency

Equation (2) explains that the gain of an antenna is directly proportional to its effective aperture. The effective aperture of an ETSA depends upon the surface current which flows over its ground plane. Hence, it can be concluded that by increasing the flowing area of surface current, effective aperture can be increased. To increase the flowing area, periodic discontinuities are provided in an ETSA antenna as shown in Fig. 1.

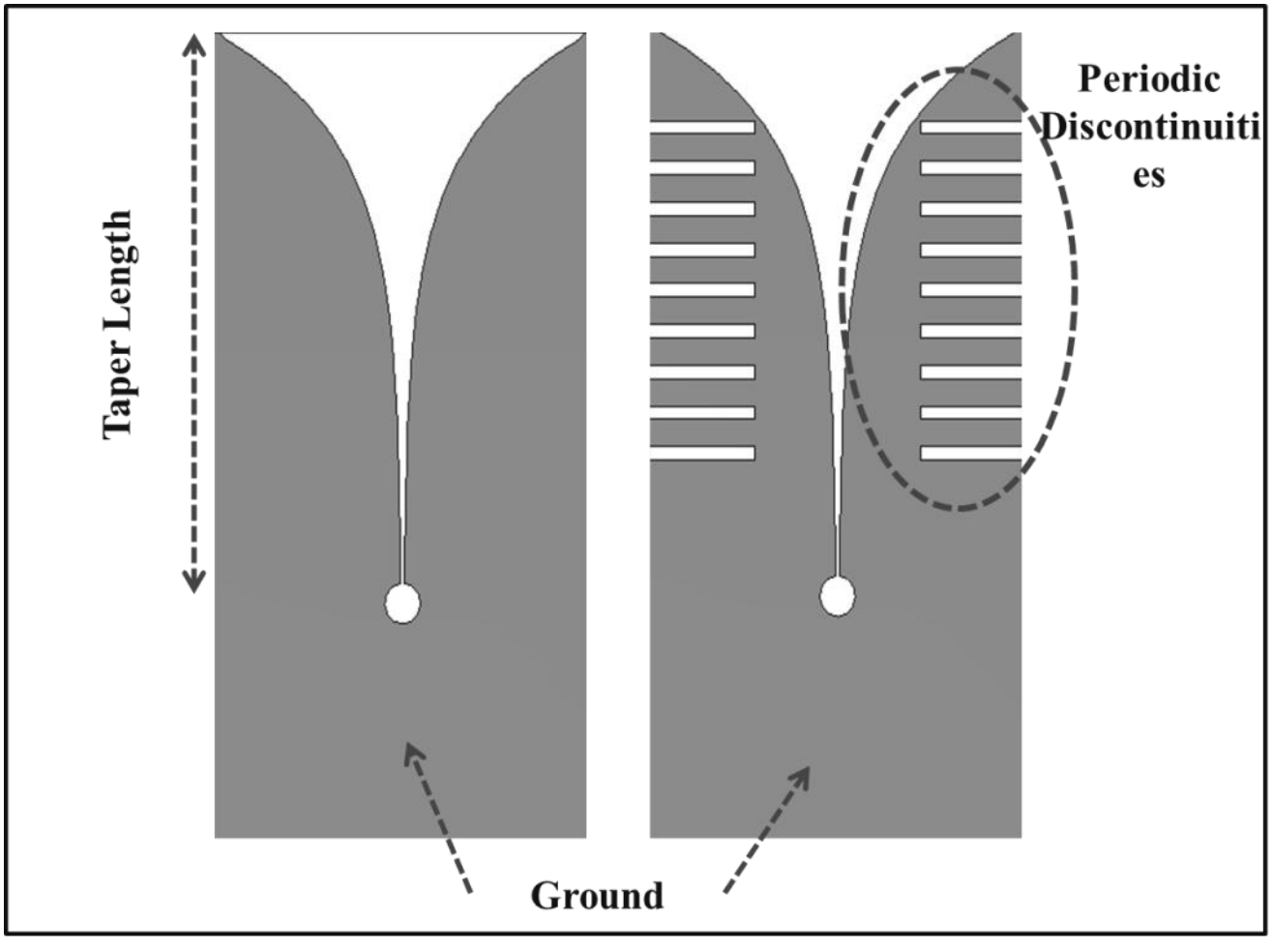

Fig. 1 ETSA ground plane & periodic discontinuitie

2. DETAILS OF PAPER

As shown in Fig.1. periodic discontinuities are provided on the ground plane of ETSA [3] [4]. Each side of the ground plane consists of eight strips etched out from the ground plane. The dimension of each strip is 9x1 mm [5]. The surface current over the ground plane at 5 GHz is shown in Fig. 2. The current flow is increased as it is travelling more electrical length towards the discontinuities. This increased flow corresponds to the gain enhancement in ETSA at lower frequency of operation.

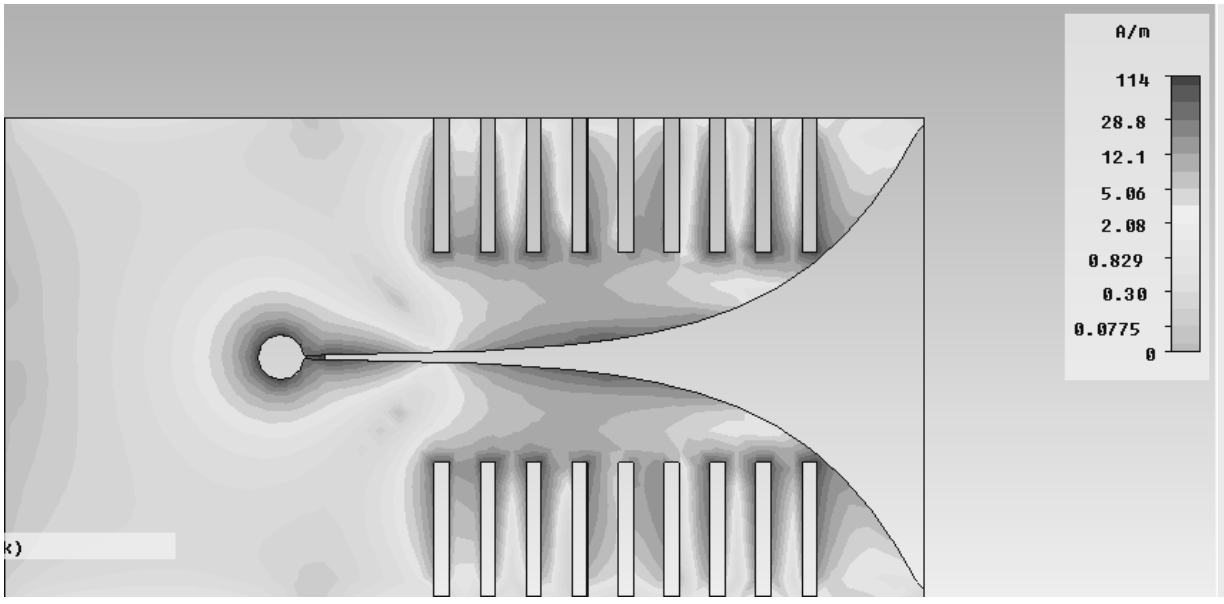

Fig. 2 Surface current on ground plane with periodic discontinuities

To study the effect of discontinuities, two types of periodic discontinuities were designed. The first one is with 9x1 mm strips and the second one is with 9x1.5 mm strips. All the three models were simulated over the 5-19 GHz frequency range and VSWR for all the three models is presented in Fig. 3.

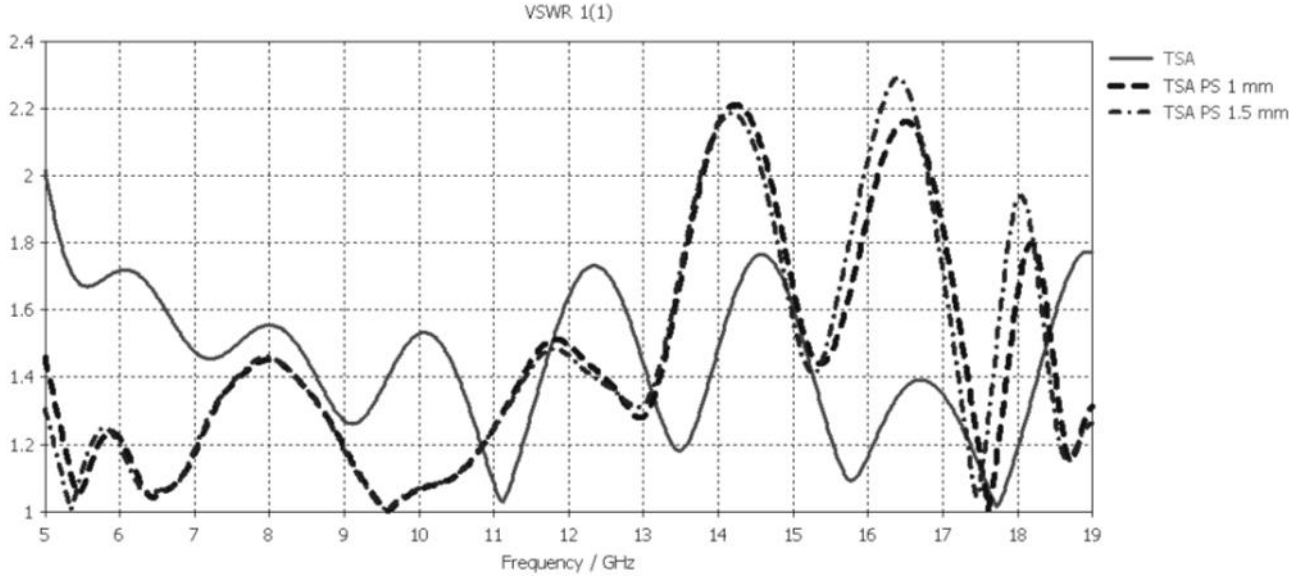

Fig. 3 VSWR comparison for three ETSA models

Fig.3. explains that the matching improves from 5-11 GHz due to the periodic discontinuities. Although there is not much difference between discontinuities with 1 mm and 1.5 mm width in this frequency range. The impact of the improved matching can be seen on the gain of the ETSA and gain comparison plot is shown in Fig.4.

From the Fig. 4, it is clear that due to the better matching, the gain of the ETSA with discontinuities increases especially in the 5-19 GHz frequency range. The gain improvement at lower frequencies is as higher as 2.5 dB. The gain improvement is visible upto 13 GHz and at 14 GHz, the gain of all the three ETSAs is almost equal. At higher frequencies (18-19 GHz), gain of ETSA with discontinuities drops by 1 dB as compared to normal ETSA.

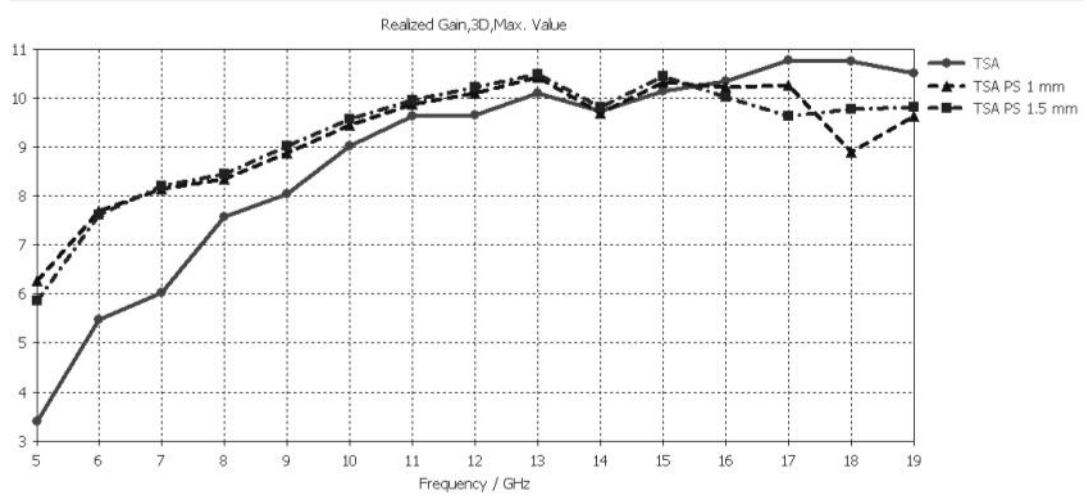

Fig. 4 Gain comparison for three ETSA models

To know the effect of gain improvement on ETSA beamwidths, comparisons plots of both Azimuth and Elevation beamwidth have been obtained and presented in Fig. 5 and Fig. 6 respectively.

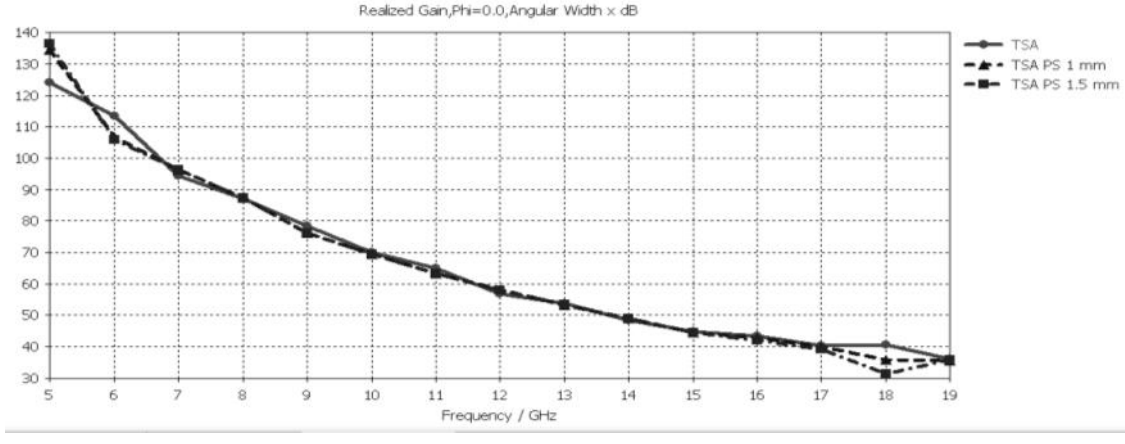

Fig. 5 Azimuth Beamwidth comparison for three ETSA models

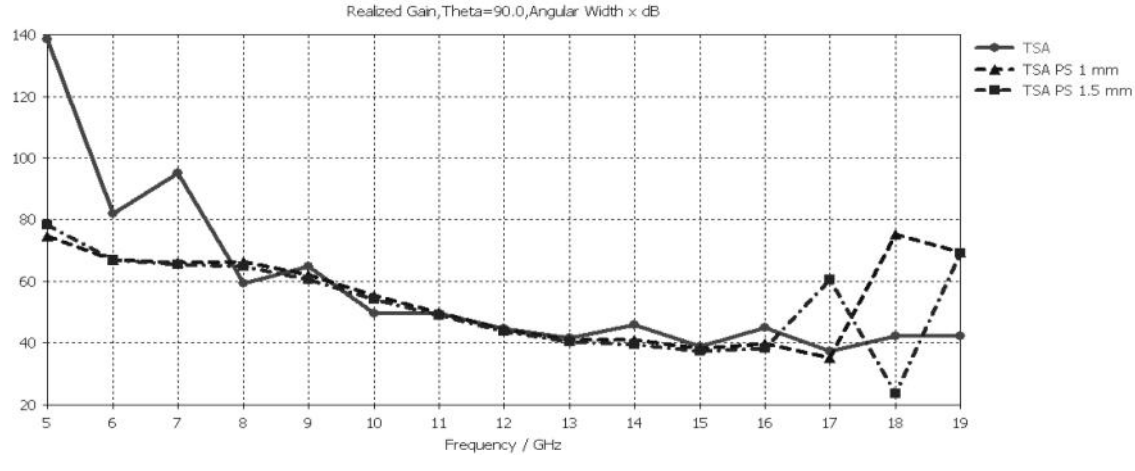

Fig. 6 Elevation Beamwidth comparison for three ETSA models

3. CONCLUSION

From the simulation results shown in Fig. 3, 4, 5 & 6, the following points can be concluded:

a) The gain of ETSA improves due to better matching at lower frequencies. The improved matching is achieved by periodic discontinuities.

b) The gain improvement reduces the elevation beamwidth at lower frequencies.

c) The azimuth beamwidth remains almost same for all the three models of ETSA (with and without discontinuities) will be developed to verify and validate the simulated results.

ACKNOWLEDGEMENTS

The authors would like to thank Director, DARE for his continuous support and encouragement for this work. All these simulations were carried out using CST Microwave Studio 2011 available at DARE, Bangalore.

REFERENCE

1. Lee, K. F. & Chen, W. (1997). *Advances in Microstrip and Printed Antennas*, John Wiley, ISBN: 0-471-04421-0, New York.

2. J.D.S. Langley, P.S. Hall, and P. Newham, Balanced Antipodal Vivaldi Antenna for wide bandwidth phased arrays. *IEEE Proc. on Microwaves and Antennas Propagation*, 143:97–102, 1996.

3. Verma Alka, EBG Structures and Its Recent Advances in Microwave Antenna, *International Journal of Scientific Research Engineering and Technology*, Vol 1, Issue 5, ISSN 2278-0882, pp 84-90, Aug 2012

4. Y. Rahmet Samii, The Marvels of EBG Structures, *ACES Journal*, Vol. 18, No.4, Nov. 2003

5. Li. Yang et al., A Spiral EBG Structure and its Application in Microstrip Antenna Arrays, IEEE APMC Proceedings, 2005.

STEGANALYSIS: DETECTING LSB STEGANOGRAPHIC TECHNIQUES

Tanmoy Sarkar
Neudesic India Pvt. Limited
Hyderabad, India
Email: tanmoy.sarkar@neudesic.com

Sugata Sanyal*
Corporate Technology Office
Tata Consultancy Services,
Mumbai, India
Email: sugata.sanyal@tcs.com
*Corresponding Author

ABSTRACT

Steganalysis means analysis of stego images. Like cryptanalysis, steganalysis is used to detect messages often encrypted using secret key from stego images produced by steganography techniques. Recently lots of new and improved steganography techniques are developed and proposed by researchers which require robust steganalysis techniques to detect the stego images having minimum false alarm rate.

This paper discusses about the different Steganalysis techniques and help to understand how, where and when this techniques can be used based on different situations.

Keywords: *Steganography, Steganalysis, Stego key, Stego image and Cryptography*

1. INTRODUCTION

With the recent technology advanced people are sharing more and more information among each other's. Some organizations like medicine, military are sharing data with are highly secretive and important. For secure communication people are using cryptography using secret key so that only authenticate receiver can decrypt the message and authentication of message remains intact. But cryptography raised suspicion among attackers and tries to attack the message to get the secretive messages. So, a novel approach of steganography is practiced which contains an innocent cover message embedded with secret message optionally encrypted so that while transferring minimum suspicion arouse among attackers. But, if this approach is used by criminal organization then it becomes necessary to identify the stego multimedia data and try to get the information embedded into it. So, like cryptanalysis which works on cryptography, steganalysis is an art of dissuading covert communication without affecting the innocent ones. The primary purpose of steganalysis is to detect the covert message and if required, try to find more information like secret message length, steganography technique used etc. The issue in steganography and steganalysis is often modeled by the prisoner's problem [20].In this paper we will discuss on various LSB steganalysis approach to attack LSB steganography techniques and there efficiency.

2. DETAILS OF PAPER

Steganography Techniques is a method to embed secret image/message into cover image so that the secret message becomes imperceptible to human eyes. To achieve steganography secret message is embedded into cover image using function F (i) and optional stego key to authenticate the data. Kayarkar et al. [16] discuss about various data hiding techniques and there comparative analysis.

Similar to Steganography, another authentication technique is used known as Digital Watermarking. The basic difference between Steganography and digital watermarking is that in digital watermarking the covert data is related to cover data but in steganography the covert data is not related to cover data.

Steganography is mainly distributed among two approaches: reversible and irreversible [14]. Using reversible technique the receiver can extract both the secret message as well as original cover image but while using irreversible technique the receiver can only extract the secret message from stego image leaving original cover image distorted.
Few irreversible techniques are:

- Battisti et al [1] approach of data hiding using Fibonacci p-sequence number to reduce stego image distortion than traditional LSB technique.
- Dey et al [2] [3] [21] proposed an improvement over Fibonacci p-sequence LSB data technique of Battisti et al [1] by decomposing pixel value using two approaches: Prime decomposition and Natural number decomposition technique.
- Nosrati et al. [4] introduced a method that embeds the secret message using linked-list in RGB 24 bit color image

Some reversible data hiding techniques are:

- Ni et al. [5] proposes a novel approach of data hiding using histogram shifting of original image
- Kuo et al. [6] presented a reversible technique that is based on the block division to conceal the data in the image.
- Tian [7] proposes a reversible data hiding technique using difference expansion.

In steganography the simplest method of data hiding is by using LSB steganography method. However, LSB steganography method is divided into two parts: LSB Substitution and LSB Matching techniques. In LSB substitution technique the LSB of cover image is substituted by hidden secret message. In this technique the hidden message bit match with cover image LSB bit. If it is different than substitute the bit otherwise leave as it is. A number of papers have reported very successful steganalysis of LSB replacement [17]–[18]. However, in this approach the even number is always increased but never decreased. Similarly, the inverse is true for odd value. LSB steganalysis methods exploit this asymmetric behavior of LSB replacement to detect secret message.

Let us consider the cover message m_o is grey scale message where each pixel is denoted by 8 bits. So, mathematically to replace the first pixel x_i of message m_o with the first bit of cover message m_c is as follows:

$$x_{LSB_i} = x_i \bmod 2$$
$$x_{covert} = x - x_{LSB_i} + m_c \bmod 2$$

In LSB matching technique the LSB bits are not simply flipped. Instead, the randomly selected sample value is increased or decreased if its LSB does not match the secret message bit to be embedded. The LSB of the cover pixel value finally equals the next bit of the hidden data. Because of this behavior the LSB matching technique is more powerful and difficult to detect then LSB replacement methods. The LSB matching techniques can be denoted as following mathematical expression:

$$p_s = \begin{cases} p_c + 1, & if\ b \neq LSB(p_c)\ and\ (k > 0\ or\ p_c = 0) \\ p_c - 1, & if\ b \neq LSB(p_c)\ and\ (k < 0\ or\ p_c = 255) \\ p_c, & if\ b \neq LSB(p_c) \end{cases}$$

The advantage of LSB embedding is its simplicity and the difference is not visible to naked eyes. But this technique has also having lot of disadvantages like LSB encoding is extremely sensitive to any kind of filtering or manipulation of the stego-image. An attack on the stego-image is very likely to destroy the message. An attacker can easily remove the message by removing (zeroing) the entire LSB plane with very little change in the perceptual quality of the modified stego-image. From Fig. 1.1 we can see that after embedding secret message into the cover image there is significant change in original image histogram pattern suggesting it is being distorted.

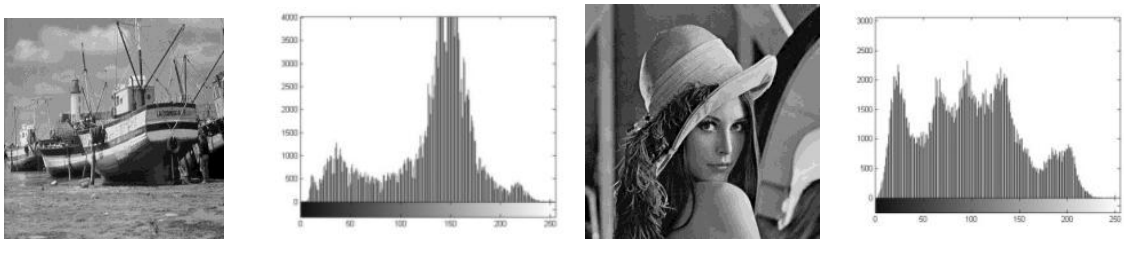

(a) (b)

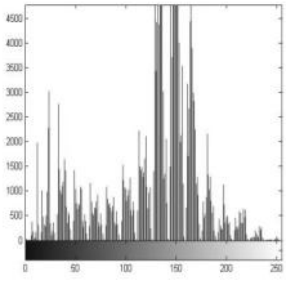

(c)

Figure 1.1 LSB Data Hiding Technique (a) Cover Image (b) Image to be embedded (c) Stego Image

STEGANALYSIS TECHNIQUES TO DETECT LSB STEGANOGRAPHY Steganalysis is an art of detecting the hidden messages inside a stego medium. Steganalysis can be passive or active. In passive steganalysis the attacker tries to detect whether the medium is a stego medium. In active steganalysis the attacker attacks the stego medium, detect and change the stego messages. The presence of embedded messages is often imperceptible but it may disturb the statistics of an image. Determining the difference of some statistical characters between the cover and stego media becomes key issue in steganalysis [19]. There are various steganalysis approaches discuss in paper [15].

Steganalysis algorithm is classified as follows:

1. Specific steganalysis: These types of techniques are established by analyzing the embedding operation and determining certain image statistics. Such techniques need a detailed knowledge of embedding process. These techniques capture very accurate results when used against a target steganography technique. Specific statistical Steganalysis tools are used for finding secret message from stego-images embedded by LSB embedding. The disadvantage of using this method is it is very limited to particular embedding algorithm as well as the image format.

2. Blind / Universal steganalysis: Universal statistical steganalysis comprise the statistical steganalysis method that is not tailored for a specific steganography embedding method. It requires less or even no priori information of the under attack steganographic methods for detection of secret message.

A. LSB EMBEDDING STEGANALYSIS TECHNIQUES Fridrich et al. [8] proposes RS algorithm for steganalysis to detect LSB embedding in 24bit color and 8bit grey scale images. In this method the total image pixel is divided into four pixels (2×2 blocks) disjoint groups and applies discriminating function $f(.)$ to these groups to capture the smoothness of these groups.

$f(G)=f(x_1,x_2,\ldots\ldots,x_n) = \sum_{i=1}^{n-1} |x_{i+1} - x_i| : x_1,x_2,\ldots\ldots,x_n$ *are pixels of group G.*

Also, three invertible function operations are used on pixel value *x.*

$F_1(x)$: $0 \leftrightarrow 1,\ 2 \leftrightarrow 3 \ldots\ 254 \leftrightarrow 255$

$F_{-1}(x)$: $-1 \leftrightarrow 0,\ 1 \leftrightarrow 2 \ldots\ 255 \leftrightarrow 256$

$F_0(x)$: *Identity function*

Operation $F_1(x)$ and $F_{-1}(x)$ are applied on group of pixel based on Mask M which is a n-tuple with values -1,0,1. For example, if the values of the four pixels of a group G are 23, 13, 45, 54 and M = (1, 0, 1, 0), then $F_M(G) = (F_1(23), F_0(13), F_1(45), F_0(54))$. The defined function, operation and mask are applied to group of pixels and distributed them into following groups:

Regular groups: $G \in R \Leftrightarrow f(F(G)) > f(G)$

Singular groups: $G \in S \Leftrightarrow f(F(G)) < f(G)$

Unusable groups: $G \in U \Leftrightarrow f(F(G)) = f(G)$

This technique is based on analyzing how the number of regular and singular groups changes with the increased message length embedded in the LSB plane. The greater the message size, the lower the difference between R_{-M} and S_{-M} and the greater the difference between and R_M and S_M. This behavior is used in detection of hidden message from the stego-image

Westfeld et al. [9] proposed method based on statistical analysis of Pairs of Values (PoVs) using chi-square attack that is exchanged during message embedding. The idea of statistical analysis is to compare the theoretically expected

frequency (which is the arithmetic mean of two frequencies in a PoV since we do not have original cover medium) distribution in steganograms with some sample distribution of stego medium.

To get the statistics for the difference between distributions of PoV's used the below mentioned equation:

$$x^2_{P0V} = \sum_{i=1}^{127} \frac{\left(Y_{2i} - \frac{1}{2}\,(Y_{2i} + Y_{2+!})\right)^2}{\frac{1}{2}\,(Y_{2i} + Y_{2+!})}$$

The probability of embedding is decided by calculating the p-value defined below:

$$p = \Pr\left(x^2_{k-1} \geq x^2_{P0V}\right) = 1 - \frac{1}{2^{\frac{k-1}{2}} \prod\left(\frac{k-1}{2}\right)} \int_0^{x^2_{P0V}} e^{-\frac{x}{2}} x^{\frac{k-1}{2}} dx$$

This p-value is calculated for a sample from the values examined which starts from the beginning of the image and gets amplified for each measurement.

This method provides very reliable results when the message placement is known (e.g., sequential). However, randomly scattered messages can only be reliably detected with this method when the message length becomes comparable with the number of pixels in the image.

Kerke et al. [10] uses a gray level co-occurrence matrix to identify LSB embedded images. Each element (*i,j*) in grey level co-occurrence specifies the number of times that the pixel with value *i* occurred horizontally adjacent to a pixel with value *j* .In this technique four different co-occurrence matrix is generated using four different direction respectively. Then the average of each four matrix is taken. Since the gray level pixel are correlated they are tend to be concentrate on diagonal. As the data embedding increase the pixels are spreads more as the correlation decreases. The author created 2^n feature vectors where n is number of diagonals of co-occurrence matrix. Classification of images as stego is determined by using Absolute distance and Euclidean distance by using following steps:

- Feature vector of the test image is generated
- Absolute distance measure and Euclidean distance measure is used to check the closeness of the test image and the training database images.
- Distance values are sorted in ascending order and minimum of the values is considered
- A threshold value is set to determine whether the image is stego image.

B. LSB MATCHING STEGANALYSIS TECHNIQUES Zang et al. [11] proposes a method of LSB Matching steganography by detecting increasing local minima and decreasing local maxima of histogram of stego. In this method the intensity of histogram is defined as:

$$h_c\,(n) = \left|\{(i,j) |\; p_c(i,j) = n\}\right|$$

: $h_c\,(n)$ indicates the pixel value of intensity n.

Considering the fact that embedding locations are uniformly distributed and independent of pixel value the embedding rate ρ is applicable to only 50% of LSB value because the rest has already had the desired value. Hence, 1-ρ/2 of the pixels have not been modified. The histogram of stego image is given as:

$$h_s(n) = \left(1 - \frac{\rho}{2}\right) h_c(n) + \frac{\rho}{4}\,(h_c(n-1) + h_c(n+1))$$

Based on this equation the following conditions are derived:

$hs\,(n^*) < hc(n^*)$ for local extremum

$h_s\,(n_*) > h_c(n_*)$ for local minimum

This condition helps in detecting steganography in images.

Harmsen [12] exploit the histogram characteristic function (HCF) to detect of steganography in color images. Ker [13] improved Harmsen's method through: (i) introduce a calibration mechanism by using a down sample technology, and (ii) substitute the usual intensity histogram for the adjacency histogram to compute the histogram characteristic function.

1. Calibrated HCF COM Detector Consider down sampling an image by a factor of two in both dimensions using a straightforward averaging filter. Precisely, let be the pixel intensities of the down sampled cover image $p'_c(i,j)$ and similarly down sampled version of the stego image $p'_s(i,j)$ is given by:

$$p'_c(i,j) = \left\lfloor \sum_{u=0}^{1}\sum_{v=0}^{1} \frac{p_c(2i+u,\ 2j+v)}{4} \right\rfloor$$

$$p'_s(i,j) = \left\lfloor \sum_{u=0}^{1}\sum_{v=0}^{1} \frac{p_s(2i+u,\ 2j+v)}{4} \right\rfloor$$

They divide the summed pixel intensities by four and take the integer part to reach images with the same range of values as the originals. They compute the HCF and COM of these two down sampled images $(H'_c[k])$, $C\ (H'_s[k])$ using below equation and they use:

$$(H[k]) = \frac{\sum_{i=0}^{n} i|H[i]|}{\sum_{i=0}^{n} |H[i]|}$$

Finally they conclude that if the image is not a steganography image then $C\ (H'_c[k]) \approx C\ (H_c[k])$ i.e. the Centre of Mass is nearly equal even after sampling the cover medium. The variation between the magnitude of the values they use $C\ (H_c[k])\ /\ C\ (H'_c[k])$ as dimensionless discriminator.

2. Compute Adjacency Histogram Here they consider the two dimensional adjacency histogram and since adjacent pixels are close to intensity the histogram is sparse off the diagonal. The intensity $h_c\ (n)$ is given by:

$$h_c\ (n) = \left|\{(i,j)|\ p_c(i,j) = n\}\right|$$

This histogram of sparse value off the diagonal is affected in case of steganography.

3. CONCLUSION

In this paper we have discussed LSB steganalysis techniques and there line of attack on images. This paper helps to understand LSB steganography and its different steganalysis methods which further help in future studies. Immense research in steganography continues to expand the perceptual transparency, robustness and capacity of information hiding systems. Since ancient times, man has found a desire in the ability to communicate covertly. The recent explosion of research in steganography to protect intellectual property is evidence that steganography is not just limited to military or espionage applications.

REFERENCES

1. F. Battisti, M. Carli, A. Neri, K. Egiaziarian, "A Generalized Fibonacci LSB Data Hiding Technique", IEEE 3rd International Conference on Computers and Devices for Communication (CODEC-06) TEA, Institute of Radio Physics and Electronics, University of Calcutta, December 18-20, 2006.
2. Sandipan Dey, Ajith Abraham, Sugata Sanyal , "An LSB Data Hiding Technique Using Prime Numbers", The Third International Symposium on information Assurance and Security, Manchester, UK, IEEE CS press, pp. 101-108,2007.
3. Sandipan Dey, Ajith Abraham, Sugata Sanyal, "An LSB Data Hiding Technique Using Natural Numbers", Intelligent Information Hiding and Multimedia Signal Processing, IIHMSP 2007. Third International Conference, Kaohsiung, Vol.2, pp. 473-476, 2007.
4. M. Nosrati, R. Karimi, H. Nosrati, and A. Nosrati, "Embedding stego-text in cover images using linked list concepts and LSB technique", Journal of American Science, Vol. 7, No. 6, 2011, pp. 97-100.
5. Z. Ni, Y. Q. Shi, N. Ansari and W. Su, "Reversible data hiding," IEEE Transactions on Circuits and Systems for Video Technology, Vol.16, No.3, pp. 354-362, 2006
6. Wen-Chung Kuo, Dong-Jin Jiang, Yu-Chih Huang, "A Reversible Data Hiding Scheme Based on Block Division", Congress on Image and Signal Processing, Vol. 1, 27-30 May 2008, pp. 365-369.
7. Jun Tian, "Reversible Data Embedding Using Difference Expansion", IEEE Transactions on Circuits and Systems

for video technology, Vol.13, No. 8, August 2003, pp. 890-896.

8. J. Fridrich, M. Goljan and R. Du, "Reliable Detection of LSB Steganography in Color and Grayscale Images". Proc. Of ACM Workshop on Multimedia and Security, Ottawa, Oct. 5, 2001, pp. 27-30.

9. A. Westfeld, A. Pfitzmann, "Attacks on Steganographic Systems", in Andreas Pfitzmann (Ed.): Information Hiding, LNCS 1768, pp. 61-76, Springer-Verlag, 1999.

10. H. B. Kekre, A.A. Athawale, S. A. Patki: "Steganalysis of LSB Embedded Images Using Gray Level Co-Occurrence Matrix", International Journal of Image Processing (IJIP), Volume (5): Issue (1): 2011, pp.36-45

11. Zhang. J., Cox Ingemar J., Doerr G: Steganalysis for LSB Matching in Images with High frequency Noise. In: Proc. IEEE 9th Workshop on Multimedia Signal Processing, MMSP 2007 (October 1-3, October 19, September 16) pp.385-388 (2007).

12. Harmsen, W. Pearlman, "Higher-order statistical Steganalysis of palette images", in Proc. SPIE, Security Watermarking Multimedia Contents, pp. 131–142, 2003.

13. Ker, A.D.: Steganalysis of LSB matching in grayscale images, IEEE signal processing letters 12(6), pp.441-444 (2005).

14. Tanmoy Sarkar, Sugata Sanyal, "Reversible and Irreversible Data Hiding Techniques" in arxiv.org, arXiv: 1045.2684, 2014.

15. Soumyendu Das, Subhendu Das, Bijoy Bandyopadhyay, Sugata Sanyal, "Steganography and Steganalysis: different approaches" in arXiv preprint arXiv: 1111.3758,2011

16. Harshavardhan Kayarkar, Sugata Sanyal, "A Survey on Various Data Hiding Techniques and their Comparative Analysis" in arXiv preprint arXiv: 1206.1957, 2012.

17. J. Fridrich, M. Goljan, and D. Soukal, "Higher-order statistical steganalysis of palette images," in Security and Watermarking of Multimedia Contents V, ser. Proceedings of SPIE, vol. 5020, January 2003, pp. 178–190.

18. A. D. Ker, "A general framework for structural analysis of LSB replacement," in Proceedings of the 7th Information Hiding Workshop, ser. Lecture Notes in Computer Science, vol. 3727, June 2005, pp. 296–311.

19. S.Geetha, Siva S. Sivatha sindhu, R. Renganathan, P. Janaki Raman and Dr. N. Kamraj, "StegoHunter: Steganalysis of LSB Embedded Images based on Stego – Sensitive Threshold Close Color Pair Signature", Sixth Indian Conference on Computer Vision, Graphics and Image Processing, 2008, pp. 281 – 288, 2008.

20. Gustavus J. Simmons, The prisoners' problem and the subliminal channel, Proc. of CRYPTO'83, pp. 51-67, 1983.

21. Sandipan Dey, Ajith Abraham, Bijoy Bandyopadhyay, Sugata Sanyal, "Data Hiding Techniques Using Prime and Natural Numbers.", Journal of Digital Information Management, vol. 6, no. 6, pp. 463-485, 2008.

FUEL SENSING MODULE

Mahesh K*
Research Scholar at Jain University
Associate Professor & HOD-EEE
New Horizon College of Engineering
Ring Road, Bellandur Post, near Marathahalli, Bangalore-560103
Email: maheshkgowda@gmail.com
Tel: +919900119252
*Corresponding author

Vipin S
New Horizon College of Engineering
Ring Road, Bellandur Post, near Marathahalli, Bangalore-560103
Mobile: +919535014568
Email: vipin_meetsu@yahoo.com

Vijay Chacko
New Horizon College of Engineering
Ring Road, Bellandur Post, near Marathahalli, Bangalore-560103
Mobile: +919008004068
Email: vijay.chacko56@gmail.com

ABSTRACT

This paper presents a digital fuel sensing module in which we mainly focus on digitalizing fuel level sensing to display the actual quantity of fuel present in vehicle fuel tank in millilitres that works on the principle of capacitance change . It is essentially an electric transducer that relates the change in capacitance to a change in the level of the fuel. This method proves to be more reliable and accurate than the commonly used resistive float type sensing method in which display unit is analog. The sensitivity of the system is also higher making it more advantageous as we get greater response for smaller changes[1]. The system mainly consists of a capacitance probe that is placed in the tank , a microcontroller that acts as a capacitance meter and an LCD display for the output. Hence it contains lesser components than the conventional system and it works on just 5v,350mA D.C supply making it energy efficient .

Keywords: *Fuel Sensing, Capacitive Fuel sensing, capacitive transducer for level indication, microcontroller based fuel sensing.*

1. INTRODUCTION

Fuel sensing is an essential and important feature in the vehicular world, be it from cars on the street to the planes that zip through the skies. The Fuel sensing system consists of two units:

1. The sensing unit that measures fuel level in the tank and
2. The gauge unit responsible to display the level to the user.

The most commonly used sensing method is the resistive float type. However this method is notoriously inaccurate. In order to make the fuel sensing system accurate, economic and more reliable-capacitance instead of resistance as a parameter of measurement was proposed[2]. Also by employing this method digitization of the system is easier. This method is useful in many Higher end automobiles and in aeronautics as accuracy in determining the amount of fuel present plays an important role.

1. Components : 1.1 Capacitance probe: It consists of two aluminum probes. One is of greater in diameter than the other. The smaller one is placed inside the larger one to form a concentric system with minimum gap between these two plates. Plastic spacers are used to maintain the gap on the inner Surface of the two probes. This forms a capacitance system. The fuel is allowed to enter the gap between the probes through holes drilled on the outer surface of the outer probe. No external power supply is given to the probe. The accuracy of the system mainly depends on this probe.

Figure 1: Self-made capacitance probe

1.2 Arduino Duemilanove ATmega328: This is the central unit of the system. The change in capacitance is sensed by this microcontroller. With its 10 bit ADC the analog values obtained in the system can be converted into digital . Through this unit we also interface the output display. Hence it is the heart of the system.. Arduino pins can be in one of two states, which are electrically very different. Input State (High Impedance (resistance) - Makes very little demand on the circuit that it is sampling .Good for reading sensors but not lighting LED's [3]. Output State -(Low Impedance) - Can provide 40 mA source (positive voltage), or sink (negative voltage)Good for lighting LED's, driving other circuits - useless for reading sensors.

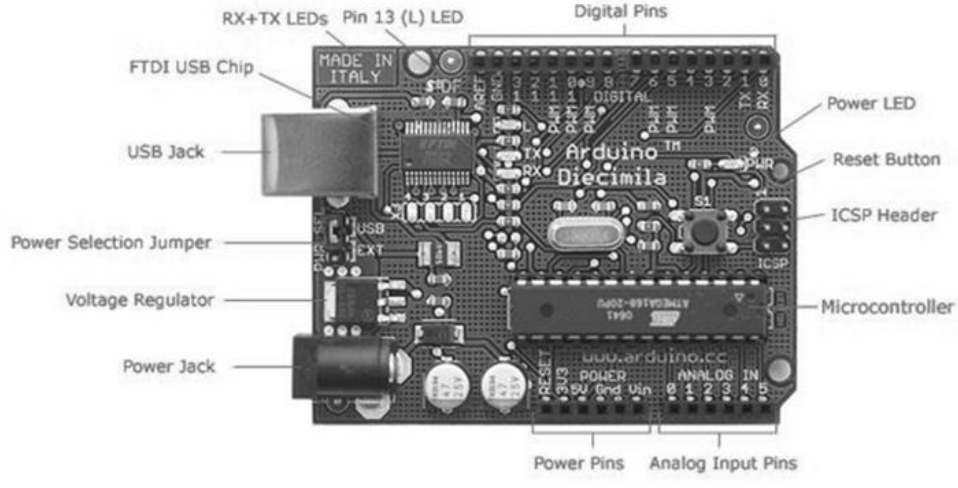

Figure 2: Arduino Microcontroller Board

1.3 LCD display: This is a 16x2 display unit that can be easily interfaced with the Arduino board. Black text on Green background. Utilizes the HD44780 parallel interface chipset. Will need 11 general I/O pins to interface to this LCD screen. Includes LED backlight.

Figure 3: LCD Display unit

2. WORKING

2.1 Block Diagram:

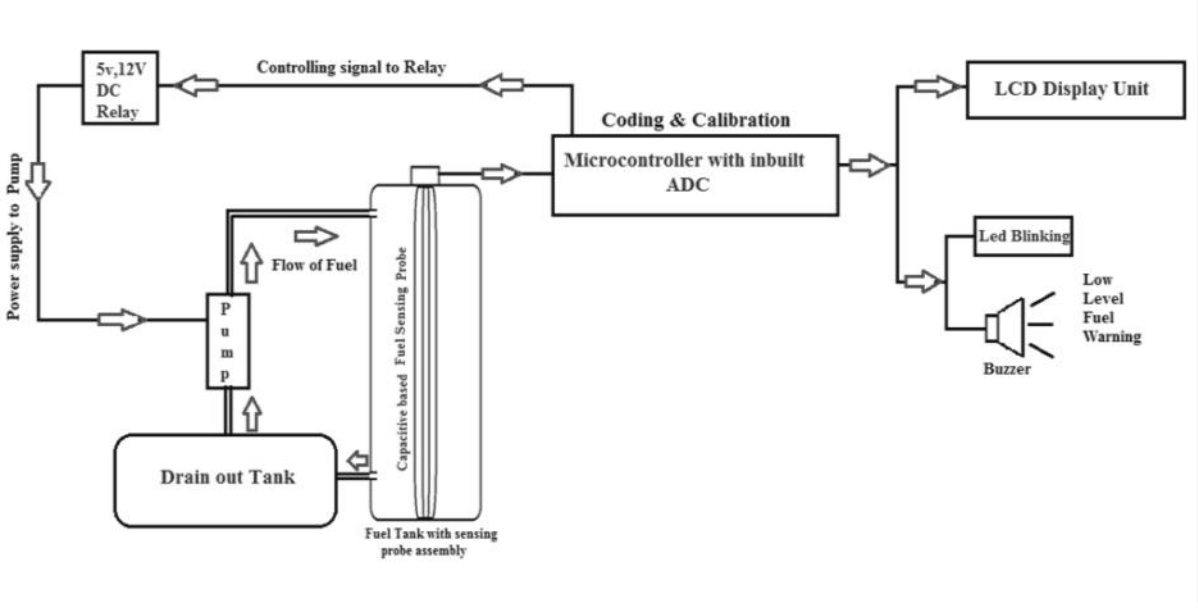

Figure 4: Block Diagram of setup

2.2 Explanation The capacitance probe is placed inside the fuel tank. As the fuel is pumped into the tank , the level increased . Hence the dielectric between the plates changes by increasing. This changes the overall capacitance of the probe. The change in capacitance is sensed by the microcontroller, where the actual coding and calibration is carried out for particular quantity of fuel and it displays the value through the LCD Display. The LED and Buzzer can be used to indicate Low Level of fuel i.e. when the fuel goes down below certain level. So, with change in quantity of fuel, the capacitance changes proportionally as the area of the electrodes, distance between the electrodes and permittivity are constant for a given setup[4].

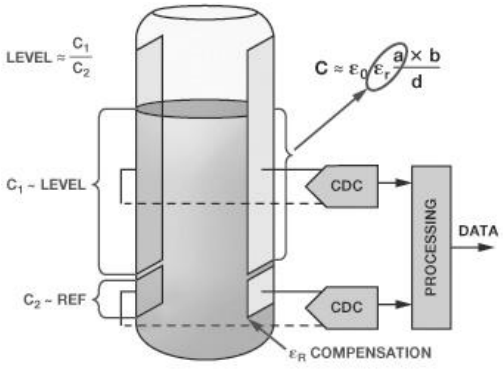

Figure 5: Capacitance sensing principle

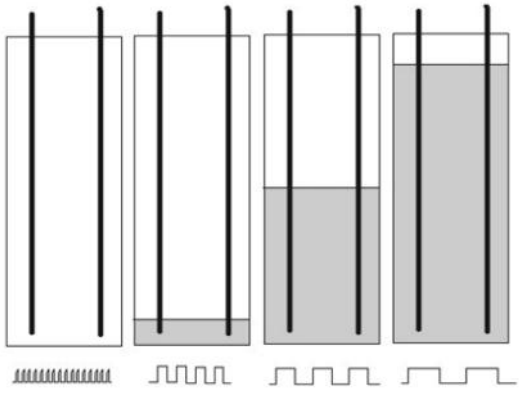

Figure 6: Diagram representing change in frequency with Change in quantity of fuel.

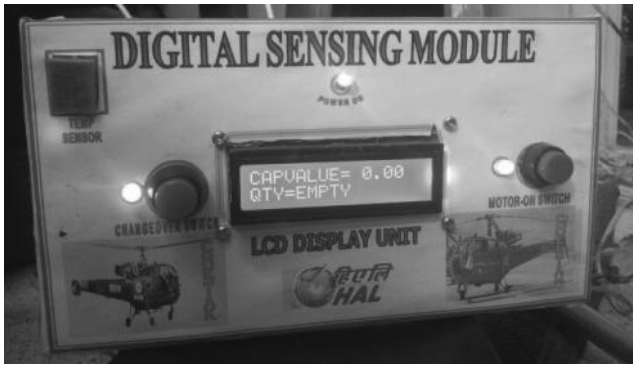

Figure 7: Model

We know that capacitance is inversely proportional to frequency. So as the frequency decreases with increase in quantity of fuel. As a result the capacitance increases and vice versa is also possible. One can make use of frequency sensing principle to sense change in quantity of fuel.

2.3 Principle Used for Capacitive Sensing The time constant of an RC circuit is defined as the time required to charge the capacitor through the resistor in the circuit, by 63.2 percent of the difference between its initial value and final value.

Hence by recording this time we can find capacitance using the formula,

C=TC/R (1)

Where,

C- capacitance value in Farad.

TC- Time constant of RC circuit in seconds.

R- resistance value in circuit in Ohms.

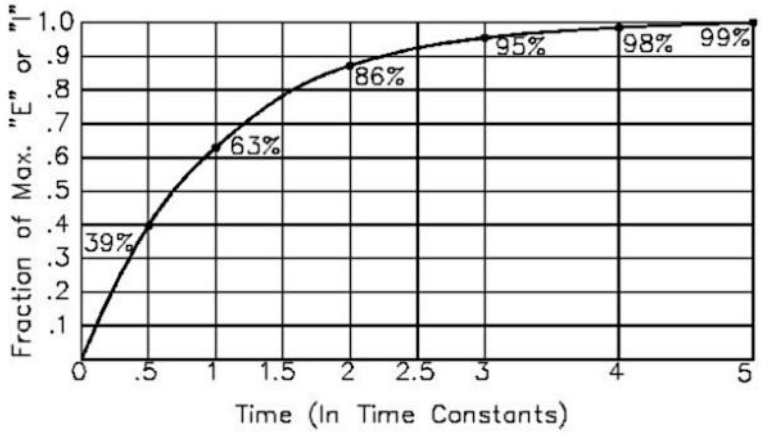

Figure 8: Charging of a capacitor

2.4. Algorithm for Coding Set discharge pin to INPUT (so it can't discharge the capacitor)

Record the start time

Set charge pin to OUTPUT and make it HIGH

Check the voltage repeatedly in a loop until it gets to 63.2% of total voltage.

After the capcitor is charged, subtract the current time from the start time to find out how long the capacitor took to charge.

Divide the Time in seconds by the charging Resistance in ohms to find the Capacitance.

For the obtained capacitance display the corresponding level of fuel .

Discharge the capacitor. To do this:

Set the charge pin to Input

Set the discharge pin to OUTPUT and make it LOW

Read the voltage to make sure the capacitor is fully discharged

Loop and do it again

3. ADVANTAGES AND FUTURE PROSPECTS

The above digital sensing module can be effectively and easily implemented on the existing system of the helicopters. It does not require any constructional change in the structure of the helicopter and is more economical than the existing system. The accuracy of the system is quite high. It can sense 50 ml change in fuel of a particular dimension tank with good dielectric constant fuel. It has fewer components than the existing system hence easier to maintain, repair and even replace if needed. In an analog system, additional resolution requires fundamental improvements in the linearity. Computer-controlled digital systems can be controlled by software, allowing new functions to be added without changing hardware. The product's design errors can be corrected even after it is in the customer's hands. Information storage can be easier in digital systems than in analog ones and can be immediately implemented on the existing system of the helicopters. It can serve as an effective foundation for more improved digital systems in the lower cost range helicopter division. The main part of the system is the Arduino Board which is the only part to be replaced in case of any defect or damage. Its design can be referred for economic designing of other complicated digital systems on the helicopter. On the whole, the digitization of the fuel sensing meter [5] (without much changes in the entire structure) would result in accuracy and precision. it not only overcomes the drawbacks of analog systems but also results as a breakthrough for the developing technology.

REFERENCES

1. Baxter L.K., *Capacitive Sensors; Design and Application*, IEEE Order Nr. PC 5594, IEEE Press, USA, 1996.
2. Toth, F.N., G.C.M. Meijer, **"***A low-cost, smart capacitive position sensor",* IEEE Trans. Instrum. Meas., vol. 41, no. 6, pp. 1041-1044, Dec. 1992
3. Schmidt W., *Sensor system zur Beruhrungsfreien Abtastung von Etiketten,* Pat. Nr: DE 4227052 C1, Deutsches Patentamt Munchen, Germany, 1994.
4. Toth, F.N., H.M.M. Kerkvliet, G.C.M. Meijer, "Ultru-lineur, low-cost measurement system for multi-electrode pF -range cuput*itors", IMTC'95, pp. 412 - 413, April 24 - 25, 1995
5. Kuipers U., Anordnung zur Kapazitiven Fullstandsmessung, Pat. Nr.: DE 4312813 C2, Deutsches Patent Munchen, Germany, 1994.

SIMPLIFIED APPROACH OF EVALUATING WATERFLOODING PERFORMANCE IN STRATIFIED RESERVOIRS USING COMBINATION OF METHODS

Prince Appiah Owusu*
College of Petroleum Engineering, Yangtze University,
No. 1 University Road, Caidian District, Wuhan, Hubei, China.
Department of Civil Engineering,
P. O. Box 854, Kumasi Polytechnic, Kumasi, Ashanti, Ghana
Tel: 008615871432290
Email: princeappiahus@gmail.com
*Corresponding author

Liu DeHua
College of Petroleum Engineering, Yangtze University
No. 1 University Road, Caidian District, Wuhan, Hubei, China.
Tel: 008613907216632
Email: ph.liu@atom.com.

Robert Dery Nagre
College of Petroleum Engineering,
Yangtze University, No. 1 University Road, Caidian District, Wuhan, Hubei, China
Department of Chemical Engineering,
P. O. Box 854, Kumasi Polytechnic, Kumasi, Ashanti, Ghana
Email: nagrerobert@yahoo.com
Tel: 008615272428385

ABSTRACT

A method of predicting waterflood performance has been developed that combines certain facets of several previously published prediction techniques. The manner of combination has requred the development and use of some new and some little-known relationships based on the assumptions inherent in the original individual prediction methods. This approach, which gives a designed template has removed the necessity of referring to plotted curves due to the development of empirical relations and permits the analytical prediction of waterflood performance in either homogeneous or stratified reservoirs. The predicted values are expressed in common oilfield units rather than in abstract or dimensionless terms.

1. INTRODUCTION

Most oil-bearing formations across the world are normally described by heterogeneous petrophysical properties. The most significant property that affects waterflooding performance is the absolute permeability and its variation normal to the direction of flow. This variation causes the displacing fluid to advance faster in zones of higher permeability and thus results in earlier breakthrough in such layers.

The prediction of waterflooding performance for a stratified reservoir has been the subject of many investigations around the world. Several methods have been proposed by many authors for predicting waterflooding performance of stratified reservoirs. A method presented by [1] shows an approach for predicting oil recovery and water cut from such stratified systems. The approach assumes that the mobility ratio is unity, piston-like displacement; all beds have the same

porosity and the same relative permeabilities to water behind the flood and to oil ahead of the flood. [2] introduced a semi-empirical treatment for calculating the recovery of oil by waterflooding stratified reservoirs. Their correlations reflect the effect of initial fluid saturations, mobility ratios, and permeability variations on the waterflooding-oil recovery. [3] developed an approach by combining the Dykstra-Parsons method and the Buckley-Leverett theory.

An extended theory of [8] to stratified reservoirs was developed by [4]. The effect of cross-flow on oil recovery due to waterflooding from stratified reservoirs has been investigated by [5] and [6].

The [5] model considers the viscous forces and neglects both capillary and gravity forces. [6] used a two-phase, two-dimensional model and concluded that waterflooding performance with crossflow is intermediate between the performance of a stratified reservoir with no cross-flow and that of a uniform system. [7] studied the effect of gravitational and capillary forces in the waterflooding of a heterogeneous linear reservoir of mixed permeability ordering. All the above authors present sophisticated and complicated approaches under inherent assumptions and limitations to analyse the performance of waterflooding. With the obvious difficulty of incorporating the vertical sweep efficiency in oil recovery computations a simplified approach which combines methods given above to analysis the performance of stratified reservoirs sets out the focus of this research. The template presented in this research combines the [8] and its graphical equivalent of [13] tangent construction method with [9] model. The procedure is set out by analyzing only one selected layer in the many layer system. The selected layer identified as the base layer, is considered of 100% vertical sweep efficiency. The performance of each the remaining layers can be obtained by sliding the timescale. The composite performance of the flood pattern at a time is derived from the summation of individual layer values. It is believe that the resulting technique is as accurate as the necessary available data will permit and that it has several distinct advantages over previously published methods.

2. MATERIALS AND METHODS

The summary of the methodology and the phases used in the study is described next. The section also provides in-depth explanation of the concepts and theories, which were employed during the process. The data for the study includes the relative permeability data and corresponding water cut as well as reservoir properties obtained from the Reservoir Engineering Aspects of Waterflooding, Craig, Dallas: Society of Petroleum Engineers, 1971 shown in Figure 1 and Table 1 -2 next.

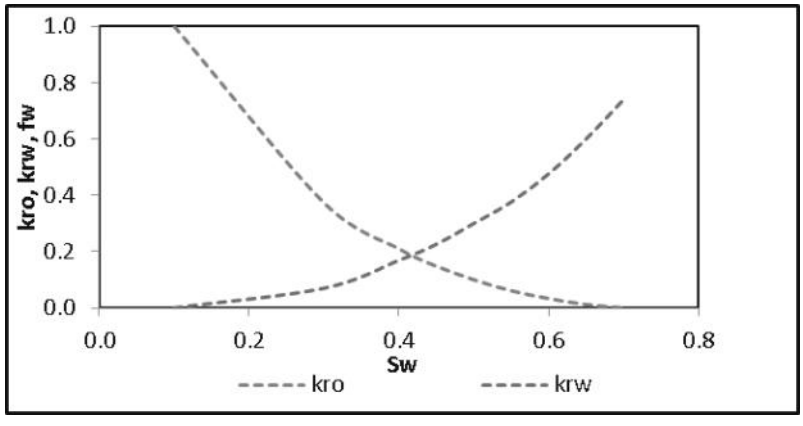

Fig. 1. Relative permeabilities

Table 1. Reservoir layer characteristics

Layer	Permeability, k,(md)	height, (ft)	porosity (φ)
Original base 1	31.50	5	0.2
2	20.50	5	0.18
3	16.00	4	0.15
4	13.00	3	0.14
5	10.90	2	0.1

Table 2. Reservoir properties are as follows Data for analysis

Flood area, acres	40
Initial water saturation, %	10
Connate water saturation, %	10

Current gas saturation, %	0
Water viscosity, c_p	0.5
Oil viscosity, c_p	1
Reservoir pressure, psi	1000
Constant B_o, bbl/STB	1.2
Flood pattern	5 spot
Wellbore radius, ft	1

2.1. Development of the Method

2.1.1. Theory of Fractional Flow

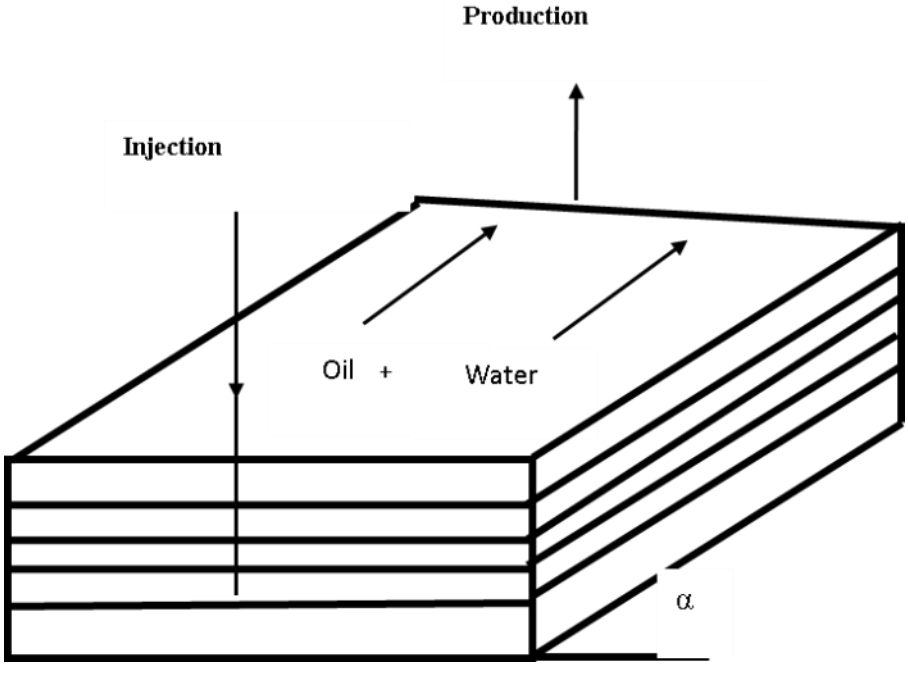

Fig. 2. Stratified Reservoir

The fractional flow equation developed by [8] from Darcy's law is the fundamental mathematical statement describing immiscible fluid-fluid displacement in porous media. A generalized form of this relationship, whose derivation is readily available in the literature, is shown in Eq. 1

$$f_w = \frac{1 + \frac{k_0 A}{q_t \mu_o}\left[\frac{\partial P_c}{\partial x} - g\rho\sin(\alpha)\right]}{1 + \frac{k_{ro}}{k_{rw}}\frac{\mu_w}{\mu_o}} \qquad (1)$$

The formation dip, (α), is usually very small in those petroleum reservoirs being considered for pattern waterflooding, hence (α) has an almost negligible value. In addition, Δρ, the difference between the density of water and the density of oil, is relatively small. For these reasons the gravitational term may often be neglected.

Capillary pressure is a function of saturation, which is in turn a function of distance from the upstream boundary of the system or the injection well. As the distance in a waterflood pattern is comparatively large and the change in water saturation with distance is usually small, the change in capillary pressure with distance is negligible. The simplified form of the fractional flow Eq. 1 is Eq. 2.

$$f_w = \frac{1}{1 + \frac{k_{ro}}{k_{rw}}\frac{\mu_w}{\mu_o}} \qquad (2)$$

Three variables must be considered in determining that fraction of the total fluid flow that consists of water-oil viscosity ratio, saturation, and relative permeability ratio. The viscosity ratio in a given case is essentially constant under the usual waterflooding conditions. The relative permeability ratio is a function of saturation. The value of f_w, is, therefore, a function of saturation, and a curve relating f_w and S_w may easily be determined (Fig. 4).

2.1.2 Frontal Advance theory A second relationship developed by Buckley and Leverett is an expression of the continuity equation known as the frontal advance equation. This equation is used to determine the location in the porous medium of any given water saturation resulting from water injection. Because the derivation has been widely published by [10] it is omitted and only the final equation is presented. The distance travelled by the front of the displacing fluid is given in Eq. 3,

$$[dx]_{Sw} = (v)_{Sw} = \left(\frac{q_t\, dt}{A\emptyset}\right)\left(\frac{df_w}{dSw}\right)_{Sw} \tag{3}$$

Where $\left(\frac{df_w}{dSw}\right)_{Sw}$, is the slope of the fractional flow-saturation curve at the saturation in question.

The saturation distribution within the porous medium is of interest in this study only at and after water breakthrough. Hence L, the length of the porous system, may be substituted for and the frontal advance equation may be rearranged as in Eq. 4:

$$\frac{q_t\, dt}{A\emptyset L} = \left(\frac{df_w}{dSw}\right)_{Sw}^{-1} \tag{4}$$

The term $q_t\, dt$, represents the total volume of water that must be injected into the system to cause the existence of the saturation defined by $\frac{df_w}{dS_w}$ at the outlet end. The quantity $A\emptyset L$ represents the swept pore volume. In waterflooded sand, therefore, the reciprocal of the slope of the fractional flow-saturation curve at a particular saturation will indicate the number of swept region pore volumes of water that must be injected to move the chosen saturation to the outlet end.

The water saturation at the flood front-i.e., the maximum saturation in the frontal zone - may be determined by a method developed by [11].

The area under the saturation distribution curve at water breakthrough may be evaluated by integration. If the initial water saturation S_{wi}, is zero, this area is representative of the volume of injected water at breakthrough. This area may be divided into two, Fig. 3.

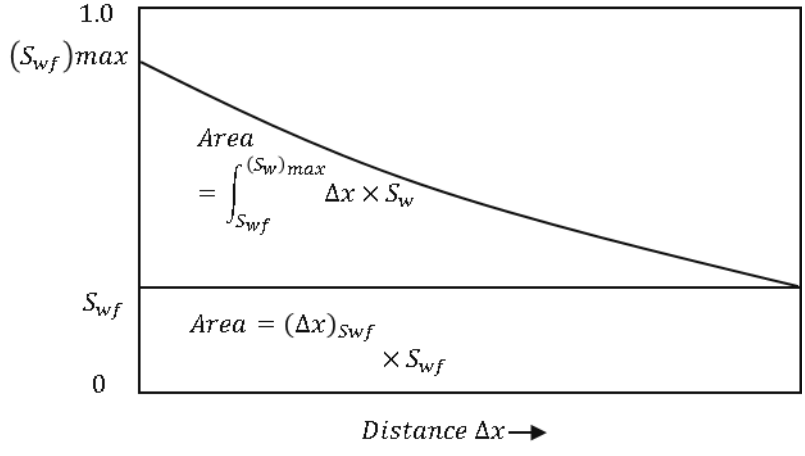

Fig. 3. Displacing phase saturation distribution

Then the total saturation is given as;

$$\int_0^x S_w dx = \int_{S_{wf}}^{(S_w)_{max}} \Delta x dS_w + (\Delta x)_{Swf} S_{wf} \tag{5}$$

Substituting Eq. 4 into above and integrating,

$$(f_w)_{S_{wf}} = S_{wf}\left(\frac{df_w}{dSw}\right)_{Swf} \tag{6}$$

Or

$$S_{wf} = \frac{(f_w)_{S_{wf}}}{\left(\frac{df_w}{dSw}\right)_{Swf}} \tag{7}$$

As pointed by [13], the saturation at the producing well or outlet end of a system is that at which a tangent from the initial water saturation to the fractional flow curve. The slope of the tangent is given in Eq. 8.

$$\left(\frac{df_w}{dSw}\right)_{Swf} = \frac{f_{wf} - f_{wi}}{S_{wf} - S_{wi}} \tag{8}$$

and

$$S_{wf} = S_{wi} + \frac{f_{wf} - f_{wi}}{\left(\frac{df_w}{dSw}\right)_{Swf}} \tag{9}$$

The saturation at the outlet end of the porous system at water breakthrough is the saturation that satisfies Eq. 9 and may be determined by a trial and error solution. This saturation can be found by tangent construction, but the trial and error method is better suited to computer solution.[13] has shown that the average water saturation in the flooded portion of the reservoirs is the value of water saturation at which a tangent to the fractional flow curve at the producing well bore saturation intersects the line f_w= 1.0, or in the generalized as Eq. 10.

$$\bar{S}_w = S_{wf} + \frac{\left[1 - (f_w)_{S_{wf}}\right]}{\left(\frac{df_w}{dSw}\right)_{Swf}} \tag{10}$$

Te average water and water saturation at breakthrough for this research are shown in Fig. 4.

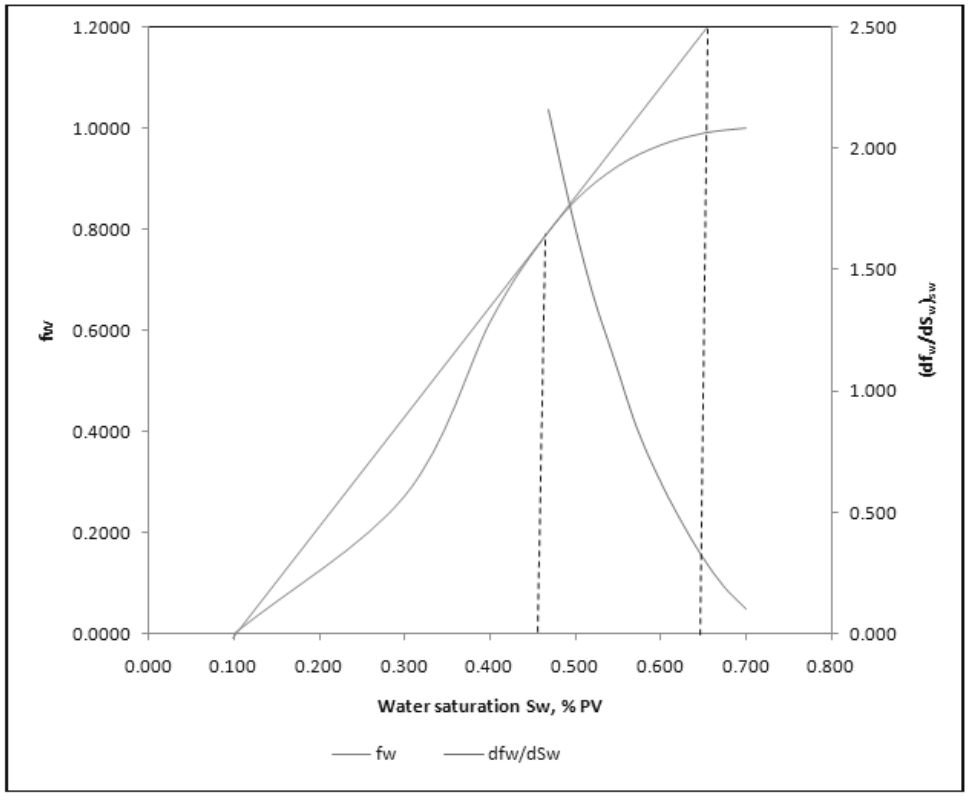

Fig. 4. Displacing fluid saturations at water breakthrough.

An equation has been determined for the relationship between breakthrough sweep efficiency and mobility ratio developed by [9]. This makes it possible to calculate breakthrough sweep efficiency when the mobility ratio has been calculated, without referring to the published curve. The equation, which was determined by regression analysis, is shown in Eq. 11.

$$E_{ABT} = 0.5133 + 0.1682\left(\frac{1}{M}\right) - 0.0015\left(\frac{1}{M^2}\right) \quad (11)$$

2.2.Water Injection Scenarios The water injection history is divided into three periods: (1) the period of radial encroachment, which extends from the start of water injection until the pressured zones (liquid-filled zones) that have formed around adjacent injection wells become tangent at a point assumed to be midway between the injection wells; (2) the period of interference, which extends from the end of radial encroachment until fillup (the time at which essentially all gas has been displaced from the particular zone or layer in question, but not necessarily the entire formation, or has gone into solution); and (3) a so-called constant flow rate period, extending from fillup until the flood is terminated, during which injection and total production rates are often assumed to be equal and constant. To determine the duration of the radial encroachment period, it is first necessary to calculate the volume of water that must be injected during this period by Eq. 12

$$W_{ir} = 0.140W^2h\emptyset S_{gi} \quad (12)$$

By substituting Eq. 12 into Eq. 13, the time necessary for injection can be determined.

$$\frac{W_{ir}}{h\emptyset S_{gi}}\left(log_{10}\frac{1.78W_{ir}}{h\emptyset S_{gi}r_{wa}{}^2} - 0.45\right) + 0.244r_{wa}{}^2 = \frac{0.00617k_w\Delta pt_r}{\mu_w q_t} \quad (13)$$

The constant injection pressure-water injection rate during the period of radial encroachment is determined as a function of time by using Eq. 14.

$$\frac{0.0253k_w h\Delta pt}{\mu_w \emptyset S_{gi} r_{wa}{}^2} = 1 + \left(\frac{0.00617k_w h\Delta p}{\mu_w q_t} - 1\right) \times 10^{\frac{0.00617k_w h\Delta p}{\mu_w q_t}} \quad (14)$$

The equation is solved through iterative approach. Iterative values for q_t are assumed and the equation is solved for the appropriate times. The injection rate decreases with time. By trial and error a value of q_t is found that corresponds to the radial encroachment period t_r . The duration of the interference period is determined by calculating the volume of water required to fill with liquid the zone or layer within the pattern. It is recognized that a small quantity of gas may remain in the sand when oil bank production begins because the displacement and sweep efficiencies of gas displaced by oil are not perfect. However, the residual gas volumes should typically be negligible. The required water volume is therefore calculated with Eq. 15 below as derived by [12]:

$$W_{if} = 0.178W^2h\emptyset S_{gi} \quad (15)$$

The volume of water to be injected during this period is given by Eq. 16.

$$\Delta W_{il} = W_{iF} - \Delta W_{ii} \quad (16)$$

and the duration of the interference period and fullup time are given by Eq. 17 and 18 respectively.

$$\Delta t_I = t_F - t_r = \frac{\Delta W_{iF}}{i_w} \quad (17)$$

$$t_F = \frac{\Delta W_{il}}{i_w} + I_r \quad (18)$$

When fillup is achieved, oil production begins at a rate (expressed in reservoir barrels per day) equal to the water injection rate. As the saturation distribution and average saturations change during oil bank production, and more importantly, after water breakthrough, the relative permeability to water will change. As a result, the mobility of the reservoir fluids will change. At constant injection pressure, the injection and production rates will change in conformity with the new mobilities. These aspects of the waterflood have been considered by [14] as given in Eq. 19.

$$\gamma = 1.9669 - 0.5262M - 3.3378E_A + 1.5599(M \times E_A) - 0.00437M^2 + 1.3965(E_A)^2 \quad (19)$$

2.3. Composite Reservoir Performance With the obvious difficulty of incorporating the vertical sweep efficiency in oil recovery calculations, the procedure advanced by [9] for the performance of stratified reservoirs gives a much useful working principle. The procedure includes performing the calculations for only one selected layer in the multilayered system as expressed above. The selected layer, identified as the base layer, is considered to have 100% vertical sweep efficiency. The performance of each of the remaining layers can be obtained by sliding the timescale. This procedure when combined with the [8] theory makes a lieu way in the analysis of stratified reservoirs. The performance of layer i, at any given time t* is obtained by selection of succession of times t and the performance of the reservoir determined from the performance of the original or base layer. The t* is expressed as a function of the succession time t as given Eq. (20),

$$t^* = t \times a \tag{20}$$

The performance of individual layers at any given time t is expressed Eq. 21 to Eq. 25.

$$N_p = N^*_p \times b = N_S \times E_D \times E_V \times b \tag{21}$$

$$W_p = W^*_p \times b = \frac{W_{inj} - N_p B_o}{B_w} \times b \tag{22}$$

$$W_{inj} = W^*_{inj} \times b = i_w \times t \times b \tag{23}$$

$$Q_o = Q^*_o \times a = \frac{i_w}{B_o + B_w WOR_s} \times a \tag{24}$$

$$Q_w = Q^*_w \times a = Q_o \times WOR_s \times a \tag{25}$$

$$i_w = i^*_w \times a = \frac{W_{inj}}{t} \times a \tag{26}$$

$$a = \frac{\left(\frac{k}{\emptyset}\right)_i}{\left(\frac{k}{\emptyset}\right)_n}, \qquad b = \frac{(\emptyset h)_i}{(\emptyset h)_n}$$

Where n is base layer, i is the individual layers, N^*_p, W^*_p, W^*_{inj}, are volumes and , Q^*_o, Q^*_w, i^*_w are rates at time t^* based on the performance of the original or base layer with (a) and (b) been dimensionless static property ratios.

The composite performance of the flood pattern at time t is obtained by summation of individual layer values. [9] method of predicting water production rates, oil production rates, injection rate, cumulative oil recovery, and WOR's as functions of time for the reservoir layers was then produced.

3. RESULTS AND DISCUSSIONS

Tables 3-5 gives the permeability ratios, time scale for individual layers at a given time and layer co-efficient respectively. The reservoir performance at a given time is determined based on Table 4-6. The composite performance of the waterflooding is obtained from the summation of the individual layer values. Tables 6-7 gives the performance of the individual layers based on original or base layer and the composite performance for all layers after 689days of flooding.

Table 3. Permeability and porosity ratios for individual layers

Layer	k/φ	hφ	kh	$(h\varphi)_i/(h\varphi)_n$
original base 1	157.50	1	157.5	1
2	113.89	0.9	102.5	0.9
3	106.67	0.6	64	0.6
4	92.86	0.42	39	0.42
5	109.00	0.2	21.8	0.2

Table 4. Time scale for different layers at t=689days

layer	$(k/\varphi)_i/(k/\varphi)_n$	$t^*=t_i[(k/\varphi)_i/(k/\varphi)_n]$
1	1.000	689
2	0.723	498
3	0.677	467
4	0.590	406
5	0.692	477

Table 5. Individual layers co-efficient

layer	$(h\varphi)_i/(h\varphi)_n$	$(k/\varphi)_i/(k/\varphi)_n$
1	1	1.000
2	0.9	0.723
3	0.6	0.677
4	0.42	0.590
5	0.2	0.692

Table 6. The performance of the individual layers based on base layer at time t = 689days

layer	$t^*=ti[(k/o)i/(k/o)n]$	N_p*	W_p*	W_{inj}*	Q_o*	Q_w*	i_W*
1	689	115772	46513.62	185440	54.45	197.7	269
2	498	106389.8	102795.2	134092.4	78.91	174.0	254.48
3	467	105360	95523.79	125589	88.67	165.8	250.71
4	406	103368.6	81647.99	109329.7	113.5	150.0	242.75
5	477	105693.6	97871.93	128336.3	85.32	167.0	251.958

Table 7. Performance of all layers after 689days

layer	$(h\varphi)_i/(h\varphi)_n$	N_p	W_p	W_{inj}	$(k/o)_i/(k/o)_n$	Q_o	Q_w	i_W	WOR_S
1	1.00	115772	46513.62	185440	1.00	54.45	197.66	269.00	
2	0.90	95750.85	92515.7	120683.2	0.72	71.02	156.6	229.03	
3	0.60	63215.99	57314.27	75353.4	0.68	53.20	99.48	150.42	
4	0.42	43414.8	34292.16	45918.48	0.59	47.67	63.00	101.95	**2.260**
5	0.20	21138.72	19574.39	25667.25	0.69	17.06	33.40	50.39	
Total		**339292.4**	**250210.1**	**453062.3**		**243.41**	**550.14**	**800.80**	

Fig. 5 shows the performance curves for the original or base layer. From these curves and base on the times scale factors the performance of the individual layers are determined.

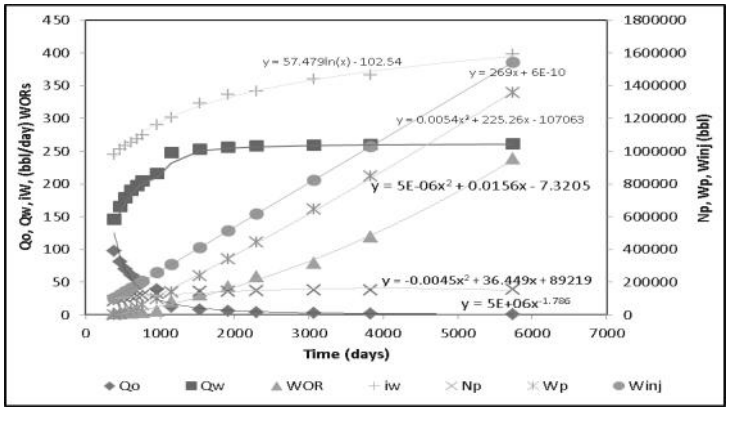

Fig. 5. Reservoir performance of the base layer

3.1. Performance characteristics of the reservoir Figs. 6-8 show the performance of the reservoir as a function of pore volume injected, fractional recovery and sweep efficiency. Initial increase in oil production rate is attributed to the increase in pore volume water injected. Production flow rate peak at an increasing high fraction of water and declines as water oil ratio increases. Oil recovery reached its maximum at 71% at maximum fraction of water. The effect of injected water in oil recovery is seen in the corresponding increase in recovery due increase in pore the pressure as a result of increase in pore volume.

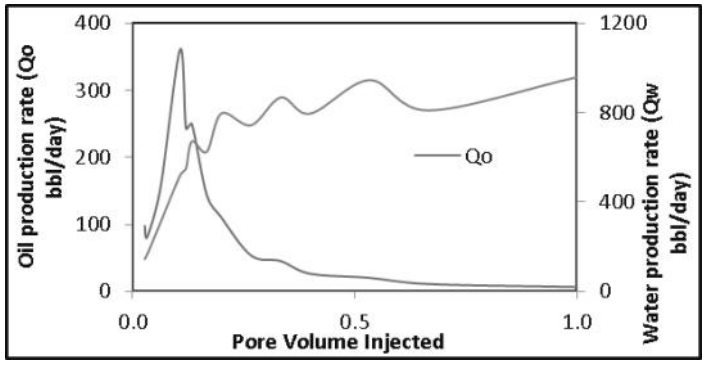

Fig. 6. Production flow rate performance

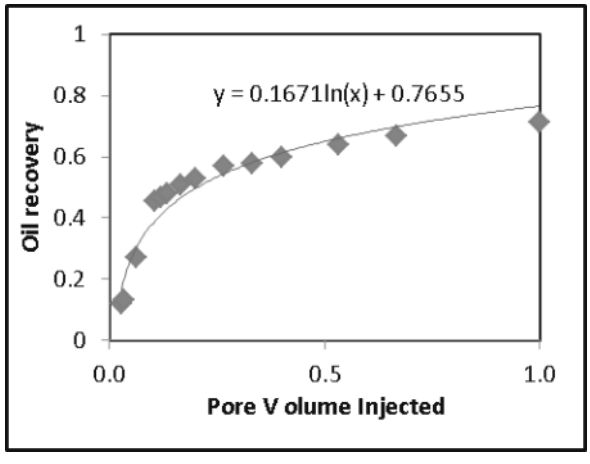

Fig. 7. Recovery against PV injected

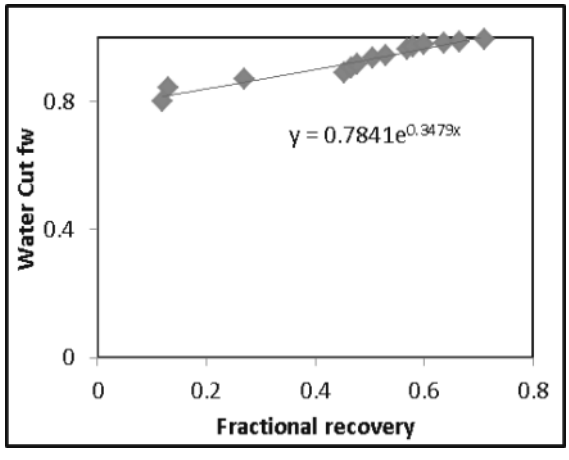

Fig. 8. Water cut vs. Recovery factor

Fig. 9 shows the generated composite reservoir performance curves which describe the entire reservoir performance till abandonment.

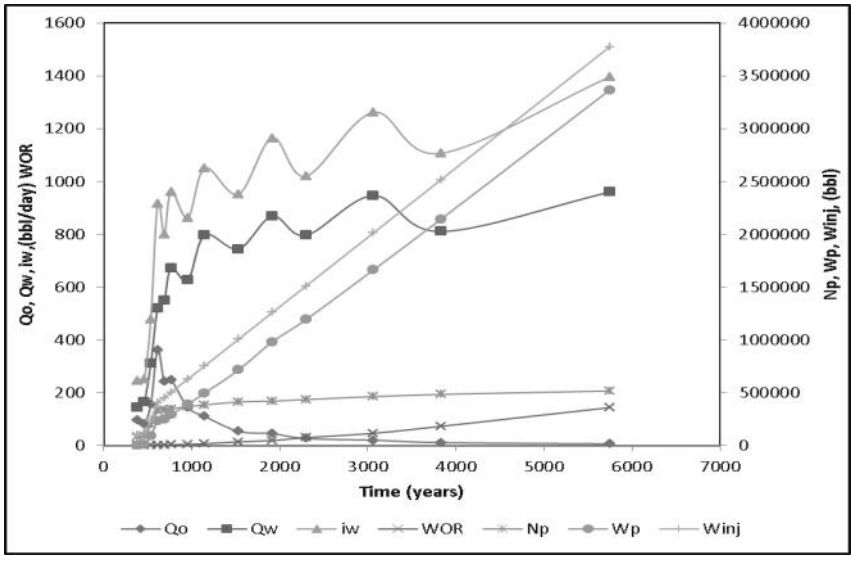

Fig. 9. Composite reservoir performance

4. CONCLUSION

A method of incorporating several recognized mathematical waterflood performance prediction methods into one composite method has been described. This combination has resultant effect in the elimination of several of the weaker assumptions inherent in the individual prediction procedures and gives a complete history of the waterflood based on available data. This gives a template for the analysis of performance of stratified reservoirs.

ACKNOWLEDGMENT

The authors fully appreciate the important support from College of Petroleum Engineering of Yangtze University, for this work. Authors, P. A. Owusu and R. D. Nagre gratefully acknowledge the Management of Kumasi Polytechnic for their immense support.

REFERENCES

1. Stiles, W. E., *Use of Permeability Distribution in Waterflood Calculations*, Trans, AIME (1949), 186, 9-13.
2. Dykstra, R.; & Parsons, R. L. *The Prediction of Oil Recovery by Waterflooding*, Secondary Recovery of Oil in the United States, 2nd ed., API, New York (1950), 160-174.
3. Kufus, H. B.; & Lynch, E. J. *Linear Frontal Displacement in Multi-Layer Sands Prod*. Monthly (December 1959), Vol. 24, No. 12, 32-35
4. Snyder, R. W.; & Ramey, H. J. Jr. *Application of Buckley-Leverett Displacement Theory to Noncommunicating Layered System*, J. Pet. Tech. (November 1967), 1500-1506.
5. Warren, J. E.; & Cosgrove, J. J. *Prediction of Waterflood Behavior in a Stratified System*, Soc. Pet. Eng. J. (June 1964), 149-157.
6. Goddin, C. S., Jr.; Craig, F. F. Jr.; Wilkes, J. O.; & Tek, M. R. *A Numerical Study of Waterflood Performance in a Stratified System with Cross Flow*, Trans. AIME (1966), 237, 765-771.
7. Coats, K. H. *An Analysis for Simulating Reservoir Performance Under Pressure Maintenance by Gas and/or Water Injection*, Soc. Pet. Eng. J. (December 1968), 331-340.
8. Buckley, S. E.; & Leverett, M. C. *Mechanism of Fluid Displacement in Sands*, Trans., AIME (1942) 146, 107-116.
9. Craig, F. F., Jr.; Geffen, T. M.; & Morse, R. A. *Oil Recovery Performance of Pattern Gas or Water Injection Operations from Model Tests*, Trans., AIME (1955) 204, 7-14.
10. Collins, R. E. *Flow of Fluids Through Porous Materials*, Reinhold Publishing Corp., New York, N. Y. (1961), 142 -149.
11. Calhoun, J. C., Jr. *Fundamentals of Reservoir Engineering*, U. of Oklahoma Press, Norman, Okla. (955) 340-342.
12. Suder, F. E.; & Calhoun, J. C., Jr. *Water-flood Calculations*, Drill. and Prod. Prac., API (1949) 260-270.
13. Welge, H. J. *A Simplified Method for Computing Oil Recovery by Gas or Water Drive*, Trans., AIME (1952) 195, 91-98
14. Caudle, B. H.; & Witte, M. D. *Production Potential Changes During Sweep-Out in a Five-Spot System*, Trans., AIME (1959) 216, 446-448.

COSTING OF OVERHEAD POWER LINES

T S Kishore
Research Scholar
Alternate Hydro Energy Centre
IIT Roorkee
Roorkee-247667, Uttarakhand, India
Email: srinivasakishoret@gmail.com

S K Singal*
Principal Scientific Officer
Alternate Hydro Energy Centre
IIT Roorkee
Roorkee-247667, Uttarakhand, India
Email: sk_teegala@yahoo.co.in
*Corresponding author

ABSTRACT

This paper presents the costing procedures for estimating the cost of overhead power lines in India by classifying them into distribution and transmission lines. Details of various cost components such as civil works, superstructure, erection and miscellaneous costs which are significant in influencing the overall cost of the line have been presented. Assumptions made in line design and cost for reducing the complexity of cost calculations have been described. Final cost estimates as worked out for distribution and transmission lines are presented in the study. The cost estimates obtained, pertain to the line designs considered in this paper, however the costing method presented is applicable to other complex line design cost estimation problems.

Key words: *Transmission Line, Distribution Line, Cost Estimation.*

1. INTRODUCTION

Overhead power lines are used for transmission and distribution of electrical energy from generating sources to load centers and are generally three phase alternating current systems. Electrical energy is transmitted at higher voltage to minimize the transmission losses, while the distribution is done at lower voltage levels. High voltage direct current systems are found to be advantageous in long distance transmission and for connecting two different alternating current systems. Power transmission and distribution is usually done through overhead systems as installation and maintenance cost is more in underground systems and also, control of voltage in long cables is difficult. The underground systems are preferred in densely populated areas keeping in view land availability, public safety and aesthetics. Overhead power lines form the least-cost method of transmitting and distributing electrical power as in most cases the medium of insulation is air. Since overhead lines are un-insulated, design of these lines requires minimum clearances to be observed to maintain safety [1].

India is a large country with 28 states, having varied geography, terrain and weather conditions. The North and North Eastern states are mostly hilly regions, while the other states are mostly plain areas and plateaus. Each state electric utility has their own design, construction and costing philosophies regarding distribution and transmission lines which are limited to 220KV. Power Grid Corporation of India, a central utility constructs lines above 220KV and is responsible for stable operation of the power grid. 400KV transmission lines form the backbone of India's power network. The present study considers the most important and common aspects followed by various utilities in estimating the cost of distribution

and transmission lines. The distribution line voltages in the country vary from single phase 240V to three phase 33KV, whereas, the transmission lines are designed to operate with three phase voltages only, which range from 132KV to 765KV. Due to increasing energy demand and lack of adequate right of way for construction of new lines, the country is focusing to develop ultra high voltage transmission lines in the order of 1200KV. In this regard an experimental 1200KV line is commissioned near Bina, Madhya Pradesh state with the participation of public and private sector power utilities.

2. COST COMPONENTS OF LINES

Cost of overhead power lines depends on the line designs, cost of materials and erection costs which vary from time to time and place to place. For a particular design, the final decision on costs is made after considering the requirements and estimates based on region in which the line is to be constructed. The cost components of overhead power lines are classified into four categories namely civil works substructure, superstructure, erection and miscellaneous costs [2].

2.1 Civil works substructure consists of surveying the line route profile and construction of the foundations. Surveying works include route surveying and peg marking for the tower positions conforming to the alignment and tower schedules. The actual construction of foundation involves excavation, piling, concreting and reinforcing steel. Foundations used for transmission line supports are designed to sustain and transfer the combined effect of various loads acting on the tower to the ground so that no settlement or movement of the foundation occurs, which otherwise would affect the stability of the structure and cause damage. The foundations cost approximately 10 to 30 % of the overall support cost or 5 to 15 % of the total line cost. The design of a safe and reliable foundation is based on soil properties, soil structure interaction, and settlement analysis of foundation, support dimensions and forces acting on the foundations. The foundations constructed for distribution line supports are mostly based on thumb rules regardless of soil conditions, wind speeds, line design parameters etc., however, scientific methods do exist for design of these foundations.

2.2 Superstructure consists of line supports, conductors, insulators and all accessories required for erecting the line supports. Line supports in an overhead power line, perform the function of carrying the conductors, withstanding reliably the conductor forces and external loads. Poles and towers are commonly used supports in overhead systems which are made of steel, reinforced concrete or wood. Support design is based on the transmission voltage, number of circuits and height. Based on the design, appropriate material is chosen for construction the supports. Operational reliability and aesthetics of an overhead power line dominate the support design and hence, contribute significantly to the cost. The cost of transmission line supports has a significant impact on total line cost, compared to distribution line supports. The type of conductor attachment through the insulators at the supports depends on the application for which the support is designed.

Conductors perform the function of carrying electrical energy between two points reasonably and reliably. Hence conductor is considered to be the most important component of overhead power line and costs upto 35 % of the total line cost [3]. Conductor design is based on power transfer capability, corona performance, impedance matching to surge impedance, capital and operation and maintenance cost, voltage levels, continuous and short term current ratings, thermal limits and environmental constraints. Insulators are the overhead line components which perform the function of insulating the live conductors with other parts of the structure. These are placed between live conductors and earthed parts of the structure and are continuously subjected to electrical and mechanical stresses. Insulators are designed for the most adverse operating conditions which can prevail in the operating area, resulting from climate impact and pollution effects. Hence, for best insulator performance, they are designed with due weightage to mechanical strength, disruptive strength and insulator material. Various designs for insulators are available in the literature over wide operating voltages.

Accessories used for line supports majorly consist of overhead line fittings which serve the purpose of mechanical attachment for electrical connections and for protection of conductors and insulators. Accessories used for conductor arrangement include clamps suitable for various supports, connectors, vibration protection fittings and spacers. Bolts, ball & socket or clevis & tongue connections, yoke plates, spark gaps, arcing horns and grading rings are used in insulator fittings. Apart from these, various other miscellaneous small accessories are also used in transmission line constructions, which may be in the form of individual elements or assemblies [4].

2.3 Erection In overhead power lines it is not possible to precisely calculate the erection cost due to multiple factors affecting the task or nature of the job. Each and every overhead power line construction is different and hence the associated erection cost will also vary. The factors responsible for erection cost variations are environment related, materials and equipment used, personal skill levels, management and operating practices. Erection job for overhead power line construction is generally categorized into three sections viz. support location and erection, installation of support-top hardware and conductor stringing.

Support location and erection requires that the supports to be moved from the delivery point to the point of erection and to set them according to the specifications. This procedure is not used for all type of supports. It is applicable to readily available supports made of wood or steel poles. In case, concrete poles are used, they are mostly casted at the site and steel towers are assembled at the site by using steel parts to form a latticed steel tower structure. Thus, cost for support location and erection depends on the type of support and required handling, which directly affects the time taken to complete the task. Support-top hardware job consists of installing the cross arms, bracings, insulators supports, insulators etc. The procedures are different for different supports and depend on type of support, affecting the operation time and cost. Lines using poles as supports require less time and simple process for performing the task as compared to lines using lattice structures or towers as supports.

Conductor stringing operation is further divided into two parts i.e. actual conductor stringing operation and conductor clipping operation. The cost of the stringing operation is relatively constant whereas the cost of clipping operation is variable depending on the number of supports per kilometer. The stringing cost also depends on the type of stringing i.e. normal or tension stringing. The methodology for the calculation of erection costs has been discussed above, although there are many other factors playing key role in affecting these costs. The geographic conditions i.e. line routing and accessibility affect the erection costs significantly. An increase of 25-40% may be there on the labour charges and transportation depending on the distance of work site from road head. Every power utility and contractors consider their own applicable rates for erection jobs. For overhead line cost estimation purpose, erection costs are generally considered in the form of a fixed percentage of the line material cost.

2.4 Miscellaneous costs These costs are included in any particular category due to their highly variable and petty nature. These costs depend on location, management, contingency and government policies. Some of the commonly applicable miscellaneous costs are storage & handling charges, contingency on materials, transport charges, cess, establishment and general charges etc. These charges are generally considered on a fixed percentage basis on the total cost of materials required for constructing an overhead power line.

3. COST ESTIMATION

For realistic cost estimation, overhead power lines are divided into distribution and transmission lines. This is mainly due to the difference in the design aspects of both the lines and procedures adopted for cost estimation. In case of distribution lines, up to 33 KV, as considered in this study, the cost of poles used as support, is very less in distribution lines as compared to latticed tower supports used in transmission line. This comparison is done to represent the cost of the support as a percentage of total cost of the line. The tower cost forms a significant portion of total cost in transmission line. The design of tower is complex and critical in the operation of the line, as compared to distribution line. The span considerations for a transmission line are determined by either insulator strength or pole strength or sag limitations or cross arm strength. In case of distribution line, span limitations are governed by environmental factors through which the line is passing such as height of buildings, public safety, government policies and rules, rather than technical concerns [5]. Usually distribution line spans are lesser as compared to transmission line span lengths.

3.1 Distribution line Costing The cost estimation of distribution line is carried out by dividing the costs into five components viz. supports, top hardware, conductor, civil works and cost of miscellaneous items, which form the total cost of materials. Further erection costs and other miscellaneous costs as discussed in sections 2.3 and 2.4 respectively, are imposed on total materials cost on fixed percentage basis to arrive at the overall cost of the distribution line. Top hardware for distribution line consists of cross arms, insulators, clamps and all other necessary hardware required for placing the conductor on the support. Since the type of foundation is not standardized for constructing the supports of distribution lines, concreting is done to the required level. Table 1 shows the various distribution line configurations considered for cost estimation. The quantity of materials required for each configuration and the computed cost per kilometer for all distribution line configurations have been worked out and given in Table 2 and Table 3 respectively. The present prevailing costs of materials was used for the cost estimation and are always subjected to change depending on market conditions.

Table 1: Line Configurations considered for Estimation of Cost

Config-uration Number	Description of Line	Wind Pressure kg/sq.m	Wind Load kg	Pole	Span in m	Conductor
1	33 KV Line	75	280	9.1 m PSCC	105	100 sq.mm AAA
2	33 KV Line	100	280	9.1 m PSCC	80	100 sq.mm AAA
3	11 KV Line	75	140	8 m PSCC	60	55 sq.mm. AAA
4	11 KV Line	100	200	8 m PSCC	65	55 sq.mm. AAA
5	11 KV Line	75	140	8 m PSCC	60	34 sq.mm AAA
6	11 KV Line	100	200	8 m PSCC	65	34 sq.mm AAA
7	LT 3-ph 5 Wire	75	140	8 m PSCC	65	3 x 5 5 + 2 x 3 4 sq.mm. AAA
8	LT 3-ph 5 Wire	100	200	8 m PSCC	60	3 x 5 5 + 2 x 3 4 sq.mm. AAA
9	LT 3-ph 5 Wire	75	140	8 m PSCC	65	5x34 sq.mm. AAA
10	LT 3-ph 5 Wire	100	200	8 m PSCC	60	5x34 sq.mm. AAA
11	LT 3-ph 4 Wire	75	140	8 m PSCC	65	3 x 5 5 + 1 x 3 4 sq.mm. AAA
12	LT 3-ph 4 Wire	100	200	8 m PSCC	60	3 x 5 5 + 1 x 3 4 sq.mm. AAA
13	LT 3-ph 4 Wire	75	140	8 m PSCC	65	4x34 sq.mm. AAA
14	LT 3-ph 4 Wire	100	200	8 m PSCC	60	4x34 sq.mm. AAA
15	LT 1-ph 3 Wire	75	140	8 m PSCC	65	3x34 sq.mm. AAA
16	LT 1-ph 2 Wire	75	140	8 m PSCC	65	2x34 sq.mm. AAA

Table 2: Estimation for quantity of materials required

S.No.	Category	Configuration →	1	2	3	4	5	6	7	8	9	10	11	12	13	14	15	16
		Material ↓	**Quantity ↓**															
1	Supports	9.1 m PSCC Poles	12	14	-	-	-	-	-	-	-	-	-	-	-	-	-	-
2		8 m PSCC Poles	-	-	18	17	18	17	16	18	16	18	16	15	16	15	16	16
3	Top hardware	1.53 m Channel Cross arm	10	12	-	-	-	15	-	-	-	-	-	-	-	-	-	-
4		1.07 m Channel Crossarm	-	-	16	15	16	-	-	-	-	-	-	-	-	-	-	-
5		LT 3-ph cross arms	-	-	-	-	-	-	18	20	18	20	18	17	18	17	-	-
6		LT 1-ph Cross arms	-	-	-	-	-	-	-	-	-	-	-	-	-	-	18	18
7		Top clamp with cleat	10	12	16	15	16	15	-	-	-	-	-	-	-	-	-	-
8		D Clamp	-	-	-	-	-	-	-	-	-	-	-	-	-	-	-	-
9		Back clamp	10	12	16	15	16	15	18	20	18	20	18	17	18	17	18	18
10		Stay sets with clamps	6	6	6	6	6	6	4	4	4	4	4	4	4	4	4	4
11		Bracing set with double crossarm (Set)	1	1	1	1	1	1	-	-	-	-	-	-	-	-	-	-
12		Shackle Insulator Set	-	-	-	-	-	-	42	42	42	42	32	32	32	32	22	12
13		33 KV Pin Insulator with Pin	33	39	-	-	-	-	-	-	-	-	-	-	-	-	-	-
14		11 KV Pin Insulator with Pin	-	-	51	48	51	48	-	-	-	-	-	-	-	-	-	-
15		LT Pin Insulator with Pin	-	-	-	-	-	-	48	56	48	56	36	33	36	33	24	12
16		Strain Insulator set with metal parts (Set)	6	6	6	6	6	6	-	-	-	-	-	-	-	-	-	-
17		CI knob	-	-	-	-	-	-	16	18	16	18	16	15	16	17	16	16
18	Conductor	100 sq.mm. AAA conductor KM	3.06	3.06	-	-	-	-	-	-	-	-	-	-	-	-	-	-
19		55 sq.mm. AAA conductor KM	-	-	3.06	3.06	-	-	3.06	3.06	-	-	3.06	3.06	-	-	-	-
20		34 sq.mm AAA conductor KM	-	-	-	-	3.06	3.06	2.04	2.04	5.1	5.1	1.02	1.02	4.08	4.08	3.06	2.04
21	Civil Works *		Lump Sum															
22	Miscllaneous items #		Lump Sum															
* Concreting of pole, stay sets, base etc. # Coil earthing, pipe earthing, danger boards, bolts & nuts etc.																		

Table 3: Final Estimated Cost and Actual Cost for Distribution Lines

Costs in Rs. ↓ / Configurations →	**1**	**2**	**3**	**4**	**5**	**6**	**9**	**10**	**11**	**12**	**13**	**14**	**15**	**16**	**17**	**18**
Supports	36690	42805	31520	32312	31520	32312	28018	34212	28018	34212	28018	28510	28018	28510	28018	28018
Top Hardware	43871	49162	26878	25715	26878	25715	17080	18753	17080	18753	14353	13665	14353	13697	10054	8685
Conductor	171993	171993	92632	92632	58538	58538	131657	131657	97563	97563	112145	112145	78050	78050	58538	39025
Concrete	22422	22422	25884	25884	25884	25884	21199	21199	21199	21199	21199	21199	21199	21199	21199	21199
Misc	4368	4368	5824	5824	5824	5824	4633	4633	4633	4633	4633	4633	4633	4633	4633	4633
Total cost of material	279343	290750	182739	182367	148644	148272	202586	210454	168492	176359	180347	180151	146253	146088	122441	101560
Storage and handling charges @ 3%	7577	7919	4531	4520	3508	3497	5303	5539	4280	4516	4635	4630	3613	3608	2898	2272
Contingencies on materials @ 3%	8380	8722	5482	5471	4459	4448	6078	6314	5055	5291	5410	5405	4388	4383	3673	3047
Labour charges @ 25%	69836	72687	45685	45592	37161	37068	50647	52613	42123	44090	45087	45038	36563	36522	30610	25390
Transport charges @ 5%	13967	14537	9137	9118	7432	7414	10129	10523	8425	8818	9017	9008	7313	7304	6122	5078
Cess on material, labour & transport @ 1%	3631	3780	2376	2371	1932	1928	2634	2736	2190	2293	2345	2342	1901	1899	1592	1320
Establishment & General Charges on materials @ 11%	30728	31982	20101	20060	16351	16310	22284	23150	18534	19400	19838	19817	16088	16070	13469	11172
Total Estimated Line Cost	**413462**	**430378**	**270050**	**269499**	**219488**	**218937**	**299660**	**311328**	**249098**	**260766**	**266680**	**266389**	**216118**	**215874**	**180805**	**149838**
Actual Line Construction Cost	**534818**	**560421**	**348745**	**345138**	**311502**	**288866**	**393923**	**375846**	**334808**	**300406**	**357340**	**357695**	**283794**	**278286**	**243436**	**191162**

3.2 Transmission Line Costing The design and cost estimation of a transmission line cannot be generalized for various designs as in the case of a distribution line [6]. This is due to the fact that each transmission line design takes into account various factors depending on the topography which affect the design. Each transmission line design is route specific and hence, the associated costs. It is not possible to estimate the cost of transmission lines for standard configurations as done in the case of distribution lines, hence practical case is considered for cost estimation. In case of distribution line, a flat 25% of the materials cost is considered for erection cost, but, in case of transmission line, it is job specific and each task of erecting a transmission line has specific rates for erection, standardized by utilities and contractors [7].

The estimation of cost for a 132KV single circuit transmission line for a route length of 31.6 kilometers located in East coast region of India has been carried out and presented in this study. The detailed design of transmission line is beyond the scope of this study. Flat land area, straight stretch, uniform level and normal foundations for all towers, no major crossings such as river, railway, and highway crossings are the major assumptions considered for cost estimation. All the design data such as wind loads, temperature, sag considerations, shield angles for earth wires, conductor properties and spacing are considered to be ideal and the data is taken based on the region (Wind Zone 5, Wind speed 50m/s) in which the line is considered [8, 9]. Table 4 shows the estimate for quantity of material required for construction of the transmission line. The description of the works associated in erecting the line and the corresponding costs and final cost estimate for the transmission line are worked out and given in Tables 5 and Table 6 respectively.

Table 4: Estimation for quantity of material required for towers

S.No	Type of tower	No. of towers	Stubs and cleats	Super Structure weight (kg)	Bolts and nuts	Erection Weight (kg)	Weight including stubs and cleats (kg)	Total Weight including stubs and cleats (kg)	Total erection Weight (kg)	Total Bolts and nuts
Towers										
1	Tangent	125	189	2810	121	2931	2999	374875	366375	15125
2	Angle	12	453	5765	221	5986	6218	74616	71832	2562
Total Weight Approximately								**450 MT**	**4 4 0 MT**	**18 MT**
Structures										
1	TND	3	154	995	42	1037	1149	3447	3110	126
2	TNS	6	109	853	42	895	962	5774	5368	251
3	BNC	6	0	566	36	601	566	3394	3608	214
Total Weight								**12615**	**12086**	**591**
Total Weight Aprroximately								**13 MT**	**12 MT**	**1 MT**
Half Round Welding										
1	Tangent	125	-	-	276	-	-	-	-	34500
2	Angle	12			580					6960
3	TND	3	-	-	140	-	-	-	-	420
4	TNS	6	-	-	140	-	-	-	-	840
Total Bolts and Nuts										42720
Toatl Bolts and Nuts Approximately (Numbers)										**43000**
Foundations										
			Concrete c.m				**Total Volume c.m**			
1	Tangent	125	2.5				313			
2	Angle	12	10				120			
Total Volume of Concrete							**433 c.m**			

Table 5: Estimation of erection works and charges

Sl. No.	Description	Unit	Insurance @ 0.5% on Cost of Material	Cost as per Utility / Contractor	Unit Cost (Total Cost + Insurance)	Works Contract Tax @ 4%	Service tax @ 10.3% on 33% of Unit Cost	Cess @ 1 %	Total Unit Cost	Quantity	Total Cost
1	Check Survey, peg marking the tower positions	Km	0	3941	3941	158	134	40	**4273**	32	136736
2	Excavation	c.m	0	100	100	4	4	1	**109**	4744	517096
3	Foundations	c.m	0	3609	3609	145	123	37	**3914**	433	1694762
4	Setting of stubs with stub-setting template										
a	For 132 KV Tangent & Angle Type towers	Loc	0	7035	7035	282	240	70	**7627**	137	1044899
b	For 132 KV TND & TNS Structures	Loc	0	2666	2666	107	91	27	**2891**	9	26019
5	Erection of towers										
a	Erection of tower structures ,including all types of extensions	MT	374	4659	5033	202	172	51	**5458**	440	2401520
b	Erection of main and auxiliary structures etc. using blots & nuts	MT	340	2649	2989	120	102	30	**3241**	13	42133
6	Stringing of power conductor (3 No's ACSR Panther conductors)	RKM	1751	31770	33521	1341	1140	336	**36338**	31	1126478
7	Stringing of Earth wire (Under Normal conditions)	RKM	119	6357	6476	260	220	65	**7021**	34.50	242224
8	Earthing										
a	Earthing of towers including cost of excavation, Back filling, Charcoal, Salt etc., and measuring of tower footing resistance.	Each	0	3528	3528	142	120	35	**3825**	137	524025
b	Counterpoise earthing including cost of 7/8 SWG high tensile galvanised steel wire	RM	0	36	36	1.43	1.22	0.36	**39**	2000	78000
9	Half round welding of GI Bolts and nuts of towers	Each	0	17	17	0.67	0.57	0.17	**18**	43000	774000
10	Tree cutting & crop compensation	Lump Sum									4000000
Total Erection Cost (All Costs are in Indian Rupees)											**12607892**

Table 6: Final cost estimate for transmission line

Cost Estimate	Cost in Rs
Material cost	54312772
Spares @ 3%	1629383
Labour cost - Electrical	10259298
Labour cost - Civil	2348594
Subtotal 1	68550047
contingencies @ 3%	2056501
Subtotal 2	70606548
Establishment & General Charges @ 10.75%	7590203
Total	**78196751**
Approximately Rs. 7.81 Crore	

4. DISCUSSION

In the present study, costing of overhead power lines has been presented in detail. The costing of distribution lines has been carried out for various configurations standardized by Rural Electrification Corporation (REC) [10]. The corporation considers various governing factors prevailing in different states for standardization of design of distribution lines. Appropriate cost inflation index has been used to assess the various costs associated in constructing these lines. The computed cost has been compared with actual construction cost. The actual construction cost data has been obtained from the developers and surveys conducted among different state utilities of the country.

Fig. 1 shows the comparison of costs and it has been found that the actual construction costs are about 30% more than the estimated costs. This is due to the fact that India being a vast country with highly diversified geography, the conditions for construction of distribution lines are not unique everywhere. Every state utility in India has its specific designs approved for construction of distribution lines taking into consideration geographic, environmental and reliability aspects. It is observed that the cost for constructing lines in hilly areas and in North Eastern states of the country are about 2 times of the cost in plain areas due to geographic constraints. It is also observed that the use of steel tubular poles for all voltage classes of distribution lines in hilly region, as a matter of approved design, increases the construction costs by 2.5 times as compared to the costs in plain areas.

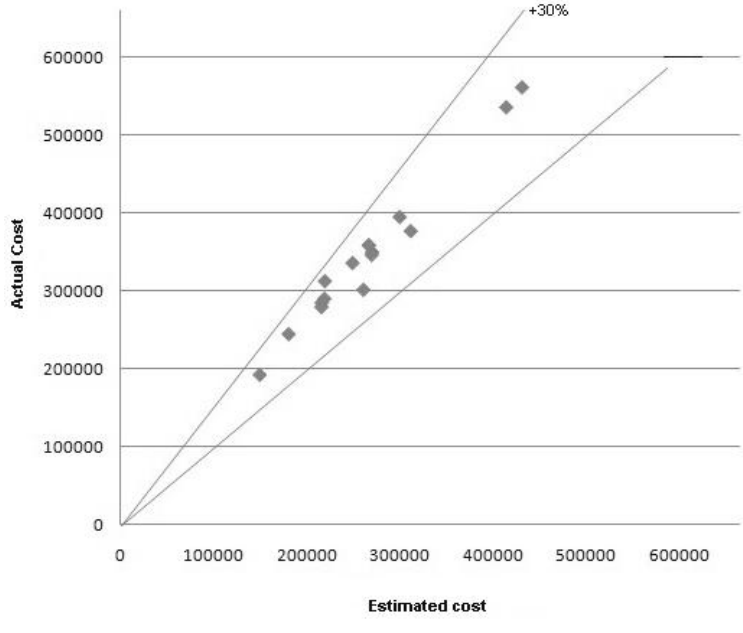

Fig.1 Comparison of estimated cost with actual cost in Indian Rupees

There is no standard design and costing procedure for a transmission line being site specific. Thus cost estimation for transmission line is presented considering a real time case study. Assumptions are made to simplify the design process and the cost calculations. For example, by assuming a straight stretch without any line deviations and major crossings, the use of angle and special towers can be avoided, which reduces the material, erection and foundation costs significantly. However, angle towers are used for sectionalization purpose. The geographic conditions in which the line is being operated are also assumed to be ideal and hence the adverse effects of environment, which increases the design complexity, safety factors and hence increase in associated costs, are eliminated. Also, right of way requirement costs are not included in the cost calculations.

5. CONCLUSIONS

In the present study, procedures for estimating the cost of overhead power lines have been presented. The approximate costs estimated for overhead power lines are validated with actual cost data and are found to be in acceptable range. The deviation in costs is due to the various assumptions made in the design aspects and the use of standardized designs for estimating the cost. However the estimated costs include all the necessary costing aspects for the design considered and hence, costing of various other line designs can be obtained in a similar manner by estimating the material quantity required and further calculating the related costs.

ACKNOWLEDGEMENTS

The author wishes to express his sincere thanks to AHEC, IIT Roorkee, India for providing research facilities and Ministry of HRD, Govt. of India for providing financial support in the form of research scholarship. The author wishes to express his gratitude to GMR Institute of Technology, Rajam, Andhra Pradesh, India for financially sponsoring him to pursue doctoral studies under QIP scheme of MHRD, Government of India.

REFERENCES

1. F. Kiessling, P. Nefzger, J.F. Nolasco, U. Kaintzyk. *Overhead Power Lines Planning, Design, Construction* New York, Springer Publications, 2003.
2. Adam J F, Bradbury J, Charman W R, Orawski G, Vanner M J. Overhead lines – some aspects of design and construction. In: Proceedings of IEE Generation Transmission Distribution, 1984, 131(5), 149-187.
3. Alain H. Peyrot, Eric M. Peyrot, Ahmed Senouci. Computer-aided design of transmission lines, Engineering. Structures, 1993, 15 (4), 229-237.
4. Orawski G. Overhead lines – the state of the art. Power Engineering Journal, 1993, 7(5), 221-231.
5. Robert D Castro. Overview of the transmission line design process. Electric Power Systems Research, 1995, 35(2), 109-118.
6. Robert D Castro. Overview of the transmission line construction process. Electric Power Systems Research, 1995, 35(2), 119-125.
7. Mario A. Marchio, Transmission Line Construction, Estimating Today, American Society of Professional Estimators, 2011.
8. IS: 5613 (Part 2/Sec.1&2) : 2007 – Indian Standard Code of Practice for Design, Installation and Maintenance of Overhead Power Lines: Lines above 11 kV and up to and including 220 kV.
9. IS: 398 (Part 2&3) : 1996 – Indian Standard Code for Aluminium conductors for overhead transmission purposes.
10. www.recindia.nic.in/consstds.html, accessed on 5th July 2013.

PARTICLE SWARM OPTIMIZATION ALGORITHM BASED ON ADVANCE AND RETREAT STRATEGY WITH CLONE MECHANISM FOR SOLVING OPTIMAL REACTIVE POWER DISPATCH PROBLEM

K.Lenin*
Research Scholar
JNTU, Hyderabad 500 085 India
Email: gklenin@gmail.com
*Corresponding author

B.Ravindhranath Reddy
Deputy Executive Engineer
JNTU, Hyderabad 500 085 India

M.Surya Kalavathi
Professor
JNTU, Hyderabad 500 085, India

ABSTRACT

This paper presents a new particle swarm optimization algorithm based on Advance and Retreat Strategy with Clone mechanism (PSOARC) for solving the multi-objective reactive power dispatch problem in power system. The standard Particle Swarm Optimization (PSO) algorithm is an innovative evolutionary algorithm in which each particle studies its own previous best solution and the group's previous best to optimize problems. It is well known that the advance-and-retreat strategy is a simple and operative method of one-dimensional search. We use the advance-and-retreat strategy to bestow the clones with faster speed to find nearby local regions before subsequent clonal operation. Besides, in the next clonal operation, the search space is enlarged prominently and the diversity of clones is augmented. When the fitness value turns better after last 'flying', the cloned particle progresses. On the divergent, the cloned particle retreats then searches in the back direction of the last "flying" with a small step-size of the preceding velocity. Thus, the swarm has robust optimization capability. The simulation results demonstrate good performance of the (PSOARC) in solving an optimal reactive power dispatch problem. In order to evaluate the efficiency of proposed algorithm, it has been tested on IEEE 30 bus system and compared to other algorithms.

Key words: *Advance and retreat strategy, clone mechanism, Particle swarm optimization, Swarm Intelligence, optimal reactive power, Transmission loss.*

1. INTRODUCTION

Optimal Reactive Power Dispatch (ORPD) problem is one of the challenging optimization problems in power systems. The sources of the reactive power are the generators, synchronous condensers, capacitors, static compensators and tap changing transformers. Here the reactive power dispatch problem involves best utilization of the existing generator bus voltage magnitudes, transformer tap setting and the output of reactive power sources so as to minimize the loss and to enhance the voltage stability of the system. It involves a non linear optimization problem. Various mathematical techniques have been adopted to solve this optimal reactive power dispatch problem. These include the gradient method [1, 2], Newton method [3] and linear programming [4-7]. Recently Global Optimization techniques such as genetic algorithms have been proposed to solve the reactive power flow problem [8, 9]. In recent years, the problem of voltage stability and voltage

collapse has become a major concern in power system planning and operation. To enhance the voltage stability, voltage magnitudes alone will not be a reliable indicator of how far an operating point is from the collapse point [10]. The reactive power support and voltage problems are intrinsically related. Hence, this paper formulates the reactive power dispatch as a multi-objective optimization problem with loss minimization and maximization of static voltage stability margin (SVSM) as the objectives. The particle swarm optimization (PSO) developed by Eberhart and Kennedy in 1995 is a stochastic global optimization technique enthused by social behaviour of bird flocking, fish schooling, or animals herding where these swarms search for food in a collective manner [11], [12]. Each particle in the swarm adjusts its search patterns to search for the comprehensive optimum in the high dimensional space by learning from its own experience and others. Since the PSO comprises a very simple concept and paradigms can be applied more easily with it, it has been proved in certain instances that PSO outperforms other population based evolutionary computing algorithms in many practical engineering fields such as function optimization, artificial neural network training, fuzzy system control, blind source separation as well as machine learning [13]. Furthermore, the PSO has also been found to be strong and reckless in solving nonlinear, non-differentiable and multi-modal problems [14]. In modern years, there have been a number of efforts to combine PSO algorithms with other techniques in order to progress the performance of the conventional standard PSO. Convergent speed, global exploration capability, and complication are the main evaluation catalogues for PSO and its variants. In this paper, the Advance and Retreat strategy is presented for the first time into the conventional standard PSO united with the Clonal mechanism, resulting in building a fresh variant of PSO.After each clonal process, the advance and retreat strategy bestows the clones with faster speed to find nearby local regions by using the history information of each particle's last performance of 'flying'. In the next clonal operation, clonal mutation and selection of the best individual of a number of subsequent generations expand the search space significantly and intensification the diversity of clones to avoid being trapped in local minima. Thus, the clones have more probabilities to find and flee the nearby local regions with faster speed. The performance of PSOARC has been evaluated in standard IEEE 30 bus test system and the results analysis shows that our proposed approach outperforms all approaches investigated in this paper.

2. VOLTAGE STABILITY EVALUATION

2.1 Modal analysis for voltage stability evaluation

The linearized steady state system power flow equations are given by.

$$\begin{bmatrix}\Delta P\\ \Delta Q\end{bmatrix} = \begin{bmatrix} J_{p\theta} & J_{pv}\\ J_{q\theta} & J_{QV}\end{bmatrix} \quad (1)$$

Where

ΔP = Incremental change in bus real power.

ΔQ = Incremental change in bus reactive

Power injection

$\Delta\theta$ = incremental change in bus voltage angle.

ΔV = Incremental change in bus voltage Magnitude

$J_{p\theta}$, J_{PV} , $J_{Q\theta}$, J_{QV} jacobian matrix are the sub-matrixes of the System voltage stability is affected by both P and Q. However at each operating point we keep P constant and evaluate voltage stability by considering incremental relationship between Q and V.

To reduce (1), let $\Delta P = 0$, then.

$$\Delta Q = \left[J_{QV} - J_{Q\theta}J_{P\theta}{}^{-1}J_{PV}\right]\Delta V = J_R\Delta V \quad (2)$$

$$\Delta V = J^{-1} - \Delta Q \quad (3)$$

Where

$$\left(J_{QV} - J_{Q\theta}J_{P\theta}{}^{-1}JPV\right) \quad (4)$$

$J_R$is called the reduced Jacobian matrix of the system.

2.2 Modes of Voltage instability: Voltage Stability characteristics of the system can be identified by computing the eigen values and eigen vectors

$$J_R = \xi \wedge \eta \quad (5)$$

LetWhere,ξ = right eigenvector matrix of J_R

η = left eigenvector matrix of J_R

Λ = diagonal eigenvalue matrix of J_R and

$$J_R^{-1} = \xi \Lambda^{-1} \eta \quad (6)$$

From (5) and (6), we have

$$\Delta V = \xi \Lambda^{-1} \eta \Delta Q \quad (7)$$

or

$$\Delta V = \sum_I \frac{\xi_i \eta_i}{\lambda_i} \Delta Q \quad (8)$$

Where ξ_i is the ith column right eigenvector and η the ith row left eigenvector of J_R.

λ_i is the ith eigen value of J_R.

The ith modal reactive power variation is,

$$\Delta Q_{mi} = K_i \xi_i \quad (9)$$

where,

$$K_j = \sum_j \xi_{ij}^2 - 1 \quad (10)$$

Where

ξ_{ji} is the jth element of ξ_i

The corresponding ith modal voltage variation is

$$\Delta V_{mi} = [1/\lambda_j] \Delta Q_{mi} \quad (11)$$

In (8), let $\Delta Q = e_k$ where e_k has all its elements zero except the kth one being 1. Then,

$$\Delta V = \sum_j \frac{\eta_{1k} \xi_1}{\lambda_1} \quad (12)$$

η_{1k} k th element of η_1

V –Q sensitivity at bus k

$$\frac{\partial V_K}{\partial Q_K} = \sum_j \frac{\eta_{1k} \xi_1}{\lambda_1} = \sum_j \frac{P_{ki}}{\lambda_1} \quad (13)$$

3. PROBLEM FORMULATION

The objectives of the reactive power dispatch problem considered here is to minimize the system real power loss and maximize the static voltage stability margins (SVSM).

3.1 Minimization of Real Power Loss Minimization of the real power loss (P_{loss}) in transmission lines has been mathematically stated as follows.

$$P_{loss} = \sum_{\substack{k=1 \\ k=(i,j)}}^{n} g_k (V_i^2 + V_j^2 - 2 V_i V_j \cos\theta_{ij}) \quad (14)$$

Where n is the number of transmission lines, g_k is the conductance of branch k, V_i and V_j are voltage magnitude at bus i and bus j, and θ_{ij} is the voltage angle difference between bus i and bus j.

3.2 Minimization of Voltage Deviation Minimization of the Deviations in voltage magnitudes (VD) at load buses is mathematically stated as follows.

$$\text{Minimize VD} = \sum_{k=1}^{nl} |V_k - 1.0| \quad (15)$$

Where nl is the number of load busses and V_k is the voltage magnitude at bus k.

3.3 System Constraints In the minimization process of objective functions, some problem constraints which one is equality and others are inequality had to be met. Objective functions are subjected to these constraints shown below.

Load flow equality constraints:

$$P_{Gi} - P_{Di} - V_i \sum_{j=1}^{nb} V_j \begin{bmatrix} G_{ij} & \cos\theta_{ij} \\ +B_{ij} & \sin\theta_{ij} \end{bmatrix} = 0, i = 1,2 \ldots., nb \quad (16)$$

$$Q_{Gi} - Q_{Di} - V_i \sum_{j=1}^{nb} V_j \begin{bmatrix} G_{ij} & \cos\theta_{ij} \\ +B_{ij} & \sin\theta_{ij} \end{bmatrix} = 0, i = 1,2 \ldots., nb \quad (17)$$

where, *nb* is the number of buses, P_G and Q_G are the real and reactive power of the generator, P_D and Q_D are the real and reactive load of the generator, and G_{ij} and B_{ij} are the mutual conductance and susceptance between bus *i* and bus *j*.

Generator bus voltage (V_{Gi}) inequality constraint:

$$V_{Gi}^{min} \leq V_{Gi} \leq V_{Gi}^{max}, i \in ng \quad (18)$$

Load bus voltage (V_{Li}) inequality constraint:

$$V_{Li}^{min} \leq V_{Li} \leq V_{Li}^{max}, i \in nl \quad (19)$$

Switchable reactive power compensations (Q_{Ci}) inequality constraint:

$$Q_{Ci}^{min} \leq Q_{Ci} \leq Q_{Ci}^{max}, i \in nc \quad (20)$$

Reactive power generation (Q_{Gi}) inequality constraint:

$$Q_{Gi}^{min} \leq Q_{Gi} \leq Q_{Gi}^{max}, i \in ng \quad (21)$$

Transformers tap setting (T_i) inequality constraint:

$$T_i^{min} \leq T_i \leq T_i^{max}, i \in nt \quad (22)$$

Transmission line flow (S_{Li}) inequality constraint:

$$S_{Li}^{min} \leq S_{Li}^{max}, i \in nl \quad (23)$$

Where, nc, ng and nt are numbers of the switchable reactive power sources, generators and transformers.

4. PARTICLE SWARM OPTIMIZATION (PSO)

The particle swarm procedure is stochastic in nature; it uses a velocity vector to update the current position of each particle in the swarm. The velocity vector is updated based on the memory gained by each particle, theoretically similar to a narrative memory, as well as the knowledge gained by the swarm as a whole. Thus, the position of each particle in the swarm is updated based on the social behaviour of the swarm which acclimatises to its environment by returning to talented regions of the space previously exposed and probing for improved positions over time. Mathematically, the position of the *i*th particle, X_i, at iteration $t + 1$ is updated as follows:

$$X_i^{t+1} = X_i^t + V_i^{t+1} \quad (24)$$

Where V_i^{t+1} is the corresponding updated velocity vector given as follows:

$$V_i^{t+1} = \omega V_i^t + c_1 r_1 \left(P_i^t - X_i^t\right) + c_2 r_2 \left(G_{best}^t - X_i^t\right) \quad (25)$$

Where V_i^t is the velocity vector at iteration *t*, r_1 and r_2 represents arbitrary numbers between 0 and 1; P_i^t represents the best ever particle position of particle *i*, and G_{best}^t corresponds to the global best position in the swarm up to iteration *t*. The remaining terms are problem dependent parameters; in this paper, cognitive parameter, c_1, and c_2, social parameter, are considered to be equal to 2. Also, ω is the inertia weight which plays an important role in the PSO convergence performance.

Due to the importance of ω in achieving efficient search behaviour the optimal updating criterion is taken as follows:

$$\omega = \omega_{max} - \frac{\omega_{max} - \omega_{min}}{k_{max}} \cdot k \quad (26)$$

Where ω_{max} and ω_{min} are the maximum and minimum values of ω, respectively. Also, k_{max}, and k are the number of maximum iterations and the number of present iteration.

4.1Modifications of PSO In [15], Tan et al. presented the immunity-clonal strategies into the PSO. By cloning the best individual often succeeding generations, CPSO can promise to uphold the respectable performance of standard PSO. In the interim, the core of the clonal operator is to produce a new particle swarm near the capable candidate solution according to the value of the fitness function such that the search space are enlarged significantly and the diversity of clones is augmented to avoid trapping in local minima. In [16], golden section search algorithm is united with particle swarm optimization algorithm together. The PSO is accountable for search direction, and the golden section search algorithm takes responsibility of step-size along this direction. After the search direction of a particle is determined by the velocity equation of PSO, the golden section algorithm is engaged to speed up the convergence along this direction. In PSO-LS [17], each particle has a chance of self improvement by applying local search algorithm before it connects information with other particles in the swarm. Then these basic PSO-LS are altered by selecting some precise good particles initial solutions for local search. In the local search, hill-climbing algorithms are amalgamated into particle swarm optimization to progress the performance of PSO. The genetic algorithm is united with local search in the hybrid algorithm. HGPSO (hybrid Gradient descent PSO) [18] algorithm makes use of gradient information to attain faster convergence. The gradient descent rule is united with the equation of the initial PSO to escape from local minima traps. Multi-Local PSO algorithm [19] uses gradient descent directions in order to drive each particle to a neighbour local minimum, thus discovering several solutions.

5. PRINCIPLE OF CONVENTIONAL ADVANCE AND RETREAT STRATEGY

The conventional advance and retreat strategy is a simple and operative method for the problem of one-dimensional search. One-dimensional search is also called linear search for optimization of a single-variable objective function. The iterative formula in one-dimension search is as follows:

$$x_{k+1} = x_k + v_k d_k \tag{27}$$

Where x_k denotes the position of a solution, v_k denotes the velocity of a solution and d_k denotes the direction of the velocity. The bottleneck problem in Eq. (27) is to define the exploration direction d_k and the step size v_k. Let

$$\varphi(v_k) = f(x_k + v_k d_k) \tag{28}$$

Where $\varphi(v_k)$ denotes the function value of the velocity v_k, f is the objective function. The determination of the step size v_k and the exploration direction d_k satisfying Eq.(29) is the one-dimensional search problem.

$$\varphi(v_k) < \varphi(0) \tag{29}$$

The one-dimensional search is also called optimal one dimensional search and the step-size v_k is called optimal step-size if the step-size v_k minimizes the objective function along the exploration direction d_k as in Eqs.(30) and (31).

$$f(x_k + v_k d_k) = min f(x_k + v d_k), where\ v > 0 \tag{30}$$

Or

$$\varphi(v_k) = min \varphi(v), where\ v > 0 \tag{31}$$

Advance and Retreat Algorithm

Step 1 Initialization: $v_0 \in [0, \infty]$, $h_0 > 0$, and the factor of Acceleration $\alpha > 1$, calculate $\varphi(v_0)$, k=0.

Step 2 Evaluations of the Fitness Values:

$v_{k+1} = v_k + h_k$

$\varphi_{k+1} = \varphi(v_{k+1})$

if $\varphi_{k+1} < \varphi_k$ **then**

go Step 3

else

go Step 4
end if
Step 3 Advance:
$h_{k+1} = \alpha h_k$
$v = v_k$
$v_k = v_{k+1}$
$\varphi_k = \varphi_{k+1}$
k = k + 1
go Step 2
Step 4 Retreat:
if k = 0 **then**
$h_k = -h_k$ //inverse the exploration direction
$v_k = v_{k+1}$
go Step 2
else
stop
end if
Step 5:
$a = \min\{v, v_{k+1}\}$
$b = \max\{v, v_{k+1}\}$
output [X,Y]

6. PARTICLE SWARM OPTIMIZATION ALGORITHM BASED ON ADVANCE AND RETREAT STRATEGY WITH CLONE MECHANISM

i) **Clonal Mechanism**: After numerous iterations, a clonal operator is used to clone the best individual of n succeeding generations as n same particles in the solution space according to their fitness values at first, then N (size of swarm) new particles are produced via clonal mutation and selection processes .Fleetingly, the clonal operator in our PSOARC from the CPSO [15] can be concise as follows
Step 1: Initialization.
Step 2: The state evolution of particles is iteratively restructured according to Eqs. (24), (25) and (35).
Step 3: Memory the global best-fit particle of each generation, P_{gB}, as a mother particle of the clonal operator in Step 4.
Step 4: After n generations, clone the memorized n global best particles, $P_{gB}^{(M)}$, i = 1,..,n.
Step 5: Mutation Procedure: all of the cloned particles are mutated to some levels to distinguish with original or mother particle by using some arbitrary disturbances such as Gaussian noise. Assume P_{gBk} be the k-th entry of the vector P_{gB} and μ is a Gaussian arbitrary variable with zero mean and unity variance, then one can have the following arbitrary mutation procedure.

$$P_{gBk} + s * (1 - \mu) * V_{max} \tag{32}$$

Where s is the scale of mutation and V_{max} is the maximum velocity.

Step 6: Selection Procedure: We pile the current $P_{gB}^{(M)}$ in memory, but the other particles are selected according to an approach of the diversity keeping of the concentration mechanism so that in next generation of particles, a certain concentration of particles will be upheld for each fitness layer. Here the attentiveness of *i*-th particle is defined as follows.

$$D(x_i) = \left(\sum_{j=1}^{N+M} \left| f(x_i) - f(x_j) \right|\right)^{-1}, i = 1,2,..,N+M. \tag{33}$$

Where x_i and $f(x_i)$ in Eq.(33) denote the i-th particle and its fitness value, respectively. Rendering to above Eq. (33), one can derive a selection probability in terms of the concentration of particles as

$$p(x_i) = \frac{\frac{1}{D(x_i)}}{\sum_{j=1}^{N+M}\frac{1}{D(x_j)}}, i = 1,2,..,N+M, \quad (34)$$

Step 7: The algorithm can be completed by some common stop criteria such as a given maximum number of fitness value evaluations or a presetting accuracy of the solution.

ii) **Advance-and-Retreat Strategy**: In each iteration, we use the advance-and-retreat strategy to substitute the first part (previous velocity of a particle) of Eq. (25) in PSO just for the cloned particles. When the fitness value turns superior after last 'flying', the cloned particle progresses according to Eq. (25). When the fitness value turns shoddier after last 'flying', the cloned particle retreats then explorations in the reverse direction of the last "flying" with a smaller step-size of the preceding velocity, which can be expressed as

$$V_{id}(t+1) = \omega\left(-\alpha V_{id}(t)\right) + c_1 r_1(P_{iBd}(t) - X_{id}(t)) + c_2 r_2\left(P_{gBd}(t) - X_{id}(t)\right) \text{ where } \alpha < 1 \quad (35)$$

With the inertia weight declining with the evolution of the swarm, clones may be controlled in a diminishing local area for searching nearby local minima. Due to the impact of the global and the local best positions, clones alter their tracks arbitrarily. Strikingly, we just use the advance-and retreat strategy for the cloned particles. Thus, the clones do not sprinkle over the exploration space, but fly toward the nearby local region rapidly. Therefore, the advance and retreat strategy empowers each clone to forecast the next direction to the local optimum conferring to its own history information rather than just memorizing the last velocity without any conclusion of the last 'flying'. In this way, the individual convergent capability of clone is improved greatly by using the history information of each particle's last 'flying' to restrict particles searching in the space around nearby local optimum. The proposed PSOARC doesn't need to stop the sprouting of the swarm like [16] and [17] to execute local search. Furthermore, the PSOARC doesn't need to compute the gradient which is computationally expensive and change the structure of the traditional PSO like [18] and [19]. In particular, the clonal operator produces a new particle swarm near the favourable candidate solution according to the value of the fitness function such that the exploration space are enlarged significantly and the diversity of clones is augmented to avoid being trapped in local minima. Through keeping the clones, the proposed improved algorithm also expands the exploration space significantly to avoid trapping in local minima. Meanwhile, the core of the advance-and-retreat strategy is to speed up clones finding nearby minima in an enlarged indefinite space. Convergence rate and performance could be elevated significantly.

7. SIMULATION RESULTS

The accuracy of the proposed PSOARC Algorithm method is demonstrated on IEEE-30 bus system. The IEEE-30 bus system has 6 generator buses, 24 load buses and 41 transmission lines of which four branches are (6-9), (6-10) , (4-12) and (28-27) - are with the tap setting transformers. The lower voltage magnitude limits at all buses are 0.95 p.u. and the upper limits are 1.1 for all the PV buses and 1.05 p.u for all the PQ buses and the reference bus. The simulation results have been presented in Tables 1, 2, 3 &4. And in the Table 5 shows clearly that proposed algorithm powerfully reduce the real power losses when compared to other given algorithms. The optimal values of the control variables along with the minimum loss obtained are given in Table 1. Equivalent to this control variable setting, it was found that there are no limit violations in any of the state variables.

Table 1: Results of PSOARC – ORPD optimal control variables

Control variables	Variable setting
V1	1.040
V2	1.041
V5	1.040
V8	1.030
V11	1.010

Control variables	Variable setting
V13	1.040
T11	1.08
T12	1.02
T15	1.0
T36	1.0
Qc10	3
Qc12	4
Qc15	2
Qc17	0
Qc20	3
Qc23	2
Qc24	1
Qc29	3
Real power loss	4.3883
SVSM	0.2479

ORPD handled as multi-objective optimization problem where both power loss and maximum voltage stability margin of the system were optimized concurrently. Table 2 indicates the optimal values of these control variables. Also it is found that there are no limit violations of the state variables. It indicates the voltage stability index has increased from 0.2479 to 0.2488, an advance in the system voltage stability. To determine the voltage security of the system, contingency analysis was conducted using the control variable setting obtained in case 1 and case 2. The Eigen values equivalents to the four critical contingencies are given in Table 3. From this result it is observed that the Eigen value has been improved considerably for all contingencies in the second case.

Table 2: Results of PSOARC -Voltage Stability Control Reactive Power Dispatch Optimal Control Variables

Control Variables	Variable Setting
V1	1.043
V2	1.043
V5	1.042
V8	1.033
V11	1.009
V13	1.035
T11	0.090
T12	0.090
T15	0.090
T36	0.090
Qc10	4
Qc12	3
Qc15	4
Qc17	3
Qc20	0
Qc23	4
Qc24	4
Qc29	3
Real power loss	4.9721
SVSM	0.2488

Table 3: Voltage Stability under Contingency State

Sl.No	Contingency	ORPD Setting	VSCRPD Setting
1	28-27	0.1410	0.1420
2	4-12	0.1658	0.1662
3	1-3	0.1774	0.1781
4	2-4	0.2032	0.2042

Table 4: Limit Violation Checking of State Variables

State variables	limits		ORPD	VSCRPD
	Lower	upper		
Q1	-20	152	1.3422	-1.3269
Q2	-20	61	8.9900	9.8232
Q5	-15	49.92	25.920	26.001
Q8	-10	63.52	38.8200	40.802
Q11	-15	42	2.9300	5.002
Q13	-15	48	8.1025	6.033
V3	0.95	1.05	1.0372	1.0392
V4	0.95	1.05	1.0307	1.0328
V6	0.95	1.05	1.0282	1.0298
V7	0.95	1.05	1.0101	1.0152
V9	0.95	1.05	1.0462	1.0412
V10	0.95	1.05	1.0482	1.0498
V12	0.95	1.05	1.0400	1.0466
V14	0.95	1.05	1.0474	1.0443
V15	0.95	1.05	1.0457	1.0413
V16	0.95	1.05	1.0426	1.0405
V17	0.95	1.05	1.0382	1.0396
V18	0.95	1.05	1.0392	1.0400
V19	0.95	1.05	1.0381	1.0394
V20	0.95	1.05	1.0112	1.0194
V21	0.95	1.05	1.0435	1.0243
V22	0.95	1.05	1.0448	1.0396
V23	0.95	1.05	1.0472	1.0372
V24	0.95	1.05	1.0484	1.0372
V25	0.95	1.05	1.0142	1.0192
V26	0.95	1.05	1.0494	1.0422
V27	0.95	1.05	1.0472	1.0452
V28	0.95	1.05	1.0243	1.0283
V29	0.95	1.05	1.0439	1.0419
V30	0.95	1.05	1.0418	1.0397

Table 5: Comparison of Real Power Loss

Method	Minimum loss
Evolutionary program-ming[20]	5.0159
Genetic algorithm[21]	4.665
Real coded GA with Lindex as SVSM[22]	4.568
Real coded genetic al-gorithm[23]	4.5015
Proposed PSOARC method	4.3883

8. CONCLUSION

In this paper a novel approach PSOARC algorithm used to solve optimal reactive power dispatch problem. The performance of the proposed algorithm has been tested in standard IEEE 30 bus test system.Simualtion results reveal about the better performance of the proposed algorithm in reducing the real power loss. Subsequently voltage profiles has been enhanced .

REFERENCES

1. O.Alsac,and B. Scott, "Optimal load flow with steady state security",IEEE Transaction. PAS -1973, pp. 745-751.
2. Lee K Y ,Paru Y M , Oritz J L –A united approach to optimal real and reactive power dispatch , IEEE Transactions on power Apparatus and systems 1985: PAS-104 : 1147-1153
3. A.Monticelli , M .V.F Pereira ,and S. Granville , "Security constrained optimal power flow with post contingency corrective rescheduling" , IEEE Transactions on Power Systems :PWRS-2, No. 1, pp.175-182.,1987.
4. Deeb N ,Shahidehpur S.M ,Linear reactive power optimization in a large power network using the decomposition approach. IEEE Transactions on power system 1990: 5(2) : 428-435
5. E. Hobson ,'Network consrained reactive power control using linear programming, ' IEEE Transactions on power systems PAS -99 (4) ,pp 868-877, 1980
6. K.Y Lee ,Y.M Park , and J.L Oritz, "Fuel –cost optimization for both real and reactive power dispatches" , IEE Proc; 131C,(3), pp.85-93.
7. M.K. Mangoli, and K.Y. Lee, "Optimal real and reactive power control using linear programming" , Electr.Power Syst.Res, Vol.26, pp.1-10,1993.
8. S.R.Paranjothi ,and K.Anburaja, "Optimal power flow using refined genetic algorithm", Electr.Power Compon.Syst , Vol. 30, 1055-1063,2002.
9. D. Devaraj, and B. Yeganarayana, "Genetic algorithm based optimal power flow for security enhancement", IEE proc-Generation.Transmission and. Distribution; 152, 6 November 2005.
10. C.A. Canizares , A.C.Z.de Souza and V.H. Quintana , " Comparison of performance indices for detection of proximity to voltage collapse ,'' vol. 11. no.3 , pp.1441-1450, Aug 1996 .
11. J. Kennedy and R. Eberhart, "Particle Swarm Optimization," Proc. Proceedings of the IEEE International Conference on Neural Networks, Perth, Australia, IEEE Service Center, Vol. 4. Piscataway, NJ, 1995, pp. 1942C1948.
12. R.C.Eberhart and J.Kennedy, "A new optimizer using particle swarm theory," Proc. Proceedings of the 6th Int. Symp. Mcro Machine Human Science, Nagoya, Japan, 1995, pp. 39 - 43.
13. R.C.Eberhart and Y.Shi, "Particle Swarm Optimization: developments, applications and resourses," Proc. Proceedings of the IIEEE Congress on Evolutionary Computation, Seoul, South Korea, Vol. 1, 2001, pp. 81- 86.
14. H. W. Ge, Y. C. Liang, Y. Zhou, X. C. Guo, "A Particle Swarm Optimization-based Algorithm for Job-shop Scheduling Problem," International Journal of Computational Methods, vol. 2, no. 3, 2005, pp.419-430.
15. Y.Tan and Z.M.Xiao, "Clonal particle swarm optimization and its applications," Proc. Proceedings of the IEEE Congress on Evolutionary Computation, Singapore, 2007, pp. 2303 - 2309.
16. Yu Liu,Zheng Qin and Zhewen Shi, "Hybrid particle swarm optimizer with line search," Proc. Proceedings of the IEEE International Conference on Systems, Man and Cybernetics, 2004, pp. 3751-3755.
17. Junying Chen, Zheng Qin, Yu Liu and Jiang Lu, "Particle swarm optimization with local search," Proc. Proceedings of the IEEE International Conference on Neural Networks and Brains, 2005, pp. 481-484.
18. Mathew Mithra Noel and Thomas C.Jannett, "Simulation of a new hybrid particle swarm optimization algorithm," Proc. Proceedings of the thirty-sixth Southeastern Symposium, 2004, pp. 150-153.
19. A.Ismael F.Vaz and Edite M.G.P.Fernandes, "Particle swarm algorithms for multi-local optimization," Proc. Congresso de Estatistica e Investigacao Operacional da Galiza e Norte de Portugal, VII Congreso Galego de Estatistica e Investigacion de Operacions, 2005.
20. Wu Q H, Ma J T. Power system optimal reactive power dispatch using evolutionary programming. IEEE Transactions on power systems 1995; 10(3): 1243-1248 .
21. S.Durairaj, D.Devaraj, P.S.Kannan ,' Genetic algorithm applications to optimal reactive power dispatch with voltage stability enhancement' , IE(I) Journal-EL Vol 87,September 2006.

22. D.Devaraj ,' Improved genetic algorithm for multi – objective reactive power dispatch problem' European Transactions on electrical power 2007 ; 17: 569-581.

23. P. Aruna Jeyanthy and Dr. D. Devaraj "Optimal Reactive Power Dispatch for Voltage Stability Enhancement Using Real Coded Genetic Algorithm" International Journal of Computer and Electrical Engineering, Vol. 2, No. 4, August, 2010 1793-8163.

DYNAMIC RESPONSE OF CLOSED LOOP CONTROLLED CHOPPER FED SEPARATELY EXCITED DC MOTOR DRIVE

Noorul Islam*
Assistant Professor
Dept. of Electrical and Electronics Engg.
ITS Engineering College, Greater Noida-201306 (UP), India
Email: noorulislam@its.edu.in
*Corresponding Author

Priti
Dept. of Electrical and Electronics Engg.
CET-IILM-AHL, Greater Noida-201306 (UP), India
Email: pritigupta100@gmail.com

Mahima Mayer
Dept. of Electrical and Electronics Engg.
ABES Engg. College, Ghaziabad – 201009 (UP), India
Email: mahimamayer@gmail

ABSTRACT

The chopper controlled separately excited dc motor has poor speed regulation at light loads with open loop operation and, therefore is not suitable for precise work. The speed of the motor can be regulated by using closed loop control having speed feedback. But this alone feedback does not control the armature current and may become excessively high particularly at the starting or braking. To control the armature current within the limits and to have fast dynamic response of the current, the speed feedback loop is usually associated with inner current feedback loop.

Keywords: *Dynamic response, Perturbation, Settling time, Speed control, Inner current loop.*

1. INTRODUCTION

If the motor supplies a separately excited dc generator load coupled to it, the load torque varies linearly with the speed instead of being constant. It affects the gain and time constant of the system and its transfer function depends on the operating point. Therefore the relevant information related to the operating point is needed to design values of parameters of current and speed controllers. It is found that if the controllers are designed for the operating point at higher load, the system may have oscillatory dynamic response at light loads or even may become unstable. However, if the design is carried out for the operating point corresponding to light load, the stability of the system is ensured at light loads but the dynamic response at high loads may be overdamped [2]. Therefore the operating point is chosen in such a way that it should not only ensure stability but also satisfactory dynamic response in the operating range.

2. OPERATION OF CHOPPER FED SEPERATELY EXCITED DC DRIVE

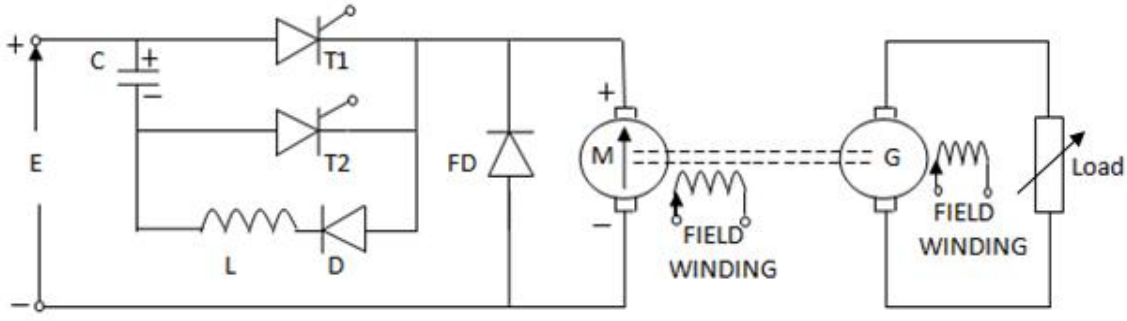

(a) Chopper Fed Separately excited dc motor

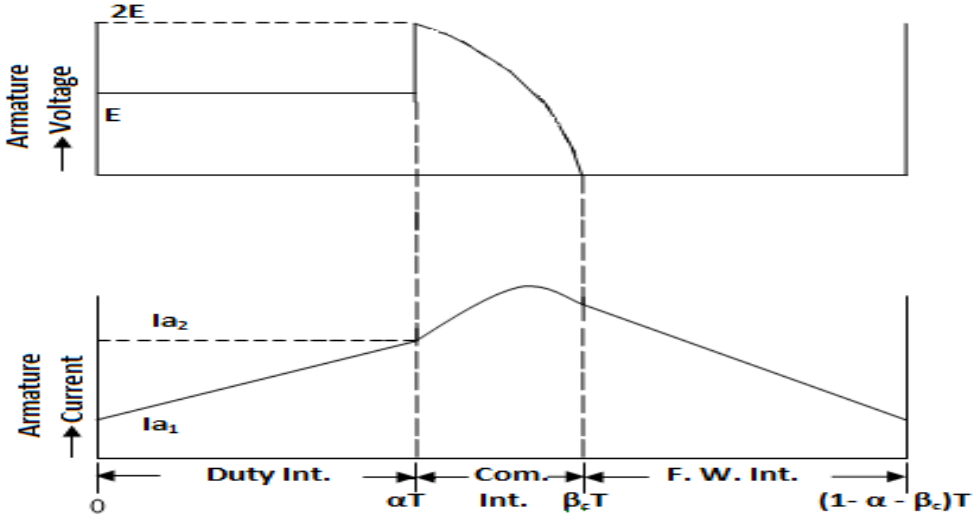

(b) Armature voltage and current waveforms

Fig.1: Separately excited D.C. Motor fed by parallel commutated Chopper

The circuit diagram of a parallel voltage commutated chopper fed separately excited dc motor coupled to a separately excited dc generator is shown in fig.1 (a). The load on the motor is varied by varying load resistance connected across the generator terminals [1, 16]. It is assumed that the speed of the motor remains constant in the chopper cycle at steady state.

Since the parallel voltage commutated chopper is used for high rating motors as in effective traction, the armature current does not fall to zero even at low value of duty ratio. Therefore, the current remains continuous in the whole cycle. There will be three distinct modes of operation, namely duty interval, commutation interval and freewheeling interval. The waveforms of the motor terminal voltage and armature current are shown in fig.1 (b).

2.1 Duty Interval [0 ≤ t ≤ αT]: Prior to start of this interval, the capacitor C is charged to voltage E by turning on thyristor T2 which is automatically turned off as the charging current flowing through it falls to zero. The duty (on) interval starts by turning on thyristor T1 and the supply connected to the motor and the armature current increases. In the mean time the capacitor C is reversed charged to voltage E through diode D and inductor L. The capacitor C is now ready to turn OFF the main thyristor T1 when thyristor T2 is turned ON. The minimum duty interval is decided by the time taken by the capacitor C to reverse its voltage polarity[6].

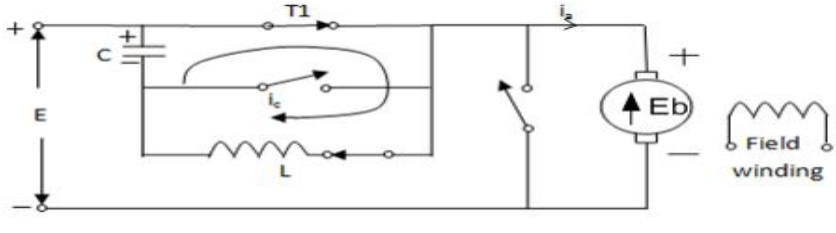

Fig.1(c): Duty Interval [0 ≤ t ≤ αT]

The equivalent circuit is shown in fig.1(c). This consists of two loops. First loop consist of E-T1-motor-E, the motor terminal voltage is equal to the supply voltage E and the armature current increases from its lowest value I_{a1}. The performance equations for this loop are written as given below,

$$E = La\frac{dI_a}{dt} + i_a R_a + K\omega \quad (1)$$

$$K\, i_a = J\frac{d\omega}{dt} + B'\omega \quad (2)$$

In the second loop, that comprising of T1- L – C - T1, the current i_c flows and charges the commutating capacitor in reverse direction. The performance equations for this loop are as follows.

$$\frac{dI_c}{dt} = \frac{V_c}{L} \quad (3)$$

$$\frac{dV_c}{dt} = -\frac{i_c}{C} \quad (4)$$

where, $B' = B + \frac{\mathrm{Kg}^2}{R}$ [see appendix 2] (5)

It is noted that as soon as capacitor C charged to E in reverse direction, the diode D stops conducting and henceforth i_c remains at zero. Duty interval ends when t is to αT.

2.2 Commutation Interval [αT ≤ t ≤ (α + β_c)T]:

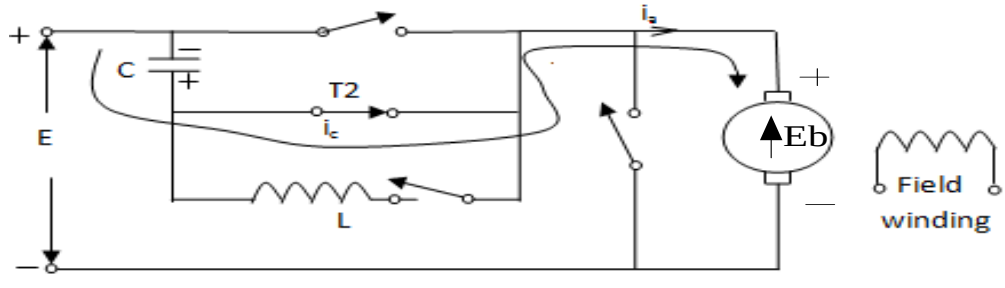

Fig.1 (d): Duty Interval [αT ≤ t ≤ (α + β_c)T]

This interval starts when auxiliary SCR T2 is fired at t = αT. The main SCR T1 stops conducting due to application of reverse voltage across it. The commutating capacitor starts charging through supply voltage E. The equivalent circuit is shown in fig.1 (d). The differential equations describing this mode of operation are as follows,

$$E + Vc = L\frac{di_a}{dt} + i_a.R_a + K\omega \quad (6)$$

$$K\, i_a = J\frac{d\omega}{dt} + B'\omega \quad (7)$$

2.3 Freewheeling Interval [(α + β_c)T ≤ t ≤ T]:

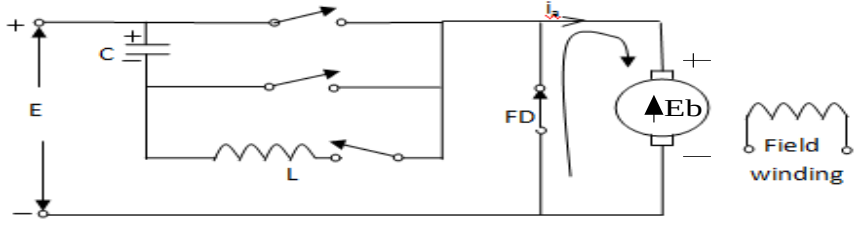

Fig.1(e): Duty Interval [(α + β_c)T ≤ t ≤ T]

This interval starts as soon as capacitor C is charged to E in forward direction, the auxiliary SCR T2 turns off, and the freewheeling diode FD gets forward biased. The armature current freewheels through the FD and the energy stored in the armature inductance makes the armature current continuous. The terminal voltage across the motor is practically zero. This mode continues till the end of the chopper cycle when SCR1 is turned on to initiate the next cycle of operation. Equivalent circuit describing this mode is shown in fig.1 (e). The differential equations given by this mode of operation are as follows,

$$0 = L\frac{di_a}{dt} + i_a.R_a + K\omega \tag{8}$$

$$K\, i_a = J\frac{d\omega}{dt} + B'\omega \tag{9}$$

3. STEADY STATE OPERATING POINT

Since parallel capacitor commutated chopper circuit is generally used for high capacity motors particularly in electric traction, the commutation time is very small due to high value of armature current and is negligible in comparison to duty interval except at its very low values [2, 14]. Neglecting commutation interval integrating equations (1), (6) and (8) and equations (2), (7) and (9) separately over one cycle and taking average the dynamic equations for the terminal voltage and the motor torque in terms of average quantities are obtained as given below.

$$\alpha E = L_a\frac{dI_{av}}{dt} + I_{av}.R_a + K\omega_{av} \tag{10}$$

$$T_{av} = KI_{av} = J\frac{d\omega_{av}}{dt} + B'\omega_{av} \tag{11}$$

At steady state, $\frac{dI_{av}}{dt} = 0,$ and $\frac{d\omega_{av}}{dt} = 0,$

Corresponding to steady state operating point, let the values of ω_{av}, I_{av} and B' be ω_{av0}, I_{av0} and B'_0 respectively. Hence,

$$\alpha\, E = I_{av0}\, R_a + K\omega_{av0} \tag{12}$$

$$T_{av0} = K\, I_{av0} = B'\omega_{av0} \tag{13}$$

Solving for I_{av0} and eliminating ω_{av0} = 0, we get,

$$I_{av0} = \left(\frac{B'_0}{B_0 R_a + \mathrm{K}^2}\right)\alpha\, E \tag{14}$$

$$\omega_{av0} = \frac{K}{B'_0} I_{av0} \tag{15}$$

4. LINEARIZED DYNAMIC MODELLING OF MOTOR

Considering small perturbation Δα and ΔB' in the input parameters α and B' respectively around the steady state operating point, the current I_{av} and speed ω_{av} changes by ΔI_{av} and $\Delta\,\omega_{av}$ respectively[4, 15].

The new values will be ($I_{av0} + \Delta\, I_{av}$), ($\omega_{av0} + \Delta\,\omega_{av}$), (α +Δα) and ($B'_0 + \Delta B'$). Substituting in equation (10) and (11), we get,

$$T_{av0} + \Delta T_{av} = K(I_{av0} + \Delta I_{av}) \tag{16}$$

$$(\alpha_0 + \Delta\alpha)E = L_a \frac{d(I_{av0} + \Delta I_{av})}{dt} + (I_{av0} + \Delta I_{av})R_a + K(\omega_{av0} + \Delta\omega_{av}) \quad (17)$$

$$K(I_{av0} + \Delta I_{av}) = J \frac{d(\omega_{av0} + \Delta\omega_{av})}{dt} + (B_0' + B')(\omega_{av0} + \Delta\omega_{av}) \quad (18)$$

Simplifying above equation, we get

$$\Delta\alpha E = L_a \frac{d\Delta I_{av}}{dt} + \Delta I_{av} R_a + K\Delta\omega_{av} \quad (19)$$

$$K\Delta I_{av} = J \frac{d\Delta\omega_{av}}{dt} + \Delta B'\omega_{av0} + B_0'\Delta\omega_{av}) \quad (20)$$

$$\Delta T_{av} = K\Delta I_{av} \quad (21)$$

Taking Laplace Transform of equations (19) and (20), we get

$$\Delta\alpha(s)\ E = (L_a S + R_a)\Delta Iav(s) + K\Delta\omega_{av}(s) \quad (22)$$

$$K\Delta I_{av}(s) = (J S + B_0')\Delta\omega_{av}(s) + \omega_{av0}\Delta B'(s) \quad (23)$$

$$\Delta T_{av}(s) = K\Delta\omega_{av}(s) \quad (24)$$

Simplifying equations (22) and (23)

$$\Delta I_{av}(s) = \frac{E\Delta\alpha(s) - K\Delta\omega_{av}(s)}{R_a(\tau_a S + 1)} \quad (25)$$

$$\Delta\omega_{av}(S) = \frac{K\Delta I_{av}(s) - \omega_{av0}\Delta B'(s)}{B_0'(\tau_m' S + 1)} \quad (26)$$

where, τ_a = Armature circuit time constant of motor,, $\frac{L_a}{R_a}$ and τ_m' = Mechanical time constant of motor with load $\frac{J}{B'}$ Since, $B' = \frac{K^2\omega_{av}}{R}$

Considering small perturbation in R_0 around the operating point by ΔR, we get

$$(B'_0 + \Delta B') = \left(\frac{K^2}{R_0 + \Delta R}\right)(\omega_{av0} + \Delta\omega_{av}) \quad (27)$$

$$(B'_0 + \Delta B') = \frac{K^2}{R_0}\left(1 + \frac{\Delta R}{R_0}\right)^{-1}(\omega_{av0} + \Delta\omega_{av})$$

or,

$$(B'_0 + \Delta B') = \frac{K^2}{R_0}\left(1 - \frac{\Delta R}{R_0}\right)(\omega_{av0} + \Delta\omega_{av})$$

or, Higher terms of $\frac{\Delta R}{R_0}$ neglected being very small

Simplifying above equations, we get

$$\Delta B' = -\frac{K^2}{R_0^2}\Delta R \quad [\left(\frac{\Delta R}{R_0}\right)\Delta\omega_{av} \text{ term neglected being very small}] \quad (28)$$

Taking Laplace Transform of equation (28), we get

$$\Delta B'(s) = -\frac{K^2}{R_0^2}\Delta R(s) \tag{29}$$

Substituting value of ΔB'(s) in equation (26), we get

$$\Delta \omega_{av}(s) = \frac{K\,\Delta I_{av}(s) - \frac{K^2}{R_0^2}\omega_{av0}(-\Delta R(s))}{B'_0(\tau'_m S + 1)} \tag{30}$$

The block diagram representation of the motor drive system is obtained as follows:

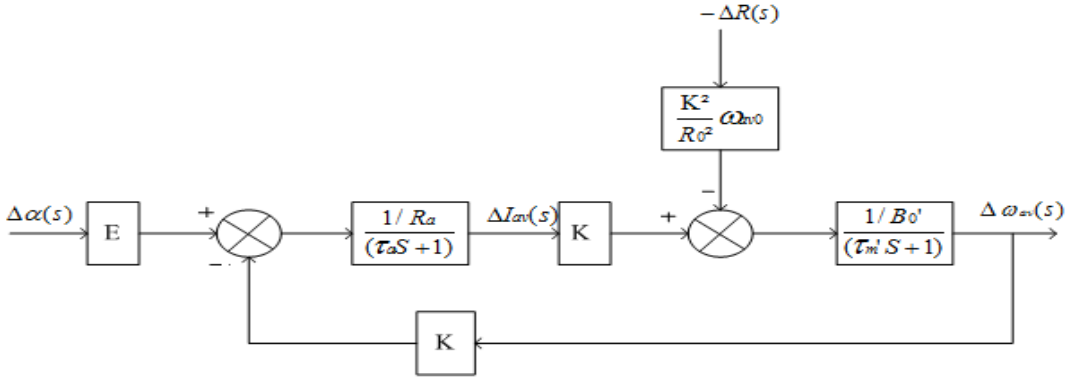

Fig. 2: Block diagram representation of motor drive system

Case 1: Small perturbation in α only, ΔR = 0.

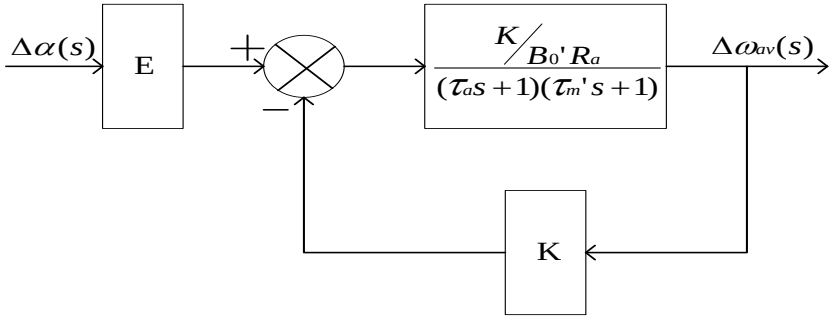

Fig. 3: Block diagram at small perturbation in α only, ΔR = 0.

$$\text{Forward Transfer Function} = \frac{K/B_0'R_a}{(\tau_a s+1)(\tau_m' s+1)}$$

Feedback Transfer Function = K

$$\frac{\Delta\omega_{av}(s)}{E\,\Delta\alpha(S)} = \frac{\frac{K/B_0'R_a}{(\tau_a s+1)(\tau_m' s+1)}}{1+\frac{K^2/B_0'R_a}{(\tau_a s+1)(\tau_m' s+1)}}$$

Therefore,

$$\frac{\Delta\omega_{av}(s)}{\Delta\alpha(s)} = \frac{E.K/B_0'R_a}{\tau_a\tau_m' s^2 + (\tau_a+\tau_m')s + 1 + \frac{K^2}{B_0'R_a}} \tag{31}$$

Case 2: Small perturbation in R only, Δ α = 0.

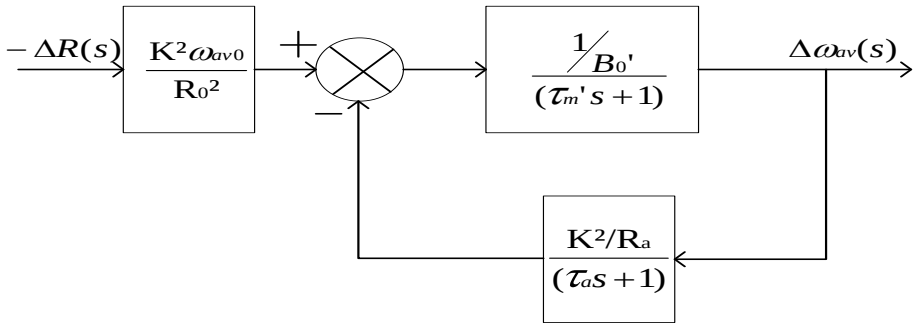

Fig.4: Block diagram at small perturbation in R only, $\Delta\alpha = 0$.

Forward Transfer Function $\frac{1/B_0'}{(\tau_m' s+1)}$ =, Feedback Transfer Function = $\frac{K^2/R_a}{(\tau_a s+1)}$

Therefore,
$$\frac{\Delta\omega_{av}(s)}{\frac{K^2\omega_{av0}}{R_0^2}(-\Delta R(s))} = \frac{\frac{1/B_0'}{(\tau_m' s+1)}}{1+\frac{K^2/B_0' R_a}{(\tau_a s+1)(\tau_m' s+1)}}$$

$$\frac{\Delta\omega_{av}(s)}{-\Delta R(s)} = \frac{\frac{K^2\omega_{av0}}{B_0' R_0^2}(\tau_a s+1)}{\tau_a\tau_m' s^2+(\tau_a+\tau_m')s+1+\frac{K^2}{B_0' R_a}} \quad (32)$$

5. MODELLING OF CLOSED LOOP CONTROLLED CHOPPER FED SEPARATELY EXCITED DC MOTOR DRIVE SYSTEM

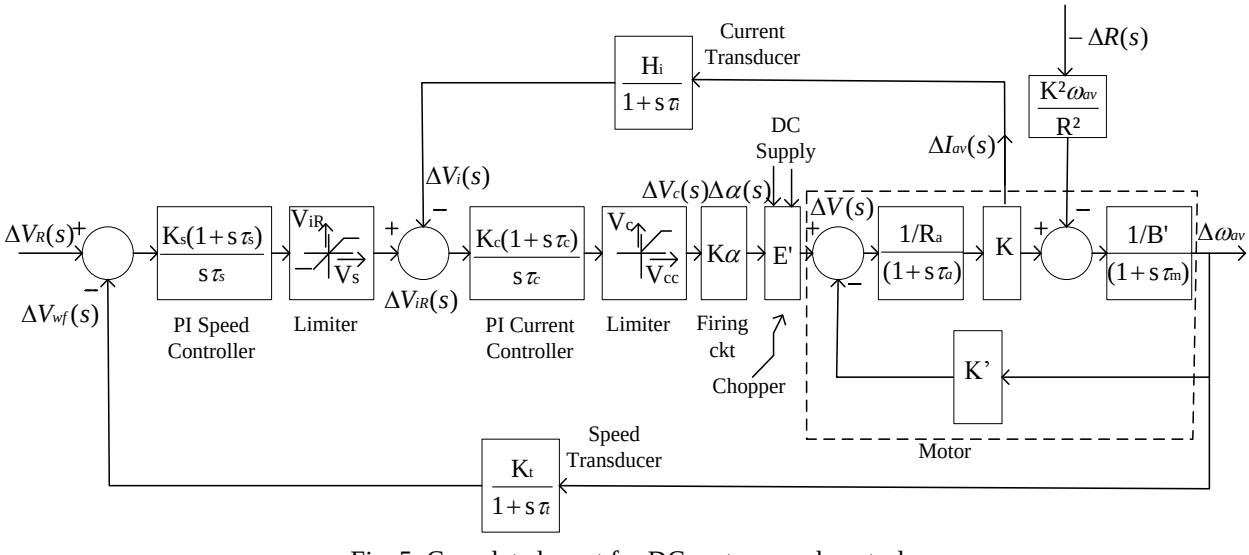

Fig. 5: Complete layout for DC motor speed control

The block diagram of the complete speed control scheme of chopper fed separately excited dc motor as proposed by K.B. Naik et. al[8-12] employing speed feedback loop with inner current loop is shown in fig.(5). It consists of separately excited dc motor fed by parallel commutated Chopper. A separately excited dc generator is coupled to the motor for loading purpose. A light inertia a.c. tachogenerator was used for sensing of speed, whose output was rectified, filtered

and scaled out to compare with the speed reference signal. The current feedback was obtained by connecting a 0.1 ohm rheostat in the armature circuit whose output was filtered and amplified to make comparable with current error to eliminate zero steady state error. Limiters were used at the output of controllers to limit their output within the desired working range. In outer loop V_R sets the speed reference. Speed feedback signal is compared with the speed reference signal and the error signal is fed to the PI speed controller.

The output of speed controller forms the reference signal of current control circuit. The current feedback signal is compared with the current reference signal and the error is amplified through PI current controller [5, 7]. The output of the controller becomes the control signal for varying duty interval of the chopper, thereby, varying the voltage applied to the motor armature. When there is a drop in speed, the speed difference which passes through the speed controller produces a higher reference voltage of current loop, thereby, higher duty interval and the higher motor terminal voltage resulting increase in speed and the error is corrected[3]. The current reference voltage can be adjusted to higher values to produce higher torque resulting fast dynamic response as long as it does not exceed the value preset by the current limiter.

6. DYNAMIC PERFORMANCE

The dynamic performance of the closed loop controlled motor is given below for small perturbation in speed reference voltage and generator load resistance at high load and light load.

(a) Small perturbation in speed reference at light load

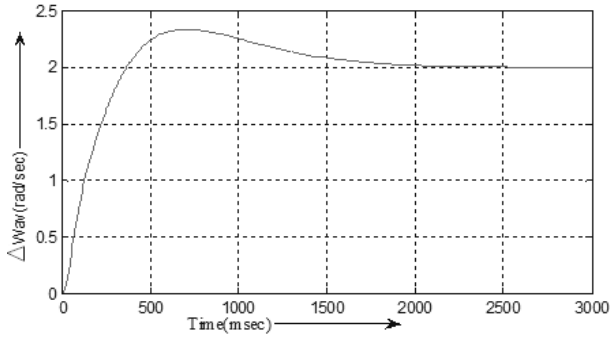

Fig.7 (a-a): Transient response of speed for small perturbation at light load,
V_R = 4.0 V, R = 40 Ω, ΔV_R = 0.2 V, ΔR = 0 V

(b) Small perturbation in load resistance at light load

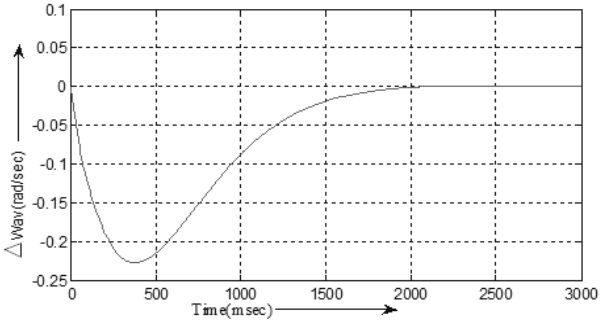

Fig.7 (a-b): Transient response of speed for small perturbation at light load,
V_R = 4.0 V, R = 40 Ω, ΔR= -1.8 Ω, ΔV_R = 0 V

(c) Small perturbation in speed reference at high load

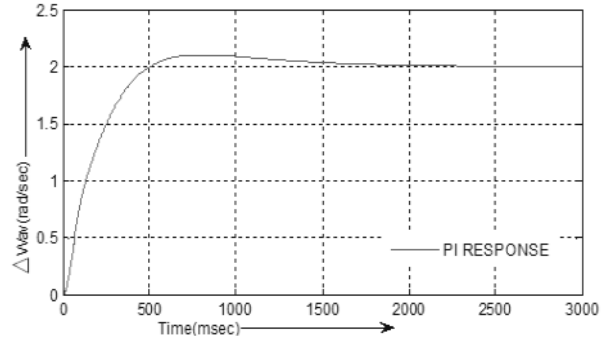

Fig.7 (b-a): Transient response of speed for small perturbation in V_R at high load,
V_R = 4.0 V, R = 19 Ω, ΔV_R = 0.2V, ΔR = 0 V

(d) Small perturbation in load resistance at high load

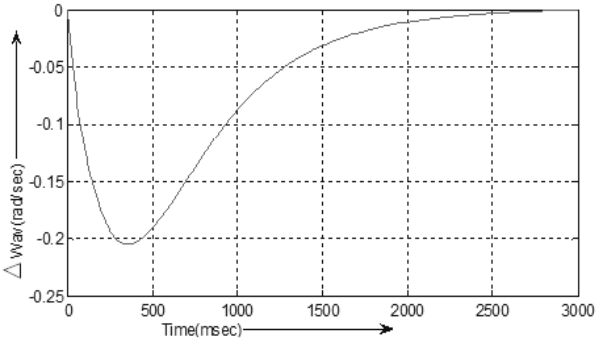

Fig.7 (b-b): Transient response of speed for small perturbation in V_R at high load,
V_R = 4.0 V, R = 19 Ω, ΔR = -0.41 Ω, ΔV_R = 0 V

7. CONCLUSION

The dynamic performance of the speed is simulated by using small perturbations in the speed and generator armature circuit resistance separately. The responses for light and heavy loads are shown in figure (7 a-a, 7 a-b) and figure (7 b-a, 7 b-b). The simulated result almost same as given by Naik et al[10] and [13]. The results show almost same values of the settling time and peak overshoot. It is also observed that the response becomes faster and peak overshoot reduces with increase in load.

REFERENCES

1. Bose B. K., "**Modern Power Electronics and A.C. Drives**", *Prentice-Hall of India Learning Private Limited*, 2002.

2. Anjaneyulu P. B., Prabhu S. S., and Dubey G. K., "**Stability analysis, design and simulation of a closed loop converter dc drive**", *IEEE Transaction on industrial electronics applications*, Vol. IE-31, No. 2, May, 1984.

3. Bonert Richard R. , "**Automatic speed control of One – Quadrant dc drives**", *IEEE Transaction on industrial applications*, Vol. IA-18, No. 4, September/October, 1982.

4. Franklin P. W. , "**Theory of the dc motor controlled by power pulses part- 1 motor operation,***" IEEE conference fifth annual meeting of industry and general application group*, pp. 59-67, 1970.

5. Hong Il Suh, Hwang Seung Ho and Bien Zeungnam , "**A design and experiment of speed controller with PI – plus bang bang action for a dc servomotor with transistorized PWM drives**", *IEEE Transaction on industrial electronics applications*, Vol. IE-31, No. 4, November, 1994.

6. Irie H., Fujii T. and Ishizaki T. , "**Thyristor chopper for separately excited dc motor control**", *Electrical Engineering in Japan*, in Vol. 88, No. 4, 1968.

7. Krishnan T. and Ramaswami B. , " **Speed control of dc motor using thyristor dual converter**", *IEEE Transaction on industrial electronics and instrumentation*, Vol. IECI - 23, No. 4, November, 1976.

8. Naik K. B., Jain V. K. and Dubey G. K., "**Dynamic model of Chopper fed dc Separately excited motor**", *Jr. of Electric Machines and Electromechanics*, 1982.

9. Naik K. B. , "**Dynamic modelling of dc separately excited motor fed by load dependent chopper**", *Jr. Institution of Engineers (India)*, Vol. 66, pt. EL-5, April, 1986.

10. Naik K. B., Dubey G.K. and Jain V.K. , "**Steady state and dynamic analysis and performance of current limit controlled chopper fed separately excited dc motor**", *Jr. Institution of Engineers (India)*, April, 1988.

11. Naik K. B., Dubey G.K. and Jain V.K. , "**Design, Modelling, Simulation and Stability analysis of a closed loop chopper fed separately excited dc motor**", *Jr. Institution of Engineers (India)*, 1992.

12. Naik K. B. and Panesar M. S., "**Analysis and Performance of a chopper fed dc separately excited motor under regenerative braking operation**", *Electric machines and power systems*, 1992.

13. Nitta K., Okitsu H. and Kinouchi Y. , "**Dynamic response of separately excited dc motor driven by a thyristor pulsating power supply**" *Electrical engineering in Japan*, Vol. 90, No. 4, 1970.

14. Parimelalagan R. and Rajagopalan V. , "**Steady state investigations a chopper fed dc with separate excitation**", *IEEE transaction on industry and general application group*, Vol. IGA-7, No. 1, January/February, 1970.

15. Praksha and Verma V. K. , "**Micro-computer based dc drive in sliding mode**", *Jr. Institution of Engineers (India)*, EL Vol. 72, February, 1992.

16. Satpathi H., Dubey G. K. and Singh L. P., "**General method of analysis of chopper fed dc separately excited motor**", *IEEE Transaction on power apparatus and systems*, vol. PAS-102, No. 4 , pp. 990-997, 1083.

APPENDICES

1. SPECIFICATIONS OF MOTOR – GENERATOR SET AND CHOPPER

Both the machines are identical and rated for 220 V, 2 hp, 8.5 A and 1000 rpm. The machine parameters as found from the tests are: $R_a = R_g = 4\ \Omega$; La = 97 mH;

$K_o = 2.1$ V/rad/s; $J = 0.122$ Kg-$m^{2;}$

B = 0.018 N-m/rad/s; L = 1 mH;

C= 10 μF

2. LOAD TORQUE OF SEPARATELY EXCITED DC GENERATOR FEEDING CONSTANT RESISTANCE LOAD

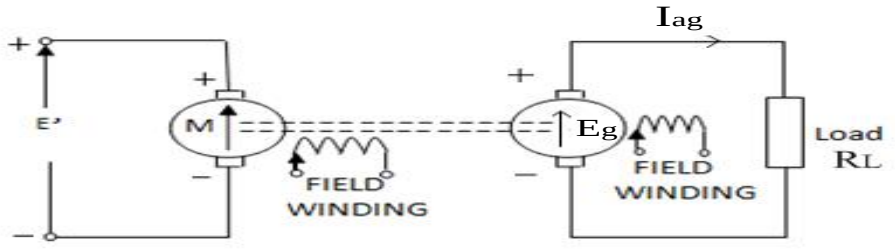

Fig.8: Modeling of separately excited dc generator load

In fig.8, a variable resistive load connected across the generator terminal to vary the loading on the motor. The current in the load resistance is given by,

$$I_{ag} = \frac{Eg}{R} \tag{33}$$

where, $R = R_a + R_L$, E_g = Induced emf of generator

But for constant excitation, the E_g is,

$$E_g = K\ \omega_{av} \tag{34}$$

Hence, $K\ \omega_{av} = R\ I_{ag}$

$$T_L = K_g\ I_{ag}$$

where, T_L = Load torque exerted by the generator on motor.

$$T_L = \frac{K\ K_g \omega_{av}}{R} \tag{35}$$

If K = Kg, Then $T_L = \frac{K^2 \omega_{av}}{R}$ (36)

or, $T_L \alpha\ \omega_{av}$

The Viscous Friction torque on motor $T_V = B\ \omega_{av}$, and $T_L = \frac{K^2 \omega_{av}}{R}$
Hence, combined viscous and load torque, i.e.

$$T_V + T_L = B\ \omega_{av} + \frac{Kg^2\ \omega_{av}}{R}$$

$$T_V + T_L = \left(B + \frac{Kg^2}{R}\right)\omega_{av}$$

or, $T_V + T_L = B'\ \omega_{av}$ (37)

$$B' = B + \frac{Kg^2}{R}$$

CO-WORKING OF BATTERY AND ULTRACAPACITORS FOR ELECTRIC VEHICLES: A COMPREHENSIVE OVERVIEW OF RECENT ADVANCEMENTS

Akshay A. Kakde
Phd Scholar
Electrical Engineering Department
G.H.Raisoni College of Engineering
Nagpur-16, Maharashtra
Tel: 07387931819
Email: Kakdeaakshay@gmail.com

Shrikrishna G. Tarnekar*
Professor
Department of Electrical Engineering
G.H.Raisoni College of Engineering
Nagpur-16, Maharashtra
Tel: 09021583008
Email: sgtarnekar@gmail.com
*Corresponding author

ABSTRACT

This paper gives a brief overview of various techniques dealing with applications of ultracapacitors for electric vehicles. It deals with some of the relevant papers and makes critical observations.

These papers include advantages of ultracapacitors, DC-DC converter, boost converter, and series/parallel recombination of ultracapacitor bank. It also includes various schemes for improving performance of the systems.

After reviewing these papers, some points lead to innovation thinking so as to plan for further improvement in system performance. This idea can be verified by software and also realised by hardware/fabrication, in our research work undertaken.

Keywords *– Ultracapacitor, DC-DC converter, Battery, series/ parallel combination.*

1. INTRODUCTION

The applications of ultracapacitors have exponentially increased from last decade. The advancements in ultracapacitor (UC) technology gives more and more importance to economically acceptable applications of ultracapacitors. An application of UC to support the battery in electric vehicle is one of the applications where lot of work is going on. Continuous R & D in UC technology further reduces the cost and size, popularizing the ultracapacitor further. Various other technologies and methods are introduced which help in energy management of UC and increases the efficiency of system.

Main focus of this submission is to identify various techniques which have been introduced in recent years for enhancing the energy efficiency of the vehicles. DC-DC converter plays an important role in this application. It acts as a common bus between UC and other source like battery. DC-DC converter acts as a boost converter during heavy load condition and provides to load. Similarly, it acts as a buck converter during regenerative condition and provide energy to UC. Implementation of various techniques for improvement in performance of DC-DC converter has been reviewed and critically compared here.

Some other techniques are dealt with here like current dependent technique, fuzzy logic controller, neural network, voltage dependent technique, predictive power optimization (PPO) algorithm, various flow charts for energy management of UC, etc.

2. LITERATURE SURVEY

Energy management between ultra capacitor and battery and energy required during ride-through period have been dealt with by Chabchoub M.H. et al[1]. Ultracapacitors are charged during regenerative braking and during normal load conditions. DC-DC converter with bidirectional dual active bridge has been utilized for energy management for Permanent Magnet Synchronous Motor (PMSM). The proposed design has been used in a DC/DC bidirectional Dual Active Bridge (DAB) with a High Frequency Transformer (HFT). The HFT is utilized to supply energy of ultracapacitors to the DC Bus. The number of ultracapacitor (UC) cells in series will be limited by keeping a high value of equivalent capacity and low Equivalent Series Resistance (ESR). In addition, it facilitates the balancing of the voltages across different cells. The ultracapacitor temporarily stores energy recovered during braking or deceleration for delivering it later to mitigate peaks of power demand during acceleration and during starting. Thus, it relieves the strain on the battery, extends its life and allows the improvement in overall performance of the electric vehicle.

These authors also suggest improvements that can bring an ultracapacitor bank for power-consolidation of batteries in electric vehicles. On the basis of simulation results, they show that the combination of electrochemical energy from the battery and UC bank makes the source more reliable, improves its efficiency, and increases its life. It is also able to provide peak power demanded by the main motor for high acceleration during starting. Control strategy for whole system which is helpful to develop new scheme as per requirement, is a special outcome of their work.

As an innovation contribution, P.R. Sawarkar et al. propose series / parallel re-configuration within Ultracapacitor bank for improvement in energy transfer [2]. Proposed scheme is simulated using MATLAB Simulink and is confirmed by experimental verification which indicates that time required to extract energy is 37% to 57 % less. Further, up to 93 % energy can be delivered for complete operation in typical cases of discharging. By using series / parallel combinations within ultracapacitor bank, discharging times are reduced. These processes become faster. Total discharging of super capacitor in minimum time is also dealt with. As a typical case, a bank with two identical UC is dealt with. Although, the proposal can be readily extended to suitably cover different number of units in any other banks of capacitors. This work is useful for understanding behavior of ultracapacitors during parallel and series recombination but this work deals only with static load. So, implementation for dynamic load (namely loaded motor) is also possible during further investigation.

O. Ladin et al [3] deal with predictive power optimization (PPO) algorithm to control power during ride through conditions. Authors use state based approach algorithm system for prediction of system load and action of bidirectional DC/ DC converter is decided. PPO optimizes the DC-DC converter current. Prediction of various stages of load, state of charge of the battery and ultracapacitor is based on the inductor currents. The algorithm has been developed by using probability weighted Markov process. li-ion battery has been used as primary source of energy and ultracapacitor acts as secondary source for peak load condition as per the prediction. Decisions on power sharing are made in real-time, based on the predictions and probabilities of state trajectories along with associated system losses. A real-time global optimizer is then used to control the appropriate power using dc-dc converters. The full hybrid storage system, along with the mechanical drive train is implemented and validated experimentally with a programmable drive-cycle having a strong regenerative component

The work is useful for understanding the PPO method and flow chart for deciding the line of action of ultracapacitor switching. Understanding the basic scheme of DC-DC converter and related aspects is useful the design of the circuit. Rate of charge, discharge and utilization of ultracapacitor and its equations are useful for calculation and formation of various equation as per utilization of ultracapacitors.

Z. Amjadi et al. explain prototype design and its control for battery and ultracapacitor switched-capacitor bidirectional dc/dc converter combination where ultracapacitor supplies energy to load and battery both [4]. They also discuss switched capacitor technique (SSC). The paper suggests SSC having good regulating capacity, with low electromagnetic interference (EMI). The proposed control strategy has been used for the power profile of the traction motor and the gradient of battery current. Complete scheme deals with sensitive current application. Proto type design and controller lead to low ripple in source current. This method has an easier control. The developed control strategy enables

simpler dynamics, compared to a standard buck converter with input filter, lower source current ripple, good regulation capability, low EMI, ease of control, and continuous input current waveform in both buck and boost modes of operation. Utilization of ultracapacitor and luo converter have been explained along with its switching method, in this paper. Their work is helpful to understand switching of luo converter and its maximum utilization. It is also helpful to implement new ideas regarding switching circuits.

Samosir A.S. et al. discuss the case of fuel cell and ultracapacitor combination. Ultracapacitor has been utilized during peak load period, because, the fuel cells have slow dynamic response. Therefore, a secondary power source is needed during start up and transient conditions [5]. By using ultracapacitor as the secondary power source and a bidirectional DC/ DC converter, that couples the ultracapacitor to the dc bus, the performance and efficiency of the overall system has been improved. Ultracapacitor is connected in parallel with fuel cell using interface converter. Interface converter topology is based upon boost converter. DC-DC Controller is based on dynamic evolution control which controls ultracapacitor current. It is based upon simple assumption that the difference between output of the system and the reference input, which is denoted by error state , must be reduced to zero all the time, regardless, whether the disturbance is present or not. Power management system is based on boost converter and switching pulse having pulse width modulation signal control. It is based on fundamental evolution control. This work shows that using a bidirectional converter as an interface between fuel cell and ultracapacitor gives better control over fuel cell voltage during transients. The controller is designed for fast changing loads which are fed by ultracapacitor. It gets charged back to its nominal voltage when the fuel cell power is larger than the demanded load. Possible utilization of paper is for boost converter operation in hybrid system. Boost converter operation for this hybrid system has been properly explained and this explanation is useful for implementation in any other project. This paper provides basic idea of implementation of Pulse Width Modulation (PWM) technique. Various parameters for controlled pulse generation have been studied. Duty cycle is generated by using constant frequency of sawtooth waveform. Hence, constant switching frequency is generated. There is some scope of improvement in this reading, choice of other sample frequency to generate suitable switching frequency for a given duty cycle.

J. Cao et al deal with two major problems of electric vehicle (EV), i.e. the short driving range and the short life of batteries[6]. The basic electric vehicle control scheme has been explained in this paper. Control scheme consists of three DC -DC converters. One for battery, another for ultracapacitor and third one for drive circuit generate switching pulse for three phase inverters. Control system operates on the basis of various signals like driving signal, braking signal, temperature signal, battery voltage and current and ultracapacitor voltage and current. From all these signals, focus is to study battery and ultracapacitor voltage and current utilization in the circuit. Signal provided to drive circuit is based on comparison of these inputs and armature current of the motor. To improve the stability and reliability of the system, fuzzy sliding mode controller (Fuzzy-SMC) has been introduced in the system. The fuzzy membership function and rule-base have been designed on the bases of error signal of actual system and reference signal. The energy-regenerative mathematical model of the system has been established, and the energy-regenerative Fuzzy-SMC for the system is designed. The experimental results show that the Fuzzy-SMC is superior to PID controller for speed of response, steady-state tracking error and minimizing the effects of perturbations. EV uses batteries as its single power source. The ultracapacitor-battery hybrid power system can recover more energy, lengthen the life of batteries, and increase the driving range of EV, by using the technique proposed herein. Information regarding control scheme for electric vehicle and drive circuit provided here are helpful for design of control strategy. The fuzzy set and sliding mode controller implementation and its utilization is useful for designing various control scheme for ultracapacitor energy utilization. Implementation of system with less number of DC-DC converter may improve the performance of the system and reduce cost of the system. Various equations and topologies provide better idea for designing related topology.

Cheng Yong et al. deal with control strategy of hybrid electric vehicle energy flow[7]. The control strategy is based upon state of charge of ultracapacitor and battery. Control strategy regulates output power of energy storage unit and directly influences the vehicle performance. Flow chart explains flow of energy and its control strategy. Simulation results show that the proposed control strategy is effective and it improves the vehicle performance. The simulation method is helpful to develop hybrid electric vehicle for any new control strategy. Their work is useful for understanding MATLAB simulation to develop mathematical model of electric vehicle and gives a better in-sight on energy flow.

Eghbali A. H. et al. deal with different control strategies. These have been explained for solving the problems to improve the performance of hybrid electric vehicles [8]. A battery and ultracapacitor energy storage system and its control strategy based on minimizing the fuel consumption and operating the engine in efficient region has been developed. The efficient control strategy is explained on the basis of ultracapacitor and battery level in steps. In this control strategy, 26 different states are possible and for each state there is a separate control strategy. But actually in only two states electrical vehicle works. This forces the engine to operate optimally. This reduces fuel consumption and increases overall efficiency. The simulation results prove this fact that ultracapacitors can be trustable secondary energy storage and increase the overall performance of system. High instantaneous power delivery regenerative braking improvement, protecting battery system from high currents are some of the ultracapacitors advantages in HEVs which have been presented in simulation results. The proposed strategy makes the engine work efficiently. Their work is very useful for studying the co-working of battery and ultracapacitor, for power flow as per the requirement of load. Proper sharing of power as per the charge-conditions of battery and ultracapacitor is monitored by using programming and flow chart. This analysis is also helpful for power balancing, wherein importance of parameters of ultra capacitor has also been indicated.

Yoong M.K. et al. deal with the improvement in regenerative braking. Moreover, it helps in energy saving resulting into higher energy efficiency of the car. In regenerative mode, the electrical machine acts as a generator, it transfers the kinetic energy to electrical form and charges the batteries or ultracapacitors. In one of the methods for improving braking, a flywheel is used along with ultracapacitor and DC-DC converter. It enhances the regenerative braking performance. In this paper, working principle and braking controller for the regenerative braking has been studied to promote the efficiency and realization of energy saving in the electric vehicle. Ultracapacitor helps in mitigating the transients during starting. It provides a relief to the battery and boosts up the overall performance of the electric vehicle system. The Buck-Boost converter helps in maintaining the power management in the regenerative braking system such as boosting the acceleration. Finally, the flywheel is used to enhance the power recovery process through the wheel of the car. Their work is very useful for implementation in regeneration system or to study effect of improved parameters. The advanced algorithms in the motor controller help to obtain good control over the motor parameters.

Haifang Yu et al. aim at practical issues concerning high charging and discharging current as well as short cycle life of the energy storage system for the hybrid electric vehicle (HEV) developed by First Automobile Works (FAW)[10]. This paper presents a hybrid energy storage system using ultracapacitor which replace primary Ni- MH energy source, without any changes in other parts of HEV. This paper deals with control strategy with all relevant operating parameters taken into account. Simulation analysis shows that the charging and discharging currents of the battery can be smoothened to some degree, especially for peak regenerative feedback current. In addition, the number of charge-discharge cycles of the battery decrease, which contributes to prolongs the battery life. Their work is helpful to understand practical approach of ultracapacitor implementation for dynamic load.

Hick J.A. et al deal with the ultracapacitor management system(UMS) controller using ultracapacitor control module(UCCM)[11]. Their work deals with the innovative concept and analyses the behavior during fault in ultracapacitor. It also comments on importance of temperature rise and its management. Some challenges regarding practical implementation of ultra capacitor bank and its possible solutions have been presented in paper. The design of controller has been focused on simplifying hardware design to reduce system cost. The subsystems consist of operator interface, control unit and plant. In the plant group various sensors and actuators are used to gather information from the bus and individual cells to protect from external interference. Plant provides sensor data to the control system and operator interface. Control system gathers all the information from sensors, and operator interface unit, and generates command signal for controlling the plant. The reliable and efficient operation of the cells requires protection against damage. This protection has been provided by ultracapacitor management system(UMS) by increasing state awareness. Management and control decisions are made by the UCCM based on measurements gathered by sensors, which report the voltage and current. The temperature of the cells has to be monitored for cooling. Designing detailed control system is based upon analysis and various fault management. The system faults include bus under-voltage/overvoltage fault, excessive temperature and current fault, ground fault, cell under-voltage and cell damage fault, sensor failure, communication faults, etc. To overcome all these fault conditions, a state machine has been developed by UCCM. A novel ultracapacitor-only energy storage system has been developed for hybrid-electric vehicles. This work also gives information regarding control strategy using sensor and data interfacing system may be helpful to develop hardware model for control system. Flow diagram of UCCM control frame and UCCM state machine is useful to develop design of control strategy of ultracapacitor bank and also useful for ultracapacitor switching scheme and energy management system and is also useful for improvement of ultracapacitor utilization. Dynamic load implementation for large value can be implemented using this system.

Lu Y. et al. present an idea of an Ultracapacitor-based Energy Storage System (UESS) for two ultracapacitor banks [12]. Boost converter has been used, control strategy for hybrid electric vehicle is based upon voltage level stability of output and on the input energy. A hybrid control strategy, namely Gain Scheduling with Fuzzy Logic Control consists of a Linear Quadratic Regulator (LQR) and a Fuzzy Logic Controller (FLC). Gain scheduling is a technique which can extend the validity of linearization method to a range of operating point. It is designed to regulate output voltage. At each system operating point, properly-designed LQR can achieve fast damping for short-term or small disturbances on input and load currents. When system operating point changes, FLC can trace the changes and adaptively adjust the parameters for the LQR controller. Boost converter with two ultracapacitors control the energy flows where one ultracapacitor is used for low voltage and other one used for high voltage. LQR is ued to reduce performance index of control system. The control strategy proposed in this paper is based on nominal operating point (NOP) which distribute in entire parameter space. Linearization of each NOP and design of LQR controller is based on that. Fuzzy logic controller has been designed to trace the system operating point or adjustment of control system parameters for new operating point. On the basis of operating point, LQP operates. Switching pulse is generated by using fuzzy output signal for boost converter. Design of fuzzy logic controller(FOC) has been explained in detail with detailing of formation of rules and membership function. Simulation results show that short-term or small disturbances on input current and load currents can be well-damped by an LQR controller; while long-term or large disturbances which may cause nominal operating point to change are adaptively controlled by FLC-based gain scheduling method.

Scope of improvement of their work is for fuzzy logic controller and complete control system is useful to develop regulated power supply system from ultracapacitor and it is also helpful to monitor output voltage of ultracapacitor for proper switching instant during reconfiguration. Fuzzy rules and membership function arrangement also provide some useful information for development of new system control strategy.

Camera M.B. et al. deal with design of DC-DC converter and its control system for controlled energy transfer from battery and ultracapacitor to hybrid electrical vehicle [13]. The main objective of ultracapacitor bank is to provide peak power for 20 sec to DC link. In the topology it has been shown that, DC-DC converter provides regulated power from ultracapacitor to DC link. This link is connected to inverter for motor load. The SABAR software package is used for simulation with lab acquisition system and PIC18F4431 microcontroller is utilized to design control strategy. In their work, modeling of each component like battery, ultracapacitor, DC-DC converter, etc has been explained in details. While designing buck boost converter modeling and control strategy, authors assume two conditions for longer time simulation. Two assumptions are , a) The semiconductor switches are ideal, that is to say, there are no losses in them during their conduction and switching. b) There are no losses in the connecting components. Second topology explained is parallel topology of buck boost converters. In this topology, two DCDC converter with separate ultracapacitor are connected in parallel with each other. This topology has been implemented because of converter saturation during transient period. This topology gives identical result of currents that charge the module and decrease in the number of current smoothing inductance of the ultracapacitor. Using this module, 75% of total power requirement has been delivered during transient condition.

After parallel topology of buck boost converter author found out some difficulties like, if one DCDC converter fails to operate then whole topology fails to perform during transient load conditions. Hence second parallel topology of buck boost converter has been developed. In this topology , two capacitors connected in parallel and two buck boost converters are connected in parallel with each other. This topology ensures the power flow to hybrid vehicle during transient load condition.

Experimental setup has been developed to a reduced scale of ten. Experimental results show that, the losses are reduced by 5% as compared to initial topology. Author also comments on utilization of ultracapacitor. As per the paper, If ultracapacitor discharges more than 75% then the current dynamic control becomes insufficient because of the weakened ultracapacitor voltage. Their work deals with some advanced information regarding assumptions mentioned in the review those are may be useful for another scheme. Various control strategy used in this paper is also helpful for new scheme. Advantages of parallel combination system. Characteristics of ultracapacitor. Assumptions made during preparation of hardware. Variation on speed and torque characteristics is not mentioned.

Some scope of improvement is also possible by using re-configuration of ultracapacitors, faster energy transactions will take place. Faster energy transaction may gives better results regarding maximum utilization of ultracapacitor. This paper forms a good basis of comparison.

Moreno j. et al. deals with very efficient energy management system between battery and ultracapacitor for hybrid electric vehicles using neural network[14]. The reference of ultracapacitor is taken after comparing with other resources. An optimal control strategy based on state of charge(SOC) control of the auxiliary source has been implemented. The strategy is based on training a neutral network. A digital signal processor (DSP) has been used for real time implementation. Researchers explain three tests. a) without regeneration, b) with regeneration but without using ultracapacitor, c) with regeneration using ultracapacitor. From the above tests, third test is the most efficient utilization of ultracapacitor. Simulation program is implemented in MATLAB. Buck boost converter modeling has been explained with the implementation ultracapacitor and battery combination. Large number of iterations has been performed for carryout optimal energy flow. Gradient iteration method has been used with assumption of linear function of current. The final charge-condition of ultracapacitor remains same as the initial condition.

Possible utilization of their work is application of neural network with PI controller gives another possible way to develop control system for smooth control. Instead of using PI system may be developed with PID, neural- fuzzy combination for better control. Experimental work can be on lines of this paper, though further work can add reconfiguration, as an attempt to contribute as original work.

Chung H.S. et al. deal with the function of generalized switch-capacitor and its function[15]. Cascaded system of ultracapacitor cell has been developed and implemented as per the requirement of input and output conversion ratio for optimizing conversion efficiency. Before explaining DC-DC converter author discuss the drawbacks of converter topology. This converter technique is based on integrating features of the power conversion techniques. This paper also deals with drawbacks of single capacitor bi-directional converter cell and its overcome technique by implementation of cascaded ultracapacitor technique in parallel and anti parallel connection combination. Design of generalized switched- capacitor and DC-DC converter has been explained in details. State space averaging technique is used for static and dynamic loads. Their work is useful for understanding basics of DC-DC converter and its designing, drawback of basic DC-DC converter, cascade operation. It is also useful for implementation of ultra capacitor in series and in parallel. The scope of improvement in this paper is converter topology modification with re-configuration of ultracapacitors. Its speed and efficiency with our re-configuration proposal will be an important, for extending the on-going work undertaken by us.

Amjadi Z.et al. deal with novel control technique for a switched capacitor converter [16]. Advantages of interleaved controlled converter have been shown over normal DC-DC converter. In this system, ultracapacitor is connected with converter and converter has three stage parallel interleaved bidirectional mode of operation. This

ultracapacitor converter combination is connected in parallel with battery. While charging the ultracapacitor get charged in parallel combination with high voltage side and while discharging it has been connected in series with low voltage side. The authors also show various modes of operation of ultra capacitor charging and discharging using novel control technique across the load. Buck and boost mode of operation has been discussed in details with proper diagrammatic representation. Ultracapacitor module and battery module flow chart explains the complete operational stages and the operating conditions with proper explanations.

Possible utilization of their findings is that charging and discharging methods have been dealt with for the modified system and application & utilization and implementation of series and parallel combination of ultracapacitor bank have also been dealt with. This paper is useful to develop and design an efficient and bidirectional DCDC converter for maximum utilization of ultracapacitors. Scope of improvement is by using recombination of ultracapacitors which should be coordinated with switching over between HV and LV. So that improved system performance will become our innovative contribution, through our proposed work.

3.CONCLUSION

Co-working of battery with ultracapacitors for extending battery-life have been reported in literature. MATLAB simulation and corresponding experimental corroboration have been reported.

A scheme of re-configuring ultracapacitor elements in its bank for faster energy transactions has been developed at GHRCE in 2012.

Hence, the comprehensive conclusion is that the work reported so far deals with the background of simulation/ experimental work for the basic battery/ ultracapacitor parallel working scheme. Various technologies like series parallel combination of ultracapacitor, PI controller, fuzzy logic controller, neural network, PPO, etc from a good background. Advantages of our proposed technique are for system performance-improvement, improved utilization of ultracapacitor energy and help in enhancing battery life in case of battery and ultracapacitor combination for electric vehicle.

REFERENCES

1. Mohamed Hedi Chabchoub, Hafedh Trabelsi "Consolidation Of The Electric Vehicle Battery By An Ulracapacitor For Performance Improvement*" 10th International Multi-conference On Systems, Signals & Devices (Ssd), Hammamet, Tunisia*, page no.1-5, INSPEC Accession Number: 13709273, March 18-21, 2013.
2. P.R.Sawarkar, Dr S.G.Tarnekar, Dr.S.B.Bodkhe"Improvement In Energy Transactions In Ultra Capacitor Banks By Series/Parallel Re-combination"— *International Journal of Electrical Engineering. ISSN 0974-2158* Volume 5, Number 5, pp. 641-652, 2012
3. O. Laldin , M. Moshirvaziri and O. Trescases "Optimal power flow for hybrid ultracapacitor systems in light electric vehicles", *Proc. IEEE Energy Convers. Congr. Expo.*, pp.2916 -2922 2011
4. Zahra Amjadi, Sheldon S. Williamson, "Prototype Design And Controller Implementation For A Battery-ultracapacitor Hybrid Electric Vehicle Energy Storage System", *IEEE Transactions On Smart Grid*, VOL. 3, No. 1, On Page(s).: 332-340,march 2012
5. A.S. Samosir ,A. H. M. Yatim," Dynamic Evolution Control of Bidirectional DC-DC Converter for Interfacing Ultracapacitor Energy Storage to Fuel Cell Electric Vehicle System" *Australasian Universities Power Engineering Conference (AUPEC'08),* Paper P-113 Page 1-7,2008
6. Jianbo Cao, Binggang Cao, Zhifeng Bai, And Wenzhi Chen," Energy-regenerative Fuzzy Sliding Mode Controller Design For Ultracapacitor-battery Hybrid Power Of Electric Vehicle", *Proceedings Of The 2007 IEEE International Conference On Mechatronics And Automation* August 5 - 8, 2007, Harbin, China
7. Yong Chen, Guiyuan Li, Fei Zhang," Simulation Study on Control Strategy for a Hybrid Electric Vehicle with Battery and Ultracapacitor" *Electric Information and Control Engineering (ICEICE), 2011 International Conference , Wuhan,* Page(s): 2601 – 2604,15-17 April 2011
8. A. H. Eghbali , B. Asaei and P. Nader "Fuel efficient control strategy, based on battery-ultracapacitor energy storage system, in parallel hybrid electric vehicles", *Proc. IEEE Veh. Power Propulsion Conf. (VPPC),* pp.1 -5 2010

9. M. K. Yoong , Y. H. Gan , G. D. Gan , C. K. Leong , Z. Y. Phuan , B. K. Cheah and K. W. Chew "Studies of regenerative braking electric vehicle", *Proc. IEEE Conf. Sustainable Utilization Development Eng. Technol.*, pp.40 -45,2010

10 Haifang Yu; Shumei Cui; Tiecheng Wang;, "Simulation and performance analysis on an energy storage system for hybrid electric vehicle using ultracapacitor," Vehicle Power and Propulsion Conference, 2008. VPPC '08. IEEE, vol., no., pp.1-5, 3-5 Sept. 2008 doi: 10.1109/VPPC.2008.4677788.

11. J.A.Hicks; R.Gruich; A.Oldja; D.Myers; T.T.Hartley; R.Veillette; I.Husain; "Ultracapacitor Energy Management and Controller Developments for a Series-Parallel 2-by-2 Hybrid Electric Vehicle", IEEE Conference on Vehicle Power and Propulsion, Page(s):328-335, September 2007

12. Y. Lu , H. Hess and D. Edwards "Adaptive control of an ultracapacitor energy storage system for hybrid electric vehicles", *Proc. IEEE Elect. Mach. Drives Conf.*, vol. 1, pp.129 -133 2007

13. M.B. Camara, H. Galous, F. Gustin and A. Berthon, "Design and new control of DC/DC converters to share energy between supercapacitors and batteries in hybrid vehicles", Vehicular Technology- IEEE transaction, pp. 2721-2735, 2008.

14. J. Moreno, M. E. Ortuzar and J. W. Dixon "Energy-management system for a hybrid electric vehicle, using ultracapacitors and neural networks", *IEEE Trans. Ind. Electron.*, vol. 53, no. 2, pp.614 -623 2006

15. H. S. Chung and A. Ioinovici "Development of a general switched-capacitor DC/DC converter with bi-directional power flow", *Proc. IEEE Int. Symp. Circuits Syst.*, vol. 3, pp.499 -502 2000

16. Z. Amjadi and S. S Williamson, "A novel control technique for a switched-capacitor-converter-based hybrid electric vehicle energy storage system," IEEE Trans. Ind. Electron., vol. 57, no. 3, pp. 926-934,Mar. 2010.

REVERSIBLE AND IRREVERSIBLE DATA HIDING TECHNIQUE

Tanmoy Sarkar
Neudesic India Pvt. Limited
Hyderabad, India
Email: tanmoy.sarkar@neudesic.com

Sugata Sanyal*
Research Advisor
Corporate Technology Office
Tata Consultancy Services
Mumbai, India
Email: sugata.sanyal@tcs.com
*Corresponding Author

ABSTRACT

Steganography (literally meaning covered writing) is the art and science of embedding secret message into seemingly harmless message. Stenography is practice from olden days where in ancient Greece people used wooden blocks to inscribe secret data and cover the date with wax and write normal message on it. Today stenography is used in various field like multimedia, networks, medical, military etc. With increasing technology trends steganography is becoming more and more advanced where people not only interested on hiding messages in multimedia data (cover data) but also at the receiving end they are willing to obtain original cover data without any distortion after extracting secret message.

This paper will discuss few irreversible and reversible data hiding techniques using images**.**

Keywords: *Steganography, Steganalysis, Stego key, Stego image and Cryptography*

1. INTRODUCTION

With the recent advancement of technology people are sharing their private data to each other using internet. The most common way to achieve this is by using encryption i.e. to change the data from one form to another. But the disadvantage of encryption is that it will arouse attention and suspicion among adversaries. Also, in cryptography the key is send as a separate message to receiver so that he/she can decrypt the incoming messages. Such techniques are vulnerable to interception by adversary and subsequent man-in-the-middle attack. In steganography there is no need to send the key as separate message. The secret messages are embedded in innocent message without raising any suspension to adversary.

In this paper we will discuss about few reversible/irreversible data hiding techniques and there advantages/ disadvantages.

A Steganography Properties and Implementation steps
The suitability of given steganography system are defined by few following important properties [14]:

1. Statistical Undetectability: The stego multimedia message containing covert message should be inconspicuous from adversary.

2. Embedding Capacity: The maximum amount of data embedded into cover image with minimum cover image

distortion (Steganographic capacity).

3. **Embedding Efficiency:** The number of secret message bits embedded into cover image with minimum distortion.

Steganography involves the following steps to embed secret image into cover image:

1. Selection of cover image.
2. Secret message where secret message size is less than cover image size. The larger the difference among two the less the distortion of cover image.
3. Function F (i) used to hide data into cover image.
4. Optional stego key to authenticate the data.

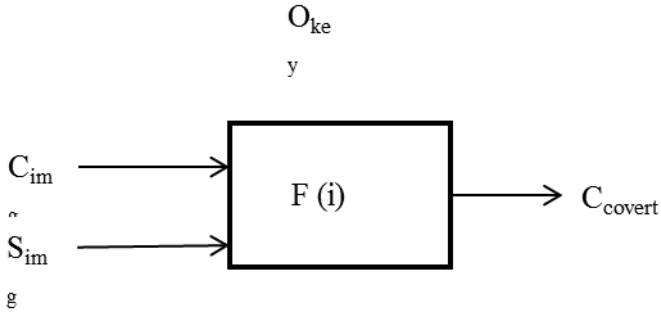

Figure1.1 Steganography steps

Where C_{img} is cover media, S_{img} is secret message, O_{key} is optional stego key, and F (i) is steganography function and C_{covert} the stego image.

B. Digital Watermarking

Similar to Steganography, for authentication of cover message digital watermarking technology is used. The basic difference between Steganography and digital watermarking is that in digital watermarking the covert data is related to cover data but in steganography the covert data is not related to cover data.

C. Data hiding domains

Spatial Domain Techniques are techniques that operated directly on single pixel of an image.

$$f_i \xrightarrow{Tp(.)} g_i$$

Where f_i is the original image, g_i is the modified image and T_p (.) is the spatial operator defined in a neighborhood p of a given pixel.

Frequency Domain Techniques are operated on frequency of an image.

$$f_i \xrightarrow{f_p} I_i \xrightarrow{-f_p} g_i$$

Where f_i is the original image, I_i is the modified image after applying frequency transformation f_p, g_i is the final modified image after implementing inverse transformation $-f_p$.

Wavelet Transform Domain is used in image processing to know the frequency and temporal information at the same time. Using this technique many papers are published which are efficiently store the secret data by shifting histogram and increases data embedded capacity.

2. DETAILS OF PAPER

There is lot of Steganography techniques used to hide data using different cover media like audio, image, video etc.

A. Irreversible data hiding techniques

Irreversible means once the covert image embedded on the original image the original image is lost i.e. from stego image original image cannot be recovered in extraction process.

The simplest method of data hiding in irreversible category is using LSB (Least Significant Bit) insertion. Let us

consider the cover message m_o is grey scale message where each pixel is denoted by 8 bits. So, mathematically to replace the first pixel x_i of message m_o with the first bit of cover message m_c is as follows:

$$x_{LSB_i} = x_i \, mod \, 2$$
$$x_{covert} = x - x_{LSB_i} + m_c \, mod \, 2$$

The advantage of LSB embedding is its simplicity and the difference is not visible to naked eyes. But this technique has also having lot of disadvantages like LSB encoding is extremely sensitive to any kind of filtering or manipulation of the stego-image. An attack on the stego-image is very likely to destroy the message. An attacker can easily remove the message by removing (zeroing) the entire LSB plane with very little change in the perceptual quality of the modified stego-image. From Fig. 1.2 we can see that after embedding secret message into the cover image there is significant change in original image histogram pattern suggesting it is being distorted.

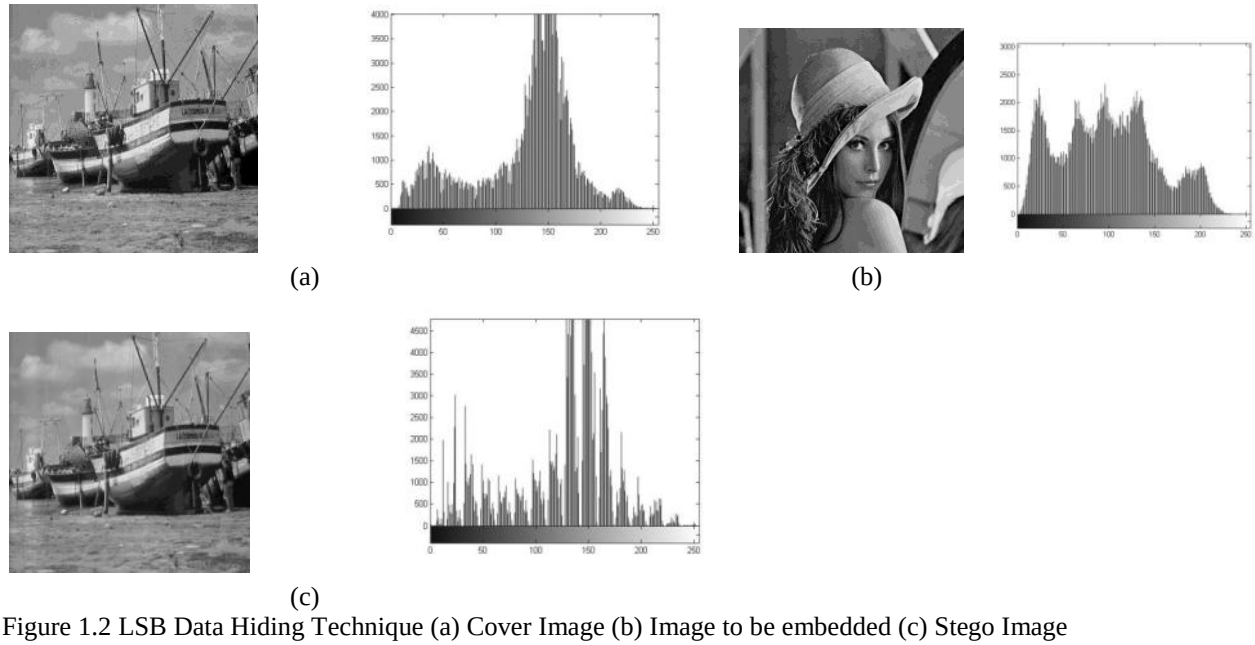

(a) (b)

(c)

Figure 1.2 LSB Data Hiding Technique (a) Cover Image (b) Image to be embedded (c) Stego Image

Chan et al [1] proposed a novel approach of LSB substitution data hiding in images by using optimal pixel adjustment process. Using this technique the stego image quality is improved than classical approach and also, capacity of embedded secret message increases.

Battisti et al [2] proposed an algorithm based on Fibonacci p-sequence number to increase the bit planes of image and also, reduced the distortion caused by than traditional LSB hiding technique. This paper proposed to decompose the original image into bit planes based on the following Fibonacci p-sequence formula:

$$F(n) = \begin{cases} 0 & n < 0 \\ 1 & n = 0 \\ F_p(n-1) + F_p(n-p-1) & n > 0 \end{cases}$$

After this the covert data is inserted into the selected plane if it satisfies Zeckendrof condition and during extraction it follows the reverse process.

Dey et al [3] [4] proposed an improvement over Fibonacci p-sequence LSB data technique of Battisti et al [2] by decomposing pixel value using two approaches: Prime decomposition and Natural number decomposition technique. Since distortion increases exponentially with the increase of decomposition plane so in these paper the existing number of bit planes increase to a new set of virtual bit planes using decomposition techniques. Unlike Battisti et al [2] these algorithms doesn't use Zeckendrof condition but rather use lexicographical order to define the number system.

Nosrati et al. [6] introduced a method that embeds the secret message in RGB 24 bit color image. This is achieved by applying the concept of the linked list data structures to link the secret messages in the images. First, the secret message that is to be transmitted is embedded in the LSBs of 24 bit RGB color space. The secret message bytes are embedded in the color image erratically and randomly and every message contains a link or a pointer to the address of the next message in the list. Also, a few bytes of the address of the first secret message are used as the stego-key. The disadvantage with this approach is that extra space is required for pointers within image obstructing the possibility of extra message and also, while

extraction process if first pointer get corrupted or not traceable on receiver location then whole message becomes unrecoverable.

B. Reversible data hiding techniques

Reversible techniques are used to recover the original image from stego image by extracting secret image/message. Areas like medical, military where original image is as important as secret message any vagaries on original image during the transmission can alter the intelligence of original image and affect the overall results.

Ni et al. [5] proposes a novel approach of data hiding using histogram shifting of original image. This algorithm first finds the peak point and zero point in the histogram, records the coordinate of these points and keep the information as overhead information. After this the peak points of the histogram shifted to right by 1 and embed the secret message into the resulting space. Since this approach is reversible the original image can also be extracted by scanning the entire stego image from left to right and apply the process in reverse order. The advantage of this method is that it is simple, reversible and efficient. The disadvantage is that this method will not able to perform when more than one peak and low point exits in the histogram as the overhead message increases. Also, this paper doesn't discuss about the transmission of peak and zero point in histogram to the receiver. If the receiving end doesn't have the knowledge of these points in a histogram then the extraction process fails.

Kuo et al. [7] presented a reversible technique that is based on the block division to conceal the data in the image. In this approach the cover image is divided into several equal blocks and then the histogram is generated for each of these blocks. Maximum and minimum points are computed for these histograms and shift the histogram right and left by 1 near the maximum points so that the embedding space can be generated to hide the data at the same time increasing the embedding capacity of the image. A one bit change is used to record the change of the minimum points in location map. In this approach the receiver will extract the location map from the stego image, gets the information about the maximum and minimum points in a histogram and extract the secret message. This method increases the data hiding capacity inside the cover image.

Tian [8] proposes a reversible data hiding technique using difference expansion using LSB. In this method the mean and average value of two neighboring pixel, with small difference value, is calculated. The calculated value is then check to see whether it is satisfying the expandable difference condition (i) and once the condition is passed the new expanded difference is calculated (ii). Finally the secret message is embedded based on the calculated values. This technique also use location map to store the values to know which difference value have been selected which are used to extract the image at the receiving end. This technique significantly improves the capacity of payload message and visual quality of embedded image.

$$.2 \times h + b \mid \le \min(2(255 - l), 2l + 1) \ldots\ldots\ldots\ldots \text{(i)}$$

$$h' = 2 \times h + b \ldots\ldots\ldots\ldots \text{(ii)}$$

In the fig. 1.3 we have embedded image (b) into image (a) by using difference expansion. From the histogram of stego image (c) we can see that the secret image is embedded on the difference of near pixel value which are expandable but the pixel having minimum intensity or zero value are not used much in this process.

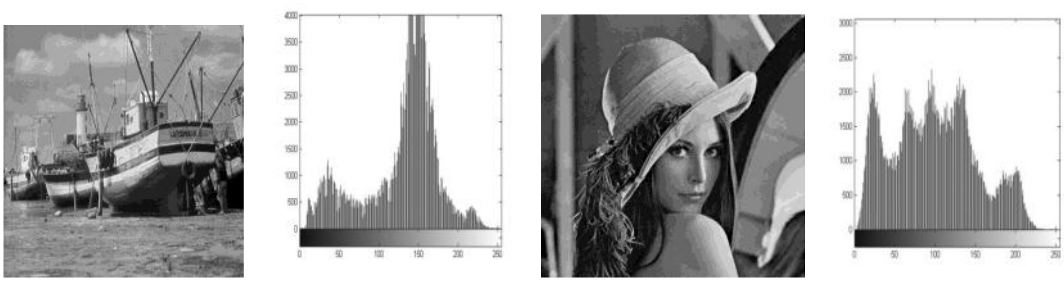

(a) (b)

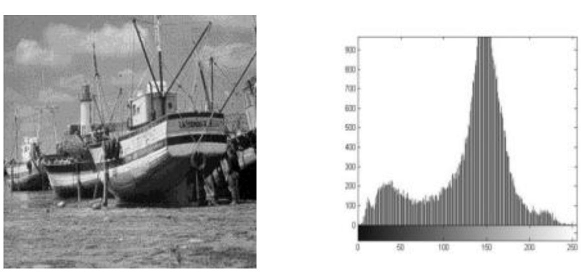

(c)

Figure 1.3 Difference Expansion using LSB (a) Cover Image (b) Secret Image (c) Stego Image

Yang et al. [9] propose another method of data hiding by embedding a secret message into the low-high (LH) and high-low (HL) sub bands of integer wavelet transform (IWT) domain. This proposed method can effectively embed the covert message without much distortion and also, stego image that get generated equipped with some robustness (protect secret message against image processing operations).The disadvantage with this approach is since this method performed on spatial domain slight changes done on stego image can lead to data extraction failure.

Rosaline et al [13] have put forward a new approach of data hiding by encrypting the original image, compressed the original image using Haar wavelet transform and then embed the secret image into the encrypted compressed data. Using this approach the author provides double protection to secret data.

Xuan et al. [11] [12] proposed reversible data hiding algorithms based on integer wavelet transform (IWT) for high capacity. These algorithms are implemented on IWT domain. The algorithms also, use histogram modification technique, in order to prevent overflow and underflow and embed data into IWT coefficient high frequency sub bands. The first algorithm [12] lossless compresses some selected middle bit-planes of IWT coefficients in high frequency sub bands to create space to hide data. The second algorithm [13] uses spread spectrum method to hide data in IWT coefficients in high frequency sub bands.

3. CONCLUSION

This paper helps to understand steganography and its reversible/irreversible techniques in spatial and frequency domain. Also we have discussed advantages/disadvantages of these techniques. Apart, from these domain some papers has also, been published in software domain [15] where authors try to embed secret message into case-insensitive programming languages, scripts like HTML, Pascal etc.

REFERENCES

1. Chi-Kwong Chan, L.M. Cheng “Hiding data in images by simple LSB substitution” The Journal of pattern recognition society, Pattern Recognition, Volume 37, Issue 3, March 2004, Pages 469–474.
2. F. Battisti, M. Carli, A. Neri, K. Egiaziarian, “A Generalized Fibonacci LSB Data Hiding Technique”, IEEE 3rd International Conference on Computers and Devices for Communication (CODEC-06) TEA, Institute of Radio Physics and Electronics, University of Calcutta, December 18-20, 2006.
3. Sandipan Dey, Ajith Abraham, Sugata Sanyal , “An LSB Data Hiding Technique Using Prime Numbers”, The Third International Symposium on information Assurance and Security, Manchester, UK, IEEE CS press, pp. 101-108,2007
4. Sandipan Dey, Ajith Abraham, Sugata Sanyal , An LSB Data Hiding Technique Using Natural Numbers, Intelligent Information Hiding and Multimedia Signal Processing, IIHMSP 2007. Third International Conference, Kaohsiung, Vol.2, pp. 473-476, 2007.
5. Z. Ni, Y. Q. Shi, N. Ansari and W. Su, “Reversible data hiding,” IEEE Transactions on Circuits and Systems for Video Technology, Vol.16, No.3, pp. 354-362, 2006
6. M. Nosrati, R. Karimi, H. Nosrati, and A. Nosrati, “Embedding stego-text in cover images using linked list concepts and LSB technique”, Journal of American Science, Vol. 7, No. 6, 2011, pp. 97-100.
7. Wen-Chung Kuo, Dong-Jin Jiang, Yu-Chih Huang, “A Reversible Data Hiding Scheme Based on Block Division”, Congress on Image and Signal Processing, Vol. 1, 27-30 May 2008, pp. 365-369
8. Jun Tian, “Reversible Data Embedding Using Difference Expansion”, IEEE Transactions on Circuits and Systems for video technology, Vol.13, No. 8, August 2003, pp. 890-896.
9. Chin-Yu Yang, Chin-Hung Lin, Wu-Chih Hu “Reversible Data Hiding for High-Quality Images based on Integer Wavelet Transform," Journal of Information Hiding and Multimedia Signal Processing, Vol. 3, April. 2012, pp. 142 -150.
10. Hameed Al-Qaheri, Sandipan Dey, Sugata Sanyal “Hiding inside Html and Other Source Codes” Image Processing & Communication, vol. 14, no. 2-3, pp. 59-68
11. G. Xuan, J. Zhu, J. Chen, Y. Q. Shi, Z. Ni, W. Su “Distortion less Data Hiding Based on Integer Wavelet Transform,” IEE journal, ELECTRONICS LETTERS, Volume 38, No 25, pp.1646-1648, Dec.2002.
12. G. Xuan, Y. Q. Shi, Z. Ni, “Lossless data hiding using integer wavelet transform and spread spectrum,” IEEE International Workshop on Multimedia Signal Processing, Siena, Italy, September 2004.

13. S. Imaculate Rosaline, C. Rengarajaswamy, “Reversible Data Hiding Technique for Stream Ciphered and Wavelet Compressed Image” Proceedings of the International Conference on Pattern Recognition, Informatics and Mobile Engineering (PRIME) February 21-22, pp.374-377 2013

14. Ingemar Cox ,Matthew Miller , Jeffrey Bloom , Jessica Fridrich , Ton Kalker , “ Digital Watermarking and Steganography” -The Morgan Kaufmann Series in Multimedia Information and Systems, ISBN-10: 0123725852, ISBN-13: 978-0123725851

15. Sandipan Dey, Ajith Abraham, Sugata Sanyal ,” Embedding Secret Data in Html Web Page "arxiv.org, arXiv: 1004.0459, 2010

IDENTIFICATION OF SIZE AND LOCATION OF CIRCUMFERENTIAL HELICAL CRACK IN MARINE PROPELLER SHAFT USING STRAIN AND DISPLACEMENT MEASUREMENT

Ridwan Hossain
Graduate Student, Faculty of Engineering & Applied Science
Memorial University of Newfoundland
230 Elizabeth Ave, St John's, NL, Canada A1B 3X9
Cell: +1 709 765 3220
E-Mail: rbh546@mun.ca

Arisi S.J. Swamidas*
B.E (Civil), M.Eng (Structures), Ph.D (Eng. Mechanics) (I.I.T Madras)
Honorary Research Professor of Civil Engineering
Faculty of Engineering and Applied Science
Memorial University
St. John's, NF, Canada A1B 3X5
Tel: (709) 737-7983
Fax: (709) 737-4042
E-Mail: aswamidas@mun.ca
*Corresponding author

ABSTRACT

The study discusses an approximated numerical method to identify and detect the presence and profile of circumferential helical cracks in a marine propeller shaft, subjected to the repeated cyclic loading effects of combined bending and torsion (Mode I + III) generated in rotating shafts. Part of such cracks remains always closed and hence conventional inspection method such as visual inspection or vibration measurement during the machine rotation fails to identify such cracks, even at very late stages of the shaft's total life. This study proposes a simple but effective method for identifying such cracks using strain and displacement measurements. The study was carried out using Finite Element Analysis on a small scale real life marine propeller shaft. It was found that due to the presence of the crack, both the percentage change and the percentage change of the slope of strains and displacements, show significant variations if measured at properly identified locations. Based on the changes in the above mentioned parameters (of strain and displacement) it is shown that the location and size of such cracks can be identified in this type of structure.

Keywords: *Spiral crack, Propeller Shaft, Static Analysis, Crack detection.*

1. INTRODUCTION

Shafts are essential components for transmitting power in all kinds of rotational machinery and high performance rotating devices. Therefore, they are subjected to one of the most strenuous working and repeated cyclic loading conditions and often fail due to fatigue cracking if not diagnosed at the appropriate time. According to Bachschmid et al[1], most often the information about the cracks and failure of rotor shafts are kept confidential by plant

management and manufacturer. In this book the authors analyzed several rotor shaft failure cases from real life scenarios and found that early identification of damage is one of the key factors for failure prevention in shafts. Another technical report by Bently-Nevada[2] mentioned that one manufacturer had logged more than 28 incidents of shaft failure in North America for only power generation industries over the previous ten years and according to the manufacturer it was only a partial list. According to an EPRI report mentioned in that bulletin, one utility paid $6.2 million to replace power alone during an outage caused by shaft crack on turbine. The replacement cost was nearly $100,000; hence crack detection on shafts had received large attention over the past few decades. Moreover, it was also reported in that bulletin that under a specific situation, the presence of a crack was noted only when it was around 90 - 95% in crack depth, and it was stated to be a 400^0 spiral crack (see page 10 in reference [2]).

Propeller shaft is one of the key components of propulsion systems. It basically serves two purposes: (i) to transmit engine power to the propeller; (ii) to transfer the axial force to the thrust bearing. The main reason for cracking in such shafts is the stress concentration caused around discontinuities or hotspots during combined bending and torsion. So far, almost all of the work related to cracked shafts considered bending cracks only [1, 3-5]. In this study, the possibility of circumferential helical crack detection has been discussed using an early crack detection method proposed in this study, based on variation of static parameters of strain and displacement.

2. CIRCUMFERENTIAL HELICAL CRACK

Circumferential helical cracks are rare in ductile materials but they have been reported in brittle materials [6, 7]. The stable planar crack under bending (mode I) becomes inclined due to the superposition of shear stress parallel to the crack front (mode III). Under this mixed mode loading (mode I + III) condition, an initial micro crack might branch along the circumference if the probability of branching is equal everywhere along the circumference, such as in a rotor shaft under ideal conditions (without much cylindrical surface discontinuities).. The combined mode I and mode III loading imposes an angle to the principle stress plane and therefore instead of being perpendicular to the principle axial plane, the crack propagates as a circumferential helical crack (see Fig 1-3). The technical bulletin of Bently-Nevada mentioned earlier [2] reported an incident of a shaft (probably constructed from a ductile metal) crack in a utility plant where they found a 400 degree spiral crack based on vibration measurement and subsequent examination after disassembly.

The major difficulty with identifying circumferential helical crack is part of the crack remains closed specially when the mode III loading dominates. Hence, it gets difficult to identify such crack at their early crack growth stage especially with the conventional methods such as visual inspection (with fiberscopes and magnifying glasses/mirrors). So far, the most common practice of identification method includes measurement of the super-synchronous 2X and 3X vibration components during machine rotation [2, 9] along with the 1X component. However, according to the report of Bently-Nevada[2], this methodology gives indication of crack only at a very late stage of crack growth development (in one analysis, it was found that there was already a 90-95% developed crack present in the rotating shaft, to show a significant change in 1X and 2X components of vibratory speed).

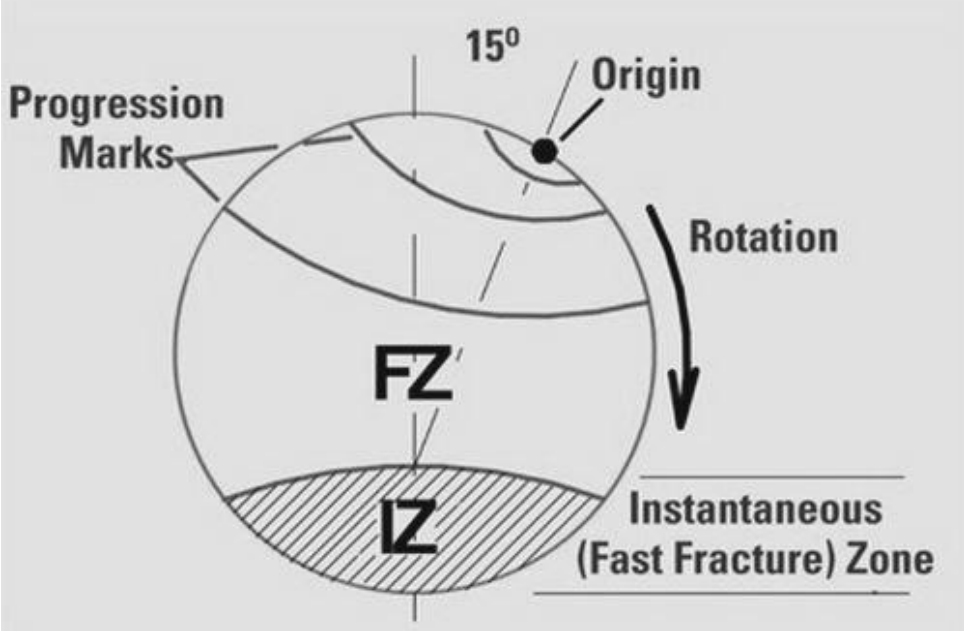

Fig. 1: Effect of rotating bending (with a heavy bending load) on Crack origin [8]

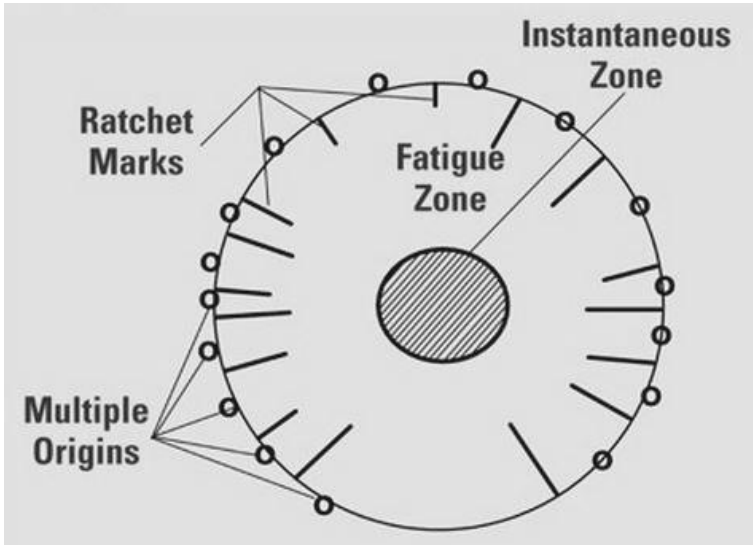

Fig..2: Schematic diagram of rotating bending failure (with a lighter bending load) of shafts showing multiple crack origin [8]

An earlier analysis carried out by Hossain et al [11] based on the use of static parameters (strain and displacement) for crack detection in rotating shafts was able to detect the presence of a bending crack at an early stage. The method was applied to a rotating marine propeller shaft with a propeller attached to an overhanging end, where crack was initiated and propagated due to the bending effects of the propeller weight. Finite element analysis using ABAQUS was used to calculate the displacement and strain at several predefined locations. A sensor placement study was carried out to determine the most optimum placement that would give the maximum change in the measured parameters of strains and displacement. It was found that due to the presence of the propagating crack, variation of strain was high near the point of contra-flexure and variation of displacement was high near the free end. An inherent relationship was shown to exist between change in these measurements of strain and displacement and the crack location and crack depth, which could be used to identify the crack location and size. In this study, the same methodology has been applied to helical circumferential crack in an overhanging marine propeller system under its weight and an identification method has been proposed for early crack detection.

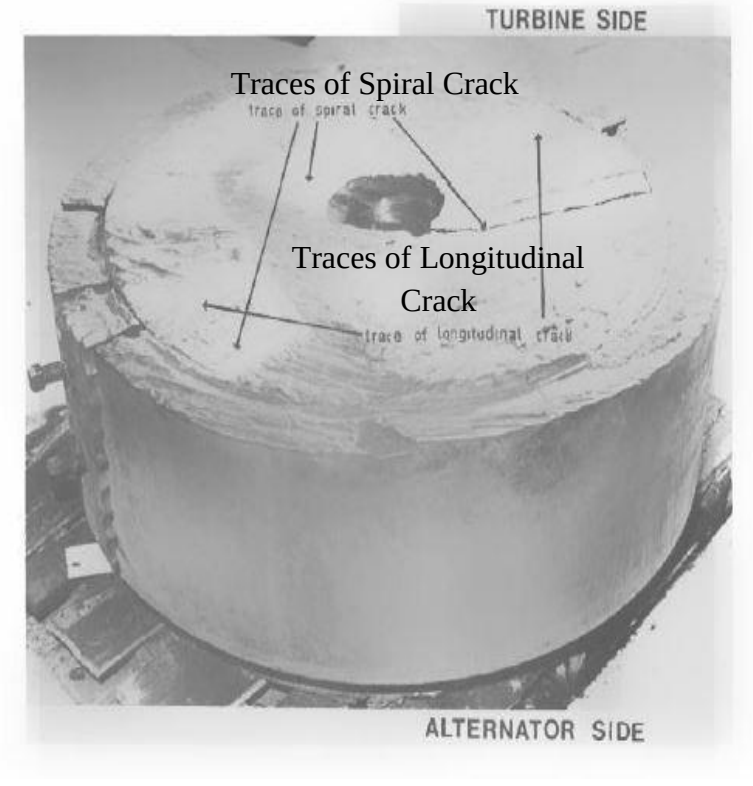

Fig. 3: Circumferential Helical Crack on a 1.2m Diameter Hydraulic Turbine Shaft [10].

3. MODEL PRE-PROCESSING AND LOAD ESTIMATION

The propeller system considered for the analysis has four major components viz. a 4-bladed propeller, a 1.3 m steel shaft (15.75mm dia) having mounted the propeller at one end, a fixed support at the other end and an intermediate support located at 1000mm from the fixed end.

The 4 bladed propeller used in this analysis and earlier one [11, 12] was made of commercial bronze and weighed 15.39N having a density of 8800 kg/m^3 (Fig. 4). The exact modelling of the propeller was very important in this case as only the influence of its weight was considered for crack initiation and propagation. To measure and model the complex nature of the blades properly, a high-speed 3D Terrestrial Laser Scanner (TLS) manufactured by FARO was used which produced dense point clouds based on the actual shape. The propeller was scanned on both sides and point clouds were generated for each side. Both of the point clouds were then merged into a single point cloud and exported to SOLIDWORKS. Based on the location of the points, the propeller was generated using SOLIDWORKS drawing (Fig. 5). By defining the materials, the weight of the CAD model was evaluated and was found to be in agreement with weight measured for the actual model used in this study.

Figure 4: 4-bladed propeller used in the analysis

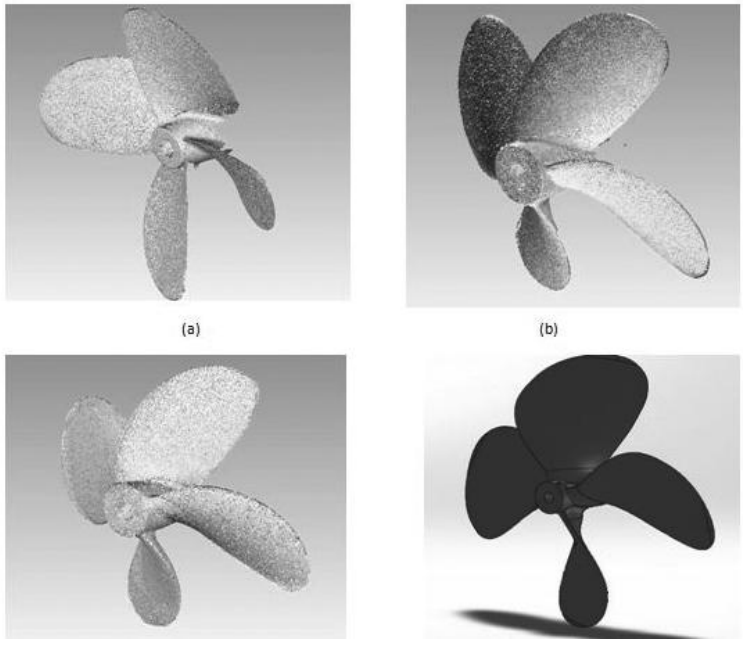

Figure 5: Propeller; (a) Scanned point cloud of side 1; (b) Scanned point cloud of side 2; (c) Combined point cloud; (d) CAD model

The other three propeller blade components were also modeled using SOLIDWORKS based on their dimensions and the four components were assembled. The assembly was then converted into a parasolid and exported to ABAQUS for

finite element analysis. The density of the cloud of points was reduced from the laser-measured 200,000 points to 40000 points to make the data to be usable by the available computer space of the authors. In the earlier analysis carried out by Hossain et al [11], a number of locations was used to measure the strains and displacements throughout the shaft. It was found that only near the point of contra-flexure, the strain showed significant variations; and displacements showed significant variations at the free end and somewhere around the middle of the shaft, due to the presence of the crack. Therefore, in this study, to reduce the number of the sensors to be located in actual measurement setup, strains were measured only at two locations (near the point of contra-flexure on either side (of the point of contra-flexure), i.e., 410mm and 530mm) and displacements were measured at the free end, i.e., at 1300mm and at 710 mm from the fixed end. The cracks were considered at 11 different locations from 75 mm to 1210 mm from the fixed end having crack depth ratios (depth of crack/ radius of the shaft) ranging from 0.05 to 0.6 at each of the above locations.

The finite element model was meshed using a total number of 36,025 quadratic tetrahedral elements (C3D10). This type of element belongs to the 3D stress family having a quadratic shape function. The cracks used in the analysis were in nature seam cracks, which remain close initially but can open or close upon the application of appropriate load (Fig. 6). As it can be seen in Fig. 3 that the pitch of the helical crack is very small, therefore it can be considered that the crack is located in the same inclined plane, instead of being helical in nature. Smaller elements were used along the crack edges and measurement locations for ease in identification and better results. The elements around the crack are clustered together to properly represent the singularity effect present at the crack tip.

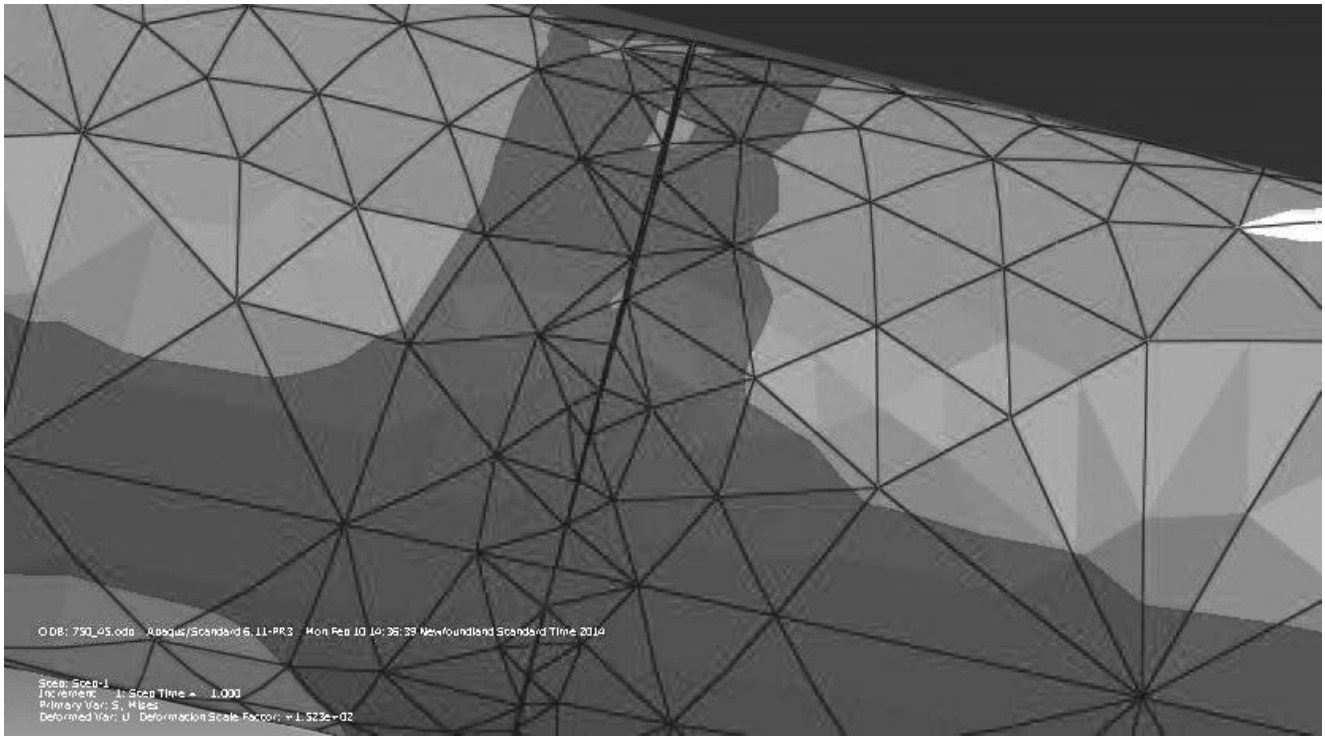

Fig. 6: Seam crack; Crack location: 750mm, Crack depth ratio: 0.45

The bending load for the system was considered to be the weight of the components. The torsional load was calculated considering the study of Parsons et al [13] and then applying the similarity method proposed by Shumin et al [14]. The mass of the model was 25,918.766 kg and the model ratio was calculated to be 0.0392. The total torsional load thus calculated was found to be 16.72N and considering the symmetry of the propeller blades, load on each blade was considered 4.18N. These loads were applied as concentrated tangential (to the shaft circumference) forces at the centroid of each of the four blades, and were applied as a torsional couple, on the pair of opposite blades.

Moreover, the angle of the helix was obtained by measuring the inclination of principle stress plane and found to be 0.035 radians; hence the crack plane was modelled as an inclined plane. The strain and displacements, used in the subsequent crack computation, were obtained manually from the output database file. In real life, strains gauge and laser technique might be implemented as the displacement change is sometimes small, especially for early cracks. A recent study by Kohut and Kurowski [15] has demonstrated how vision systems can be used to detect modal parameters. In addition the possibility of crack initiation was discussed in an earlier study carried out on bending crack development in marine propeller shafts [16].

4. RESULTS & DISCUSSION

4.1 Displacement Plots Displacements were measured at both the locations (given earlier) for the uncracked condition at first. Then for every crack depth ratio at each location, they were measured and the change computed; and the results were plotted as percentage change against crack depth ratio for each location (Figure 7 & 8). From both the figures it is clear that the percentage change in displacements increase rapidly with the crack depth ratio. For the same crack depth ratio, the percentage change differs from point to point, depending on the crack location, and it was found that for a 0.6 crack depth ratio, the maximum change (26.71%) obtained at first measuring point (710 mm from fixed end) was for crack located at 750 mm from fixed end. For the same crack depth ratio, the maximum change (27.94%) obtained at the second measuring point (1300 mm from fixed end) was for crack located at 1030 mm from fixed end. Although only small changes were observed for crack depth ratios less than 0.3, they would definitely give better results due to scaled model amplification ratios, if they were measured with suitable sensitive devices, under real life situations.

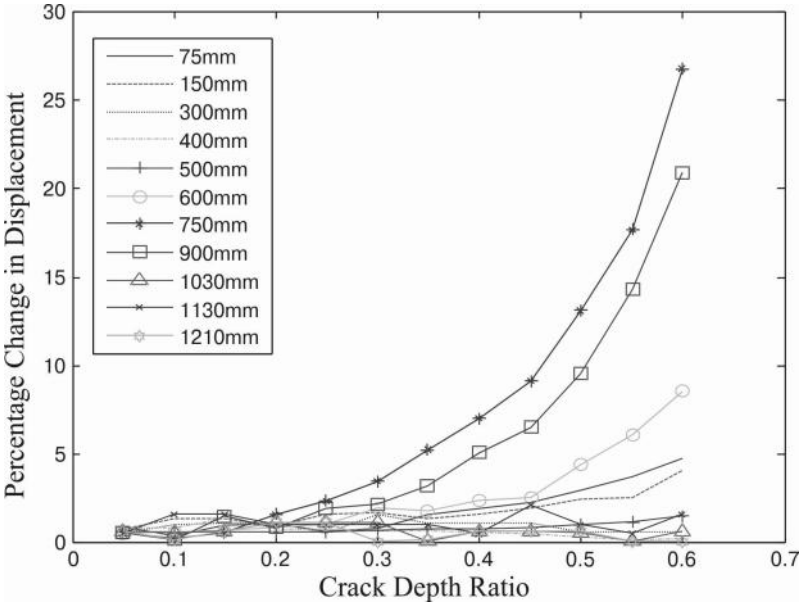

Fig. 7: Percentage change in displacement against crack depth ratio for the displacement sensor located at 710mm from the fixed end (different curves show the location of the crack from fixed end).

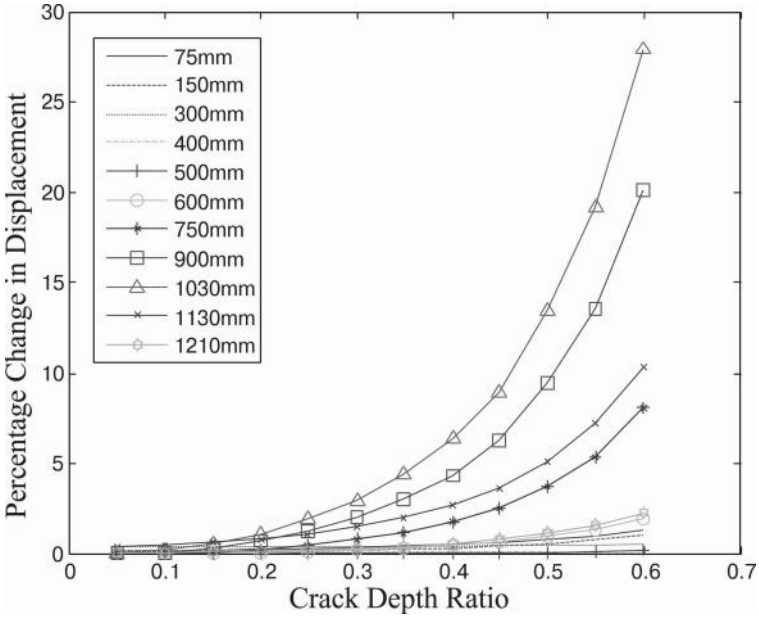

Fig. 8: Percentage change in displacement against crack depth ratio for the displacement sensor located at 1300mm from the fixed end (different curves show the location of the crack from fixed end)

4.2 Strain Plots Similar to displacements, strains were also plotted as percentage difference against crack depth ratios (Figure 9 & 10). Both the plots show similar trends like displacements but the change is a little higher than displacements. For the first measuring point (410 mm from fixed end), the highest percentage change (31.31%) for crack depth ratio of 0.6 was obtained for the crack located at 750 mm from fixed end. For the second measuring point (530 mm from fixed end), the highest percentage change (22.05%) was for the crack located at same location as well. It is also clearly seen that although strain percentage shows greater variation for location in between fixed and overhanging support, they show almost no variation for cracks located beyond the overhanging support, for both the locations. Hence it can be concluded that the strain measurements cannot be used for detecting cracks located on the overhanging end of the propeller. In addition, since the strain locations and nodal locations were manually identified from the data output obtained from the numerical computations, the improper identification of nodes and corresponding locations exist, which could have led to the fluctuations seen for the strain sensor located at 530 mm from the fixed end (see Figure 10).

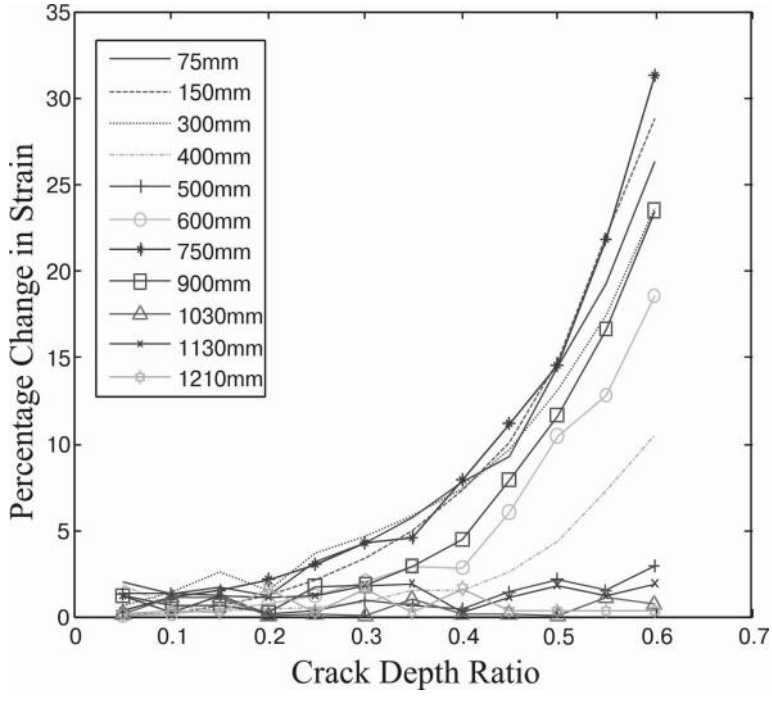

Fig. 9: Percentage change in strain against crack depth ratio for strain sensor located at 410mm from the fixed end (different curves show the location of the crack from fixed end)

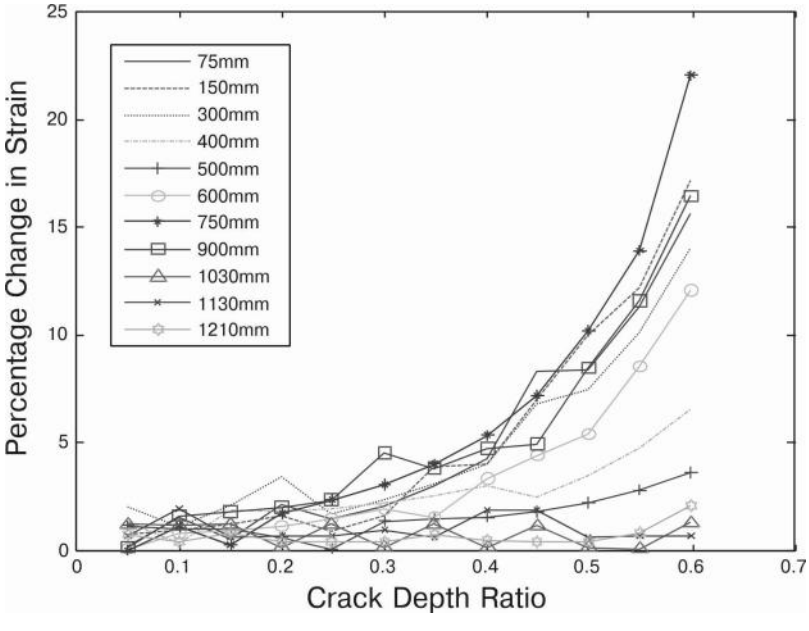

Fig. 10: Percentage change in strain against crack depth ratio for strain sensor located at 530mm from the fixed end (different curves show the location of the crack from fixed end)

4.3 Slope of Percentage Change in Displacement and Strain Although, the percentage changes in displacement and strain show significant variations with crack size, for crack depth ratios below 0.3 their values are very close to each other. Even with the scaled model amplification ratio, it will be difficult to identify the variation in actual case. To overcome this problem for crack identification in earlier crack growth stages, slopes of percentage changes for both displacements and strains were plotted against crack depth ratios (see Figures 11, 12, 13 & 14). Since large fluctuations were observed initially when slopes were computed from raw data, a 5-point average was done for all the values to reduce such fluctuations. The first value, viz., at a crack depth ratio of 0.05 was not considered since the obtained initial change of slope value was very high Thereafter all the values were considered since the computed average was the average of the five values, with two on either side of the assumed crack. The maximum slope for strain (or percentage change of slope of strain as a function of crack depth increase) was found to be up to 257.6% and 155.4%, at 410 mm and 530 mm respectively, for the 0.6 crack depth ratio. For the same crack depth ratios, the maximum slope for change of displacement was found to increase to 215.04% and 227.7%, at 710 mm and 1300 mm, respectively. These plots could be used as an effective tool for early crack detection as they provide a significant amount of change (5-10%) even for a very small crack depth ratio (0.1-0.15).

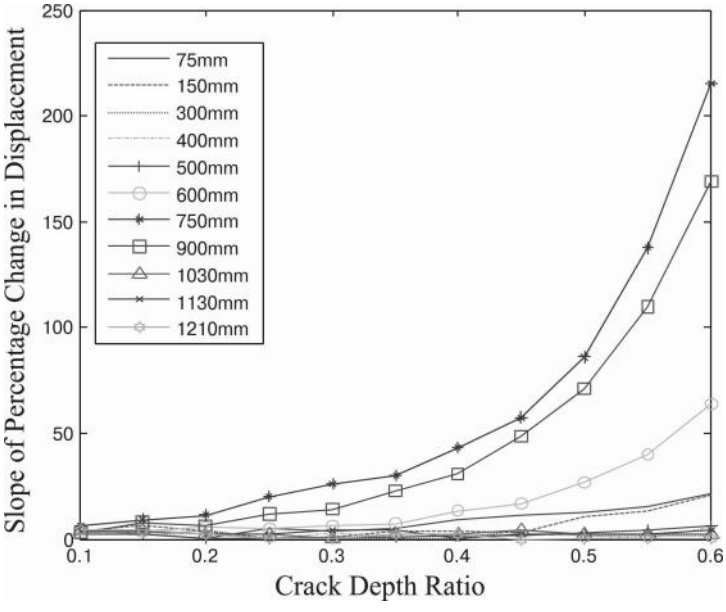

Figure 11: Slope of percentage change in displacement against crack depth ratio for displacement sensor located at 710mm from the fixed end (different curves show the location of the crack from fixed end)

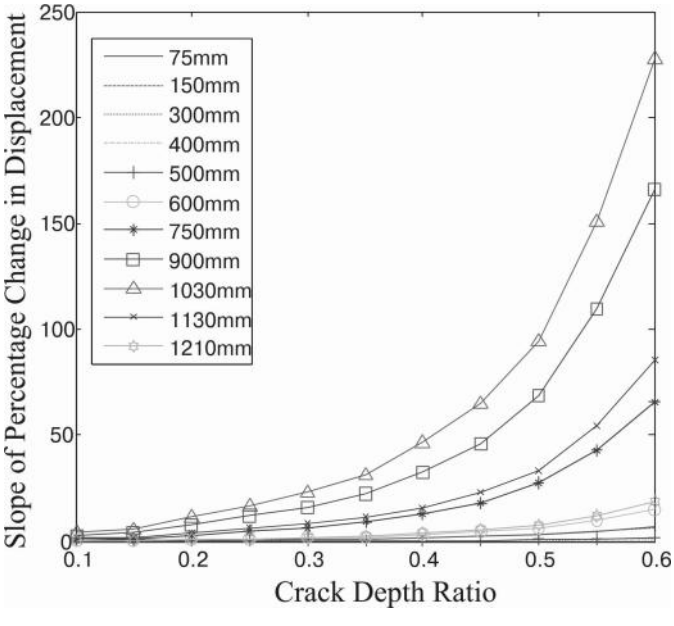

Fig. 12: Slope of percentage change in displacement against crack depth ratio for displacement sensor located at 1300mm from the fixed end (different curves show the location of the crack from fixed end)

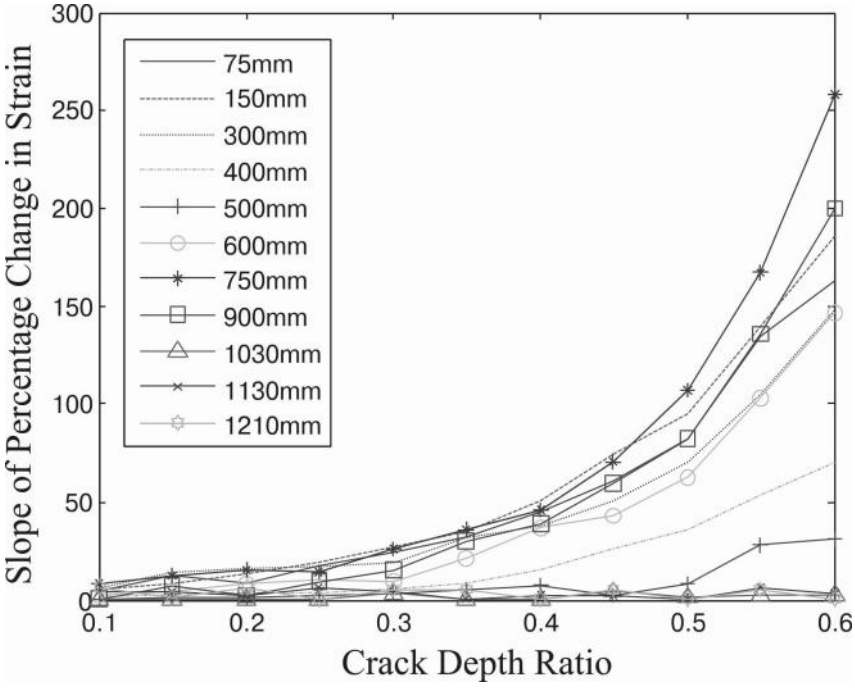

Fig. 13: Slope of percentage change in strain against crack depth ratio for strain sensor located at 410mm from the fixed end (different curves show the location of the crack from fixed end)

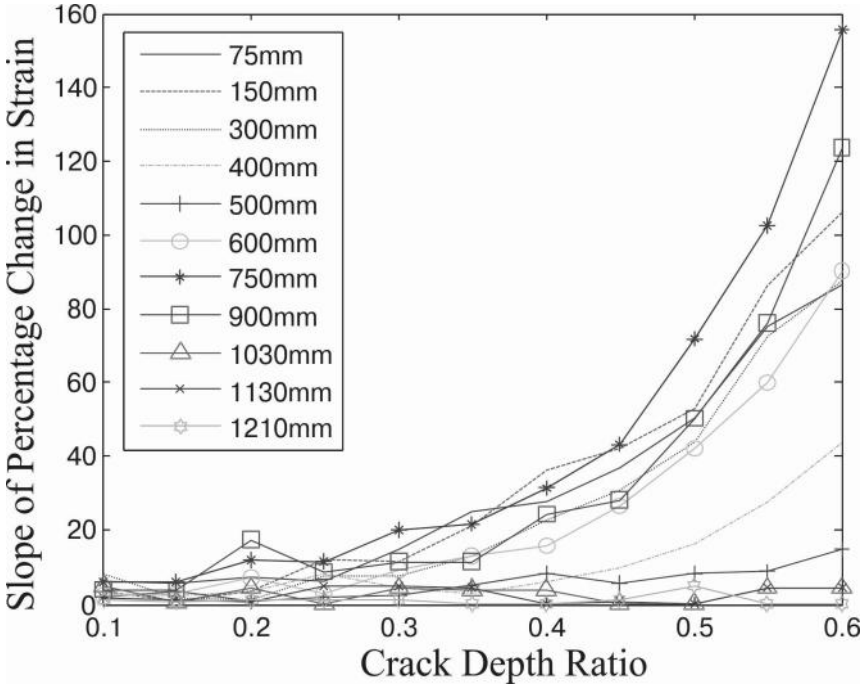

Fig. 14: Slope of percentage change in strain against crack depth ratio for strain sensor located at 530mm from the fixed end (different curves show the location of the crack from fixed end)

It is also visualized that in real life crack growth scenarios, since the crack depth will not be known beforehand, and since the total crack growth life is analogous to the crack depth, the estimated total fatigue (or crack development) life of the specimen could be related to these percentage changes. An as alternate, instead of normalized crack depth or total fatigue life, even the total life (in terms of days or months) can be used to relate these changes in displacements and strains.

4.4 Crack Detection Method The earlier study by Hossain et al [11] showed that using the percentage difference, a crack identification method (both location and size) can be developed. It was also shown in that paper that the use of percentage of strain or displacement was able to detect crack depth ratio sizes greater than 0.30. But in the present study, it can be seen that slope of percentage differences provides much larger values than percentage difference and hence slope of percentage differences was used in this paper for crack detection. All the slope values (for percentage changes in displacement and

strain) were saved in a Microsoft Excel workbook along with their corresponding crack location and size. A MATLAB script was then developed which read those values and asked for input parameters (defined – by the researcher - strain & displacement or displacement & displacement or strain & strain). The script interpolated the input values using spline interpolation and for the various specified crack locations, it calculated the crack depth ratios. The crack depth ratios beyond range (below 0.1 and above 0.6) were eliminated along with their locations and the rest were plotted against their corresponding locations. Two curves for the two given parameters (either strain & displacement or displacement & displacement) give a common point of intersection, which indicates the crack location and size. If multiple points of intersection are noted in one combination, then the other combination can be used to confirm the unique intersection point. That means for most of cases in actual situation only two sensors would be good enough to identify both the crack location and size.

A few examples of identifying crack location and size has been illustrated below:

4.4.1 Strain-Displacement Plot The first example explains the crack identification method using the slope of percentage change in difference for strain (measured at 410mm) and displacement (measured at 1300mm). Let's say both the strain and displacement sensors provide 5% change in slope value (in an actual measurement situation). By putting both the values as 5 in input dialogue box in MATLAB script, the plot shows a point of intersection having a Y value of 0.18 and X value of 910 (Figure 15). That means the crack is located at 910mm having a crack depth ratio of 0.18.

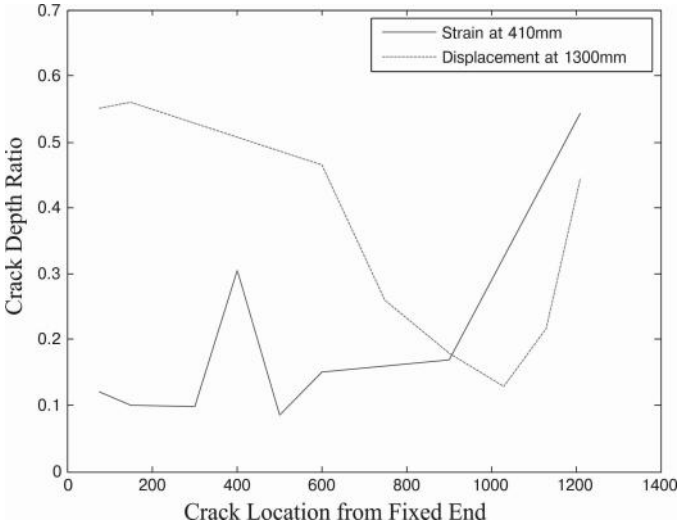

Fig. 15: Computed crack depth ratio against crack location; the point of intersection gives the size and location of the crack

4.4.2 Displacement - Displacement Plot Another way of crack identification is using the percentage change of displacement slope values (measured at 710mm and 1300mm) instead of strain changes. Now in this case let the % change values obtained (from actual measurements) be higher (for illustration), having a change of slope values of 15% at 710mm and 12% at 1300mm. The intersection shows a crack depth ratio of 0.29 to exist at 860mm (Figure 16).

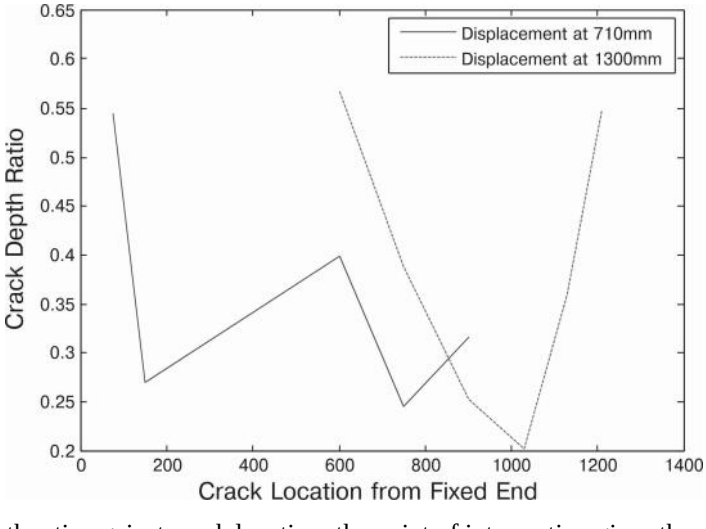

Fig. 16: Computed crack depth ratio against crack location; the point of intersection gives the size and location of the crack

4.4.3 Strain-Strain Plot Another plot was drawn using strain-strain combination having 5% change for slope values, at both the measured locations (viz., at 410 mm, and 530 mm, from the fixed end). The curves in this case showed two point of intersection; one near 400mm having a crack depth ratio of 0.3 and another is near 860mm having a crack depth ratio of 0.16 (Fig. 17). Such type of scenarios would require a third measurement location whose value would be used for cross-reference.

4.5 Difference between Bending and Circumferential Helical Crack Scenarios A significance difference was found in the crack identification method for circumferential helical crack and bending crack (analyzed earlier by Hossain and Swamidas [16]). It was found that, both for displacement and strain, the slope showed higher percentage changes in case of helical crack. Fig. 18 shows an example, where strain measurements at 410mm were plotted for both type of cracks and it can be seen that the percentage change in slopes is much more rapid in the case of circumferential helical crack than bending crack specially at later stages. Also, it was found that if the strain sensors were located near the crack location, in case of bending crack, it showed a higher percentage change. Fig.19 represents a scenario where strain sensors were located at 410mm for both type of crack at 400mm. It was found that percentage change for bending crack was up to 33.31% for bending crack whereas percentage change for helical crack was up to 10.57% only. Thus a suitable combination of slope strain-displacement change measurements and strain-displacement change measurements could be used to differentiate between the existence of bending and axisymmetric crack in the rotating shaft.

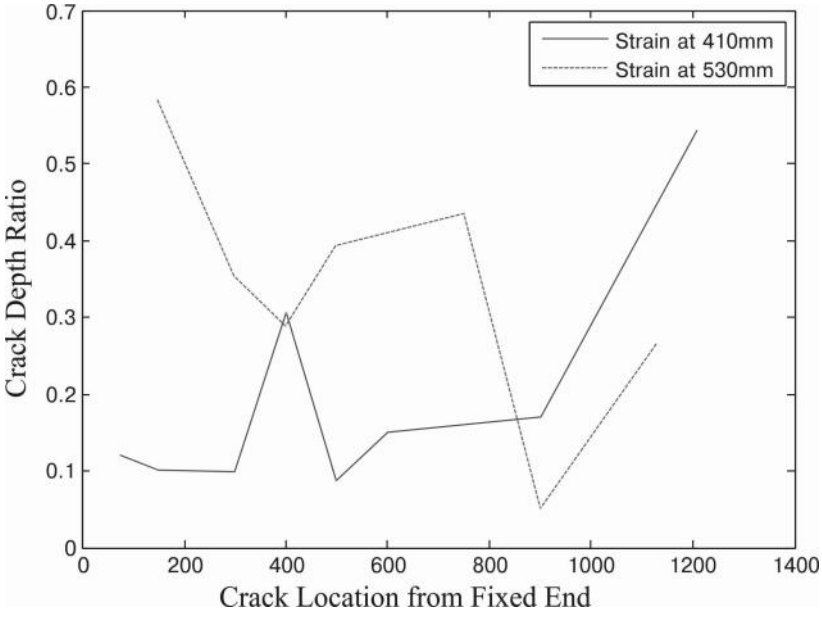

Fig. 17: Computed crack depth ratio against crack location; the point of intersection gives the size and location of the crack

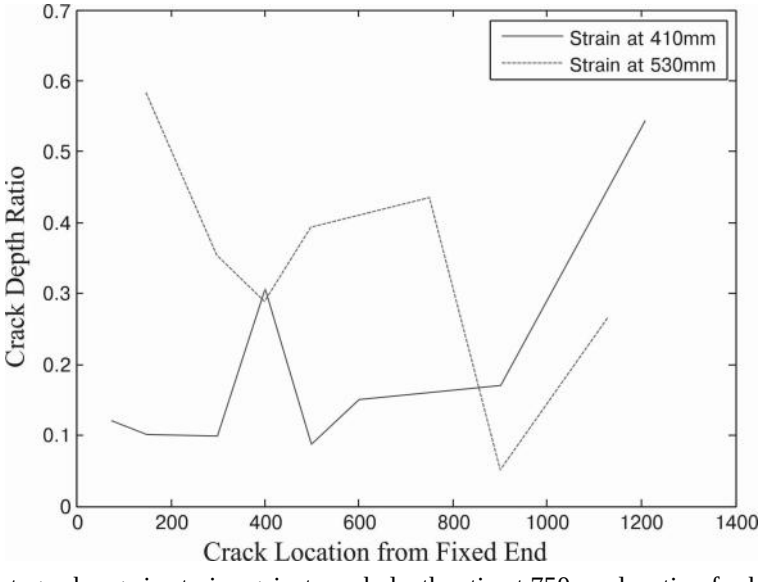

Fig. 18: Slope of percentage change in strain against crack depth ratio at 750mm location for both crack types (strain measured at 410mm)

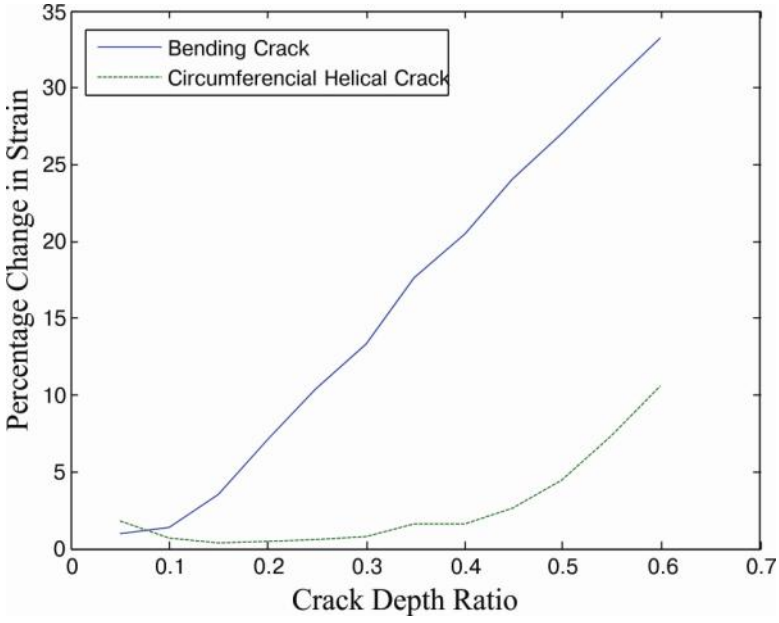

Fig. 19: Percentage change in strain against crack depth ratio at 400mm location for both crack types (strain measured at 410mm)

5.CONCLUSION

The study outlines a simple and effective way to identify the size and location of the crack in a marine propeller shaft. The following conclusions can be made based on the outcome:

a) Circumferential helical crack can be caused in marine propeller shafts due to the rotating and bending nature of the shaft; moreover, it has also been observed from earlier research studies that even the combination of the 2X-components of the rotating shaft (at the super-synchronous speed) and/or visual inspection are not very effective in identifying such cracks as part of the crack remains always closed.

b) Both the percentage changes in strains and displacements show significant changes due to the presence of the crack and thus can be used to identify crack size and location. A change of 5% in the displacement and strain values are sufficient to detect crack around a crack depth of 0.2%.

c) The slopes of percentage changes in strains and displacements are much higher than strains/displacements and show significant changes even during the earlier stage of crack growth; hence these changes can be used for early crack detection but precision in measurement is required.

d) Although strains show much higher percentage changes than displacements these changes are negligible beyond the intermediate support; hence they should be combined with at least with one displacement measurement for identifying crack in the whole shaft.

e) Crack can be detected without disassembling the whole system and for most cases two sensors are sufficient to identify cracks.

REFERENCES

1. N. Bachschmid, P. Pennacchi and E. Tanzi, *Cracked Rotors: A Survey on Static and Dynamic Behaviour Including Modelling and Diagnosis.* Springer-Verlag, 2010.

2. Bently Nevada, "Early shaft crack detection on rotating machinery using vibration monitoring and diagnostics," Tech. Rep. 270, 1988.

3. J. Wauer, "On the dynamics of cracked rotors: A literature survey" *Applied Mechanics Reviews*, vol. 43, *(1)*, pp. 13-17, January 1, 1990.

4. G. Sabnavis, R. G. Kirk, M. Kasarda and D. Quinn, "Cracked shaft detection and diagnostics: A literature review" *Shock Vib Dig*, vol. 36, *(4)*, 2004.

5. V. Rastogi and C. Kumar, "A brief review on dynamics of a cracked rotor" *International Journal of Rotating Machinery*, vol. vol. 2009, pp. 6 pages, 2009.

6. A. J. Pons and A. Karma, "Helical crack-front instability in mixed-mode fracture" *Nature*, vol. 464, *(7285)*, pp. 85 -89, 2010.

7. P. P. Milella, "Morphological aspects of fatigue crack growth and formation," in *Fatigue and Corrosion in Metals*, 1st ed.Springer, 2012, pp. 82.

8. N. Sachs. (July, 2012). *Failure Analysis Of Machine Shafts, Maintenance Technology and Asset Performance*. Available: http://www.maintenancetechnology.com/2012/07/failure-analysis-of-machine-shafts/.

9. A. Vania, P. Pennacchi and S. Chatterton, "Super-synchronous vibrations caused by transverse annular cracks in rotating machines," in *Proc. of International Conference on Surveillance-6*, Compiègne, France, pp. 1-13.

10. P. Nguyen-Duy, "Failure analysis of a hydraulic turbine shaft," in *Fractography of Ceramic and Metal Failures*ASTM International, 1984, pp. 368.

11. R. B. Hossain, R. Seshadri and A. S. Swamidas, "Identification of the size and location of A crack, using statical deformations of A marine rotor shaft with A propeller at the overhanging end," in *International Workshop on Smart Materials, Structures & SHM in Conjunction with NDT in Canada 2013 Conference & NDT for the Energy Industry*, Calgary, Alberta, CANADA, 2013, .

12. A. Tlaisi, A. S. J. Swamidas, A. Akinturk and M. R. Haddara, "Crack Detection in Shafts Using Mechanical Impedance Measurements" *Mechanical Engineering Research*, vol. 2, *(2)*, 2012.

13. M. G. Parsons, W. S. Vorus and E. M. Richard. "Added mass and damping of vibrating propellers," PhD Thesis, University of Michigan. 1980.

14. C. Shumin, A. Swamidas and J. Sharp, "Similarity method for modelling hydroelastic offshore platforms" *Ocean Eng.*, vol. 23, *(7)*, pp. 575-595, 1996.

15. P. Kohut and P. Kurowski, "Application of modal analysis supported by 3D vision-based measurements" *Journal of Theoretical and Applied Mechanics*, vol. 47, pp. 855-870, 2009.

16. R. B. Hossain and A. S. Swamidas, "Identification of Size and Location a Single Bending Crack in a Mrine Propeller Shaft using Static Parameters of Strain and Displacement," *Int. J. Eng. Sci. & Mgmnt*, 2014. (accepted)

DESIGN OF ELECTRICALLY SMALL ANTENNA FOR BIOMEDICAL APPLICATIONS USING HFSS

G. Guru Prasad*
Asst Professor
Department of Electronics and Communication Engineering
Sri Vidyanikethan Engineering College, Tirupathi
E-mail id: guru.p6@gmail.com
Mobile : 9492657579
*Correspondence author

V. R Anitha
Professor
Department of Electronics and Communication Engineering
Sri Vidyanikethan Engineering College, Tirupathi.
E-mail id: anithavr@gmail.com

T. Ramashree
Professor
Department of Electronics and Communication Engineering
Sri Venkateswara university college of Engineering , Tirupathi.
E-mail id: rama.jaypee@gmail.com

ABSTRACT

This paper introduces the design of a Electrically small rectangular patch antennas for biotelemetry applications. In the recent years the development in communication systems requires the development of low cost, minimal weight, low profile antennas that are capable of maintaining high performance over a wide spectrum of frequencies. This technological trend has focused much effort into the design of a nanostrip patch antenna. The design of antennas for communication with implants inside the human body has received considerable attention from the research community. The design of these antennas is quite challenging, as there is a limit on the amount on power that can be transmitted and also on the size of these devices. The limitation on the transmit power is due to the amount of battery power available as well as due to concerns about the exposure of the human body to electromagnetic radiation. Typically these devices are allowed to have a peak transmit power of 25 microwatts which is quite insufficient at higher frequencies especially when embedded deep into the tissue. Today these implants are being used to monitor as well as facilitate the working of various human organs, for example, as cardiac pacemakers.This paper introduces the design of a wideband rectangular patch antennas for biotelemetry applications using hfss13.0 software. The rectangular antenna is designed using FR4 material whose dielectric constant is 4.4 with thickness of 1.6mm and operates at 31.5GHz frequency. The coaxial line feeding technique is used instead of microstrip line feed because they are more practical for test purpose.

Keywords*: Electrically small antenna, Biomedical applications, FR4 substrate, probe feed, Ansoft hfss13.0*

1. INTRODUCTION

Recently there are more than thousand new cases of breast cancer were expected in the United States and more than 40 thousand women were estimated to lose their lives [1]. In 2007, 1.3 million new cases of breast cancer and 465 thousand deaths were estimated worldwide [2]. Early detection of breast cancer by regular breast screening has been shown to sharply reduce the breast cancer related mortality and increase the survival rate [3]. Despite the benefits of the regular breast cancer screening, only 66.5% women of forty years age and older conducted mammogram screening in 2005. This has been particularly due to the health risk associated with the X-ray used in mammography and its accuracy

in detecting the early breast tumors [4]. Recently, the U.S. Preventive Services Task

Force (USPSTF) has updated its guidelines, recommending a regular mammogram screening at the age of fifty and above, once every two years. This is a change from its previous recommendation of yearly screening at the age of forty [5]. This change has fueled additional debates on the health risk of X-ray mammography, its accuracy, and the merits of using it as the primary screening modality. However, the benefits of early breast tumor detection are well accepted. Thus, the development of a safer and more accurate breast scanning and imaging modality has been pursued for a relatively long period, with microwave breast imaging being one of the most viable technologies [6]. In MBI technique, an antenna transmits a microwave signal to the breast and the scattered signal is received and analyzed to extract dielectric properties of the tissues.

Another key challenge in breast cancer detection and treatment has been to design and develop a standard method that heightens efficiency coincided with nondestructive cancer psychoanalysis. The overall ideal for this innovative concept is to detect with potential benefits of adequate depth penetration via microwave imaging, while minimizing cumulative side-effects to healthy tissue due to ionized radiation. Due to the complexity that coincides with a successful methodology, these biological systems must endure heterogeneous characteristics [7]. Key functions for microwave- based breast cancer diagnosis would be (i) low health risk, (ii) the ability to detect breast cancer at a curable stage, (iii) is sensitive to tumors and specific to malignancies, (iv) involves minimal discomfort for lesion tolerability to women, and (v) provides easy to interpret, objective, and consistent results [8]. Such medical devices that posses adequate depth penetration while avoiding the use of ionized radiation and breast compression would be of great interest for malignant purposes. Further, the infrastructure of microwave breast imaging for cancer detection contains a bevy of algorithms alongside geometric configurations, which can overcome the problems associated with current methodologies.

Microwave imaging of biological compositions have developed an enormous amount of attention because of its ability to access the breast for imaging (e.g., image reconstruction algorithms, computational methods, increased computing supremacy.) MBI infrastructure consists of several decencies that conclude ex-vivo circumstances, electromagnetic (EM) signals coupled with giga- hertz signal frequencies [9]. Further, the electromagnetic phenomenon is an approach that mirrors the electromagnetic properties of breast tissue allowing for a more efficient exam. Therefore, as mentioned before, the coupling with the signals in gigahertz range are considerable because of the significant absorption and scattering that occurs during EM exposure to the breast [9]. In particular, the latter two features of self-propagating waves could lead to enormous amplification of one particular attribute, or complicated instrumentation from the need to place transmitting and receiving RF transmitters to avoid spatial resolution. For example, significant electromagnetic loss in tissue, and it's extremely high contrast with surrounding air [9]. Furthermore, the development of microwave patch transceivers (antennas) operating at 2.45 GHz is known to reduce cluttered data, producing well-localized images or real and imaginary parts of the wave numbers [10]. Concluding all of which may be etched to comply with current breast cancer research, resulting with a more promising approach.

Despite the popularity, there are several proposed ideals that could potentially become historical due to promising results via microwave imaging. Such methodologies consist of ultrasound and digital mammography, magnetic resonance imaging (MRI), position emission tomography, and electrical impedance scanning. According to previous studies, the above cutting edge portrays some success in reference to cancer detection, but in accordance to early detection and unnecessary mas- tectomies, significant approaches are in high regard. For example, MRIs, a computer aided method that uses a magnet to create detailed images of internal structures without the use of radiation. In compliance with the rest (e.g., mammograms), the above treats with radioactive techniques which could pose significant side-effects, and worsen a patient's current condition. Therefore, an under-standing of the breast tissue and skin diplomacy is documented to help one better understand how current methods detect as well as acknowledge between healthy and malignant tissue. In the field of enhancing breast detection applications, there are substantial interests in the development of new and effective approaches to demonstrate the use of microwave imaging for tumor detection. The interactions of EM and gigahertz signals are mainly being investigated for a significant and consistent contrast between malignant and other breast tissues [8].One of the major impediments of MBI technology has been a large signal refection from the breast skin. Many techniques to reducing the signal refection at the breast skin have been employed . Most of the approaches use an intermediate solution between the antenna and the breast, but no significant success has been achieved thus far. In this paper, we present the design and simulation of microwave breast imaging using 2.54 GHz signal. HFSS (ver. 13) has been used for the modeling and simulation. While, the experimental implementation of the concept is still in progress, the simulation results presented shows that the direct placement of the antenna on the breast skin can significantly increases the sensitivity of the MBI systems.

The microwave breast imaging technique utilizes the signal scattering by an object when the object is illuminated by an electromagnetic signal. The signal scattering by an object depends on various factors, including the environment, signal strength, and the material properties of the object [14]. For a given signal source and the environment, the scattered signal depends on the electrical properties of the object, especially dielectric and conductivity. This principal is utilized to detect the tumor in the breast using microwave signals. The breast tumors have very distinct electrical properties (higher dielectric permittivity and higher conductivity), which allows them to detect by analyzing the scattered signals. As shown in Figure 1, the amount of signal scattered by a breast tumor is higher than that of normal breast tissues, which can be received

by a separate antenna or the property change of the transmitting antenna due to the scattered signals, can be analyzed and utilized for the tumor detection.

2. DESIGN PROCEDURE USING HFSS

The first step in the design is to specify the dimensions of a nanostrip patch antenna. The patch conductor can be assumed at any shape, but generally simple geometries are used, and this simplifies the analysis and performance prediction. Here, the half-wavelength rectangular patch element is chosen as the array element Its characteristic parameters are the length L, the width w, and the thickness h, as shown in below Figure .

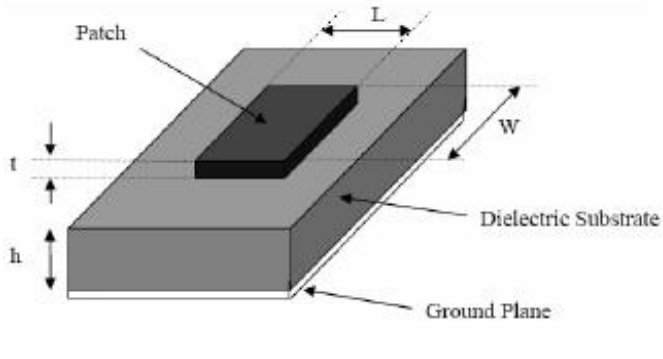

To meet the initial design requirements (operating frequency = 31.5 GHz, and height of the substrate h= 0.254) various analytical approximate approaches may be used. Here, the calculations are based on the transmission line model [7]. Although not critical, the width w of the radiating edge is specified first. In practice, the length L is slightly less than a half wavelength (in the dielectric). The length may also be specified by calculating the half wavelength value and then subtracting a small length to take into account the fringing fields [7-9]

F=31.5GHz Er=2.9(rogrer duroid) h=0.254mm

1.Create substrate(Roger Duroid)

X=-2.84 y=-3 z=0

dx=5.68 dy=6 dz=0.254

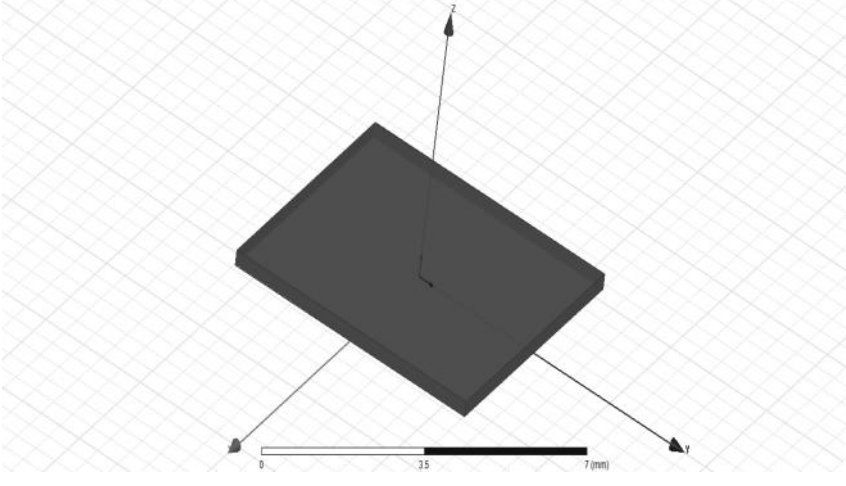

2.Create inf_gnd & cut_out assign perfect_E infinite gnd :

X=-2.84 y=-3 z=0

dx=5.68 dy=6 dz=0

cut_out:

X=0 y=0.5 z=0

dx=0.2 dy=0 dz=0

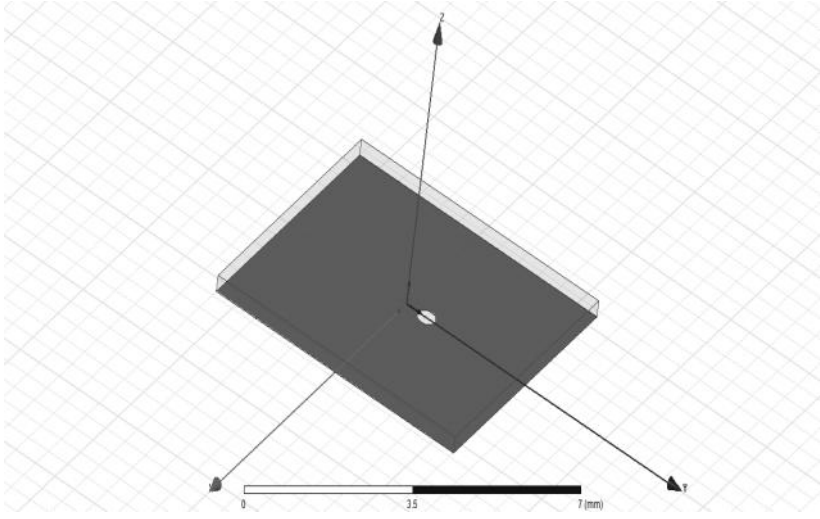

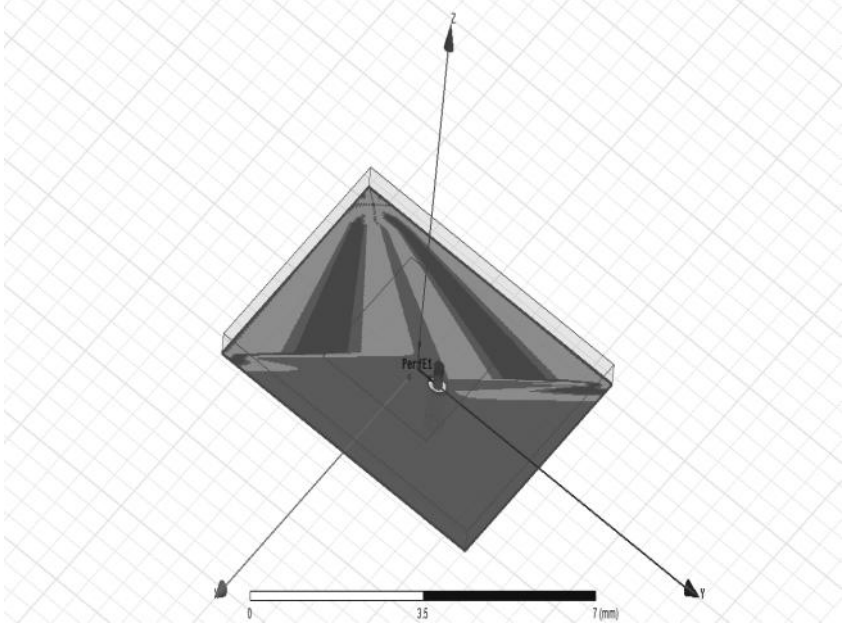

3.Create patch & assign perfect E

X=-1.69 y=-1.27 z=0.254

dx=3.39 dy=2.54 dz=0

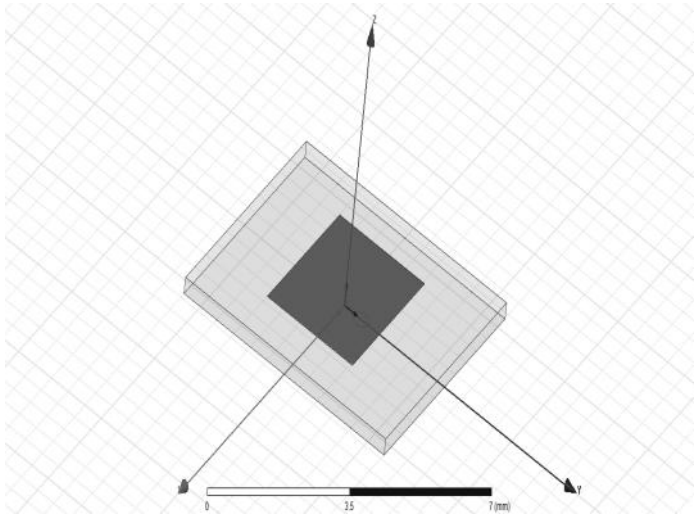

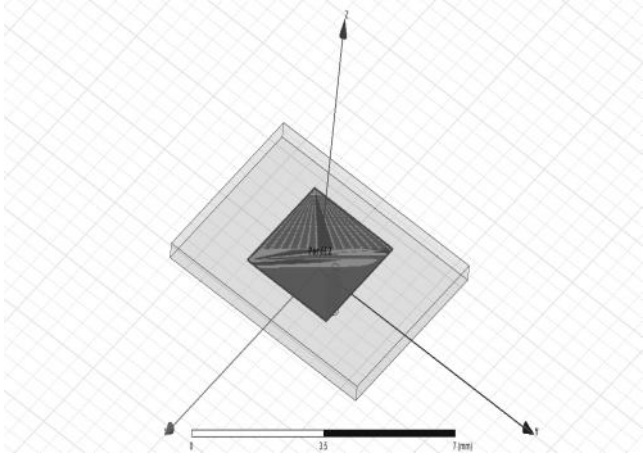

4.Create coax(vaccum)

X=0.5	y=0	z=0
dx=0.2	dy=0	dz=0
dx=0	dy=0	dz=-0.5

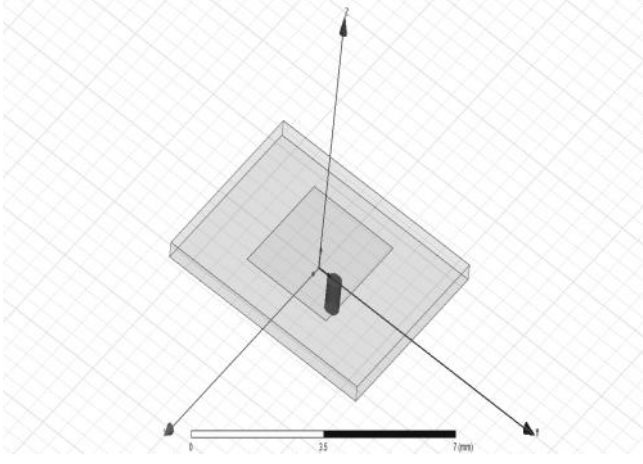

5.Create coax_pin(pec)

X=0	y=0.5	z=0
dx=0.1	dy=0	dz=0
dx=0	dy=0	dz=-0.5

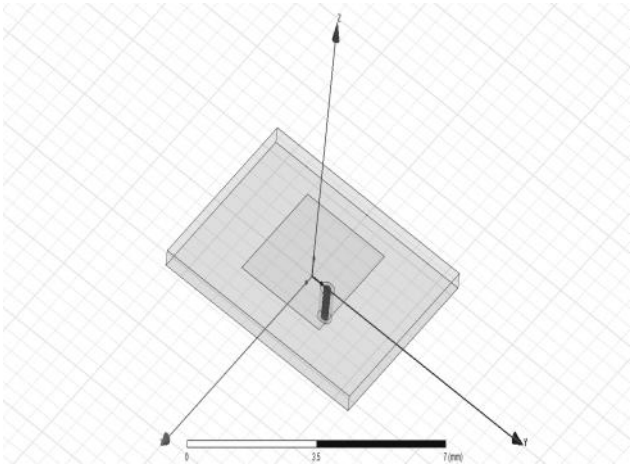

6.Assign wave port

X=0	y=0.5	z=-0.5
dx=0.2	dy=0	dz=0

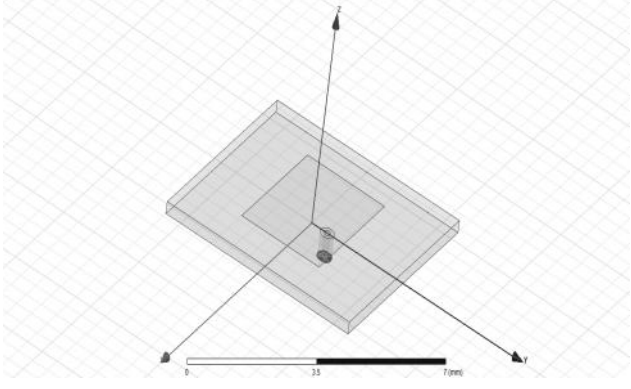

7.Create probe(pec)

X=0	y=0.5	z=0
dx=0.1	dy=0	dz=0
dx=0	dy=0	dz=0.25

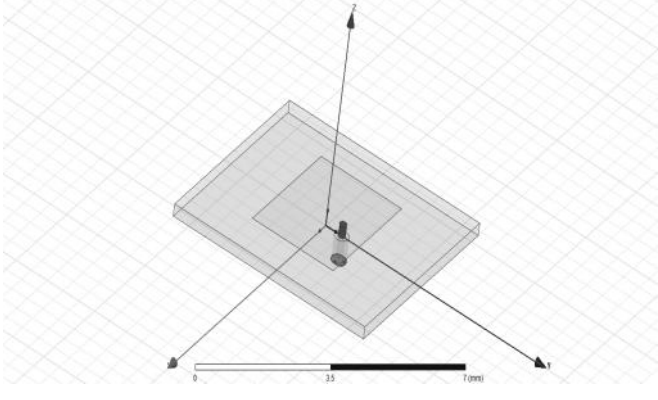

8.Creating air box & assign radiation

X=-2.84	y=-3	z=0
dx=5.68	dy=6	dz=2

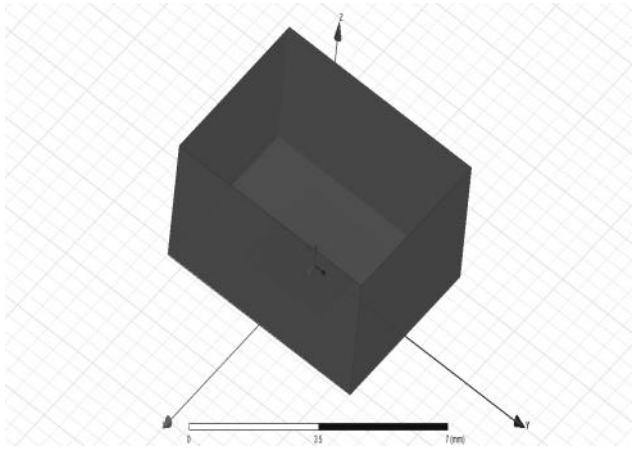

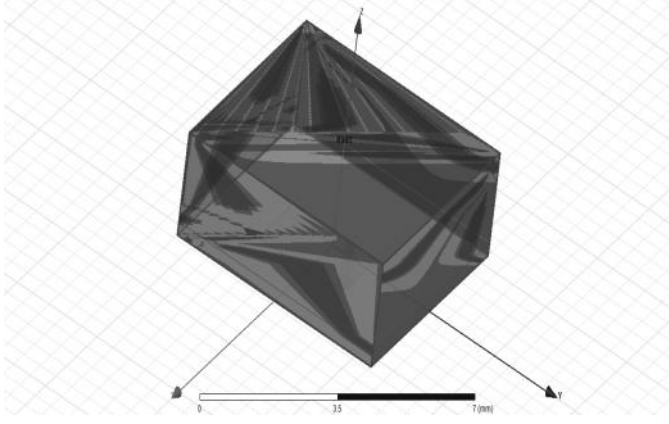

3. SIMULATED RESULTS USING HFSS

1. Return loss Measurement:

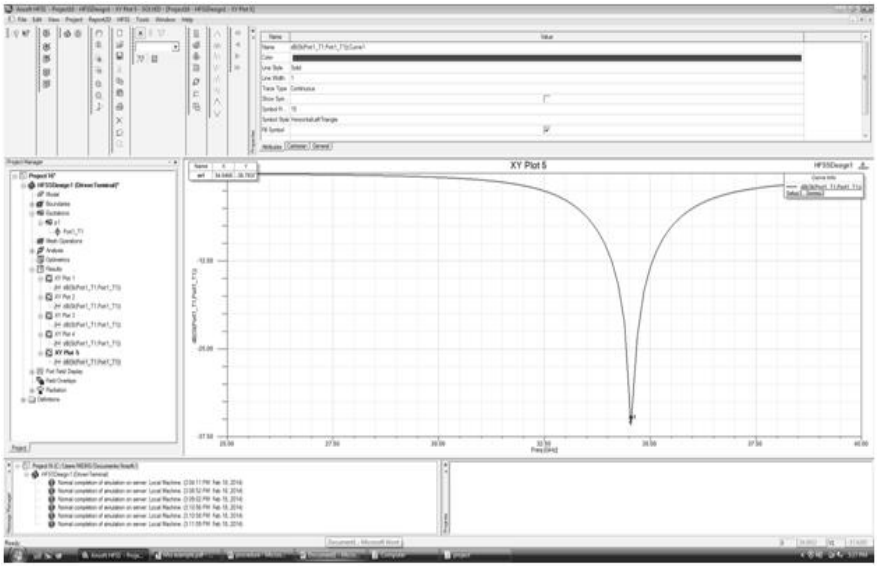

Figure: 1

From figure 1 The Return loss obtained at 34.5 GHz is -30 dB and 3dB band width is about 2 GHZ.

2 . VSWR Measurement:

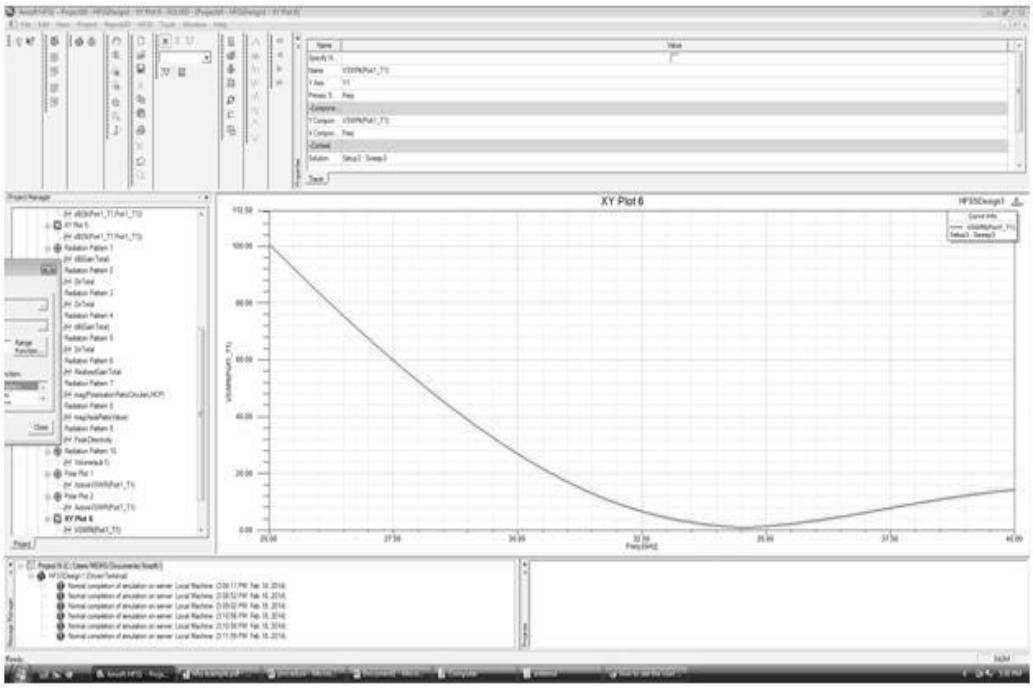

Figure 2

From the figure 2.the VSWR obtained at 34.5 GHz is 1.25

3. Directivity vs. Frequency:

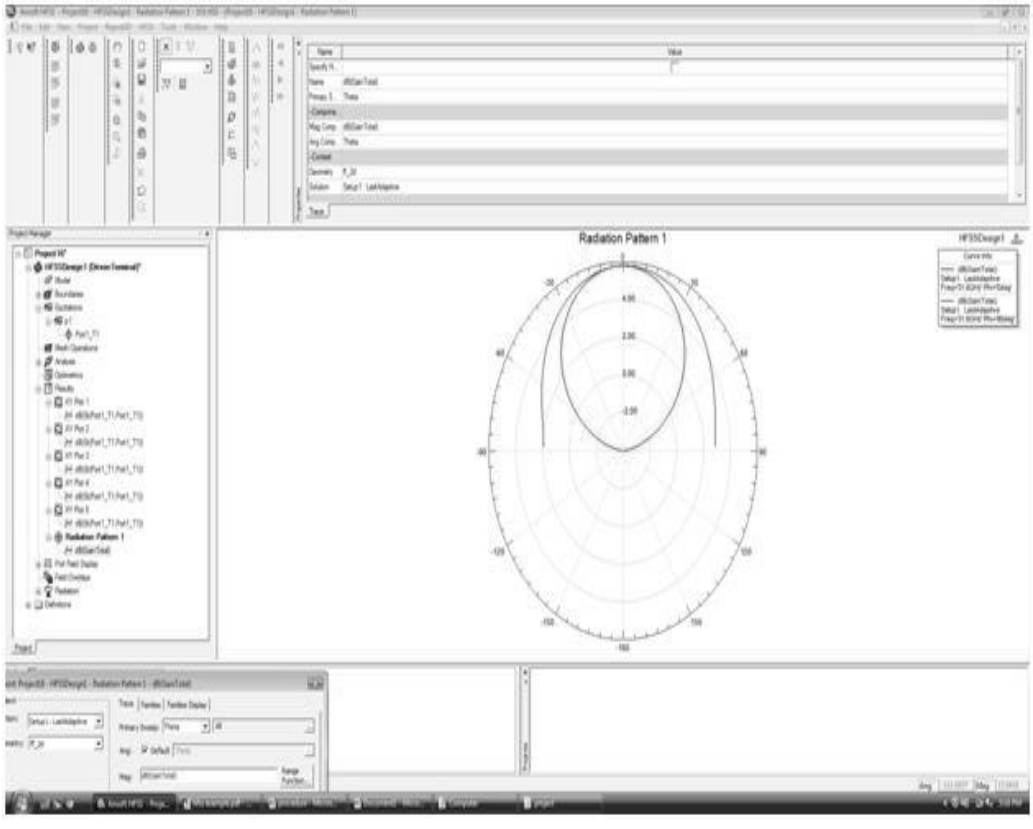

Figure 3

From the figure 3, gain obtained at 34.5 GHz is 6dBi

4. Gain vs frequency:

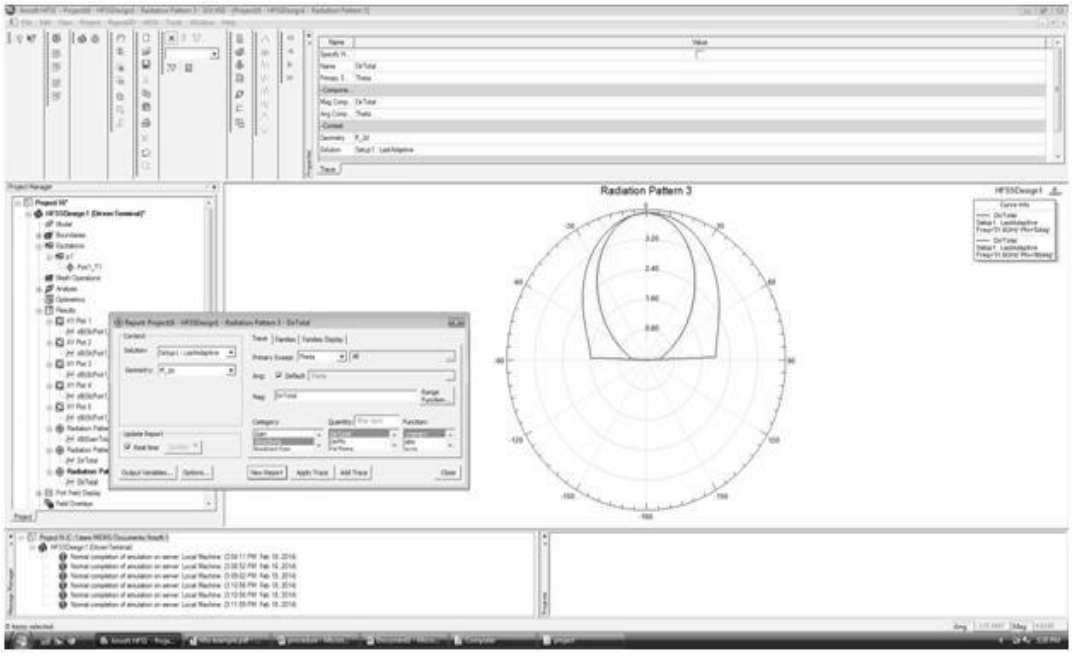

Figure 4

From the figure 4, Pi - field gain obtained at 34.5 GHz is 6 dBi

4. CONCLUSION

The simulation models developed and the results presented show that the sensitivity of the tumor detection increases when the antenna makes contact with surface of the breast as opposed to when it is placed away from the breast. It is due to the fact that, the breast skin has electrical properties comparable to the breast tumors and when the antenna is placed away, most of the received scattered signal is from the breast skin. This results in masking of the tumor scattered signal by strong skin scattered signals. For the case when the antenna is placed on the breast surface, the effect of the skin can be included in the antenna design, improving the signal strength received from the tumor.

The simulation results show that the current densities inside the tumor is about six times higher when the antenna is in contact compared to when it is placed 5 cm away from the breast, and thus this provides us a proof of the concept presented. In this paper, the prospect of an antenna that can be placed on the breast skin has been presented and a simple antenna design for the case has been discussed. However, the design of an antenna which will be attached minimally when the properties of the skin vary, the experimental implementation of such an antenna, and the complete modeling and the experimental implementation of the system are still in progress. The results obtained from the further wok will be reported in the conference presentation.

REFRENCES

1. POZAR D.M., and SCHAUBERT D.H., “Microstrip Antennas, the Analysis and Design of Microstrip Antennas and Arrays”, IEEE Press, New York, USA, 1995.
2. M. Amman, *Design of Microstrip Patch Antenna for the 2.4 Ghz Band*, Applied Microwave and Wireless, pp. 24-34, November /December 1997.
3. K. L. Wong, Design of Nonplanar Microstrip Antennas and Transmission Lines, John Wiley & Sons, New York, 1999.
4. W. L. Stutzman , G. A. Thiele, Antenna Theory and Design , John Wiley & Sons,2nd Edition ,New York, 1998.
5. M. Amman, “Design of Rectangular Microstrip Patch Antennas for the 2.4 GHz Band”, Applied Microwave &

Wireless, PP. 24- 34, November/December 1997.

6. K. L. Wong, Compact and Broadband Microstrip Antennas, Wiley, New York, 2002.

7. M.O.Ozyalcm, Modeling and Simulation of Electromagnetic Problems via Transmission Line Matrix Method, Ph.D. Dissertation, Istanbul Technical University, Institute of Science, October 2002.

8. C. Furse, R. Mohan, A. Jakayar, S. Kharidehal, B. McCleod, S. Going, L. Griffiths, P. Soontornpipit, D. Flamm, J. Bailey, I. H. Budiman, and M. Hullinger, "A biocompatible antenna for communication with implantable medical devices," in IEEE AP/URSI Int. Symp. Dig., June 2002, p. 131.

9. O. Gandhi, G. Lazzi, and C. M. Furse, "Electromagnetic absorption in the human head and neck for mobile telephones at 835 and 1900 MHz," IEEE Trans. Microwave Theory Tech., vol. 44, pp. 1884–1897, Oct. 1996.

10. R. Johnson, J. R. James, J. W. Hand, J. W. Hopewell, P. Dunlop, and R. Dickinson, "New low-profile applicators for local heating of tissues," IEEE Trans. Biomed. Eng., vol. BME-31, pp. 28–36, Jan. 1984.

11. C. M. Furse and M. F. Iskander, "Three-dimensional electromagnetic power deposition in tumors using interstitial antenna arrays," IEEE Trans. Biomed. Eng., vol. 36, pp. 977–986, Oct. 1989.

12. "Medical Implant Communications Service (MICS) federal register," Rules and Regulations, vol. 64, no. 240, pp. 69 926–69 934, Dec. 1999.

13. "Occupational and environmental health directorate," Radiofreq. Rad.Div., Brooks Air Force Base, Brooks AFB, TX, June 1996.

14. R. D. Nevels, D. Arndt, J. Carl, G. Raffoul, and A. Pacifico, "Microwave antenna design for myocardial tissue ablation applications," in IEEE AP-S Int. Symp. Dig., vol. 3, Newport Beach, CA, June 1995, p. 1572.+

MICROFINANCE AS AN ANTI POVERTY VACCINE FOR RURAL INDIA

Jaiprakash Paliwal*
RTM Nagpur University,
Raisoni Group of Institutions,
Mobile: 9881068980
Email: jaiprakash.paliwal@raisoni.net, jpi_0002@yahoo.com
*Corresponding author

Ojita Mishra
RTM Nagpur University,
Raisoni Group of Institutions,
Mobile: 7774001750
Email: ojita.mishra@raisoni.net

ABSTRACT

This paper looks at the growth and transformation of microfinance organizations (MFO) in India. At the outset, we try to define microfinance and identify the "value attributes" of microfinance, which differentiates MFO¨s from other forms of organizations. We then look at the setting of MFO¨s- identifying who promotes MFO¨s and what would be their objectives. The setting helps us to map various organizations undertaking microfinance and how central is it to the NGO¨s developmental agenda. Having chosen only those MFO¨s that have microfinance as the core, we look at the transformational experiences.

In order to understand the transformation experiences better, it is important for us to find out what are the issues that tri gger transformation. Due to the limitations the issues that trigger a movement for the microfinance operations to move away from NGO format to the mainstream format have been restricted to five major issues in all. These issues are: size, diversity of services, financial sustainability, focus and taxation.

We then move to look at the Indian experiences. In the Indian case, we argue that the transformation experiences in numbers are not significant enough. However, this research has found that there are three forms of organizations that seem to be popular in the microfinance sector – the Non-Banking Finance Companies, the Banks- both local area banks and Urban Co-operative Banks and the Co-operatives. It is also seen that the MFO¨s spins off from the NGO rather that the NGO transforming itself.

Having examined the various options for moving into the mainstream, we conclude that there is no ideal or easy path for MFO¨s to mainstream in India. This has implications for regulatory framework. We argue that there should be regulatory changes that allow smaller MFO¨s to get into more complex forms as they grow organically.

1. INTRODUCTION

From small efforts of starting informal self- help groups (SHG) to access the much needed savings and credit services in the early 1980's, the microfinance sector has grown significantly today. The fact that national bodies like Small Industries Development Bank of India (SIDBI) and National for Agriculture and Rural Development (NABARD) and devoting significant time, energy Bank and financial resources on microfinance is an indication of the reckoning of the sector.

The strength of microfinance organisations (MFO"s) in India is in the diversity of approaches and forms that have evolved over a period of time. While India has its home-grown model of SHG"s, and mutually aided co-operative societies (MAC"s) there is significant learning from other microfinance experiments.

Microfinance is an economically disadvantaged segment of the society, for enabling them to raise their income levels. India"s GDP ranks among the top 15 economies of the world. However, around 300 million people or about 80 million households are living below the poverty line, i.e. less than $ 2 per day according to the World Bank and the poorest are which earns $ 1 per day. It is further estimated that of these households, only about 20% have access to credit from the formal sector. Out of these 80 million households, 80% take credit from the informal sources i.e. local Zamindars, Chit Funds, etc. With about 80 million households below MFI"s include nongovernmental organizations (NGO"s), credit unions, non-bank financial intermediaries and even a few commercial banks.

1.1 Need of the Study The need of microfinance arises because the rural India requires sources of finance for poverty alleviation, procurement of agriculture and farms input.

Microfinance is a program to support the poor rural people to pay its debt and maintain social and economic status in villages.

As we know that India is agriculture based economy so microfinance may be a tool to empower the farmers and rural people to make agriculture profitable.

So the researchers are interested to find out the scopes of microfinance in rural India. This research paper highlights a picture of rural India and how microfinance has witnessed transformation due to rural India.

1.2 Objective of the study To analyse the growth of microfinance sector developed in India and see potential for the microfinance institutions, NGO"s, SHG"s in the market.

To analyse the structure and pattern of microfinance program in rural India by the MFI"s, NBFC"s.

To understand the issues that triggers the movement of transformation of microfinance.

To understand the importance and role of microfinance in poverty alleviation and other profitable options available.

1.3 Hypothesis Ho1: There has not been any considerable growth in microfinance with the help of MFI"s like SHG as compared to banks.

Ho2: The client outreach of MFI"s has not given any considerable contribution in the poverty alleviation over the years.

1.4 Research Methodology This is a descriptive research paper based on secondary data. Data has been collected by searching on various search engines, websites and research papers.

1.5 Issues that trigger the movement of Transformation It is evident that NGO″s have existed for a long time and never in the history has the issue of transformation come in under such a detailed scrutiny. When we examine these issues, we will be confronted with some generic issues- the ones that affect MFO″s across the world and some specific issues- these pertaining to the local laws. Below are the specific issues on transformation.

1.5.1 Size The most significant issue that triggers a transformation is growth. Both promoters and providers of microfinance encounter this- though at different stages of growth. Invariably the promoters of microfinance find that the existing institutions are unwilling to provide finance at the same pace at which the providers expect them to provide finance. Working with the attitudes of these organizations is not an easy task. For instance, MYRADA in India was working hard on linking SHG″s to the local banks and often found that the mainstream organizations have the limitations. In several cases the initiative was individual driven- and depended on the manager. In such a situation impatience creeps in and the NGO would get into action to either start lending on their own (they need not necessarily transform, but open a division for microfinance), or set up a MFO. The story appears to be familiar with several Indian MFO″s, if one looks at their gestures carefully.

1.5.2 Diversity of services Another trigger for transformation is the trigger to in the diversity of financial services offered. While in most cases credit is the trigger to start microfinance activities, MFO″s soon realizes the need to provide other support services. One service is risk mitigation. How does one ensure that the loan given does not turn bad? Microfinance sector has evolved good systems to address the issues of willful default through the mechanism of group guarantees. However the issue is also of non-willful default. This is to be addressed to a combination of self-insurance, group insurance and re-insurance. Savings is one mechanism of self insurance. However when MFO″s get into saving services, it is seen that NGO format is not suited and they have to look at transformation options.

1.5.3 Financial sustainability This issue is closely linked to the growth. Beyond a level of operations, the MFO″s will have to seek external funds. Donor money can only help start up a microfinance activity. Donors cannot be a sustainable source of funding. Then, the only alternatives left for the MFO would be to either seek investments or loans. When MFO″s seek investments or loans from ht mainstream organizations, questions will be asked on the ownership structure and capital adequacy. For a MFO to survive in a long run, it has to transform itself into a financial institution that is accountable.

1.5.4 Focus In several NGO″s, there is a need to maintain focus of the original mandate. Carrying out microfinance related activities is transaction intensive and requires a different orientation and skill sets. There is always a conflict between microfinance stream-which earns returns, and therefore could be called “commercial” and other activities that are promotional in nature. The NGO might trigger a spin off because of this. Obviously when the mandate of working in the microfinance arena is clear, the financial institutions will be working where the mainstream microfinance works.

1.5.5 Taxation In the India n context, significant issues pertaining to taxation are raised in some form. The argument is if a NGO- that is usually tax-exempted entity, carries out commercial activities (microfinance) on a large scale, then it would attract the attention of the taxation authorities. It is possible that in the process of building up a microfinance NGO, we might jeopardize the tax status of the other activities, making even grants taxable. This is one of the concerns of NGO-MFO″s. This triggers a search for an alternative where microfinance could be kept isolated.

2. REGULATORY FRAMEWORK FOR THE MICROFINANCE INSTITUTIONS IN INDIA.

2.1 Societies Registration Act, 1860: NGO″s are mostly registered under the Societies Registration Act, 1860. Since these entities were established as voluntary, not-for-profit development organizations, their microfinance activities were also established under the same legal umbrella. The main purpose is:

Relief of poverty

Advancement of education

Advancement of religion

Purpose beneficial to the community or a section of the community.

2.2 Indian Trusts Act, 1882: Some MFI″s are registered under the Indian Trust Act, 1882 either as public charitable trusts or as private, determinable trusts with specified beneficiaries or members. As per Section 6 of the Indian Trust Act 1882, the essential constituents of a trust are:

three parties – the author, trustees and beneficiary;

declaration of a trust;
certainty of the subject matter of a trust; and
Certainty of objects of the trust.

According to Section 3 of the Act, the person who reposes or declares confidence in another person, in some property for the benefits of the beneficiary, is called the „author‟ or „settler‟ of the Trust. The author is the creator of the Trust; he gives birth to the Trust. Under the Section 7 of the Indian Trust Act 1882, a Trust may be created by any person or institution competent to contract. In the context of MFIs, the author of the Trust is an individual with the noble intention of providing financial services to the poor. He arranges for funds from various sources and then deploys the funds to the Trust for the sake of the beneficiaries.

2.3 Not-For-Profit Companies registered under section 25 of Companies Act, 1956 An organisation given a license under Section 25 of the Companies Act, 1956, is allowed to be registered as a company with limited liability without the addition of the words „Limited‟ or „Private Limited‟ to its name. It is also eligible for exemption from some of the provisions of the Companies Act, 1956. For companies that are already registered under the Companies Act, 1956, if the central government is satisfied that the objects of that company are restricted to the promotion of commerce, science, art, religion, charity or any other useful purpose; and the constitution of such company provides for the application of funds or other income in promoting these objects and prohibits payment of any dividend to its members, then it may allow such a company to register under Section 25 of the Companies Act.

2.4 Nidhi Companies Section 620 of the Companies Act allows for the formation of a special type of company called „Nidhi‟ company also known as „Mutual Benefit Society‟. Certain provisions of the Companies Act have been modified under this section. Accordingly, provisions on the service of documents, issue of additional capital, annual returns, dividends, loans and remuneration to directors and winding up processes have been modified for companies recognised as Nidhi or Mutual Benefit Society.

3. A PROFILE OF INDIA

Population Profile of India

Parts of India	Total Population (in millions)	Total no. of Households (in millions)	Average household size
Rural	741.6	148.3	5.0
Urban	285.4	63.4	4.5
Total	**1027.0**	**211.7**	**4.9**

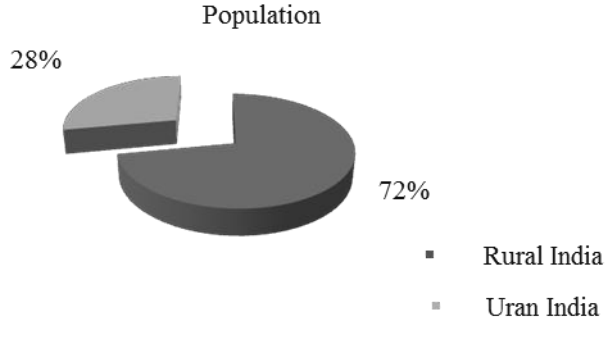

350 million Below Poverty Line
95% have no access to microfinance
56% people still borrow from informal sources
70% don‟t have any deposit account
87% no access to credit from formal sources
Annual credit demand is about Rs. 70,000 crores
95% households are without any kind of insurance
Informally Microfinance has been in practice for ages

4. MICROFINANCE IN INTERNATIONAL CONTEXT

Fueled by the attractiveness of the industry‟s social mission and strong performance of microfinance institutions (MFIs), MIVs grew rapidly over the last five years. In 2009, that growth slowed only marginally (to 22% from 28% in 2008). However, microfinance assets grew much more slowly than total MIV assets with the result that MIV liquidity increased dramatically. Interestingly, despite weak demand for funding from MFIs and against the backdrop of a worldwide recession, a number of new MIVs appeared during 2009. At the end of 2009, too many MIVs were chasing too few MFI lending opportunities.

In the MicroRate‟s1 5th annual Survey of microfinance investment vehicles (MIVs) the development of a relatively new category of funds and other intermediaries that mobilize Investments in rich countries and channel them to microfinance institutions (MFIs) in the developing world were measured. The assets of MIVs have grown from $ 1.2 billion in 2005 to over $ 6 billion at the end of 2009. It is one of the triumphs of development that such a large amount has been made available by investors for on-lending to the poor in the slums of cities like Mumbai, Lima and Addis.

4.1 Rural India and Microfinance In India for micro financing to succeed, agribusiness must empower the farmer by making agriculture profitable, not by expropriating him. For this particular purpose the farmer should be funded for their basic and small needs. Micro finance is expected to play a significant role in poverty alleviation and development. The need, therefore, is to share experiences and materials which will help not only in understanding successes and failures but also provide knowledge and guidelines to strengthen and expand microfinance programs.

The development process to escape from poverty can be achieved by breaking the viscious cycle of poverty. The ultimate aim is to attain social and economic empowerment. Successful intervention is therefore, dependent on how each individual treats the opportunity that arises in front of him.

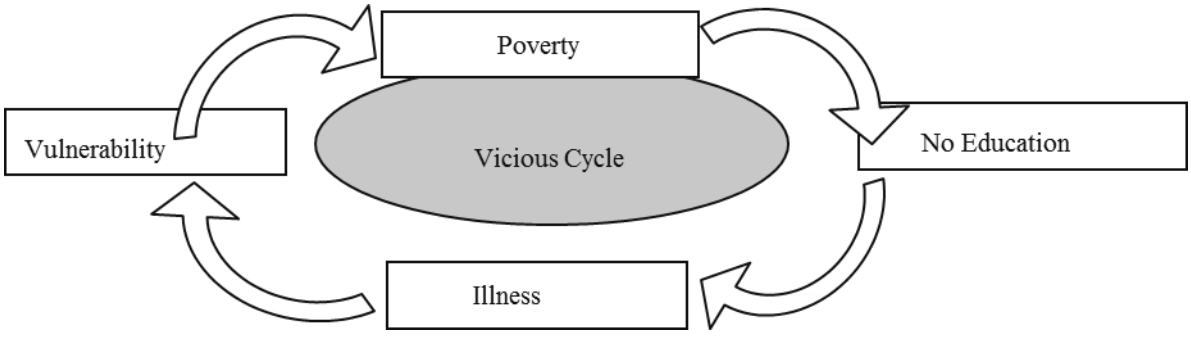

1 Fueled by the attractiveness of the industry‟s social mission and strong performance of microfinance institutions (MFIs), MIVs grew rapidly over the last five years. In 2009, that growth slowed only marginally (to 22% from 28% in 2008). However, microfinance assets grew much more slowly than total MIV assets with the result that MIV liquidity increased dramatically. Interestingly, despite weak demand for funding from MFIs and against the backdrop of a worldwide recession, a number of new MIVs appeared during 2009. At the end of 2009, too many MIVs were chasing too few MFI lending opportunities.

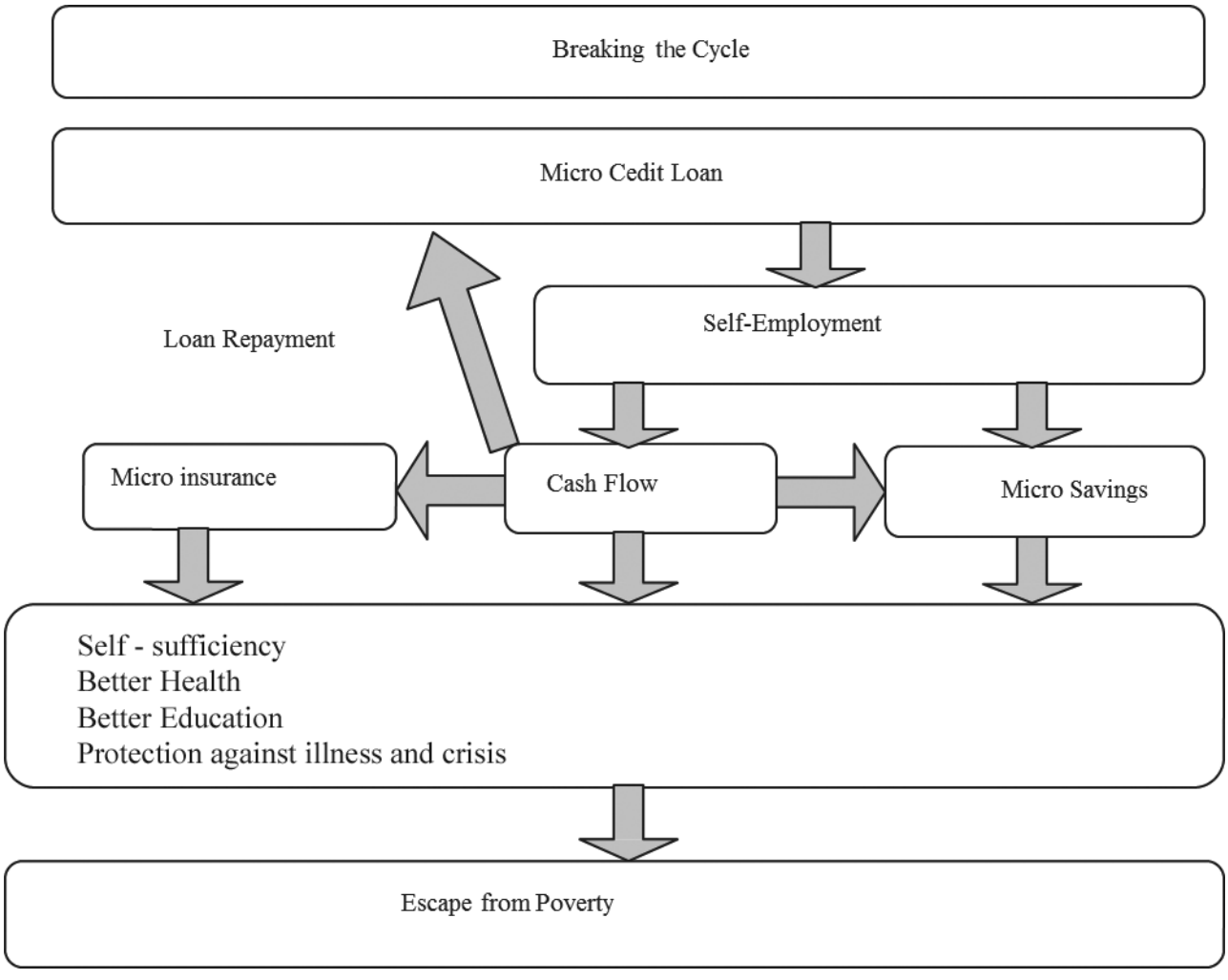

4.2 Success Factors of Microfinance in Rural India Over the last ten years, successful experiences in providing finance to small entrepreneurs and producers demonstrate that poor people, when given access to responsive and timely financial services at market rates, repay their loans and use the proceeds to increase their income and assets. This is not surprising since the only realistic alternative for them is to borrow from informal market at an interest much higher than market rates. Community banks, NGOs, grass root savings, and credit groups around the world have shown that these micro enterprise loans can be profitable for borrowers and for the lenders, making micro finance one of the most effective poverty reducing strategies.

4.2.1 For NGOs The field of development itself expands and shifts emphasis with Full of ideas, and NGOs perhaps more readily adopt new ideas, especially if the resources required are small, entry and exit are easy, tasks are (perceived to be) simple and people‟s acceptance is high – all characteristics (real or presumed) of microfinance. Canvassing by various actors, including the National Bank for Agriculture and Rural Development (NABARD), Small Industries Development Bank of India (SIDBI), Friends of Women‟s World Banking (FWWB), Rashtriya Mahila Kosh (RMK), Council for Advancement of People‟s Action and Rural Technologies (CAPART), Rashtriya Gramin Vikas Nidhi (RGVN), various donor funded programmes especially by the International Fund for Agricultural Development (IFAD), United Nations Development Programme (UNDP), World Bank and Department for International Development, UK (DFID), and lately commercial banks, has greatly added to the idea pull. Induced by the worldwide focus on microfinance, donor NGOs too have been funding microfinance projects. One might call it the supply push. All kinds of things from Khadi spinning to Nadep compost to Balwadis do not produce such concrete results and sustained interest among beneficiaries as microfinance. Most NGO-led microfinance is with poor women, for whom access to small loans to meet dire emergencies is a valued outcome. Thus, quick and high "customer satisfaction" is the USP that has attracted NGOs to this trade

4.2.2 For Financial Institutions and banks Microfinance has been attractive to the lending agencies because of demonstrated sustainability and of low costs of operation. Institutions like SIDBI and NABARD are hard-nosed bankers and would not work with the idea if they did not see a long-term engagement – which only comes out of sustainability (that is economic attractiveness). On the supply side, it is also true that it has all the trappings of a business enterprise, its output is tangible and it is easily understood by the mainstream. This also seems to sound nice to the government, which in the post liberalization era is trying to explain the logic of every rupee spent. That is the reason why microfinance has attracted

mainstream institutions like no other developmental project. Perhaps the most important factor that got banks involved is what one might call the policy push. Given that most of our banks are in the public sector, public policy does have some influence on what they will or will not do. In this case, policy was followed by diligent, if meandering, promotional work by NABARD. A seven-page memo by NABARD initially followed the policy change about a decade ago by RBI to allow banks to lend to SHGs to all bank Chairpersons, and later by sensitization and training programmes for bank staff across the country. Several hundred such programmes were conducted by NGOs alone, each involving 15 to 20 bank staff, all paid for by NABARD. The policy push was sweetened by the NABARD refinance scheme that offers much more favorable terms (100% refinance, wider spread) than for other rural lending by banks. NABARD also did some system setting work and banks Page 30 of 7 lately have been given targets. The canvassing, training, refinance and close follow up by NABARD has resulted in widespread bank involvement.

5. DATA ANALYSIS AND INTERPRETATION

The total client outreach of MFI‟s was recorded at 26.7 millions in the year 2009-2010. The growth rate of client outreach came down by 15.7 percent in the year 2011-12 as against an increase of 19.1 percent recorded in the previous year. Customer outreach has recorded a relatively higher deceleration in growth rate which suggests that MFI‟s are unable to service existing and perhaps not acquiring new customers. This trend could be attributed to the liquidity crisis which affected the MFI‟s during the year 2011-12 but remained almost unchanged for the entire year.

Figure 5.1 : SHG and MFI outreach

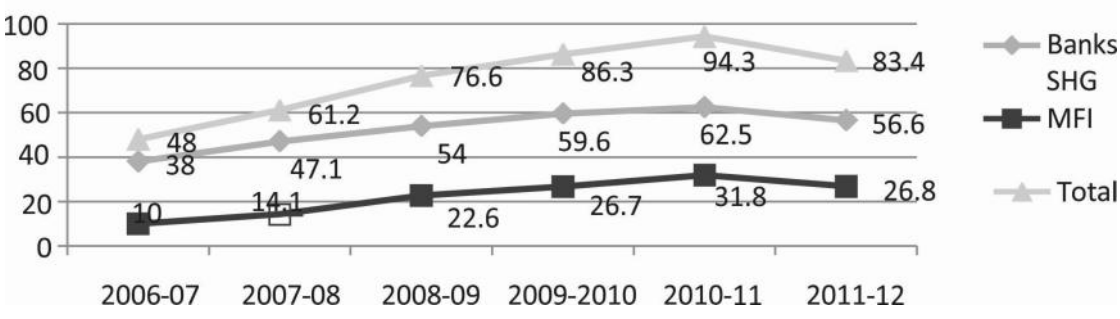

Figure 1 Source: SHG data from provisional data provided by NABARD and MFI data from Sa-Dhan. The Bharat Micro finance Quick Report 2012 and Mix Market Data

Table 5.1: Estimate of Microfinance Credit clients (millions)

	2008	2009	2010	2011
Commercial Banks (including RRB's)	41	39.2	45.2	43.3
PACS borrowers	28.5	28.7	30	31.0
SHG Members	47.1	54	59.6	62.5
MFI Clients	14.1	22.6	26.7	31.8
Total	130.7	144.5	161.5	168.6

Source: SHG data from provisional data provided by NABARD and MFI data from Sa-Dhan. The Bharat Micro finance Quick Report 2012 and Mix Market Data

The total number of microfinance sector clients stood 168.6 million as at the end of March 2011. Out of this 43.3 million were customers form Commercial Banks. This number had declined from the previous years‟ mark of 45.2 millions. SHG members were 62.5 millions while MFI clients were 31.8 millions.

Table 5.2: Short term refinance for the last five years

Short Term Refinance for the last five years

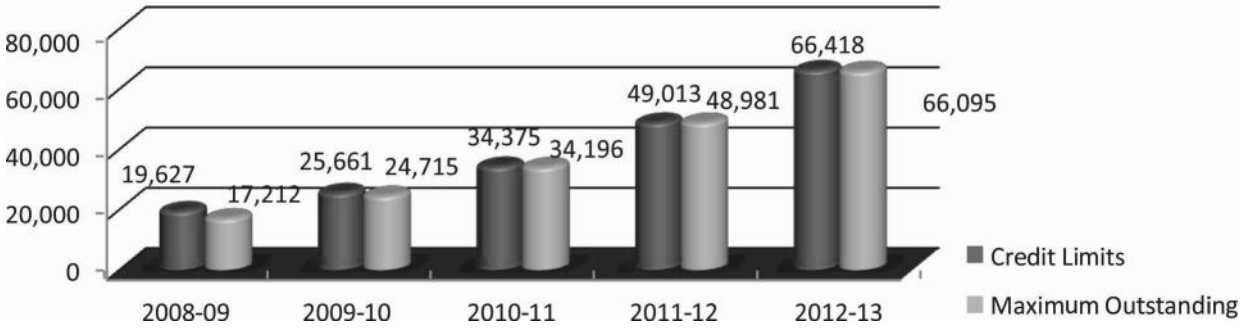

Under the short term refinance portfolio, during 2012-13, NABARD sanctioned credit limits aggregating 66,418 crore which was almost 36% higher than that of the previous year (2011-12). The short term refinance sanctioned has in fact maintained an increasing trend (more than 30% annual growth) during the last four years.

6. CONCLUSION FROM TESTING OF HYPOTHESIS

Ho1: The growth of microfinance in rural India can help in poverty alleviation.
Hypothesis rejected as the growth rate of microfinance lending is higher than that of the banks.

Ho2: The client outreach of MFI‟s has not given any considerable contribution in the poverty alleviation over the years
Hypothesis rejected as there has been considerable growth in the Microfinance credit clients over the years to contribute to the total amount.

7. FINDINGS

Considerable gap between demand and supply for all financial services and majority of poor are excluded from financial services [Source: Status of Micro Finance in India 2008-09 (NABARD)].

Savings of SHGs has increased by 46.5% in the year 2008-2009. The increased deposits in banks indicate changing trends in rural savings, where the farmer intends to retain liquidity in his assets.

Regional Rural Banks are very popular among villagers as a place to save. It has attracted nearly 70.6% savings of SHGs. The shift in investment to formal financial institutions has allowed rural consumers higher liquidity in recent years.

Commercial Bank had lead in disbursement of loans to SHG‟s during 2008 – 2009 with 49.2% followed by Co-operative banks with a share of 26% and Regional Rural Banks with a share of 20.4%.

Bankers feel that it is risky to finance poor peoples because of their creditworthiness. Commercial banks had the maximum share of outstanding bank loan to SHG‟s with a share of 40.7% followed by cooperative banks with a share of 18.4% and regional rural banks with a share of 18.2%.

Outstanding bank loan to SHG are due to high transaction costs.

8. CONCLUSION

The potential for growing micro finance institutions in India is very high. Major cross-section can have benefit if this sector will grow in its fastest pace. Financial institutions will need to educate villagers on the ease of procedures for availing loans and at reasonable rates of interest. The repayment schedule will have to be designed to suit the seasonality of rural income (e.g. availability of money after harvest). Nationalized banks have not encouraged loans for SHGs for lack of creditworthiness, but these banks have excellent reach to SHGs so that they should come forward

to exploit this business opportunity. Similarly, the lakhs of SHGs can be trapped by nationalized banks to encourage monthly savings among members. NABARD is working for the 360-degree development of rural India. Annual growth rate of about 20% can be achieved during the next five years. As the data has not been updated on the websites the data could be analysed only till the year 2013. Being a descriptive paper the data is dependent on the availability on websites the source of which cannot be reliable.

Due to certain limitations only five attributes that trigger the transformation of microfinance were analysed.

REFERENCES

Print Publications

1. David Roodman (2011). Due Diligence: An Impertinent Inquiry into Microfinance.

2. Micro finance: Perspectives & Opertaions. Macmillan education, (2012).

3. Jha, A.S., Kulshrestha, S., & Chauhan, R. (2009). *Research Methodology*. New Delhi: APH Publishing Corporation.

4. Sriram M. S. and Rajesh Upadhyayula, (2002), "*The Transfomation of Micro Finance in India: Experiences, Options and Future*"

5. Manish Kumar, Narendra Singh Bohra and Amar Johari, (2010), International Review of Business and Finance, *Micro-Finance as an Anti Poverty Vaccine for Rural India*, ISSN 0976- 5891 Volume 2 Number 1.

MEDICAL TOURISM: A STUDY OF MEDICAL TOURISTS IN NATIONAL CAPITAL REGION

Manjula Chaudhary
Senior Professor
Department of Tourism and Hotel Management
Kurukshetra University, Kurukshetra

Arpita Agrawal*
Asst. Professor
Department of management studies
Sikkim Manipal University, Bangalore
Email: Arpita_agl@rediffmail.com
Tel: 9632244021
*Corresponding author

ABSTRACT

Thomas Friedman said "the world is flat". National boundaries are diminishing and the consumers want the best value for their money. They are accepting foreign products and services more easily. Even the conservative service sectors health services are open to foreign nationals. This paper tries to analyse the state of medical tourism and the factors causing medical tourism in India in National Capital Region. The data is collected from foreign patients visiting NCR for treatment and their opinion these factors is obtained. Factor Analysis is conducted and the results show that there are mainly six factors which affect medical tourism. These factors are hospital facilities, communication during treatment, easy entry in the country, good quality treatment, low cost and quick access.

Keywords: *Medical tourism, foreign patients, health tourism, medical travel, trade in health services*

1. INTRODUCTION

Globalization is influenced by a number of forces which may promote or limit it. These could be technological developments, political influences, and economic pressures, changing ideas, and increasing social and environmental concerns. (Woodward, Drager, Beaglehole & Lipson, 2001)[1]. Globalization in itself may have various impacts on an economy. On one hand it may create benefits such as trade liberalization and technology transfer which increases efficiency, welfare and health of the economy. But premature, rapid and unconditional globalization may worsen the condition of an already weak economy (Cornia, 2001)[2]. The impact of globalization on health sector can be positive when the potential gains like advance technology or monetary benefits are transferred to health system and individuals' healthcare.

Carrera & Bridges (2006)[3] defined health tourism as "the organized travel outside one's local environment for the maintenance, enhancement or restoration of an individual's wellbeing in mind and body". A subset of this is medical tourism, which is "the organized travel outside one's natural healthcare jurisdiction for the enhancement or restoration of the individual's health through medical intervention".

Crooks, Kingsbury, Snyder & Johnston (2010)[4] identified four themes for study on medical tourism based on the literature as decision-making (e.g., push and pull factors that operate to shape patients' decisions); motivations (e.g., procedure-, cost-, and travel-based factors motivating patients to seek care abroad); risks (e.g., health and travel risks); and

first-hand accounts (e.g., patients' experiential accounts of having gone abroad for medical care). They also found a dearth of empirical work (only 5 out of 291 articles studied). They concluded that there is a scope of research on many areas including the use of multiple information sources by patients before deciding upon medical tourism; examining how patients understand the risks of care abroad; gathering patients' prospective and retrospective accounts; and the push and pull factors, as well as the motives of patients to participate in medical tourism.

Horowitz & Rosenweig (2007)[5] pointed that medical tourism is becoming popular day by day. The reasons include no or less insurance coverage, plastic or cosmetic surgery, low cost, timely care, unavailability or restriction by legal system of a particular treatment, privacy, newly developed procedures not approved by regulatory agencies or the opportunity of an exotic vacation along with treatment.

Helble (2011)[6] assessed the implications of medical travel on public health systems and access to healthcare. The paper stated there is lack of statistics and common methodology of data collection in different countries. Hence the number of medical travellers is not known. It also discussed the push and pull factors for medical travel including globalization, better transport services, waiting lists, unavailability of treatments, quality of healthcare, cost and legal issues. There are various implications of such travel both on sender and receiver countries. For sender countries, in case of lack of insurance or long waiting period, medical travel helps in clearing backlogs and supports local healthcare system. But it may also create an underdeveloped healthcare system and shortage of health workers who may move to other countries for better growth. Continuum of care is another issue and sometimes doctors in sender countries are not willing to correct the malpractice done by other countries. For receiving countries, the revenues from medical travellers may be used in developing better health infrastructure which will help the locals also. On the other hand, the growing demand due to medical travellers may also increase the prices of healthcare which will adversely affect the local population. There may be more opportunities for health workforce which may reduce brain drain to developed nations but this may also lead to internal brain drain that diverts resources from public to private sector. Human body resources and organs typically more available in poor countries is another cause of ethical concern for receiving countries.

Woodman (2008)[7] suggests that cost saving, quality healthcare, treatments not covered under insurance, specialty treatments, shorter waiting periods, more inpatient friendliness and the lure of new and different are the main factors for growth of medical travel. While compiling the experiences of medical travellers he found that there is lack of reliable data and information sources.

Chaudhary, Prakash, Tyagi & Devrath (2011)[8] reported that 'mere patients' are the major segment for Indian medical tourism. The main source market is low GDP countries of Africa and Middle East. As a country, policy makers must consciously decide which segment to target and position India as medical tourism destination accordingly. Deployment of resources needs to be in line with stated position.

2. WHY MEDICAL TOURISM

Medical tourism provides a cost effective yet modern sophisticated healthcare in developing countries. There could be various issues involved in such travel ranging from cost to quality, availability to timeliness, and insurance coverage to legal matters.

When a patient travels to a developed country for treatment it is for better quality or availability of treatment. But when a patient travels to developing nation, there could be many motivational or compulsive forces.
The Renub Research report[9] titled "Asia Medical Tourism Analysis and Forecast to 2015" provides the current status and future outlook of Asia medical tourism market survey analysis. According to this report, Asia medical tourist number of arrivals is expected to cross the figure of 10 Million numbers by 2015. Asia medical tourism market is expected to double by 2015 from its current market in 2011. The report states that out of 7 countries (Thailand, India, Singapore, Malaysia, Philippines, South Korea and Taiwan), 3 countries (Thailand, India and Singapore) are expected to control more than 80% market share in 2015.

3. OBJECTIVES

The objectives of the study were selected after analysis of the medical tourism industry through study of existing academic literature, websites of Ministry of Tourism, medical facilitators and hospitals and discussion with experts. The objective of the study include:

- To find out the factors affecting the growth of Medical Tourism in NCR.
- To examine the role of Government in promoting Medical Tourism.

4. DATA COLLECTION AND SAMPLE SELECTION

The study is confined to National Capital Region (includes Delhi, Ghaziabad, Noida, Gurgaon and Faridabad). Delhi is the capital of India and well connected with other countries of the world. It has a good infrastructure and renowned hospitals. It has various tourists' places at short distances. Hence the NCR seemed to be an appropriate selection for the study. The sample elements of this study included 177 medical tourists visiting NCR for treatment.

For this study both primary and secondary data were used. The questionnaire was designed for foreign patients visiting NCR for treatment. Only Inpatients which means those patients who were admitted to the hospital for the treatment were considered. The questions asked in the questionnaire were pertaining to the factors which are important while choosing a destination for medical tourism and how satisfied foreign patients were on those factors. This was measured on a 5 point Likert scale. Apart from this some demographic questions were included.

5. DATA ANALYSIS

A survey of 177 foreign patients was made to understand their satisfaction level on the various factors related to medical tourism in India. The twenty one factors used were identified based on secondary data. These are Low cost of treatment, Cost including travel, Less waiting time, Connectivity of countries, Good quality of overall treatment, Competent doctors and paramedical staff, Good quality of medical treatment, clinical infrastructure, Easily available visa tour operators assistance, simple documentation, privacy and confidentiality, sensitivity of the daily care staff, nursing staff knowledge and skill, timely nursing care, doctor's competence, timely availability of doctors, medical staff communication, non-medical staff communication, good food, arrangement for accomplice, connectivity to home country, sharing of information by doctors and quality of accommodation. These were taken as variables and responses were collected on five point. Likert scale ranging from highly satisfied represented through the score 5 to highly dissatisfied at 1. Factor analysis was used on the data obtained. The Cronbach alpha reliability analysis (Table 2) for the data was 0.878 which is considered to be acceptable for internal consistency.

Table2: Reliability Statistics

Cronbach's Alpha	Cronbach's Alpha Based on Standardized Items	N of Items
.878	.883	21

As shown in table Kaiser-Meyer-Olin measure (Table 3) of sampling adequacy was found to be equal to 0.717 that indicated goodness of sample being higher than 0.05. Bartlett's test of sphericity for the data provided a value of 0.00 less than 0.05 and supported the validity of the data for factor analysis.

Table 3: KMO and Bartlett's Test

Kaiser-Meyer-Olkin Measure of Sampling Adequacy.		.717
Bartlett's Test of Sphericity	Approx. Chi-Square	2.348E3
	Df	210
	Sig.	.000

The communalities of all factors are higher than 0.5. Hence there is no need to remove any factor from factor analysis.

An exploratory factor analysis was done on 21 variables to reduce the number of variables and condense them into factors. The variables loaded into 6 factors with eigen value more than 1 and the total variance explained being 71.82 % which is considered good (table 4).

Table 4: Total Variance Explained

Component	Initial Eigenvalues			Extraction Sums of Squared Loadings			Rotation Sums of Squared Loadings		
	Total	% of Variance	Cumulative %	Total	% of Variance	Cumulative %	Total	% of Variance	Cumulative %
1	6.929	32.993	32.993	6.929	32.993	32.993	4.966	23.650	23.650
2	2.509	11.948	44.941	2.509	11.948	44.941	2.352	11.202	34.851
3	1.823	8.682	53.624	1.823	8.682	53.624	2.131	10.146	44.998
4	1.635	7.785	61.409	1.635	7.785	61.409	2.127	10.130	55.128
5	1.160	5.523	66.932	1.160	5.523	66.932	2.010	9.572	64.700
6	1.027	4.888	71.820	1.027	4.888	71.820	1.495	7.120	71.820
7	.970	4.618	76.438						
8	.899	4.281	80.719						
9	.716	3.408	84.127						
10	.614	2.926	87.053						
11	.534	2.543	89.596						
12	.451	2.148	91.744						
13	.391	1.862	93.606						
14	.302	1.439	95.045						
15	.228	1.087	96.132						
16	.198	.943	97.075						
17	.171	.814	97.889						
18	.159	.757	98.646						
19	.118	.564	99.210						
20	.089	.425	99.635						
21	.077	.365	100.000						

Table 5: Rotated Component Matrix[a]

Table 5: Rotated Component Matrix[a]

	Component					
	1	2	3	4	5	6
Timely nursing care	**.824**	.303	.055	.186	.023	-.039
Non-medical staff communication	**.808**	.157	.200	-.031	.086	.107
Sensitivity of daily care staff	**.803**	.274	.262	.013	-.096	-.096
Arrangement for accomplice	**.779**	-.022	-.045	.205	.092	.170
Quality of accommodation	**.728**	-.201	.306	.045	-.119	-.218
Nursing staffs knowledge and skill	**.652**	.336	-.016	.159	.207	-.292

Good food	**.646**	.201	.126	.120	.220	.219
Privacy and confidentiality	**.611**	.346	.078	-.093	.181	.340
Sharing of information by doctors	.095	**.784**	.177	-.011	.000	.107
Medical staff communication	.454	**.657**	.046	.263	-.059	.034
Timely availability of doctors	.452	**.606**	.111	.271	.012	-.188
Tour operators assistance	.201	-.002	**.882**	.148	-.036	-.024
Simple documentation	.162	.328	**.723**	.084	.045	.343
Easy visa	.161	.388	**.621**	-.414	.084	.079
Good quality of medical treatment	.089	.132	-.125	**.790**	.237	.106
Clinical infrastructure	.218	.075	.219	**.724**	.173	.071
Doctors competence	.197	.366	.265	**.379**	-.182	-.276
Overall cost of Treatment	.051	-.010	.000	.059	**.947**	.047
Low cost of Treatment	.158	-.019	.003	.283	**.861**	.164
Less waiting time	.003	.121	-.006	.530	-.063	**.748**
Connectivity to home country	.070	-.052	.186	-.036	.268	**.542**

Table 5 loads the six factors that emerge after exploratory factor analysis. The rotated component matrix shows the convergence of the twenty one factors into six using varimax rotation.

The factor extraction (Table 6) with variables for each factor further explains the important factors and corresponding variables. These factors are named according to the variables included in that factor.

Table 6: Factor Extraction Table which is shows the variables in each factor with corresponding loading and percentage of variance

Factors	% of Variance	Factor Interpretation	Variables Included in the factor	Loadings
F1	23.650	**Hospital facilities**	Timely nursing care Non-medical staff communication Sensitivity of daily care staff Arrangement for accomplice Quality of accommodation Nursing staffs knowledge and skill Good food Privacy and confidentiality	**.824** **.808** **.803** **.779** **.728** **.652** **.646** **.611**
F2	11.202	**Communication during treatment**	Sharing of information by doctors Medical staff communication Timely availability of doctors	**.784** **.657** **.606**
F3	10.146	**Easy entry in the country**	Tour operators assistance Simple documentation Easy visa	**.882** **.723** **.621**
F4	10.130	**Good Quality treatment**	Good quality of medical treatment Clinical infrastructure Doctors competence	**.790** **.724** **.379**
F5	9.572	**Low Cost**	Overall cost of Treatment Low cost of Treatment	**.947** **.861**
F6	7.120	**Quick access for treatment**	Less waiting time Connectivity to home country	**.748** **.542**

The above table shows the factors affecting the medical tourism in NCR.

6. CONCLUSIONS

Objective 1: *To find out the factors affecting the growth of Medical Tourism.*

As explained above in the Table 6, there are six important factors affecting the medical tourism in NCR. These are hospital facilities, communication during treatment, easy entry in the country, good quality treatment, low cost and quick access.

Hospital facilities -The facilities in the hospital are a major attraction for the patients as the patients relate it to the quality and comfortable stay in the hospital. It includes the quality of nursing care as well as daily care staff. The accommodation provided and the quality and taste of food are also important for patients and affects their satisfaction level. Various hospitals in NCR are providing additional facilities to foreign patients including special food and foreign language translators to lure them. VIP lounges, deluxe hospital rooms, affiliations with hotels for special discounted rates and low cost meal plans are provided by hospitals.

Communication during treatment -As patients come from different countries with different languages, communication becomes a challenge for them. Hence good communication skills of medical staff is very important so that the patient can discuss their problems with them. It is also important to share the information related to treatment with them. This also helps in making doctors aware about the problems of patients and doctors are available on time when required by the patients. The patients can take direct phone numbers of doctors and communicate with them.

Easy entry in the country -Since patients are required to obtain visa for taking treatment in another country, it is important for any country to simplify the visa rules in order to promote medical tourism. Government of India provides Medical Visa or M-Visa to foreign patients for taking treatment in India. Simple documentation and tour operator's assistance are also important for the growth of medical tourism in India. The Indian government has amended the visa norms for foreign tourists by extending the visa-on-arrival facility to 180 countries vs. 11 countries currently (to be implemented from Oct-14), which we believe would be a positive for medical tourism.

Good Quality treatment -The basic purpose of medical travel is good quality treatment. Hence the quality of treatment, clinical infrastructure and doctor's competence forms a major factor for medical tourism. Hospitals are investing in infrastructure and offering attractive salaries to qualified doctors in order to build a brand name in medical tourism. The medical tourism destination hospitals make sure they provide best quality treatment and care to foreign travellers. Not only this some treatments like the hip resurfacing which was now allowed till recently in US can be done in Asian countries where it is a routine and hence superior.

Low Cost - One of the main reasons for leaving the home country and going abroad for treatment is low cost of treatment in medical tourism destination. India is providing high quality treatment at the lowest cost and this a major attraction for foreign patients. India is receiving many patients from African and Middle Eastern countries. For these low income countries, cost is a major concern. When they compare cost of treatment in India and other developed countries, India proves to be a very cost effective destination with good quality.

The cost of medical procedures is very high in developed nations. It is perceived that this is due to better quality and advance technology. If the person has taken insurance, the insurance companies cover this cost. Hence the premium charged by these insurance companies is also high. But if the person has not taken insurance or a particular procedure is not covered under insurance like dental or cosmetic, it becomes very difficult for the person to pay from his own pocket. So he starts looking for cheaper options and medical tourism proves to be a worthwhile choice for him. The doctors abroad are well qualified and may be trained or worked in developed countries. The hospitals catering to medical tourists also have state of art technology and infrastructure. Therefore the risk is less and savings are huge. In fact the same dental or eye surgery can be done in in a fraction of the cost in some countries leading to savings up to 90%.

According to a medical tourism market report (2014)[10], patients travelling abroad can save up to 85% of the cost of a procedure by travelling abroad. The report also mentions that India is one of the highest quality and lowest cost destination.

Table 7: Cost comparison of medical tourism destinations

PROCEDURE	INDIA	THAILAND	SINGAPORE	MALAYSIA	COSTARICA	UAE	USA
Heart Bypass	7,000	22,000	16,300	12,000	24,100	40,900	83,514
Heart valve replace-ment with bypass	9,500	25,000	22,000	13,400	30,000	50,600	87,895
Hip Replacement	7,020	12,700	1,200	7,500	11,400	46,000	35,783
Knee Replacement	9,200	11,500	9,600	12,000	10,700	40,200	33,273
Face Lift	4,800	5,000	7,500	6,400	4,900	n/a	10,046
Lap. Gastric Bypass	9,300	13,000	16,500	12,700	n/a	n/a	32,648

Note: This is an indicative cost in USD. Actual cost of treatment may change depending on patient's medical condition.

Source : http://www.mynriclub.com/site/Medical-Tourism/Cost-comparison-Medical - Treatment - or - Surgery - in - India retrieved on 29th August, 2013, and http://www.arzoo.com/uk/medicalTourismOther.do?pr=XDE987SE retrieved on 29th August, 2013

Insurance plays an important role as a deciding factor in medical tourism. But the insurance companies do not cover medical tourism and do not pay for it. According to Reese (2007)[11] for the more than 44 million uninsured and millions more underinsured in USA, overseas care represents an affordable alternative worthy of consideration. But employers are still hesitant to make the first move for covering overseas care due to legal issues. Hence people who are covered or partially covered may not want to travel for healthcare.

It is possible to stay in world class hospitals with best facilities for a longer duration also as the cost is very less compared to home country hospitals. This allows patients to take the recuperative therapies also in the hospital if required.

Quick access for treatment - In many European countries like United Kingdom, Spain and Italy, and Canada, the health system is governed by Universal Healthcare. It is a system where the healthcare is funded by the Government either fully or partially. Different models are adopted by different countries for providing this. It could be a combination of public and private contributions. It could also be a completely public funded healthcare system like the NHS (National Health Service) for England.

The NHS provides easily accessible, free healthcare to all residents at the point of delivery depending upon the need and urgency of treatment. It is not related to the capacity of the resident to pay. Due to this, patients have to wait for their turn to obtain healthcare. They even have to wait for a specialist appointment. There are the patients who have long waiting queues in their home country and they want an early treatment. For instance, in US some war veterans who get free treatment under Veterans Administration Act have to wait for treatment due to long queues. In UK the fertility treatment may take a long time and if the waiting period is also very high, it may result in loss of important fertility time period in couples. Some other established procedures may have a waiting time of two years also. Patients feel it is better to pay from their pocket and get relief from pain, frustration and anxiety. Hence they look for overseas medical treatment. The treatment in India is quick with no waiting period. India is also connected to most of the countries which is an important factor for patients suffering from pain and illness.

Objective 2- To examine the role of Government in promoting Medical Tourism.

The Ministry of Tourism, Government of India is promoting medical tourism through numerous initiatives. It acts as a facilitator for supporting the private players in this industry.

While quoting from a McKinsey study commissioned by the CII, Mr Vayalar Ravi, Union Minister for Overseas Affairs, Government of India, highlighted that the health tourism industry in India could become a US$ 5 billion business by 2015.

With the finest and experienced specialists and technological edge along with latest equipment and state-of-the-art infrastructure, Indian health tourism industry is gaining momentum. Some of the initiatives taken by the Ministry of tourism to encourage medical tourism are:

1. **Medical Visa**: Indian government provides medical visa to the foreign patients visiting India for treatment. The initial period for such a visa may be up to a period of one year or the period of treatment whichever less, which can be extended for a further period up to one year. The documents proving the need for medical treatment are to be obtained from a registered medical institution or doctor for obtaining M-visa. The guidelines are attached as annexure.

2. **Market development scheme:** Under this scheme, the approved medical tourism service providers get some financial aid from the Ministry of tourism subject to some terms and conditions. This approved service providers can be the medical tour facilitators or the hospital representatives with accreditation.

3. **Trade fairs:** An exclusive exhibition space at ITB Berlin (Internationale Tourismus-Börse Berlin) which is the world's leading travel trade fair. This helps to position Indian medical tourism industry well in the international forum. A dedicated space of 4 sq m was allotted to medical fraternity at ITB Berlin for this.

4. **Road shows**: Road shows are conducted in various countries as discussed with various stakeholders of the industry to promote medical tourism. It was conducted in West Asia in 2009 which covered countries like Riyadh, Kuwait, Doha and Dubai.

5. **Publicity:** Advertising and Publicity material are produced by the Ministry of Tourism and circulated in different target markets. The material includes CDs, brochures and other publicity material.

Medical tourism is helping the country in earning foreign exchange and adding to the revenues of the country. It is also helping in improving the general and health infrastructure. Hospitals are giving higher remuneration to doctors, which is possible due to earnings from medical tourism. This in a way is good as it is preventing brain drain and we are able to retain good doctors within the country.

If India is able to utilize the earnings from foreign patients in creating health resources for the country's poor and needy, we will be able to justify the promotion of medical tourism and create a balance.

REFERENCES

1. Woodward, D., Drager, N., Beaglehole, R., & Lipson, D. (2001). Globalization and health: a framework for analysis and action. *Bulletin of the World Health Organization*, *79*(9), 875-881.
2. Cornia, G. A. (2001). Globalization and health: results and options. *Bulletin of the World Health Organization*, *79* (9), 834-841.
3. Carrera, P. M., & Bridges, J. FP.(2006). Globalization and healthcare: Understanding health and medical tourism. *Expert Review of Pharmacoeconomics & Outcomes Research*, *6*(4), 447-454.
4. Crooks, V. A., Kingsbury, P., Snyder, J., & Johnston, R. (2010). What is known about the patient's experience of medical tourism? A scoping review. *BMC Health Services Research*, *10*(1), 266.
5. Horowitz, M., & Rosenweig, J. (2007). Medical Tourism -- Health Care in the Global Economy. *Physician Executive*, *33*(6), 24-30.
6. Helble, M. (2011). The movement of patients across borders: challenges and opportunities for public health. *Bulletin of the World Health Organization*, *89*(1), 68-72
7. Woodman, J. (2008). *Patients beyond borders: Everybody's guide to affordable, world-class medical travel*. (2 ed.). NC, USA: Healthy travel media.
8. Chaudhary, M., Prakash, M., Tyagi, N., &Devrath, R. Government of India, Department of Tourism. (2011). *A study of problems and challenges faced by medical tourists visiting India*
9. Renub Research (2012). India Medical Tourist Arrivals, medical Tourism Market & Forecast to 2015. http:// www.renub.com/report/india-medical-tourist-arrivals-medical-tourism-market-forecast-to-2015-62 accessed 20.05.2014
10. Koncept Analytics (2014). Medical Tourism Market Report: 2014 Edition. http:// www.marketreportsonline.com/344924.html accessed 28. 07.2014
11. Reese, S. (2007). CARE Beyond Borders. *Managed Healthcare Executive*, *17*(5), 33-36

INTERNATIONAL JOURNAL OF ENGINEERING SCIENCES AND MANAGEMENT (ISSN: 2231-3273)

International Journal of Engineering Sciences and Management is a bi-annual journal of Dronacharya Group of Institutions, Greater Noida, UP, India.

1. SCOPE OF THE JOURNAL

To publish full-length research papers in any one or more of the following disciplines:
Computer Science & Engineering, Information Technology, Electrical, Electronics & Communication Engineering, Mechanical Engineering, Civil Engineering, Physics, Mathematics, Economics, and Management.

2. PURPOSE OF THE JOURNAL

To keep the academic community abreast of the research and technical scenario in the stated disciplines in the world.

3. CHERISHED AIM OF THE JOURNAL

To excite and ignite the young minds and to motivate them for involving themselves in research and development activities. This will empower our manpower in the context of fast changing technologies across the globe.

4. GUIDELINES FOR AUTHORS

SUBMISSION OF MANUSCRIPTS: Soft copy of the manuscript for consideration of publication should be sent (as MS Word Windows 2007 attachment) by Email to the Executive Editor at advisor.r&d@gnindia.dronacharya.info

All papers, received for consideration of publication and complying with the below-mentioned format will be sent for review to at least two referees. In accepting the paper for publication, the Editors and reviewers will give special weight to readability and interest value for a wide readership besides the originality and the high-standard of its contents. The Executive Editor's decision is final in case of non-unanimity of opinion of referees. Under normal circumstances, the authors will be informed about the status of their papers by the Executive Editor within eight weeks of their submission.

PREPARATION OF MANUSCRIPTS:

- **Manuscript** : Manuscript should be in English, the preferred spelling being that of the Concise Oxford Dictionary. It should be in 'Times New Roman', single-spaced, and typed on 8.5" x 11" or A4-size paper with margins of 1" (25 mm) on each side. Manuscript should be typed in ***single column*** only (and not in double or triple columns).

- **Title of Paper** : Font size 16, ALL CAPITALS, bold, centered, and ***not underlined***. The title must be 12.5 mm below the top of the page (in addition to the standard 25 mm margin). The Title should adequately describe the contents of the paper.

- **Full names of all Authors**, with * as superscript with corresponding author's name and his/her Email ID (Font size 12, centered) and also the contact number. A blank line should be left between the title and the author's name(s).

- **Full postal address** along with affiliations (Font size 10, centered).

- **Abstract** (Font size 10, centered) All papers must have a non-mathematical abstract of not more than 200 words. The abstract should indicate the general scope of the paper, the important findings and the conclusions drawn. The abstract should include only text. It should be specific about the methodologies used and the conclusion drawn of the work reported. Please avoid the use of abbreviations and references. (Text of the Abstract: Font size 9, single-space, justified).

- **Keywords:** Include up to six keywords that describe your paper for indexing and for web searches. The more discriminating your keywords are, the greater is the likelihood that your article will be found and cited. (Font size 9, italics, left-justified).

- **Text:** (Font size 10, Justified). The paper must be divided into sections starting preferably with "Introduction" and ending with "Conclusion". The main sections should be numbered 1, 2, 3 etc and subsections as 2.1, 2.2 etc. Main headings should be typed in capitals, subheadings in lower case. Both types of heading should be underlined and left-justified. Footnotes should be avoided. Equations should be typewritten and with the equation number placed in parentheses at the right margin. Reference to the equation should use the form 'Eq. (3)'. Use extra line spacing between equations, illustrations, figures and tables. The use of SI units is strongly recommended.

- **Tables and Figures**: Tables and Figures should be integrated with the text (and not sent separately at the end of the manuscript) and numbered consecutively in the order in which reference is made to them in the text of the paper. All captions must be centrally located above a Table and below a Figure (Font size 10). All tables and figures must be numbered consecutively in Arabic numerals (not Roman) (e.g., Table 3 or Fig. 3) in the order of appearance in the text. Tables & Figures should be reproduced in the exact format and at the exact place as desired to appear in the journal.

- **Conclusion:** A conclusion section must be included and should indicate clearly the advantages, limitations and possible applications of the paper. Authors may also discuss about the scope of future work.

- **Acknowledgements:** An acknowledgement section may be included after the 'Conclusion'.

- **References:** It is mandatory for references to be quoted in the text and be placed at the **end of the text.** They should be **numbered consecutively in order of their citation** in the text and be indicated by **superscripts** in the text of the manuscript. Examples of different citations as References are given below:

(i) In case of referring to an Article in a Journal

Kuebel, D.; Lahiri, M. & Wolf, E. *An Inverse Problem in the Theory of Stochastic Electromagnetic Beams*, Opt. Commn., **282**, 2009, p.141.

(ii) In case of referring to a Book/Monograph

Rao, C.N.R. & Raveau, B. (Eds.). *Transition Metal Oxides*, Wiley-VCH, 2nd Edition, 1998, Ch. 2.

(iii) In case of referring to a Conference Paper

Ctvrtnickova, T.; Mateo, M; Yanez, A. & Nicolas, G. *Characterization of Coal Fly Ash Components by Laser-Induced Breakdown Spectroscopy*. Presented at the Fifth International Conf. on Laser-Induced Breakdown Spectroscopy, Berlin, Adlershof, Germany. Sep 22-26, 2008, CP-15, p. 67-68.

(iv) In case of referring to a Report

Marine, R.E. & Iliff, K.W. *Application of Parameter Estimation to Aircraft Stability and Control.* NASA, USA, 1986, Report No. NASA-RP-1168.

Papers quoting the LATEST references from the referred journals will be preferred for publication unless the original contribution from the author/s is of a very high standard.

UNDERTAKING

Authors must include, in the covering Email that their paper has not been published//accepted/submitted for publication/ presentation to any other journal/ book/conference in any form and the work submitted by them is their own and original. The same 'Undertaking' should also be attached, on a separate page, along with the manuscript. This ethical policy of the Journal will be strictly adhered to.

Note : Manuscripts not in conformity with these 'Guidelines' will not be forwarded to the experts for review.

DRONACHARYA
GROUP OF INSTITUTIONS

EMPOWERING
you to turn your dreams into reality

B. TECH Courses
Computer Science & Engineering

Information Technology

Computer Science & Information Technology

Electronics & Communication Engineering

Electrical & Electronics Engineering

Electronics & Computer Engineering

Mechanical Engineering

Civil Engineering

POST GRADUATE Courses
MBA | MCA

Approved by:
All India Council for Technical Education, New Delhi (India)

Affiliated To:
Uttar Pradesh Technical University (UPTU), Lucknow (India)

DRONACHARYA GROUP OF INSTITUTIONS
Campus: #27, Knowledge Park- III, Greater Noida (UP)
Phone: 0120-2323851-58 | Email: info@dronacharya.info

IJESM SIGHTINGS

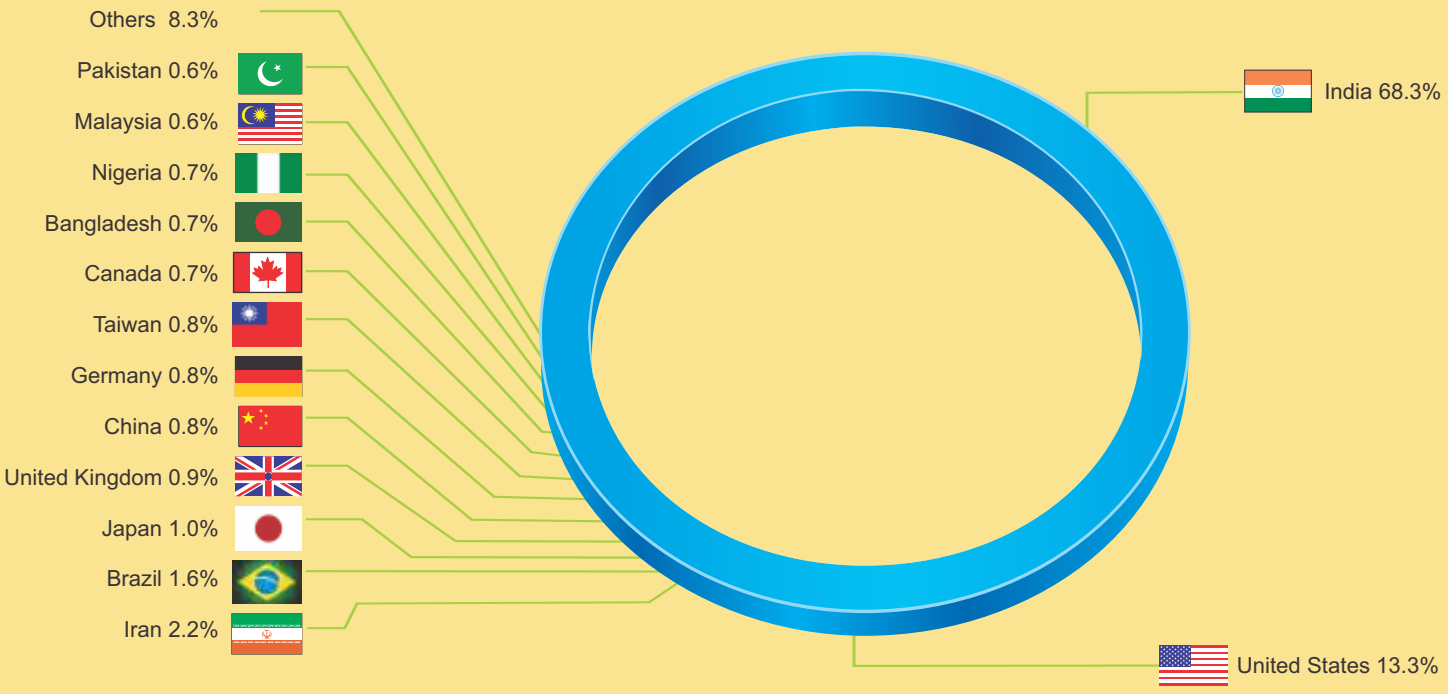

www.dronacharya.info

Approved by
All India Council for Technical Education, New Delhi (India)

Affiliated To:
Uttar Pradesh Technical University (UPTU), Lucknow (India)

Campus:
27, Knowledge Park-III, Greater Noida (U.P.) – 201308 (India)
Phone: 0120-2323854-58, Email: director@gnindia.dronacharya.info

Corporate Office:
76P, Part-III, Sector-5, Gurgaon, 122001, Haryana (India)
Phone: 0124-2251602, 2253144, Email: info@dronacharya.info